University of Imperial College London
Department of Aeronautics

Computational modelling of airflow and transport in the upper respiratory tract

Qiwei Xiao

Submitted in part fulfilment of the requirements for the degree of
Doctor of Philosophy in Aeronautics and
the Diploma of Imperial College London, April 2019

Abstract

This thesis comprises an investigation of the dynamics of airflow in the upper respiratory tract from the nose to the carina using computational modelling. The work primarily considers inspiratory flow and comprises separate detailed studies of airflow in three distinct regions: the nose, the larynx and the trachea.

In the nose, both airflow dynamics and the associated processes of heat and water exchange are studied. The geometry of the nasal cavity is highly variable both inter- and intra- subjectively. The consequences of inter- and intra-subject variability for both airflow and exchange processes during inspiration is investigated using 10 subject geometries obtained by MRI scans in the decongested and congested states. Non-dimensional scalings are applied to quantify the effects of flowrate and geometry on wall shear stress, heat and water transport . It is found that the anterior nasal cavity contributes most to the exchange process and that decongestion generally affects the distribution of inspiratory flow, promoting a switch towards more inferior pathways.

Flow in the larynx is controlled by the position of the vocal folds, which determine the glottis aperture. Even with the vocal folds fully abducted, inspiratory airflow experiences a degree of constriction and exits the glottis as a jet which dissipates in the trachea. The effect of glottis aperture on pressure loss and flow structure is examined, and the results compared with those from a separate experimental investigation.

In pathological tracheal geometries, characterized by severe constriction and deviation as caused by compressive retrosternal goitre, far more severe pressure losses may occur than in the normal trachea. The third investigation performed in this work describes a computational approach to assess pathological tracheal resistance. Direct and large eddy simulation results are applied to determine the profile of energy dissipation in the case of a progressive tracheal compression. The study examines the effects of inflow disturbances on the breakup of the jet downstream of the constriction and the consequent loss characteristics. The effect of domain truncation, associated with the typical field of view of clinical imaging, is an important consideration and is investigated.

Declaration

This is the statement of clarification that in this thesis all my original works are carried out at Imperial College London. It has not been submitted to any other university or technical institution for any degree or award. The acknowledgement are made where appropriate.

Signature: _____

Qiwei Xiao

Copyright Declaration

The copyright of this thesis rests with the author Creative Commons Attribution-Non Commercial No Derivatives Licence. Under this licence, researchers may copy and redistribute the material in any medium or format. However, you are not allowed to alter it, conduct any other derivative works or build up on it, for any commercial purpose. When reusing or sharing this work, ensure you make the licence terms clear to others by naming the licence and linking to the licence text.

Acknowledgements

Firstly, I would like to give my appreciation to my supervisor Professor Denis Doorly who has guided me throughout my PhD, although the completion of this thesis is attributed to a number of colleagues. Professor Denis Doorly as my supervisor, he provide me with consistent help for my transition to academia through his patience, motivation and immense knowledge. I could not have imagined having a better advisor and mentor for my PhD study. Besides my supervisor, I would like to give my appreciation to Professor Bob Schroter as well, his advices on the physiology side especially are invaluable.

Secondly, I want to give my gratitude to all my colleagues who have helped me. Dr. Alister J. Bates who has given me enormous help on the technical side when I just started my PhD study. Dr. Raul Cetto and Dr. Lulu Ritchie who have performed the medical image segmentation on the nasal cavity and tracheal geometries respectively. Furthermore, Dr. Lulu Ritchie also helped me with the understanding of the airways from the surgeon's perspective. Jan N Rose as my current colleague, he provided some technical help on the post processing of the results.

Last but not least, I want to thank my family: my parents who give me the financial support to finish this PhD and my wife who have been through this with me all the time.

Contents

Abstract **1**

Declaration **2**

Copyright Declaration **3**

Acknowledgements **4**

1 Introduction **34**

1.1 Airway geometry 34

1.2 Mechanics of breathing 38

1.2.1 Temporal flow profiles 38

1.2.2 Fluid mechanics of upper airway flow 40

1.2.3 Heat and water exchange in the upper airways 41

1.2.4 Laryngotracheal flow studies 47

1.2.5 Energy cost of flow transport through upper airways 49

1.2.6 Outline of the thesis 50

2 Methodology **52**

2.1 Models of flow and heat transfer 53

2.2 Nasal cavity flow 65

2.2.1 Definition of simulation 65

2.2.2 Spatial convergence 66

2.2.3 Temporal convergence 67

2.2.4 Water flux balance 69

2.3 Nasal cavity boundary conditions 70

2.3.1 Heat and water flux boundary condition: choice of model and definition of exchange region 72

2.3.2 Membrane thickness sensitivity 76

2.4 Laryngo-tracheal flow 77

2.4.1 Transitional and turbulent flow models 77

2.4.2 Definition of simulation 81

2.4.3 Spatial convergence 81

2.4.4 Temporal convergence 82

2.5 Laryngo-tracheal boundary conditions 83

2.6 Definition of flow metrics 84

3 Geometry and airflow in congested and decongested nasal cavities. **94**

3.1 Subject specific analysis of nasal airflow 95

3.1.1 Definition of planes 95

3.1.2 Cross-sectional area variation 96

3.1.3 Reynolds number variation 97

3.1.4 Flow field variation 99

3.1.5 Wall shear stress distributions 101

3.1.6 Effect of flowrate 104

3.2 Bilateral nasal cavity geometric and flow analysis 111

3.2.1 Geometry comparison 111

3.2.2 Reynolds number 116

3.2.3 Flow partitioning: top, middle and lower 117

3.2.4 Pressure loss and resistance 120

3.2.5 Friction coefficient and Poiseuille number 126

3.2.6 Correlation analysis 130

3.3 Unilateral nasal cavity geometric and flow analysis 132

3.3.1 Geometric comparison 132

3.3.2 Flow partitioning: left and right 134

3.3.3 Resistance 135

3.3.4 Friction coefficient and Poiseuille number 137

3.3.5 Correlation analysis 141

4 Heat and water transport in congested and decongested nasal cavities. 143

4.1 Subject specific analysis of heat and water transport within nasal cavity 144

4.1.1 Surface maps of dry heat exchange 144

4.1.2 Surface maps of water exchange 147

4.1.3 Comparison with previous studies. 150

4.1.4 Effect of different flowrates 151

4.1.5 Effect of different ambient conditions 154

4.1.6 How similarly do results scale with flowrate for other subjects? 159

4.2 Bilateral heat and water analysis 160

4.2.1 Temperature and moisture 160

4.2.2 Heat and moisture transfer coefficients analysis 164

4.2.3 Correlation analysis 175

4.3 Unilateral heat and water analysis 178

4.3.1 Temperature and moisture 178

4.3.2 Heat and moisture transfer coefficients analysis 180

4.3.3 Correlation analysis 186

5 Laryngo-tracheal flow analysis **188**

5.1 CFD and Experiment results 190

5.2 Effect of glottis aperture and flowrates 195

6 Tracheal stenosis flow analysis **201**

6.1 Material and Methods 202

6.1.1 Image Data 202

6.1.2 Airway Geometry Definition 204

6.2 Results and Discussion 205

6.2.1 Geometry 205

6.2.2 Flow Analysis 208

7 Discussion, conclusions and suggestions for further work 222

7.1 Nasal airway flow: discussion and conclusions 223

7.2 Laryngeal airway flow: discussion and conclusions 229

7.3 Tracheal airway flow: discussion and conclusions 230

7.4 Further work 232

Bibliography 232

Appendices 251

A For chapter 2 252

A.1 Mesh quality check guidelines 252

A.2 Temporal mean range 252

A.3 Nasal cavity mesh statistics 253

A.4 Subject D cavity mesh independent check 256

A.5 Two-film theory 258

A.6 Complete airway mesh statistics 258

A.7 T15 mesh statistics 261

B For chapter 3 **263**

B.1 Bilateral geometric data 263

B.2 Bilateral Correlations 265

B.3 Unilateral geometric data 266

B.4 Unilateral correlations 268

C For chapter 4 **269**

C.1 Bilateral SAVR and THF, TH2OF 270

C.2 Unilateral SAVR correlations 271

D For chapter 6 **272**

D.1 Convergence Analysis 272

D.2 Work-Energy Balance 273

D.3 Turbulence Intensity and Wall Shear Stress 273

D.4 Pressure Loss of T4-L 275

D.5 Flow loss factors 275

List of Tables

2.1 Nasal cavity simulation setup details. 65

2.2 Subject-D temporal resolution independent check. Besides total pressure loss, there are two other quantities that being studied: total amount of heat transferred as well as the total amount of water. D(c) represents the subject D congested cavity with 4 million mesh elements. 68

2.3 Transition region heat and moisture boundary conditions. In the transition region, the surface value is calculated by interpolating between conditions specified at the planes denoting start and end of the transition region. Lower case d_x, e.g. d_1, d_2, d_3 and d_{AS} represent distances of an arbitrary point on the surface to the bounding planes of the appropriate transition region, for example d_1, d_3 are used between planes 1 and 3 and d_2 , d_{AS} between planes 2 and AS. The surface mass fraction of water of BC5 is calculated using two-film theory rather than simply assuming a fully saturated condition on the cavity surface. 74

2.4 Mesh independence checks for trachea simulations with nasal cavity attached. . 82

2.5 Temporal resolution effect on the overall mean total pressure loss of laminar model simulation. 83

3.1 Mass flow split ratio with various flow rate. 104

3.2 This table shows the mean location of each plane of all the subjects in the second row and the third row lists the SD of each plane accordingly. 115

3.3 Dominant side of nasal cavity with value one and non-dominant side identified by value zero. 132

4.1 Simulation results at anatomic similar locations as Keck et al. [1]. 151

4.2 Convertin of relative humidity to absolute humidity. 155

4.3 This table lists the ratio between inflow temperature at the nasopharynx plane of the cavity over the difference between inflow temperature and alveoli temperature. 162

4.4 This table lists the mean heat film coefficient and Nusselt number for the cohort subjects of different geometry regions, e.g., the whole nasal cavity (between plane Nos and PS), anterior cavity (between plane Nos and plane 1V), posterior cavity that defined by plane 1V and PS. 168

4.5 This table shows the mean heat film coefficient ratios of different geometric partitions between the higher and lower flowrates. 168

4.6 The ratios of friction coefficient over multiple quantities, i.e, Nusselt number, Sherwood number, both heat and mass Stanton number. All the ratios are using the mean values of the whole cavity of each quantity. The last row gives the mean ratio of flowrate at 30 L.min^{-1} directly, without showing each value of every subjects. Ideally, the ratio between frictional coefficient and Stanton number is 2 for laminar flow. 170

4.7 This table lists the mean mass film coefficient at different flowrates of the same geometric partitions as described in table 4.4. 174

4.8 This table shows the mass film coefficient ratio between higher and lower flowrates within three geometric partitions: whole cavity (Nos-PS), anterior cavity (Nos-1V) and posterior cavity (1V-PS). 174

5.1 Flowrate at 50 L.min^{-1} for partly abducted glottis (10 degrees). This table compares the overall total pressure loss of different flow models. The relative errors compared to qDNS simulation are shown in the right column. 193

6.1 Geometric data of tracheal lumens. The percentage constriction is defined as the CSA ratio: $(CSA_{FirstRing} - CSA_{min})/CSA_{FirstRing}$ and is 82.5% for T15. 207

6.2 Geometric data for T15 and short cases 215

6.3 Turbulence intensity value for all T15 geometries 216

6.4 Data for power law fit for flow rate vs pressure loss of the most constricted geometry T15-Long. 220

A.1 Nasal cavity mesh statistics with multiple mesh settings. 254

A.2 Subject D congested mesh independent check. The finest case D(f) have the same amount mesh element of D(e) but with one tenth of its times step. 256

A.3 Subject D decongested mesh independent check. 257

A.4 Simulation of complete airway mesh statistics. 259

A.5 qDNS mesh refinement details of complete airway 259

A.6 Simulation of T15 mesh statistics. 261

A.7 qDNS mesh refinement details of T15 261

B.1 Nasal cavity surface area and volume data. 263

B.2 Congested area volume ratio. 264

B.3 Decongested area volume ratio. 264

B.4 Unilateral nasal cavity surface area and cavity volume. 266

B.5 Unilateral nasal cavity area volume ratio. 267

D.1 Mesh convergence check. 272

D.2 Pressure loss over bronchi of T4-L. 275

List of Figures

1.1 Nasal cavity anatomical diagram. 35

1.2 Trachea anatomy. 37

2.1 Heat model diagram. 59

2.2 Water model diagram. 61

2.3 Initial state of the boundary value: δ_{wall} is the thickness of the first cell of the volume mesh and δ_{memb} is the membrane thickness and where 'n=0' indicates the initial state. Note: first order in space treatment of the boundary condition is using and is more stable 63

2.4 Total pressure loss plot along with simulation physical time. 69

2.5 Comparison between integrated water flux from nasal cavity surface and the difference of water flux between inflow and outflow. 70

2.6 Demonstration of artificial inlet and outlet boundaries. The diameter of half sphere inlet is 1m and the outlet extrusion length is 0.05m to assure the ideal flow profile. 71

2.7 Partition defined for transitions from 'dry' surface to water exchanging surface. T_1, T_2, T_3 and T_{AS} represents the temperature at location of plane 1, 2, 3 and AS; T_a means the temperature of inflow stream. 73

2.8 Initial condition with displayed by scalar map of multiple boundary conditions. . 75

2.9 Cumulative anterior to posterior local water flux from cavity surface. 76

2.10 Comparison between water flux transferred from cavity surface and the difference between inflow and outflow within the geometry range of plane AS and PS. . . . 77

2.11 Figure a shows the boundaries for healthy subject laryngotracheal flow simulation, while figure b shows the boundaries for pathological laryngo-tracheal flow simulation. 84

3.1 Subject D congested cavity geometric view that rendered by STAR-CCM+. Blue lines are planes that defined according to anatomical landmarks and the red dashed line is an indication of nasal cavity centerline within normalized value between 0 and 1. The grey lines are the projection view of cross-sectional slices along the cavity centerline. 96

3.2 The horizontal axis represents the normalised centerline distance and labelling with the anatomical markers that defined previously. Those abbreviations are: Nos = nostril plane, NV = nasal valve plane, AS = anterior septum plane. 1V = first vertical plane, 2V = second vertical plane, 3V = third vertical plane and PS = posterior septum plane. The magenta line in the figure shows the results from Zhao et al [2]. For both congested (left figure) and decongested (right figure) cavities, the unilateral and bilateral cavity cross-sectional area distribution are plotted and compared with Zhao et al. results. 97

3.3 Decongestion effect on Reynolds number variations of subject D at flowrate of 30 L.min^{-1}. 99

3.4 Subject D cavity cross-sectional planes view of velocity field at flowrate of 30 L.min^{-1}. Figure 3.4a is congested cavity and figure 3.4b is the decongested cavity. 100

3.5 Subject D sagittal plane view of total pressure distribution at flowrate of 30 L.min^{-1} for both congested and decongested cavities. Figures on the left are representing the left cavity while the right side means the right cavity. Same sagittal plane is taken on each side of the cavity before and after decongestion. . 100

3.6 Subject-D congested VS decongested WSS distribution on turbinates. Figure 3.6a-3.6d are the turbinates views that with the removal of septum, while figure 3.6e-3.6h are the turbinates that viewed from outside of the turbinates. . . 102

3.7 Subject D congested VS decongested WSS distribution on septum. Figure 3.7a and 3.7b are the congested left and right cavity separately, while the lower pair are the decongested cavities. 103

3.8 Bilateral cavity pressure and resistance distribution comparison before and after decongestion with multiple flowrates. Figure a shows the total pressure loss across the cavity from nostril plane until the posterior septum. Similarly, figure b shows the same results but after decongestion. Correspondingly, resistance is plotted for congested and decongested cavities as shown in figure c and d separately. 105

3.9 Left and right cavity pressure and resistance distribution. Figure a-d show the distribution for total pressure loss on each single side of the cavity with flow rate raising from 15 to 30 L.min^{-1}. Resistance distribution is displayed by figure e-f in the same way as total pressure loss. 106

3.10 Static pressure distribution across the cavity with multiple flowrate on each single side of the cavity. Figure a-b are the results under congested states and c-d are the results after decongestion. 107

3.11 Decongestion effect on bilateral cavity Fanning drag coefficient and Poiseuille number with multiple flowrate studied. The left pair show the results for congested cavities, while the right pair are for decongested cavities. 109

3.12 All the plots show the Fanning drag coefficient distribution along the cavity centerline of subject D. For each single plot, it shows the comparison with multiple flowrates. Figure 3.12a and 3.12c are the results for congested cavity and figure 3.12b and 3.12d are for decongested cavity. 110

3.13 All the plots show the Poiseuille number distribution along the cavity centerline of subject D. For each single plot, it shows the comparison with multiple flowrates. Figure 3.13a and 3.13c are the results for congested cavity and figure 3.13b and 3.13d are for decongested cavity. 111

3.14 This figure shows the decongestion effect on geometric changes by showing the results of Wilcoxon signed-rank test. Reading from a to c, plots show comparisons for: bilateral area, bilateral volume and bilateral SAVR separately. 112

3.15 Anterior cavity minimum cross-sectional area comparisons for congested and decongested cavities, with h value shown for application of the Wilcoxon signed-rank test; h = 0 means the null hypothesis has been accepted. 113

3.16 Bilateral significance test of top, middle and lower cavity SAVR before and after decongestion. 114

3.17 Comparison between congested and decongested bilateral cross-sectional area distribution with one standard deviation error bar. Red line represents the mean value of cross-sectional area distribution among all the congested cavities and blue line shows the results for decongested cavities. Zhao et al.'s results are plotted together with the congested cavities plot. 116

3.18 Mean Reynolds number comparison. Left pair (red line) represent the congested cavity and right pair (blue line) represent the decongested cavity. 117

3.19 Decongestion effect on the mass flow split ratio over top, middle and lower regions of all the bilateral cavities. Each line represents the mean value of the 10 subjects and two flowrates are compared: 15 and 30 L.min^{-1}. 118

3.20 Flow rate and decongestion effect on frictional force split ratio among top, middle and lower sections of nasal cavity. 120

3.21 Intranasal cross-sectional plane averaged total pressure distribution along the cavity. Figure 3.21a and 3.21b show the results of 15 L.min^{-1} and 3.21c and 3.21d are the results for 30 L.min^{-1}. 121

3.22 Significance test between congested and decongested cavity of total pressure loss. Left figure shows the result of 15 L.min^{-1} and right figure is the result of 30 L.min^{-1}. 122

3.23 Intranasal cross-sectional plane averaged static pressure distribution along cavity centerline with two different flow rate as label in the figure. 123

3.24 Significant test of static pressure loss between congested and decongested cavity. Left figure shows the flow rate at 15 and right is 30 L.min^{-1} 123

3.25 Intranasal cross-sectional plane averaged resistance distribution along cavity centerline. The solid line is the mean value among all the subjects considered and the errorbar is the value of one standard deviation. 124

3.26 Significance test of cavity total resistance between congested and decongested conditions. Left figure shows the result of flow rate 15 L.min^{-1} and right figure is the result of flow rate 30 L.min^{-1}. 125

3.27 Anterior and posterior nasal airway resistance. Upper left right pair: anterior resistance. Nos-1V denotes nostril (Nos) to approximate location of anterior head of middle turbinate (plane 1V), Lower left right pair: posterior resistance. 1V-PS denotes plane 1V to posterior septum (PS). 126

3.28 Effects of decongestion and change of flowrate on frictional coefficient and Poiseuille number distribution. Figure 3.28a and 3.28b are the frictional coefficient distribution and figure 3.28c and 3.28d are the Poiseuille number distribution under two flowrates as labelled. 127

3.29 Decongestion effect on bilateral cavity mean Fanning drag coefficient and Poiseuille number. 128

3.30 Flow rate effect on bilateral cavity mean Fanning drag coefficient and Poiseuille number. 128

3.31 Decongestion and flow rate effects on the anterior and posterior part of the cavity for Fanning drag coefficient. 'Nos-1V' means the cavity region defined by nostril plane and 1V plane and the corresponding plot shows the value that averaged with this region. '1V-PS' defined the same way but by plane 1V and PS. Figure 3.31a and 3.31b are the test of decongestion effect, while the lower pair are the test of the effect of change of flowrate. 129

3.32 Decongestion and flow rate effects on the anterior and posterior part of the cavity for Fanning drag coefficient. 'Nos-1V' means the cavity region defined by nostril plane and 1V plane and the corresponding plot shows the value that averaged with this region. '1V-PS' defined the same way but with plane 1V and PS. . . . 130

3.33 Bilateral SAVR, TPL and TWSS. 131

3.34 Unilateral SAVR before and after decongestion comparison. 133

3.35 Decongestion effect on mass flow split ratio between left and right cavity, or dominant and non-dominant side. 135

3.36 This figure shows the unilateral resistance distribution across the cavity for both congested and decongested cavities of two flowrates. Red line represents the congested cavity and blue line represents decongested cavity. 136

3.37 Unilateral total resistance before and after decongestion at two flowrates. Median values and significance test results for comparisons are overlaid. 137

3.38 Fanning drag coefficient distribution along the cavity centerline from anterior to posterior at two flowrates of congested and decongested cavities. 137

3.39 Poiseuille number distribution across the cavity for both congested and decongested cavities at two flowrates. 138

3.40 Effects of decongestion and of flowrate on the cavity mean value of both Fanning drag coefficient and Poiseuille number. In the top pair figure 3.40a and 3.40b, results are compared between congested and decongested cavities at the same flowrate for Fanning drag coefficient and Poiseuille number separately, while the lower pair figure 3.40c and 3.40d, the results are paired to aid comparison of the flowrate effect for the same state (congested or decongested) on same quantities. 139

3.41 This figure computed friction coefficient results arranged to facilitate comparisons of effect size. Top pair (a and b): comparing effect of decongestion on friction coefficient for anterior nose (Nos-1V) and for posterior nose (1V-PS) at the same flowrate. Lower pair (c and d): comparing effect of flowrate on friction coefficient for anterior nose (Nos-1V) and for posterior nose (1V-PS) under the same geometric states (congestion or decongestion). This is a breakdown of the results from figure 3.40. 140

3.42 Figure 3.42a is the comparison of decongestion effect size n mean Poiseuille number at same flowrate. Unilateral cavity results are partitioned into anterior region (between nostril and 1V) and posterior cavity (between 1V and PS). Figure 3.42c and 3.42d compare the effect of flowrate on Poiseuille number for the same geometry. 141

3.43 Correlations of SAVR to TPL and TWSS. The top pair shows the correlations of SAVR to TPL at both lower and higher flowrates, while the lower pair is the same but for correlation between SAVR and TWSS. 142

4.1 Comparison of dry heat flux for left and right noses of subject D, with superimposed surface streamlines indicating the near wall flow direction. Figure 4.1a-4.1d are organized so that left and right column views correspond respectively to the left and right cavities; the top pair compare left and right for the congested cavities and the lower pair are for the decongested cavities; in these four views (a to d), the septum has been removed to expose the turbinates. Similarly, figure 4.1e-4.1h also show the dry heat flux on the cavity surface, but viewed from the opposite (maxillary sinus side, but with the sinus removed). 146

4.2 This figure shows the dry heat flux map on the cavity septum surface between congested and decongested cavities. Again, sub-figure 4.2a on the left side represents the congested left cavity surface with the view of septum. Similarly, the top right corner (sub-figure 4.2b) represents the congested right cavity septum view. Furthermore, sub-figures 4.2c and 4.2d show the same quantity with the same view but for decongested cavities. 147

4.3 Comparison of surface water flux values between congested and decongested cavities of subject D. Sub-figures a and c compare the left cavity with the septum removed to expose the turbinates. Correspondingly, sub-figures b and d compare congested and decongested right cavities. Sub-figures e to h display the surface water flux on the cavity turbinate, but with the view from the outside of the turbinates. 149

4.4 The surface water flux distribution on the cavity septum are shown here. The patterns of water flux seen on the turbinated wall in the previous views are broadly similar to those on the septal surfaces. 150

4.5 Effect of flowrate on the distribution of temperature, water content level, heat film coefficient and mass film coefficient, plotted along the cavity centerline of subject D congested cavity. 152

4.6 This figure shows the distributions for the same quantities as figure 4.5, but plotted in the left and right cavity individually of congested cavity of subject D. Figures on the left are representing the left cavity and figures on the right side represent those for the right cavity. 153

4.7 This figure shows the intranasal distributions of multiple measurements of the bilateral subject D cavity. Following the reading orders are: temperature, moisture content level, heat film coefficient and mass film coefficient respectively. 155

4.8 Unilateral temperature, moisture content level, heat and mass film coefficient distribution along the cavity centerline. Figures on the left column (a,c,e,g) represent the left cavity while figures on the right column (b,d,f,h) represent the right cavity. 157

4.9 Figure a shows the log of flowrate versus log of mean heat film coefficient of the bilateral cavity for subject D, whilst figure b shows the same but for mass film coefficient. Figure c and d apply the mean gradient calculated from the curves shown in figures a and b to predict the corresponding values for the other subject geometries. 159

4.10 Mean temperature and one standard deviation bilateral temperature distribution for all 10 subjects from anterior to posterior of the cavity. Left are for subjects in congested state and right for decongested conditions. Upper pair are for the lower flowrate and lower pair for higher flowrate. For reference, inhaled air is at 25°C and 50% relative humidity. 161

4.11 This figure compares the temperature at the nasopharynx plane between congested and decongested cavities. Appling the Wilcoxon singed-rank test shows the significant changes due to decongestion. Figure on the left is for a flowrate of 15 L.min^{-1} and on the right for a higher flowrate at 30 L.min^{-1}. 162

4.12 Mean moisture content level of all the subjects distribution from anterior to posterior part of the cavity. Figure a to b are comparing the decongestion effect of flowrate at 15 L.min^{-1}, while figure c to d are the same but with the flowrate doubled. 163

4.13 Nasopharynx plane moisture content level between congested and decongested cavities are tested by Wilcoxon singed-rank test at two flowrates. The results for both flowrates show that there is significant decrease statistically of moisture content level at nasopharynx plane after decongestion. 164

4.14 Bilateral heat film coefficient and Nusselt number distribution between congested and decongested cavities as well as different flowrate. 165

4.15 Heat film coefficient box plots for the anterior cavity (plane Nos-1V) and for the posterior cavity (plane 1V-PS). The upper pair (a,b) compares effect of decongestion at a given flowrate and the lower pair (c,d) compares the effect of flowrate for give state (congested or decongested). 166

4.16 Decongestion and flowrate effect on mean Nusselt number within anterior (between plane Nos and 1V) and posterior (between plane 1V and PS) separately. Figure a and b are the test of decongestion, whilst c and d are for the flowrate change test. 167

4.17 Mass film coefficient and Sherwood number between congested and decongested cavities under both higher and lower flowrates. The upper pair (a,b) are the intranasal mass film coefficient distribution along the cavity centerline, while the lower pair are the same but for Sherwood number. 171

4.18 Bilateral mean mass film coefficient, within anterior part (between plane Nos and 1V) and within posterior part (between plane 1V and PS), Wilcoxon singed-rank test, before and after decongestion as well as before and after increase of flowrate, are distributed by this figure. 172

4.19 This figure distributes the same test results as figure 4.18, but for quantity Sherwood number instead. 173

4.20 Figure a shows the correlations between bilateral SAVR and temperature at nasopharynx plane. Figure b shows the correlations between bilateral SAVR and moisture content level at nasopharynx plane. 175

4.21 The correlation plots between surface total wall shear stress (TWSS) and both the total heat flux transferred and total amount of water transferred. 176

4.22 Correlation between total heat flux and total water flux transferred under two flowrates. 177

4.23 Mean temperature distribution of all the unilateral cavities from nostril to posterior septum. The upper pair represents the results for lower flowrate (15 L.min^{-1}) simulations before and after decongestion, while the lower pair is the results for higher flowrate (30 L.min^{-1}). Note particularly the flowrate labelled represents the bilateral flowrate and the unilateral values need to deduce from the mass flow split ratio. 178

4.24 Unilateral Wilcoxon signed-rank test for temperature at posterior septum plane before and after decongestion. 179

4.25 This figure, again, shows the same distributions but for quantity moisture content level for unilateral cavities. 179

4.26 Wilcoxon singed-rank test for the moisture content level at plane PS of unilateral cavitites. 180

4.27 This figure shows the same distribution as figure 4.14, but this is for unilateral cavities instead. The upper pair (a,b) represent the heat film coefficient result, whilst the lower pair (c,d) are for the intranasal Nusselt number. 181

4.28 This figure shows the significance test results for the heat film coefficient for both the effect of decongestion and the effect of double the total mass flowrate. The upper pair (a,b) represent the effect of decongestion on heat film coefficient within both the anterior (between plane Nos to 1V) and posterior (between plane 1V and PS) cavity, while the lower pair (c,d) are the same but for the effect of doubling the total mass flowrate. 182

4.29 Decongestion and flowrate effect on the mean Nusselt number within anterior (plane Nos to 1V) and posterior (plane 1V to PS) cavity separately. The upper pair are for the effect of decongestion, while the lower pair are for the effect of change of flowrate. 183

4.30 Unilateral cavities mass film coefficient and Sherwood number intranasal cavity distribution. Figure a and b are the mass film coefficient at lower and higher flowrates, while the lower pair (c,d) represent the Sherwood number at two flowrates. 184

4.31 Unilateral mean mass film coefficient, within anterior part (between plane Nos and 1V) and within posterior part (between plane 1V and PS), Wilcoxon signed-rank test, before and after decongestion as well as before and after increase of bilateral flowrate, are distributed by this figure. 185

4.32 This figure shows the same results as figure 4.31, but for quantity Sherwood number instead. 186

4.33 Unilateral correlations between SAVR and the conditioned temperature and moisture content level at posterior septum of both lower and higher flowrate. . . 187

5.1 Figure a shows the complete upper airway geometry with detailed images that show the glottis cross-sectional plane of both 53 (fully abducted) and 10 (partly abducted) degrees. The predefined cross-sectional planes, each oriented normal to the geometric centerline are shown by the grey lines that above the surface rendering. Figure b shows the corresponding CSA distribution along the airway centerline from slightly below nasopharynx to just above the carina as marked by a solid black line on the surface rendering. 190

5.2 Mean static pressure of 10 degrees glottis between laminar simulation results and experimental results at flowrate of 50 L.min^{-1}. The blue dots with the margin bar of ± 3.5 Pa are the experimental results and the red dots are the simulation results. The scale of the vertical axis of each plot is the same as probe locations, as represented by the small dots, on each side of the airway. Value of 0 means the first probe location of each side separately. 191

5.3 Comparison of different CFD models applied for flowrate of 50 L.min^{-1} to partly abducted glottis. Maps of vorticity magnitude are shown on the same sagittal plane for different turbulence models. Reading from left to right, the first two models feature highly resolved meshes: qDNS (15 million) and LES (11 million); the remaining three simulations use the same mesh which contains only 2.9 million elements. 192

5.4 Cumulative losses in energy flux among qDNS, LES and laminar simulations. . . 194

5.5 Left two views (above and below the velocity bar) show sagittal plane images of the 10 degrees glottis model.Right: same but for 53 glottis geometry. Both of them are viewed from the same sagittal planes with the mean velocity (top) and static pressure (bottom) are shown on the planes with the inlet static pressure preset as 0. 195

5.6 Total pressure loss distribution along the tracheal centerline of fully and partly abducted glottis at flowrate of 50 L.min^{-1}. 197

5.7 53 and 10 degrees glottis resistance of flowrate 50 L.min^{-1}. 198

5.8 10 degrees glottis total pressure loss variations with multiple flowrates. 199

5.9 Log_{10} flowrate versus log_{10} total pressure loss. 200

6.1 Sagittal view comparison corresponding to the point of maximal constriction in all scans. The yellow line in the picture indicates the location of minimum cross-sectional area (except T23). 203

6.2 Volume rendering of the subject's anatomy at T15 showing the skeleton with a surface rendering of the segmented airway. 204

6.3 The cross-sectional area distribution for all the tracheal geometries within this research. 206

6.4 Geometries in sagittal orientation with centerline 207

6.5 Resistance and cumulative energy flux of two pre-operative cases and the post-operative case. The extra maker of each line corresponds to the latter two locations of area minima as described above, namely the glottis and the most constricted region in the trachea. 209

6.6 Jet structure: Top is T4-L and bottom is T15. Plane labelled as G and Min represent the planes located at glottis and minimum area position. Plane P1 means the first posterior plane after the jet and P2 is the second posterior plane further downstream. 211

6.7 Jet structure of T4-L compared with T4-Short. Plane SGI means supraglottic inlet plane, the other three planes are as described above. 212

6.8 Jet structure of T15 compared with T15-S. Plane SGI means subglottic inlet plane while the other three planes as described above. 213

6.9 Resistance and energy flux plot for T15 and T15-S. The extra square marker represents the glottis and minimum point position. 214

6.10 Turbulence intensity average on the T15 first tracheal ring mean velocity 215

6.11 Energy flux comparison with various inflow conditions 217

6.12 Resistance comparison with various inflow conditions 217

6.13 Resistance and energy flux plot for T15-Long at both inhalation and exhalation condition. The extra square marker represent the glottis and minimum point position. 218

6.14 Jet structure of T15-Long exhalation. 218

6.15 Power law predictions of T15 geometry with four different flow rates. 221

A.1 Cumulative averaging of total pressure loss with simulation physical time. 253

A.2 The mesh structure difference between 4 million cells and 6 million cells simulations. There are one sagittal and 3 cross-sectional planes (nasal valve, plane 1V and plane 3V) are used for distribution and with one zoomed in view of plane 1V. For three cross-sectional views, the left pair corresponds to the 4 million cells mesh while the right side is the 6 million cells mesh. 255

A.3 Total pressure loss within left cavity of Subject-D congested case. The x-axis origin from the nostril plane until the posterior septum plane. 257

A.4 Mesh details comparison between laminar model and qDNS model for complete airway simulation. 260

A.5 Mesh details comparison between LES model and qDNS model for pathological tracheal simulations. 262

B.1 Bilateral NVArea, TPL and TWSS. 265

B.2 Correlations between NV area and other physical measures. 268

C.1 Bilateral cavity correlations between SAVR and THF and TH2OF. 270

C.2 Unilateral cavity correlations between SAVR and posterior septum temperature and moisture content level. 271

C.3 Unilateral cavity correlations between total cavity WSS with THF and TH2OF. 271

D.1 Wall shear stress is shown on the back of trachea surface. 274

D.2 Static pressure distribution of T15 related geometries. 275

List of Abbreviations and Symbols

2D two dimensioanl

AS Anterior septum

ATA Amercian Thyroid Association

CFD Computational Fluid Dynamics

CFL Courant Friedrich Lewy

CSA cross-sectional area

CT Computed tomography

DNS Direct numerical simulation

ENT Ear, nose and throat

FOV Filed of view

LES Large Eddy Simulation

MRI Magnetic resonance imaging

NAR Nasal airway resistance

NHS National Health Service

Nos Nostril

NS Navier-Stokes

Nu Nusselt number

NV Nasal valve

PS Posterior septum

qDNS quasi direct numerical simulation

RH Relative humidity

SAVR Surface area volume ratio

SD Standard deviation

SGS subgrid-scale

Sh Sherwood number

URANS Unsteady RANS

WALE Wall Adapting Local Eddy

WSS Wall shear stress

Chapter 1

Introduction

1.1 Airway geometry

The process of transporting air in and out of the lungs is properly referred to as ventilation. The upper airways of the human respiratory tract, which are the concern of this work, are the interface between the external environment and the lower respiratory system. Consequently, the airways are not only conduits to channel air from the environment to the lungs, but the house organs that perform additional functions. The main physiological functions of nasal cavity are air-conditioning, filtration and olfaction. The inhaled ambient air can be conditioned to nearly alveolar conditions when it reaches the nasopharynx [3], and the conditioning process will be continued in the trachea to protect the internal environment of the delicate lung tissues. The amount of water required for conditioning depends on the external environment, whilst the expiratory process will recover about 20% of the water consumed during inspiration. Filtration is another important function of the nasal cavity, with nearly all larger particles of diameter over 5 μm trapped during transit through the curved geometry and narrow passages largely due to the inertial force. Moreover, roughly 50% of the particles of diameter between 2 to 4 μm are deposited on the mucosal membrane. Smaller particles pass through the cavity and continue to the lower airway [4, 5, 6, 7], though diffusion aids trapping for nano-particles.

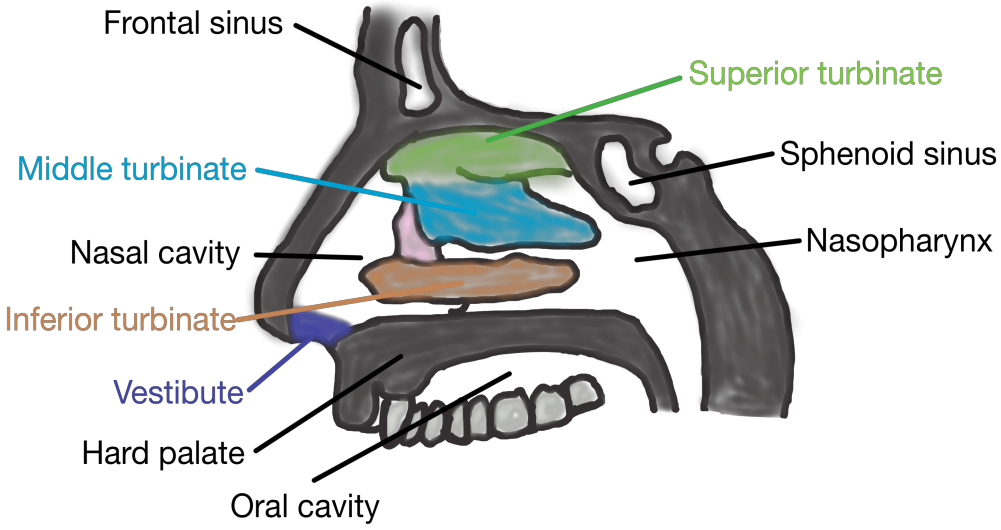


Figure 1.1: Nasal cavity anatomical diagram.

The respiratory tract considered here, contains three main parts, which are respectively the nasal cavity, the pharynx and larynx treated as a single unit, and the trachea continuing to the carina and including the first generation bronchi (higher order bronchi are out of the scope of this study).

Figure 1.1 shows the anatomy of the nasal cavity. As we can see, the nasal cavity contains three turbinates: superior, middle and inferior. The olfactory cells are primarily located in the superior portion of the cavity, though they are not confined to a highly defined region but distributed over the cavity [8, 9, 10, 11, 12, 13]. From anterior to posterior of the cavity, significant anatomical landmarks can be identified such as: nostril, nasal valve, anterior septum, posterior septum and nasopharynx. The nasal valve normally operates as the first restriction of inspiratory air entering the nasal cavity and is usually expected to represent the smallest passage cross-sectional area in the anterior nose. As a consequence, a pronounced jet is generally formed at the nasal valve that progresses to impact on the head of the turbinates [14]. There-

after the turbinates will direct the flow into different sections of the cavity. The turbinates act to increase the rate of local heat and moisture transport by protruding into the flow, leading to thinner boundary layers and by narrowing the passageways for air. Several studies point out that the turbinates can introduce laminar swirls downstream of the turbinate wall, which would further augment exchange processes. However, abnormal blood supply or mucous generation may reduce the rate of heat or moisture flux into the inspired air [15].

A large proportion of the air-conditioning process is completed by the time inspired air exits the turbinate region and passes on to the nasopharynx. The separate left and right nasal inspiratory air streams merge downstream of the posterior septum, bending sharply to continue through the pharynx region where the oral cavity and nasal cavity connect. The directing of flow from pharynx to larynx is controlled by the epiglottis fold that opens while breathing; it is temperately closed during the swallowing process to protect from being choked during eating (or drinking).

The glottis is a natural restriction of the airway and the angle of opening depends on different physiological demands of various activities such as speaking and doing exercise. For healthy subjects, the glottis at the larynx forms a weak restriction with a weak laryngeal jet. However, for patients with glottic compression, there is strong jet formation and flow separation. In each case, since the glottis strongly affects both the direction of flow and the peak velocity, the laryngotracheal jet will affect the flow further downstream in the trachea [16].

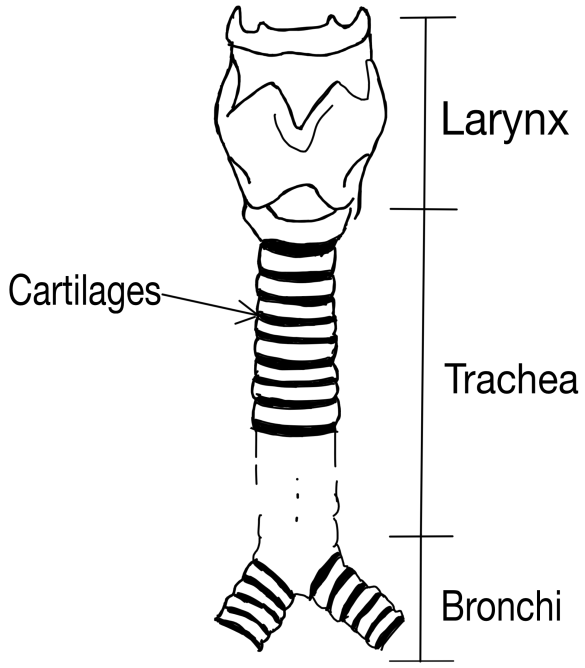


Figure 1.2: Trachea anatomy.

The tracheal lumen begins below the glottis. The trachea has the form of a mildly undulating conduit due to the impression of the U-shaped supporting rings of fibrous cartilage (figure 1.2), which act to maintain a certain rigidity whilst permitting limited tracheal extension during breathing. During quiet breathing, the work required for delivering air through trachea to and from lungs is negligible [17, 18], however, it can increase significantly if the subject suffers pathological compression of the trachea such as retrosternal goitre. With either intrinsic or extrinsic tracheal compression, the airway obstruction can become severe while the compression worsens. Often tracheal constriction progresses gradually so that patients remain asymptomatic and stable for a long time before suddenly deteriorating [19]. Amongst the most common causes of intrinsic compressions are laryngotracheal stenosis, lymphovascular malformations and idiopathic inflammatory conditions such as granulomatosis with polyangitis (Wegner's granulomatosis) [20]. Extrinsic compressions may be attributed to: retrosternal goitre, anatomical variants of the great vessels, oesophageal tumours, lung tumours, cardiac enlargement or exercise induced laryngeal obstruction (EILO) [21, 22, 23],.

1.2 Mechanics of breathing

1.2.1 Temporal flow profiles

Human breathing is cyclic but varies from breath to breath, even under the same physical condition. For a standard tidal volume of 0.5 L and a respiratory rate of 12 to 15 times per minute, the equivalent breathing rate is 6 to 7.5 L.min^{-1} with the total volume being about 10000 L per day [3, 24]; other studies suggest higher values associated with postures other than recumbent [25, 26]. Assuming equal duration of inspiratory and expiratory portions of the ventilation cycle, an equivalent steady flow is double the ventilation rate, i.e. 12 to 15 L.min^{-1}. The intra subject variations of breathing can be caused by multiple reasons during rest, and restful breathing is very different from that in strenuous exercise or in sniffing. The ventilatory pattern also varies inter-subject and with gender and age. For a healthy subject, the measurement from rhinomanometry gives a functional measure of the pressure-flow relationship.

From the study of Wheatley et al [27], it was shown that the pressure-flow relationship follows a sigmoid shape that can be fitted by power law function of the form: $\Delta P = a\dot{V}^b$, where $\dot{V}$ represents the volumetric flowrate, whilst a, b are empirical constants. The total nasal airway resistance measured by rhinomanometry of resting breathing was reported within the range of 0.15-0.39 Pa.m^{-3}.s by multiple researchers [28, 29, 30]. Another interesting finding was that the nasal resistance in the infant is higher than adult at about 1.2 Pa.m^{-3}.s and with the increase of age it decreases. Vig et al. [31] reported that for males the nasal resistance decreases from to 0.29 Pa.m^{-3}.s between age 5-12 years old, to 0.22 Pa.m^{-3}.s within age of 13-19 and to 0.22 Pa.m^{-3}.s beyond 20 years of age. Similar trends were also found in females but with slightly lower values.

As is also well known, spontaneous and reciprocal changes occur in the nasal cavity which makes the unilateral nasal cavity resistance variations almost a fourfold change [32, 33]. This cyclic changes of the nasal cavity were described in many studies and were first proposed by

Kayser et al. [34] and named as nasal cycle. However, the study from Heetderks et al found that only 80% of 60 subjects showed this so-called nasal cycle [35]. The current understanding of the nasal cycle is not certain and the hypothesis that the nasal cycle acts to share the burden of the air conditioning between two nasal passageways so that dominance of airflow alternates cannot be proven. The effect of exercise on reducing nasal resistance has been studied both on pathological (asthma or rhinitis) and healthy subjects [36, 37, 38, 39]. The first study was conducted by Richardson et al [40] and he found that when a patient performed exercise there was a marked reduction in nasal airway resistance. They claimed that the reduction in resistance was due to the increase in sympathetic vasoconstrictor tone to the nasal venous sinuses.

Rennie et al. have performed an experimental study of the inspiratory flow profile at rest and sniffing [41]. Her study revealed that the time taken for flow to build up to a level equivalent to that in restful breathing was 130 ms on average in normal inspiration while this reduced to 90 ms in sniffing and was as short as 20 ms in a rapid inhalation. Bates et al. studied the dynamics of airflow in a short inhalation using a realistic breathing profile measured from experiment [42].

Although there are some studies that use the temporal profile of breathing cycle as the boundary condition [43], there still many studies that use the equivalent steady state flow rate to represent the dynamic breathing process [44, 45]. Some works claim the importance of using unsteady breathing cycle while doing simulation, especially when the turbulent effects are dominant such as particle distribution and deposition studies [46, 47]. Since deposition and most likely olfaction depend on the Lagrangian dynamics of the trajectories of inhaled particles, it can be expected that the time history of the breathing profile is significant. However the study of Bates et al. [42] suggest that the pattern of flow and partitioning between different regions is rapidly established. Thus for comparative studies of airflow distribution and exchange performance, steady models appear sufficient.

1.2.2 Fluid mechanics of upper airway flow

The poor accessibility of the nasal cavity does not permit the detailed distribution of nasal cavity flow to be measured. With the blooming of Computational Fluid Dynamics (CFD) in the recent decades, this technique provides the full accessibility of the nasal cavity and can give the flow details at any location within the cavity. Determining the flow characteristic across the nasal cavity is important in order to understand how the nose performs functions such as: air-conditioning and filtration. The first step is to establish not just how well different normal geometries perform, but to assess the contribution of the different regions to the overall effort.

Hahn et al. [48] measured the velocity profiles in a 20 times enlarged nasal cavity replica at three different steady state flowrates that equivalent to 1100, 560 and 180 ml.s^{-1}. Their findings suggest the Reynolds number to be normally less than 500 and the peak velocity less than 15 m.s^{-1}. Similar results were also found by Keyhani et al. [49]. Multiple researchers[49, 50, 51] all reported that laminar flow was assumed in most CFD studies of human nasal airflow during quiet breathing, with experimental support by Kelly et al. [52], Proctor et al. [53], Hahn et al. [48] and Girardin et al. [54]. In addition, Zhao et al. [51] also claim that the flow can be assumed as laminar up to about twice of the resting breathing flow rate. He also found out that change of the geometry of the cavity at specific locations can change the flow patterns significantly and affect the corresponding nasal functions.

Ingolf et al. [55] claims that the inhalation phase is more sensitive to the geometry change than expiration by applying the Saint-Venant and Wanzel equation. Inthavong et al. [56] studied multiple nasal cavities (6) at resting breathing rate of 15 L.min^{-1} and found common characteristics: (1) high velocity in the nasal valve area; (2) most of the flow passes through the inferior cavity; (3) air from the front of the face tends to reach the olfactory region while the air from lateral side of the face tends to go through the inferior half of the cavity. Both flow and heat transfer are simulated using laminar flow model and two-film theory for heat and moisture wall boundary model. Other studies of particle deposition from nasal sprays reveals that the most

important parameter that affects the deposition efficiency is the particle's Stokes number [57].

Whereas most model studies up to now have considered one or at most a couple of nasal geometries, Zhao and Jiang. [2] performed a study of 22 subjects to determine the normal nasal airflow, but found there are significant variations of nasal airflow among healthy subjects. However, for pathological nasal cavities such as chronic nasal obstruction, there was a fourfold higher velocity and 35% less negative pressure at the eustachian tube orifice [58, 59]. Post surgical results are not always satisfactory, as reported by Singh et al. [60]; this shows the objective benefits of septal surgery are limited and there is a need for long-term studies. Within 50 patients, only 43% patients are reported fully satisfied with the long-term results of septoplasty [61]. Kimbell et al. [62] studied 10 nasal cavities of nasal airway obstruction patients before and after surgery using laminar model at rest breathing. Paired t-test is used to evaluate the change of airflow and resistance. In addition, the moderate linear correlation between subjective symptom and flow measures indicate the usefulness of concurrently tracking during future surgery planning. Dinis et al. [63] evaluated the accuracy of surgeon's decision on septoplasty and it shows the subjects with anterior septal deformities benefited the most within a scope of 2 to 10 year retrospective study; also preoperative rhinomanometry was shown to be not useful in predicting the long-term surgical outcome.

1.2.3 Heat and water exchange in the upper airways

The nasal cavity inner surface is covered with mucosa that act as the heat and water source during the air-conditioning process. The nasal mucosa has multiple specific cell types such as basal cells, columnar cells and ciliated cells etc [64], and it has the potential that increase the mucosal blood supply to compensate cooling at the mucosal surface and to warm the surrounding air. There are multiple studies that show in vivo measurements of nasal mucosal temperature varies, but without the precise site of the detection and the exact time of the detection within the breathing cycle. Willatt et al. measured the septal mucosal temperature by thermometry that shows the temperature varies from 30.4°C to 32.0°C during inspiration to

expiration separately [65]. Another measurement reported by Fabricant et al. [66] shows that the temperature in the nose is within 29.7-34.7°C and in the pharynx is within 32.2-35.6°C. Interestingly Assanasen et al. found over 1.9°C temperature increase in septum of the anterior part of nasal cavity after warming the feet in 42°C warm water. In addition, the measurement was taken at prone posture by Molony et al. [67] that shows the nasal septum temperature is 34.5°C, while the upright posture showed much higher values (36°C). Furthermore, Jun and Qingping [68] measured the inferior nasal turbinate temperature before and after the puncture of the nasal cavity as 26.9°C before and 27.4°C after separately.

The variation of those experimental measurements are not only due to the exact time and site of the measurements were taken being unclear, but also due to the types of equipment that were used for measuring. A copper-constantan thermocouple, as used by Keck et al [69, 70] and Webb et al. [71], allows the nasal mucosa temperature to be measured without affecting the breathing cycle and irritating the nasal mucosa [72, 73]. For example, Lindemann et al. [43] continuously measured the septal mucosal temperature at defined intranasal sites during respiration and found the highest temperature values were measured at the end of expiration. The mean nasal mucosa temperature measured ranged from 30.2°C to 34.4 °C depending on the exact time and sites where the measurements were taken. In addition, they also found that in regions of turbulent flow, the temperature changes are more pronounced compared to regions of laminar flow. However, the commonly used infrared thermometers could not achieve breathing synchronic measurements due to the long reaction time.

Another factor that can affect the nasal mucosal temperature is the age of the human subject. One of the studies compared the nasal air-conditioning between the younger group and the elder group [74]. The results showed that both temperature and humidity were significantly lower in the elder group. The degenerative atrophy of nasal mucosa of the elder group also induced an enlarged nasal cavity and minimum cross-sectional area.

The amount of daily heat and water transferred as a result of nasal conditioning can vary with the breathing rate and the ambient environment. It has been reported that for quiet breathing of room air, the net loss per day in man is about 359 kcal of heat and 250-400 ml of water as a result of conditioning process [75, 76]. Naftali et al. [15] proposed that there is ample time for heat and water exchange to enable equilibration to near intra-alveolar conditions; furthermore it consumes about 265 kcal and 370 ml water daily of the nasal cavity to condition the air from 25°C, 20% relative humidity (RH) to alveolar condition. The in vivo measurements by Keck et al. [69], who measured a group of 50 healthy volunteers showed the inhaled air temperature can significantly increase within the anterior part of the nasal airways and the humidification process is almost synchronous as the heating process [70]. The nasopharynx temperature is approximately 34°C [71, 77, 78]. Similarly results also were found in this study which is discussed in the following chapter. However, at the end of the inspiratory phase, temperature at nasopharynx only about 29°C at the ambient air temperature of 7°C [71].

For CFD studies, without considering humidity and water exchange, Lindemann et al. [79] numerically simulated the temperature distribution during inspiration in an anatomically realistic nasal cavity. Their simulations used a constant inspiratory flowrate of 36 L.min^{-1} with a constant mucosal wall temperature of 34 °C throughout and found that the inspired air (20 °C) was heated to 33.9 °C at the nasopharynx. While a study of the heat recovery during expiration was conducted accordingly by Pless et al. [80] that showed a closed relationship between the cooling of warm air and airflow patterns during expiration. The simulation was performed assuming constant wall temperature (31°C) and also without considering the humidity, but the results showed good concordance with experimental in-vivo temperature measurements. Rather using constant boundary conditions, Lindemann et al. [81] performed another study that applied time-varying boundary conditions for both the flowrate and the cavity surface temperature. Saksono et al. [82] studied a subject specific nasal cavity heat transfer patterns without considering water by specifying constant wall temperature. They found that the inhaled air will reach the body temperature by the time it arrives at the distal nasopharyngeal region; also they reported that the anterior head of the cavity contributes most of the heat transfer.

However, the lack of consideration of water vapor transport is important because the latent heat effect accounts 85% of the total heat loss during normal room air breathing [83]. This should draw attention to the mass transfer coefficient rather than the heat transfer coefficient only, especially in the nasal cavity where most of the air conditioning occurs. The modelling of the real structure of the nasal membrane can be difficult and not practical, however, Gavin [84] showed that the properties of the mucosa membrane can be assumed to be the same as water. This assumption can highly simplify the modelling of mucosal membrane.

Naftali et al. [15, 85] simulated heat and water transfer in the nasal cavity including the latent heat effect but using constant wall temperature and fully saturated mass fraction of water vapor as the mucosal surface boundary conditions. By using these boundary conditions, they first studied the heat and water transfer in two dimensional (2D) of an idealised nasal cavity. The results show that a normal nose can handle a range of ambient condition, but the abnormal nose (such as less blood supply or mucus deficiency) has reduced rate of heating and moistening. After the 2D study, they investigated another two idealised geometries and one anatomical geometry and compared the CFD estimated of daily heat and water transfer with the estimates from the psychrometric chart.

After these important studies of Naftali and colleagues, Garcia et al. [86] performed a study that considered both heat and water transfer in the nasal cavity by using the heat model proposed by Naftali et al. [85], however, their study was focused on the air conditioning performance comparison between pathological (atrophic rhinitis) subject and healthy subject. Their results indicate that the atrophic nose does not condition the air as effectively as the healthy nose. Inthavong et al. [87] compared the nasal cavity air-conditioning between the left and right side of the cavity. Their results indicate that a smaller cross-sectional area of the cavity has greater heating and the residence time of inhaled air affects the ability of heating of the cavity in laminar flows. Kumahata et al. [88] introduced a two-film membrane model that used to study

the heat and water transfer within the cavity without considering the latent heat effect. They suggest their model is verified by comparing with previous studies; their results show that both the temperature and mass fraction of water experience large variations within the anterior part of the cavity. In addition, as in the previous study [87], their study also indicated that the narrow section of the cavity experience the largest heat and moisture change. By implementing the same model, Hanida et al. [44] performed another study using the same cavity model but including consideration of the latent heat flux from evaporation (or condensation) during the cavity conditioning process.

Wu et al. [89] studied the heat and water transfer in the tracheal airway with a mouth cavity attached. Ma et al. [90] studied the effect of anterior geometry of the nasal cavity on the heat and water transfer by using a two-film heat model. It shows the anterior change of the geometry can have a significant effect at the vicinity of the notch. Tsu et al. [91] studied not only the heat and water exchange but also considering the interaction of the water with nasal mucosa. Lee et al. [92] using Large Eddy Simulation (LES) model studied the dynamics of nasal airflow and temperature shows that the expiration process is more unsteady than inspiratory process. And most of the heating process is occurring in the nasal cavity and the nasal cavity is a very high efficient heat exchanger during inspiration period. Zhao et al. [93] investigated the correlations of nasal patency with other measures. It shows that mucosal cooling has a strong correlation with the nasal patency. They suggest that the quantification of dynamic cooling between airstream and the mucosal can lead to new clinical evaluation tools.

The clinical evaluation of pathological nasal cavities before and after surgery have been studied extensively as well. At early 1942, Moe et al. [94] evaluated the effect of excessive turbinate surgery on the respiratory functions of nasal cavities. Although there was no significant deterioration of nasal climatisation, the obvious reduction in heat and moisture of surgically altered cavities were observed. Furthermore, Lindemann et al. [95] compared the nasal conditioning within pre and post operative cavities that show the patient would benefit overall from nasal surgery, with and without a preserving bilateral turbinoplasty. Septoplasty has been reported

recently by Wiesmiller et al. [96] that it can significantly improve nasal air conditioning, although it has a clear benefit on the subjective nasal patency [97, 98]. In addition, patients after septorhinoplasty and closure of septal perforations all claim experience improvements on nasal air-conditioning [99, 100]. Nevertheless, not all the nasal surgery have positive feedback, such as extensive sinus surgery can deteriorate the nasal air conditioning [101, 102].

The ease of applying CFD analyses over any pre and post-surgical geometries provides the possibilities of virtual surgery that ideally can improve the surgical outcomes. From the previous studies that analyzed pathological (due to atrophic rhinitis) nasal cavities before and after surgery through CFD, the results indicate that regularising the airstream to eliminate flow disorder and to correct for the reduction of flow mucosa contact time is beneficial [86, 103]. Those results also gave instructions for nasal surgeries that should aim to restore the original surface area of the nose and the physiological airflow distribution. Another pure virtual surgery conducted by Xiong et al. [104] showed the potential of CFD as an effective virtual surgery tool to aid clinical decision making.

Although there have been multiple studies that investigating the both the flow mechanism as well as the air-conditioning of the nasal cavity, most analyses were limited to one or a couple of geometries. However, Zhao et al. [2] completed a study that comprised 22 healthy nasal geometries with the aim of identifying the common nasal flow features.

The present study includes 10 healthy nasal geometries and considering these were obtained for two conditions (before and after decongestion), this results in a total of 20 nasal cavity geometries. Furthermore, not only the flow features are investigated through a systemic manner, but also the heat and water transfer are studied. This cohort nasal cavity simulations study aims to review the characteristic features of both flow mechanics and energy transfer. In addition, the comparison between congested and decongested simulation results is also conducted.

1.2.4 Laryngotracheal flow studies

Upper airway abnormalities serve as the pathophysiologic basis for many pulmonary diseases [105]. There are multiple kinds of abnormalities of upper airway such as stenosis at vocal folds or subglottic stenosis. The diagnosis of airway obstruction may not only depend on the clinical presentation but also depends on the patient's age [105, 106]. The upper airway obstruction is fairly common among both children and adults as reported by Loevner [106]. The idiopathic upper airway abnormality for children are mostly caused by laryngeal malacia, subglottic stenosis, laryngeal webs and vascular rings, while for adults that are mainly dominated by malignant neoplasms of the aerodigestive tract [106, 107]. Other causes that may induce the upper airway obstruction include inhalation burns, foreign body aspiration, subglottic edema due to anaphylaxis or prolonged intubation, mechanical ventilation or even the subtle change associated with asthma [105, 106]. Prolonged intubation is one of the most often used stenosis management for patients with breathing difficulty. At early 1976, Hawkins et al. [108] conducted a study of the glottic stenosis caused by prolonged endotracheal intubation as the complications of intubation were being seen more often. The results show that the complications of intubation are mostly due to the trauma in the glottic posterior commissure. And he also proposed that the endoscopic management can be more successful if it is conducted early enough and as much as necessary.

More recently, CFD is well accepted for analysing respiratory flow due to its non-invasive character as well as the unsatisfactory of laryngotracheal reconstruction [109]. A patient specific study was carried out by Nithiarasu et al. [45] that focused on the effect of steady inhalation flow in the pharynx. The results show that the major pressure drop occurs while flow passes through the narrowest section of the airway (around oropharynx). The necessity of including laryngopharynx or even the complete nasal airway for reproducing an appropriate flow profile upstream was also pointed out. Choi et al. [110] performed a limited study of the effect of intra and inter subject variability in airway geometry effect on upper airway flow using LES flow model including the effect of inflow domain truncation on the tracheal flow. Their results

point to the necessity of including the glottis in studies of tracheal flow that if the full geometry were not available, a cut at midpharynx could be used to improve the solution accuracy. Jeong et al. [111] conducted a study on the flow characteristic in the upper airway with nasal cavity attached with obstructive sleep apnea using CFD. The maximum aerodynamic force was found at the velopharynx. Similarly, Lin et al. [16] investigated the effect of the laryngeal jet on intra-thoracic airways through comparing two simulations that with and without mouthpiece geometry. It shows that the jet induced by laryngeal geometry could significantly affect the airway flow patterns as well as the wall shear stress downstream. Mihaescu et al. [112] simulated flow in an accurate upper airway of a patient with obstructive sleep apnea. The results show the airway narrowing can lead to the increased flow velocity and reduced static pressure, as a result of increasing airway collapsibility. Additionally, wall shear stress might be an important indicator of assessing obstructive sleep apnea.

For pathological tracheal geometries, the simulation results before and after surgical correction show that post-surgical airway flow field showed minor instabilities and both airway resistance and wall shear stress were significantly reduced compared with pre-surgical case [113]. Similarly, Chen et al. [114] also investigated the effect of applying surgical correction by trachea vascular ring surgery on the flow characteristics. The simulation results indicate that after the treatment, the pressure drop in the tracheal airway was significantly decreased, especially for the low respiratory rate. Rather than applying steady inhalation as the boundary condition, Liu et al. [115] studied the flow characteristic within an obstructed realistic human upper airway (caused by pharyngeal collapse) with the simulated respiratory cycle through sine wave. Their LES simulation results show that the airflow experience unsteadiness (transitional/turbulent) under low Reynolds number. Although previous researchers have claimed that CFD computations based on (RANS) modelling is adequate for analyzing respiratory flow [45, 114], there is some doubt regarding its accuracy, since the use of a turbulence model does not capture the flow dynamics in the upper airway [116].

1.2.5 Energy cost of flow transport through upper airways

During quiet nasal breathing, the resistance of the nasal passage is about one half that of the entire respiratory tract and 50% more effort is required when compared with oral breathing [117], although the anterior part of the nasal cavity is the critical resistive area [118]. The effort required to drive airflow through the normal trachea represents a minor contribution to the total work of breathing [17, 18].

As described above, similar flow characteristics can be found in the laryngopharynx region for different subject specific CFD studies. However, in order to understand the mechanism of stenosis jet formation. Jayaraju et al. [119] tested different level of tracheal stenosis, showing the pressure drop only start to increase steeply after the constriction passes a certain level. This is consistent with the patient's symptoms experience a sudden increase in severity, although a very marked stenosis has already been shown (an exactly analogous case exists for the coronary arteries). In addition, he also tested that by applying heliox as an alternative breathing fluid [120], the breathing effort can be reduced more than 50%.

Lin et al. [121] studied the effect of sub-glottic stenosis on the tracheal pressure loss. They showed the constriction area to be more important than the constriction length and found the airway resistance can be well represented by a simple power law. Kin et al. [16] studied the effect of laryngotracheal jet on the tracheal flow and wall shear stress. Their geometry includes the oral cavity rather than the nasal cavity. Cheng et al. [122] studied the laryngotracheal stenosis at various locations. Their results show that the mouth breathing can compensate for the increased resistance partially that caused by stenosis and the variations of stenosis have different effects on the airway resistance. In addition, they also found that glottic stenosis has a greater effect on resistance than the tracheal stenosis. Nithiarasu et al.[45] studied the air flow through the upper airway geometry using an in-house CFD code. Their study indicates the locations such as oropharynx and laryngopharynx should be focused for any studies that aimed at understanding the human upper airway collapse. Bates et al. [17] analyzed the effects

of tracheal constriction and curvature on the power loss mechanism of the flow in the trachea with the comparison of a normal geometry. The results show that the curvature has strong effects on the jet impingement and breakdown patterns in the pathological geometries.

However, none of the previous studies has ever analyzed the different level of upper airway natural constrictions (glottis opening) of a same healthy subject or a retrospective study of a pathological subject under a series of scans as the constriction worsens. The present study analyzed the effects of glottis opening on the upper airway resistance by using a complete geometry (from nostril to first generation bronchi) and with the comparison to experimental results. Furthermore, the sub-glottic stenosis effect was conducted in a retrospective way associated with CFD simulations before and after surgical correction.

Energy flux calculated in this study is defined as the product of total pressure and the cross-sectional plane normal velocity. As the flow passes through the airway conduit, the pressure losses come from two components: wall shear stress and viscous dissipation. Energy flux is an indicator for assessing the flow energy dissipation along the airway. It is useful to evaluate the energy loss patterns and to help quantify the flow mechanisms responsible.

1.2.6 Outline of the thesis

This thesis aims to answer several questions.

Firstly, inspired by the enormous number of individual studies of the nasal cavity, where most concern a specific geometry, and although recently a few studies start to consider multiple geometries, the question of how inter and intra subject variations affect detailed flow and function are not well established.

Specific questions to be addressed include the following:

- What are characteristic ranges for the patterns of flow within the nasal cavity?
- How does the air-conditioning performance of the nasal cavity range across individuals and intra-individual?

For this part of the work, the intranasal cavity pressure loss and resistance are quantified and analysed along the cavity cross-sectional planes in a manner of bilateral and unilateral separately. Accordingly, the effects of cavity geometry change (caused by decongestion) are studied through the comparison of the intranasal simulation results, and subjected to tests for statistical significance, (Wilcoxon signed-rank test). Following the analysis of nasal airway flow, the heat and water transfer within the nasal cavity are also invested. As for the flow analysis, both the geometry change caused by decongestion and the change of flowrates and ambient conditions are discussed.

Secondly, the analysis moves from the nasal airway to flow in the larynx. There the two key questions are:

- How do different CFD predictions of the pressure distribution compare with experimental results?
- What effect does glottis aperture area exert on inspiratory flow behaviour and pressure loss?

Thirdly, the study finally considers airflow in the pathological constricted and deviated trachea, in the context of a patient specific study of a progressive compression and surgical correction. Main questions raised are:

- How does the profile of energy dissipation relate to the geometry?
- What are the effects of inflow domain truncation on the loss profile and how can this be modelled?
- How does pressure loss change with geometry and flowrate?

Chapter 2

Methodology

This chapter is intended to provide a brief but systematic description of the methods used within this study. In order to provide a complete description, not only are the computational methods described, but some details regarding the process of segmentation and ascribing landmarks for the clinical datasets are included. The author acknowledges that the latter work was performed by others, primarily Dr. Raul Cetto. Ethical approval was granted for all studies: for Magnetic Resonance Imaging (MRI) of volunteers for the nasal airway studies, by the National Health Service (NHS) Health Research Authority NRES Committee South East Coast-Surrey reference number 06/Q0602/18; for retrospective use of patient scan data, hospital and ethics compliance was obtained from the local Joint Research Compliance Office (reference 15SM2566).

1. For the nose, the images originate from MRI. For nasal cavity scans, 10 non-pathological subjects are studied and each in two conditions: congested and decongested, where congested actually refers to the normal state and decongested refers to images acquired after application of a topical decongestant, oxymetazoline nasal spray as described by Dr. Cetto [123].

2. Laryngeal geometries were obtained from a clinically acquired Computed Tomography (CT) of a 46-year-old male patient, and the variations in the vocal fold position were

created by manual alteration of the subject image data by an Ear Nose and Throat (ENT) surgeon as described by Dr. Lulu [124].

3. The pathological trachea data was likewise obtained from retrospective clinical image data: first scan was conducted in January of 2012 and three more scans in the following 23 months. The CT neck and thorax with intravenous contrast was performed in a Philips ICT 256 helical scanner with the patient in the supine position. A series of 323 slices 2 mm thickness with a 1 mm slice increment were acquired with a field of view (FOV) of 430 mm and a pixel size of 0.56 mm. The image segmentation process is following the American Thyroid Association (ATA) imaging test guidelines and also done by ENT surgeon Dr. Cetto.

2.1 Models of flow and heat transfer

Within this study, the Navier-Stokes (NS) equations that describe incompressible flow are discretised and solved in a segregated (as opposed to a coupled) approach using the commercial software (STAR-CCM+ 11.04). The solver selected employs a co-located variable arrangement and a Rhie and Chow-type pressure velocity coupling combined with a semi-implicit method for pressure-linked methods (SIMPLE-type) algorithm [125]. This method is capable of handling both incompressible and mildly compressible flows although it originated for the solution of constant-density flows. For flow transfer with heat and moisture, density varies due to warming and the addition of water vapour; although these effects are relatively small for respiratory tract flows, they are accounted for in the computation. Note that density is considered to vary only with temperature and not with pressure, so the flow is still strictly considered as incompressible. As gravity is not considered, buoyancy effects are also neglected.

The mechanics of fluid flow are governed by equations that express the physical conservation laws for the quantities mass, momentum, and energy. Assuming a continuum, the balance of

mass through a control volume can be expressed by the continuity equation:

$$\frac{\partial \rho}{\partial t} + \nabla \cdot (\rho \mathbf{u}) = 0 \tag{2.1}$$

where ρ is the density and $\mathbf{u}$ is the velocity vector.

The balance of momentum can be expressed as follows:

$$\underbrace{\rho(\overbrace{\frac{\partial \mathbf{u}}{\partial t}}^{\text{Unsteady Acceleration}} + \overbrace{\mathbf{u} \cdot \nabla \mathbf{u})}^{Convective Acceleration}}_{\text{Inertia}} = \overbrace{-\nabla p}^{\text{Pressure Gradient}} + \overbrace{\mu \nabla^2 \mathbf{u}}^{\text{Viscosity}} \tag{2.2}$$

where $\mathbf{u}$, ρ and μ represents the fluid velocity, density and dynamic viscosity. As STAR-CCM+ uses finite volume method, the differential equations of mass continuity and momentum equations are written in integral form. From the Gauss theorem, the volume integral of divergence of a given vector can be related to the integral over the surface bounding the elemental volume of the scalar product of the vector and the normal to the surface:

$$\int_V \nabla \cdot \mathbf{g} dV = \oint_A \mathbf{n} \cdot \mathbf{g} dA \tag{2.3}$$

Consequently, integrating the differential form of the continuity equation over an elemental volume gives the condition that the net flux into or out of the volume is zero:

$$\oint_A \rho \mathbf{u} \cdot d\mathbf{a} = 0 \tag{2.4}$$

where $d\mathbf{a}$ represents an element of the surface of $d\mathbf{V}$ pointing in the local surface normal direction. The momentum balance in integral form is written as:

$$\underbrace{\frac{\partial}{\partial t} \int_V \rho \mathbf{u} dV}_{\text{Rate of Change}} + \overbrace{\oint_A \rho \mathbf{u} \otimes \mathbf{u} \cdot d\mathbf{a}}^{\text{Convective Flux}} = \underbrace{-\oint_A p\mathbf{I} \cdot d\mathbf{a}}_{\text{Pressure Gradient}} + \overbrace{\oint_A \mathbf{T} \cdot d\mathbf{a}}^{\text{Viscous Flux}} \tag{2.5}$$

where t, V, ρ, $\mathbf{I}$ and $\mathbf{T}$ is time, cell volume, density, identity matrix and the viscosity stress tensor. A general species transport equation for any fluid property ϕ can be written as:

$$\frac{\partial \rho\phi}{\partial t} + \nabla \cdot (\rho\phi\mathbf{u}) = \nabla \cdot (D\nabla\phi) + S_\phi, \tag{2.6}$$

where ϕ represents the general source term and D is the diffusion coefficient; however, within this study, there are no sources in the region of interest, so that the source term can be ignored. This equation can be adapted for the internal energy equation by changing ϕ into T by means of an equation of state. The key step of the finite volume method is the integration of equation 2.6 over a control volume which gives the form below:

$$\int_V \frac{\partial(\rho\phi)}{\partial t} dV + \int_V \nabla \cdot (\rho\phi\mathbf{u}) dV = \int_V \nabla \cdot (D\nabla\phi) dV \tag{2.7}$$

Applying the Gauss divergence theorem, the formula can be simplified further into the form below:

$$\frac{\partial}{\partial t} \int_V \rho\phi dV + \oint_A (\rho\phi\mathbf{u}) d\mathbf{a} = \oint_A (D\nabla\phi) d\mathbf{a} \tag{2.8}$$

where the physical meaning of $d\mathbf{a}$, as above, is the normal vector to an element of the surface A of magnitude da. The physical meaning of the left side is the net rate of change of fluid property ϕ within the elemental volume due to changes in ϕ with time and the net increase or decrease due to transport into the volume across the surface boundary of area A. The right side represents the rate of change of ϕ due to transport by diffusion across the boundary. The equation therefore equates the change in the stored value of ϕ with the sum of all transfers into and out of the volume. The last step is making this integral form suitable for solution on each cell, by reducing the continuous formulation to a discretized form:

$$\frac{d}{dt}(\rho\phi V) + \sum [\rho\phi(\mathbf{u} \cdot \mathbf{a})]_f = \sum (D\nabla\phi \cdot \mathbf{a})_f \tag{2.9}$$

where the f represents the face of each element surface.

The transient term in the left hand side of the equation is discretized by a second order implicit unsteady approach. Within STAR-CCM+, a second order temporal discretization of the unsteady solver uses the solution at the current level, as well as the solutions from the previous two time levels. However, for the first time-step, even for the second order discretization, a first order Euler implicit scheme is used since only two time levels are available. As the scheme is implicit, it does not have to respect the Courant-Friedrich-Lewy (CFL) condition for stability; what is necessary is to check instead that the time step is sufficiently fine to capture the flow dynamics. Consequently, time-step independent checks were also carried out to assure the accuracy. All the simulations consider the flow as incompressible since the maximum flow Mach number throughout the airway is much less than 0.3 where the compressibility of the flow starts to become significant.

Within STAR-CCM+, a plot of solution residuals is one of the means of indicating the degree of convergence of the iteration process of the solver. Residuals are given for the continuity and three momentum components (energy and species if applicable) that is normalized by the maximum value of the first five iterations. The needed number of inner iterations of each time step depends on how quickly the residuals decrease and is easily monitored graphically. The simulation will advance to the next time step once the residuals decrease to a predefined level of accuracy. From STAR-CCM+ manual [125], a three order of relative magnitude drop in residuals is recommended as acceptable results, because the normalization of the residuals plot, each simulation will be affected by the initial condition. For instance, if the initial solution satisfies the discretized equations perfectly (the final solution is the same as the initial solution), the residuals plot will not drop at all. Within this study, all the simulation residuals dropped below the order of five. Both heat flux and species flux monitors are created between inlet and outlet to monitor the time required for a steady-state solution to be reached. In practice, it is more important to monitor how physical quantities (for example mass flow difference between in and out or pressure loss over the volume) are affected by mesh and time step refinement

to assess the reliability of the simulation, since judging a simulation well converged solely by residuals can mask an inaccurate result.

The transport of thermal energy can be modelled as an equation for the temperature field :

$$\frac{\partial T}{\partial t} + (\mathbf{u} \cdot \nabla)T = \frac{k}{\rho C_p}\nabla^2 T \tag{2.10}$$

where $\mathbf{u}$ is the velocity vector, t is time and T is temperature, C_p is the specific heat, k is the thermal conductivity. The transport equation for the water vapour is modelled using the species transport equation:

$$\frac{\partial Y_{wv}}{\partial t} + (\mathbf{u} \cdot \nabla)Y_{wv} = D\nabla^2 Y_{wv} \tag{2.11}$$

where $\mathbf{u}$ is the velocity vector; t the time; Y_{wv} the mass fraction of water vapour; D the molecular mass diffusion coefficient of water vapour. Thus the density in each cell is determined by the relative proportion, in terms of mass fraction, of air and of water.

Heat

For all the simulations performed in this research, the upper airway is modelled as a rigid body, and only the nasal cavity simulations are solving the heat equations described above. The inhaled air for both nasal cavity and trachea simulations has density of 1.184 kg.m^{-3} and viscosity of 1.855 Pa.s^{-1} (corresponding to 25 °C and 1 bar ambient pressure).

For nasal cavity simulations, the challenge for this work is to model the liquid-lined mucosa of the internal surface of the nasal cavity. Although the mucus will be shifted when the flow passes through, the actual moving distance of mucous is four orders smaller than the flow velocity [1]. Thus a non-slip condition can be applied to the internal walls. In reality, the nose draws air from the surrounding environment, so an artificial hemispherical section named 'Atmosphere' is attached in front of the human face and this geometry is created by using Boolean subtract between a sphere and a square cube within STAR-CCM+. The effect of simply apply a pre-

scribed inflow profile at the nostril has been studied by previous researchers [126, 127], and a diameter of 1 m is used of this study which is well in excess of that required for an unbiased inspiratory flow [128]. The flat part of the 'Atmosphere' geometry is intersected with the human face and slightly behind the chin and it is also treated as rigid wall. The 'mass flow rate' boundary type is applied to the half sphere surface of the 'Atmosphere' section as the inlet boundary, with values that equivalent to various breathing conditions (will be addressed in detail in the corresponding chapters). The inflow direction is parallel to the normal of the sphere surface of the inlet. Constant pressure outlet is applied at the (nasopharyngeal) outlet with reference value zero. For tracheal simulations, no heat model is added, but multiple flowrates are studied. For some of the tracheal simulations, the nasal cavity surface is attached with a relatively coarser mesh (compared to that of the trachea) to prescribe a realistic inflow profile downstream. However, only a simple extrusion at inlet and outlet are used for studies of the pathological tracheal geometries.

The nasal cavity internal surface is covered by a layer of tissue called the nasal mucosa that secretes a liquid film and provides all the heat and water needed during the air conditioning in the nose. However within this study, we model this complex tissue bed simply by a zero heat capacity membrane with a constant thickness of 1 mm everywhere; this is as proposed previously [44], however here we will not apply film theory, but proceed more directly as will be described.

The 1 mm layer provides a thermal resistance between the underlying vascular network (which is named as 'Organ') and the airway surface. From experimental measurements [70], a constant organ temperature of 34 °C is assumed and represented by symbol T_o. The nasal cavity surface temperature, which is named as T_s, is calculated within the airspace volume mesh. The heat flux through the membrane from organ side to air side is given by the steady state (since heat capacity neglected) relation:

$$\dot{q}_{memb} = -k_{memb}\frac{T_s - T_o}{\delta_{memb}} \tag{2.12}$$

where $\dot{q}_{memb}$ is the flux through the membrane and k_{memb} and δ_{memb} are respectively the thermal conductivity and thickness of the membrane layer. The above relation determines the heat flow per unit time and unit area, i.e. the heat flux, with a unit of $\mathrm{J.s^{-1}.m^{-2}}$.

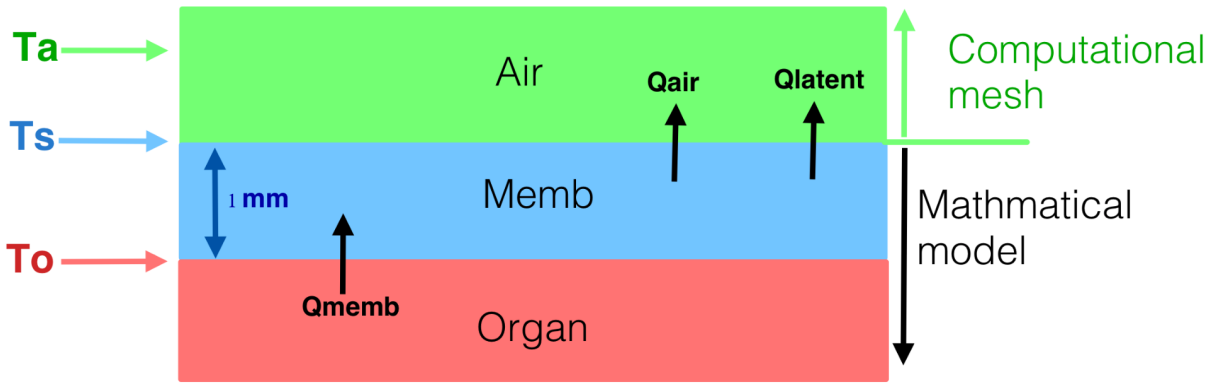


Figure 2.1: Heat model diagram.

Figure 2.1 displays the simplified model of the nasal airway surface. The nasal mucous membrane thickness is assumed constant. The upper (green) layer, labelled with 'Air' corresponds to the first layer of the computational mesh. The membrane and organ side are represented by a mathematical model instead of being calculated within the CFD solver. In addition to the heat flux from the organ through the membrane to the air, according to the temperature differences, there is an additional heat flux into or out of the membrane associated with evaporation or condensation processes. Evaporation of surface water requires an additional energy transfer from the membrane, termed the latent heat of evaporation. The inverse process, namely condensation results in an equivalent heat transfer back to the membrane. The specific latent heat coefficient is defined by the equation below which is calculated by cubic fit to Rogers et al. data [129].

$$L_{H2O} = 2500.8 - 0.00006 \cdot T_s^3 + 0.0016 \cdot T_s^2 - 2.36 \cdot T_s \tag{2.13}$$

where the T_s is in Celsius and L_{H2O} have a unit of $\mathrm{J.g^{-1}}$. Thus the total amount of heat flux

into the nasal cavity is the sum of the flux from membrane and the latent heat flux generated during the evaporation (or condensation) process. Summing the heat flux from the membrane surface into the cavity,

$$\dot{q}_{air} = -k_{air}\frac{\partial T}{\partial n}, \tag{2.14}$$

together with latent heat flux, defined as

$$\dot{q}_L = L_{H2O} \cdot \dot{w}, \tag{2.15}$$

(where $\dot{w}$ means the water mass flux and is defined by formula 2.19), yields the total amount of heat flux from human body into nasal cavity:

$$\dot{q}_{Total} = \dot{q}_{air} + \dot{q}_L = \dot{q}_{memb}. \tag{2.16}$$

The heat flux and indirectly the water flux into the domain are determined by the surface temperature T_s, which is updated at each time step so that heat and water fluxes at the membrane side and at the air side balance at each time step. Starting again with the total heat flux,

$$\dot{q}_{memb} = \dot{q}_{air} + \dot{q}_L,$$

and expanding the terms:

$$-k_{air}\frac{\partial T}{\partial n} + L_{H2O} \cdot \dot{w} = -k_{memb}\frac{T_s - T_o}{\delta_{memb}}.$$

Expanding the air-side gradient:

$$k_{air}\frac{T_a - T_s}{\delta_{wall}} - L_{H2O} \cdot \dot{w} = k_{memb}\frac{T_s - T_o}{\delta_{memb}}$$

so that the interface temperature T_s to balance the energy transfers is given by:

$$T_s = \frac{k_{air}T_a + k_{memb}T_o - L_{H2O}\dot{w}\delta_{wall}\delta_{memb}}{k_{memb}\delta_{wall} + k_{air}\delta_{memb}} \tag{2.17}$$

where δw is the thickness of the first layer of the cell. The value of T_s in the above can be thought of as a Dirichlet boundary condition for each iteration of the air side energy equation; it is constantly updated during the iteration at each time step.

Moisture

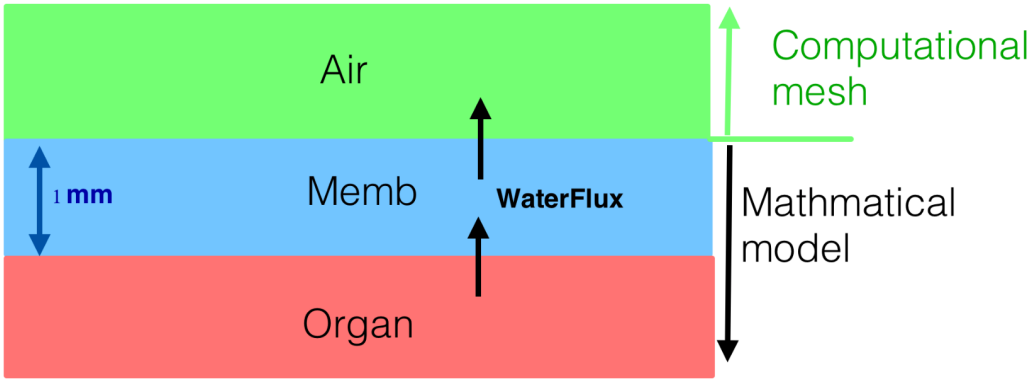


Figure 2.2: Water model diagram.

The water species transport through the boundary is displayed diagrammatically in figure 2.2. As is known [130], the water vapour is continuously supplied by the water-based mucous layer within the nasal cavity surface, for simplicity, the fully saturated condition at the interface between membrane and air is assumed and the mass fraction of water at 100% relative humidity on the interface is shown below which is a function of temperature:

$$Y_{wv} = 2 \cdot 10^{-5}T_s^2 + 0.0003T_s + 0.0025 \tag{2.18}$$

where T_s means the interface temperature. This relationship is based on the empirical relation from psychometric charts.

The mass fraction of water vapour near the wall can be calculated by equation 2.18, and the water mass flux through the membrane to the nasal cavity is calculated using Fick's law of diffusion [131]:

$$\dot{w} = -\rho_{fluid} D \frac{\partial Y_{wv}}{\partial n} \tag{2.19}$$

where ρ_{fluid} is the mixture of air and water vapour density and weighted by the mass fraction of each component ($\rho_{fluid} = \rho_{air} \cdot (1 - Y_{wv}) + \rho_{H2O} \cdot Y_{wv}$). Equation 2.20 shows the details of calculating water flux gradient near the wall. Ideally, the difference of mass fraction of water vapour between the first cell and the wall will eventually converge to zero ($\dot{w} = 0$), which indicates there is no water exchange occurring between the membrane and the nasal cavity. Then the air would have reached a fully saturated state; however this is unlikely to be fully achieved even at the nasopharynx for many or most external environmental conditions.

$$\frac{\partial Y_{wv}}{\partial n} = \frac{Y_{wv-firstcell} - Y_{wv-wall}}{\delta_{wall}} \tag{2.20}$$

Interpolation of heat and moisture boundary conditions

Within STAR-CCM+, one can either specify the boundary as a 'Temperature' or 'Heat flux' condition for heat transport; either choice allows the option of applying 'User Defined Function' which provides a mechanism for customizing the boundary values. For species transport, it provides 'Species Flux' and 'Species Mass Fraction' as the boundary condition and one can specify the boundary value as a 'User Defined Function' as well. Here we choose 'Temperature' and 'Species Mass Fraction' as the boundary condition, with both using 'User Defined Function' to customize the value.

The iterative procedure described above is used to update the wall boundary values, applying the formula 2.17 and 2.18 to define the boundary value separately. Figure 2.3 shows the initial state of the boundary condition.

1. For initial boundary values, we specify $T_{inflow} = T_a(i,n)$ (air temperature at first time step, where i represents the mesh node and n represents the time node) equal to 25 °C .

2. From this, $T_s(i,n=0)$ (surface temperature at first time step iteration) will be calculated by equation 2.17.

3. Since the organ temperature is assumed constant, $T_o(i,n)$ is set equal to 34 °C at all stages.

4. For the inflow condition of 50% relative humidity at 25 °C, the mass fraction $Y_{inflow} = Y_{wv}(i,n)$ is given the corresponding value of 0.01125 .

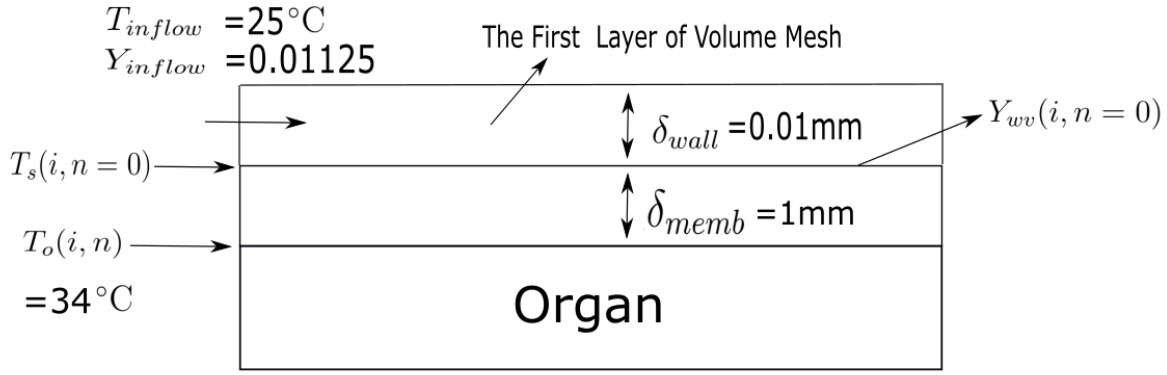


Figure 2.3: Initial state of the boundary value: δ_{wall} is the thickness of the first cell of the volume mesh and δ_{memb} is the membrane thickness and where 'n=0' indicates the initial state. Note: first order in space treatment of the boundary condition is using and is more stable

As the simulation is unsteady, the surface temperature ($T_s(i,n)$) will be iterated to convergence among all variables in the solution domain and updated at each time step. Meanwhile, the value of the water flux from the boundary into each cell in the first layer of the volume mesh is determined by the concentration gradient between the surface value of mass fraction and the mass fraction in the first cell. This concentration gradient is determined by a simple

first order difference between cell mass fraction and wall mass fraction, according to the height of the first mesh layer, δ_{wall}. The wall mass fraction corresponds to 100% relative humidity at the temperature $T_s(i,n)$.

After the current time step is finished, the surface temperature for the next time step will be replaced by the sum of the previous time step value and a fraction of the difference between the value calculated at the current time step and previous time step, i.e. under-relaxation is performed. The mass fraction of water vapour on the wall will be updated by the same procedure as the interface temperature (T_s). Equation 2.21 and 2.22 details the iteration used to effect the updating process of the surface temperature and mass fraction of water vapour on the interface between air and membrane:

$$T_s(i,n+1)_{applied} = T_s(i,n) + \alpha(T_s(i,n+1)_{calculated} - T_s(i,n)) \tag{2.21}$$

$$Y_{wv}(i,n+1)_{applied} = Y_{wv}(i,n) + \alpha(Y_{wv}(i,n+1)_{calculated} - Y_{wv}(i,n)) \tag{2.22}$$

where α is the under-relaxation number used to control the stability of the iteration process. $T_s(i,n+1)_{calculated}$ indicates the interface temperature calculated by formula 2.17 and $T_s(i,n+1)_{applied}$ represents the boundary temperature applied and used for next time step calculation by under-relaxation control. The subscript of formula 2.22 is using the same logic as formula 2.21. Testing showed a value of 0.9 to be the maximum to assure convergence from the first time step and was used here throughout; the choice of value of α could potentially be adapted during the process as the first time steps require the greatest adjustment of boundary values to achieve equilibrium between heat flux from the organ and into the air.

2.2 Nasal cavity flow

2.2.1 Definition of simulation

The physical models used for nasal cavity simulations are listed in table 2.1

	Nasal cavity geometry
Flow model	Laminar
Energy model	Segregated fluid temperature
Flow property	Ideal gas law
Transient term	Implicit unsteady
Solver	Segregated flow solver

Table 2.1: Nasal cavity simulation setup details.

The unsteady laminar flow model is used for solving the NS equations. The unsteady equations are solved with a relatively coarse time step and without applying turbulence modelling. This is because previous studies [127, 132] show flow is predominantly laminar in the nose in quiet and moderate breathing regimes. By contrast, some previous studies have applied a RANS-type turbulence model [133]. Given the experimental evidence for laminar flow at lower flow rates, and weakly transitional flow at rates as high as almost 1 L per second [42] , justification for the use of RANS modelling is lacking. However whilst computations performed in this study show unsteadiness to be largely absent up to the merging of flow at the posterior septum, some 'flapping' of flow occurs in the nasopharynx but with negligible effect on resistance or other metrics. The presence of flapping produces small fluctuations in flow resistance, so that a steady laminar flow solution does not exist; computationally this should be manifest as an inability to achieve a well-converged solution, except at very low flow rates where the nasopharyngeal jet is steady. Compared to the fully resolved computations of [42], the time step employed here is much coarser but was found in a temporal convergence study to be sufficient to capture the low frequency flapping at the nasopharynx, which is the only significant source of unsteadiness at the flow rates studied here. A further advantage of applying an unsteady solver is that it

enables the time course for water and heat flux equilibration to be determined.

For heat transfer within the nasal cavity, the segregated fluid temperature model solves the total energy equation with temperature as the solved variable, then the enthalpy is computed from temperature according to the equation of state.

2.2.2 Spatial convergence

The volume mesh for simulations was generated by STAR-CCM+ 11.04. The mesh in the bulk of the geometry consist of a polyhedral mesh which is about five times efficient than tetrahedral mesh [134], and a layer of prismatic cells near the wall comprising sheets stacked on top of each other so that the gradients of velocity, temperature and water vapour concentration near the wall can be accurately resolved. The height of the prism layer has been controlled to locate within the viscous sub-layer of the boundary layer to ensure near-wall accuracy. Local mesh refinement was applied on the geometry wherever is necessary. The details of the mesh statistics of each simulation is documented in the associated chapters. Mesh quality is always one of the most important parameters to increase the robustness and accuracy of the simulation results. Low quality cells might direct to the wrong simulation results or even lead to divergence of the solution process. An essential step before running simulation is conducting a mesh diagnostic check within STAR-CCM+; two measurements can be used to judge the mesh quality which is face validity and volume change. The specific guidelines of STAR-CCM+ can be found in appendix A.1.

The cohort of nasal cavity simulations are running with an order of 4 million mesh elements that comprise a polyhedral mesh in the bulk of the flow and prism layers at the near wall region. The mesh independent check was conducted with a range of mesh elements from 2.5 million to 6.3 million on subject D and ideally this can be used as a guidance for other nasal cavity simulations. The details of mesh statistics and the mesh structures can be found in appendix A.3.

The overall total pressure loss of subject D congested cavity with various mesh elements is listed in table A.2 at flow rate 30 $l.min^{-1}$. It shows the total pressure loss converging to the same value while increasing the total amount of mesh elements. The total pressure loss is a temporal mean value between solution time 0.1 s and 0.3 s and the reason is explained in appendix figure A.1. The relative error is calculated using the finest simulation (case D(f)) as the reference case and is listed in percentage. As shown, the simulation with 4 million mesh elements has only 1.2% difference in pressure loss compared to the reference simulation and that was chosen as the mesh setting for the cohort nasal cavity simulations. Similarly, the subject D decongested cavity mesh independent check details are displayed in appendix A.4

2.2.3 Temporal convergence

For the temporal convergence study, table 2.2 lists simulations with various time step parameters but with the same amount of mesh elements (4 million). It shows that when the time step changes from 5 ms to 0.1 ms, the effect on total pressure loss is not pronounced and the fluctuation of different cases are within 2%. This is also similar for quantities of total heat transferred and water flux transferred, although it has been found that the existences of unsteadiness through the nasal cavity [92]. In other words, we can conclude that for quantities concerned of this study, the simulation results of nasal cavity flow are not sensitive to the temporal resolution.

Subject(mesh identifier)	D(c)	D(c)	D(c)	D(c)	D(c)	D(f)
Time step (ms)	5	2	1	0.5	0.1	0.1
Mean total pressure loss between inlet and outlet(Pa)	24.3	24.3	24.2	24.1	24.2	24.5
Relative error (%)	0.8	0.8	1.2	1.6	1.2	0
Total heat transfer across the cavity (W)	5.22	5.19	5.19	5.18	5.2	5.19
Relative error (%)	-0.58	0	0	0.19	-0.19	0
Total water transfer across the cavity (e-5) (kg/s)	1.12	1.12	1.12	1.12	1.12	1.12
Relative error (%)	0	0	0	0	0	0

Table 2.2: Subject-D temporal resolution independent check. Besides total pressure loss, there are two other quantities that being studied: total amount of heat transferred as well as the total amount of water. D(c) represents the subject D congested cavity with 4 million mesh elements.

To further investigate the effect of temporal resolution on the simulation results. Figure 2.4 shows the total pressure drop between inlet and outlet during the simulation in physical time. As can be seen the evolution of pressure loss for case D(c) with 1 ms time step approximately matches that of case D(c) with 0.1 ms time step, in terms of level and oscillatory character although it appears out of phase both in magnitude and time. To achieve the similar level of accuracy of simulation results, the temporal resolution of 1 ms is chosen and applied to the rest nasal cavity simulations, as it is shown the mean total pressure loss and total amount of heat and water exchange does not show significant difference (table 2.2). (The oscillatory behaviour is principally due to flapping of the flow from the nasal choanae leading to the nasopharynx, as shown the flow recirculation in figure 3.4.) Even further, the plot of simulation with 6 million and 0.1 ms time step shows extremely similar to results of case D(c) of 0.1ms time step in frequency and 1.2 % mean offset in magnitude.

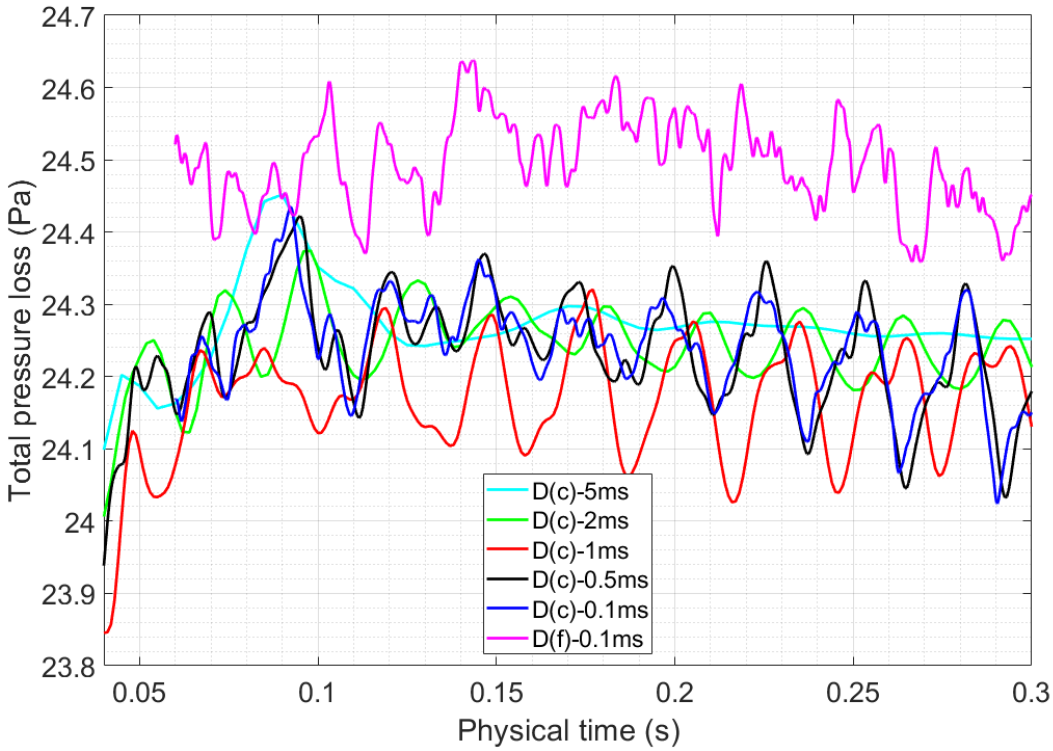


Figure 2.4: Total pressure loss plot along with simulation physical time.

2.2.4 Water flux balance

According to the heat flux model described for the nasal cavity simulations, the heat flux originating from the virtual membrane should take time to reach equilibrium with that lost at the surface, due to thermal inertia of the mucosa and the development of a thermal boundary layer in the flow. The current model neglects thermal inertia effects and we consider only steady flows. After an initial transient, a steady state needs to be reached numerically at which point the amount of water flux from the cavity surface should equal to the amount of water increased within the same geometry range. Figure 2.5 shows the comparison of water flux from the cavity surface and the amount of water added between AS and PS plane. It shows that after 0.07 s, these two quantities start to converge to a same value, although the plot for both quantities shows fluctuation which is due to the unsteady nature of the nasal cavity flow. Whilst the total amount of water coming from the cavity wall and the increased amount of water within the

same geometry range should be the same, there is a small numerical difference of 0.6% which we ascribe to differences in the computation procedure for each flux requiring evaluation and summation of gradients versus summation over interior cell values for moisture content.

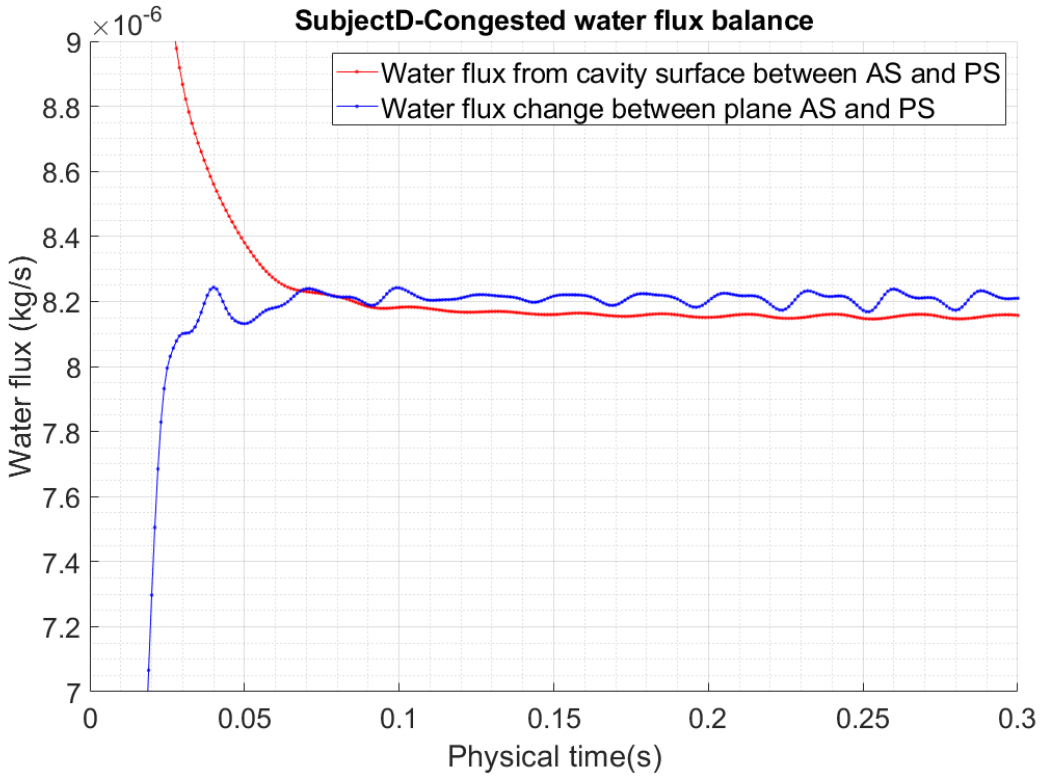


Figure 2.5: Comparison between integrated water flux from nasal cavity surface and the difference of water flux between inflow and outflow.

2.3 Nasal cavity boundary conditions

To make the simulation as realistic as possible, the nasal cavity surface from segmentation is defined with the in-vivo conditions. As mentioned above, the artificial surfaces that needed to seal the volume of interest which used by CFD solver were created and named as 'Atmosphere' for inlet and for outlet there is only simple extrusion created from the end of the original surface. Figure 2.6 shows the location and size of the half sphere inlet as well as the outlet extrusion.

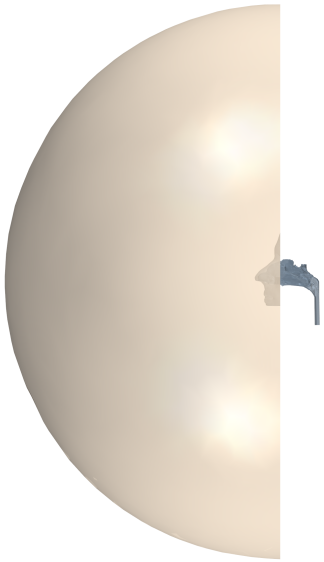


Figure 2.6: Demonstration of artificial inlet and outlet boundaries. The diameter of half sphere inlet is 1m and the outlet extrusion length is 0.05m to assure the ideal flow profile.

All the simulations are performed specifying the mass flowrate at the inlet. The outlet is set as a pressure outlet with a value of zero of the static pressure. The inflow farfield boundary corresponds to a half sphere of radius 0.5 m. Previously it was shown [127] that air entering the nostrils rapidly approaches a simple sink type flow with increasing distance from the nostrils, so the influence of the farfield diminishes rapidly with distance. Effectively, this renders the flow largely insensitive to the location of boundary condition specified. Subsequently Bates [128] confirmed that the choice of velocity vs pressure as the prescribed inflow does not alter the flow dynamics, by comparing the solution obtained using pressure vs the solution using velocity as the prescribed inflow, (figure 4.4 of Bates thesis [128]). Since the transnasal resistance fluctuates slightly depending on the instantaneous flow pattern, if pressure is held constant, flowrate will fluctuate and vice versa when flow is held constant. Since these fluctuations are small and moreover since the applied inspiratory pressure in-vivo is not constant, the different forms of boundary specification may be considered immaterial for the simulations reported here. The direction of flow into the volume is normal to the inlet surface boundary. Both inlet and outlet are located far away sufficiently from the volume of nasal cavity to avoid the flow being affected by the well-posed boundary conditions. This study simulated two flow rate of the nasal cavity simulations: (1) 15 L.min^{-1}, for restful breathing; (2) 30 L.min^{-1} for representing light exercise

breathing rate. The heat and water boundary values have been specified in the previous sections where the implementation process of heat and water model is described.

Although most parts of human airway tract surfaces are covered with soft tissues, in the CFD simulations they are treated as rigid wall and with non-slip condition (velocity equals to zero on the surface). In addition, the movement of airway surface during breathing process is also not in the scope of this study, but it has been studied by Bates lately [135]. Furthermore, simulations without individual description, the boundary conditions described here are applied.

2.3.1 Heat and water flux boundary condition: choice of model and definition of exchange region

As has been discussed above, the human nasal cavity inner surface is covered with mucous that directly provides the source of heat and water while doing air-conditioning during breathing. However, the nostril inner surface is not as humid as the turbinate surface. The way that the nasal cavity surface changes from relative dry surface (nostril inner surface) to humid surface (turbinate surface) is not clear. The effects of different ways of defining the transition from dry to complete mucus film in the simulation are addressed and compared here.

At the vestibule, the human nose is lined with a mucous membrane of squamous epithelium, which is tissue then transitions to become columnar respiratory epithelium, a pseudo-stratified, ciliated (lash-like) tissue with abundant seromucinous glands, which maintains the nasal moisture and protects the respiratory tract from bacteriologic infection and foreign objects.

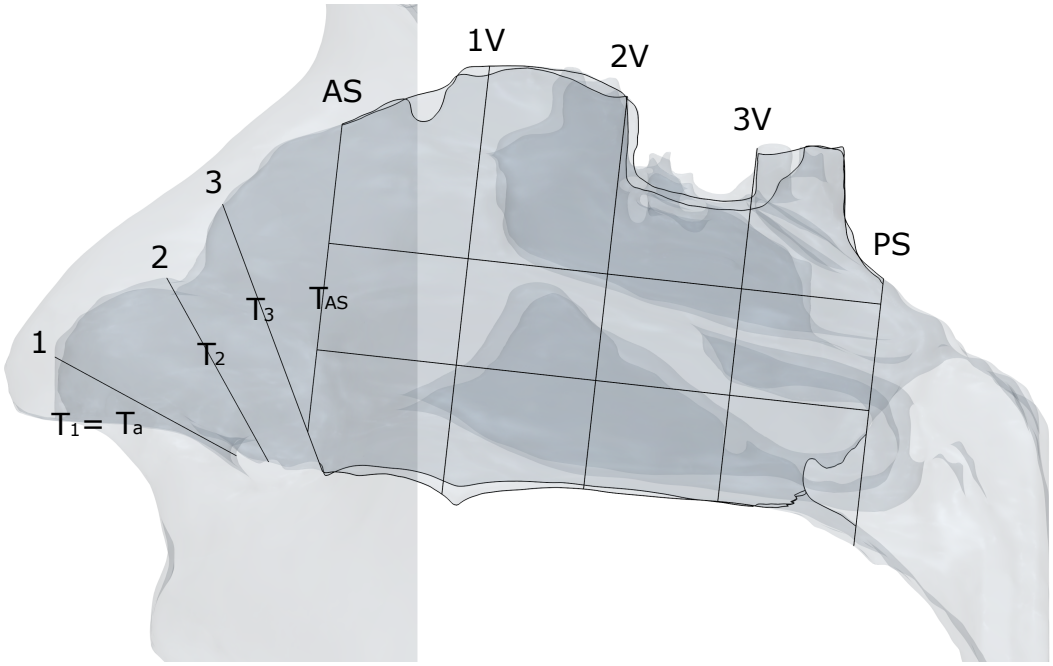


Figure 2.7: Partition defined for transitions from 'dry' surface to water exchanging surface. T_1, T_2, T_3 and T_{AS} represents the temperature at location of plane 1, 2, 3 and AS; T_a means the temperature of inflow stream.

Figure 2.7 displays the partitions that used for defining the transition from 'dry' surface to water exchanging surface. As defined, (1) section within 1 and 2 represents the nostril; (2) section between plane 2 and 3 indicates the vestibule; (3) section between plane 3 and AS is a part of the anterior cavity. The transitions of heat and water are only discussing within the region formed by plane 1 and AS. Transition from 'dry' surface to water exchanging surface varies from (1) BC1, no transition for both heat and water: the surface is treated as the same as the fully saturated from plane 1; (2) BC2, for heat, transition between plane 1 to 3; for water, transition between plane 2 to 3; (3) BC3, for heat, transition between plane 1 to 3; for water, transition from plane 2 to AS; (4) BC4, for heat, transition between plane 1 and 3; for water, transition from plane 1 to 3; (5) BC5 is the same as BC2 and the surface mass fraction value is different. The calculation of $\dot{m}_s$ is the same as previous study [44] and the details are shown in appendix A.5. Table 2.3 illustrates the exact boundary values used for various transition combinations.

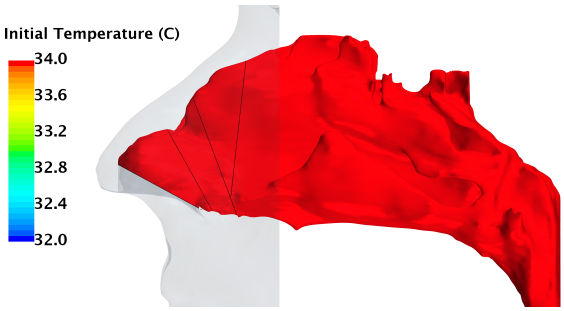
BC1	$T_1 = T_{face}$; $T_{1-AS} = T_s$ $\dot{m}_{H2O}^{1-AS} = \dot{m}_{H2O}^{s}$
BC2	$T_1 = T_{face}$; $T_{1-3} = T_1 * \frac{d_3}{d_1+d_3} + T_3 * \frac{d_1}{d_1+d_3}$; $\mathrm{T}_{3-AS} = \mathrm{T}_s$ $\dot{m}_{H2O}^{1-2} = 0$; $\dot{m}_{H2O}^{2} = \dot{m}_{H2O}^{air}$; $\dot{m}_{H2O}^{2-3} = \dot{m}_{H2O}^{2} * \frac{d3}{d2+d3} + \dot{m}_{H2O}^{3} * \frac{d2}{d2+d3}$;$\dot{m}_{H2O}^{3-AS} = \dot{m}_{H2O}^{s}$
BC3	$T_1 = T_{face}$; $T_{1-3} = T_1 * \frac{d_3}{d_1+d_3} + T_3 * \frac{d_1}{d_1+d_3}$; $\mathrm{T}_{3-AS} = \mathrm{T}_s$ $\dot{m}_{H2O}^{1-2} = 0$; $\dot{m}_{H2O}^{2} = \dot{m}_{H2O}^{air}$; $\dot{m}_{H2O}^{2-AS} = \dot{m}_{H2O}^{2} * \frac{d_{AS}}{d_2+d_{AS}} + \dot{m}_{H2O}^{AS} * \frac{d2}{d_2+d_{AS}}$; $\dot{m}_{H2O}^{AS} = \dot{m}_{H2O}^{s}$
BC4	$T_1 = T_{face}$; $T_{1-3} = T_1 * \frac{d_3}{d_1+d_3} + T_3 * \frac{d_1}{d_1+d_3}$; $\mathrm{T}_{3-AS} = \mathrm{T}_s$ $\dot{m}_{H2O}^{1} = \dot{m}_{H2O}^{air}$; $\dot{m}_{H2O}^{1-3} = \dot{m}_{H2O}^{1} * \frac{d_3}{d_1+d_3} + \dot{m}_{H2O}^{3} * \frac{d_1}{d_1+d_3}$; $\dot{m}_{H2O}^{3-AS} = \dot{m}_{H2O}^{s}$
BC5	Same as BC2, but the value of $\dot{m}_{H2O}$ is calculated with two-film theory.

Table 2.3: Transition region heat and moisture boundary conditions. In the transition region, the surface value is calculated by interpolating between conditions specified at the planes denoting start and end of the transition region. Lower case d_x, e.g. d_1, d_2, d_3 and d_{AS} represent distances of an arbitrary point on the surface to the bounding planes of the appropriate transition region, for example d_1, d_3 are used between planes 1 and 3 and d_2 , d_{AS} between planes 2 and AS. The surface mass fraction of water of BC5 is calculated using two-film theory rather than simply assuming a fully saturated condition on the cavity surface.

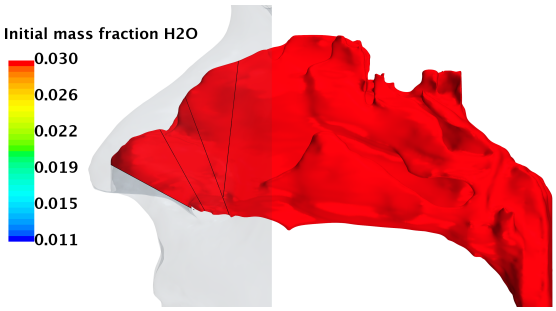
Figure 2.8 show the initial values when applying each of the boundary conditions described, except BC5. As can be seen the change of boundary conditions from BC1 to BC 4 for both temperature and water mass fraction on the anterior cavity surface shows different heat and water maps accordingly.

The cumulative sum of the amount of water transferred into the cavity along the nasal cavity centerline for the various surface treatments is plotted in figure 2.9. As can be seen, the total amount of water flux transferred are similar for all cases with the notable exception of BC5, although there is a relatively larger mismatch in the anterior part of the cavity. The varies anterior transition combinations does affect the amount of water transferred into the cavity. The dashed line of BC1 represents the boundary condition that with no transition, has the maximum amount of the total water flux into the cavity. However, the significant difference of water model between BC5 and the others is that BC5 is using the two-film transfer model for water as well [44], just like the way how heat flux is treated in this study. Consequently, the

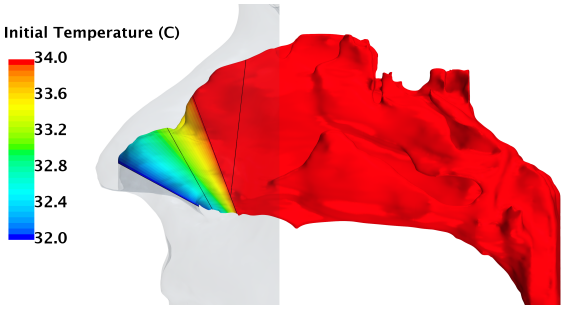
relative humidity on the interface between airflow and cavity surface will not be able to reach fully saturated condition, not the same as this study. Thus as can be seen from the plot, this will lead to nearly 40% less water flux transfer into the cavity compared to BC2, which is used for cohort study.



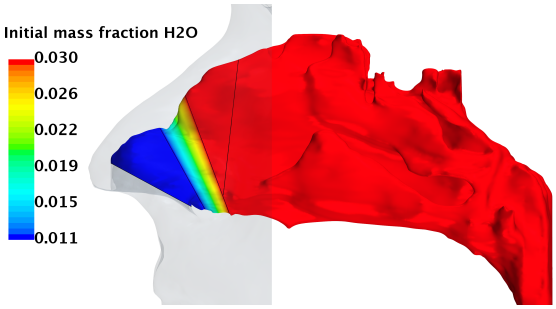
(a) Initial temperature condition of BC1.



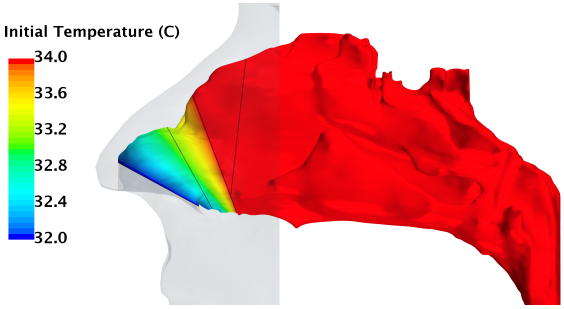
(b) Initial water condition of BC1.



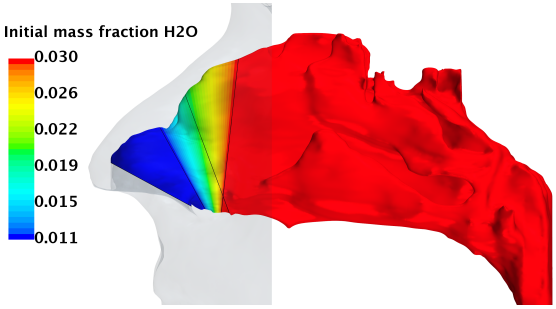
(c) Initial temperature condition of BC2.



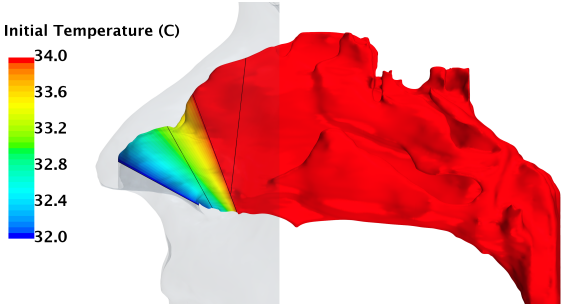
(d) Initial water condition of BC2.



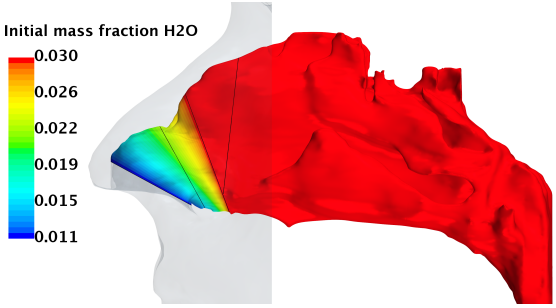
(e) Initial temperature condition of BC3.



(f) Initial water condition of BC3.



(g) Initial temperature condition of BC4.



(h) Initial water condition of BC4.

Figure 2.8: Initial condition with displayed by scalar map of multiple boundary conditions.

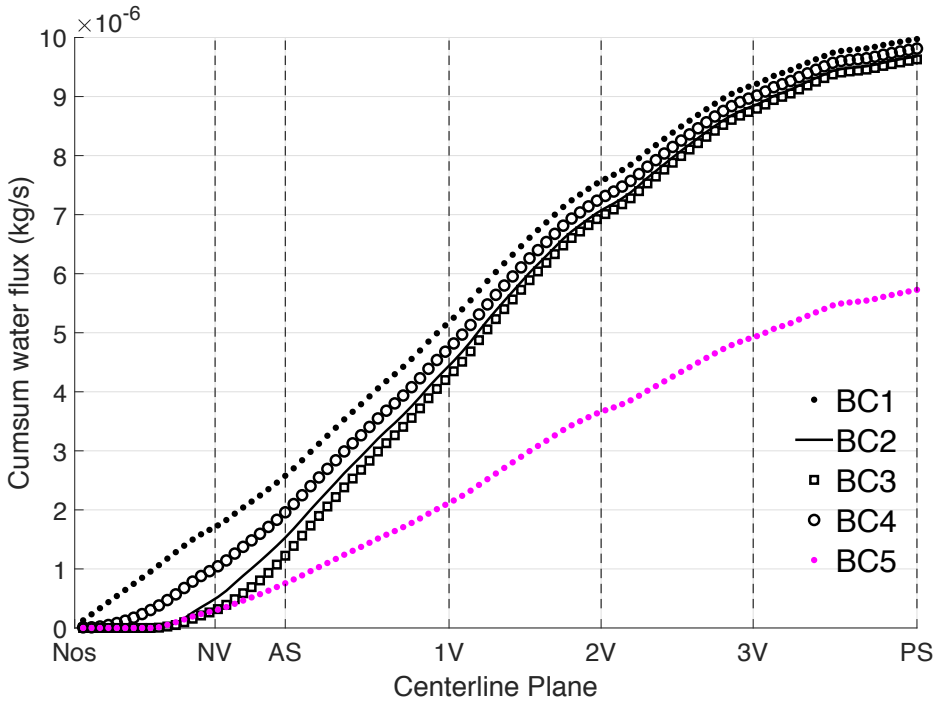


Figure 2.9: Cumulative anterior to posterior local water flux from cavity surface.

2.3.2 Membrane thickness sensitivity

The membrane thickness of the heat and water model will affect the amount of water that can be transferred through the cavity surface. For the 4 different values of thickness and the flux limited condition, the evolution of the flux balance is plotted, in figure 2.10. From this figure, it can be seen that the rate of the water flux from a volume balance (water inflow - outflow in the cavity) reaches equilibrium with the water flux transmitted through the cavity wall surface more rapidly with reducing the membrane thickness. This means thinner membrane thickness allows a quicker water flux equilibrium to be reached under the same boundary condition. The plot of BC5 (flux-limited) not only shows a slower rate of reaching the equilibrium of water flux, but also a much lower value compare to the same membrane thickness of BC2. The results show that the time required for the water flux from the cavity surface and the water flux increase between the inflow and outflow of the same geometry to equilibrate depends on both the membrane thickness and also on the amount of the water transferred from the surface.

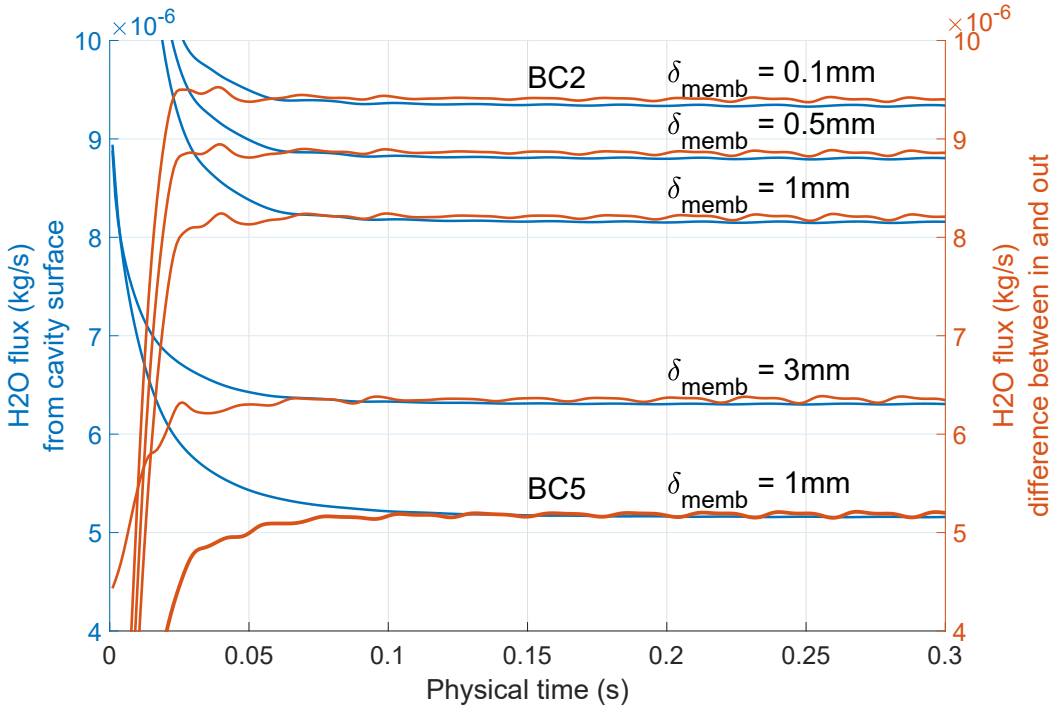


Figure 2.10: Comparison between water flux transferred from cavity surface and the difference between inflow and outflow within the geometry range of plane AS and PS.

2.4 Laryngo-tracheal flow

Flow in the nasal airways is predominantly laminar under quiet breathing conditions, owing to the relatively low Reynolds numbers of O(1000). Flow entering the nasopharynx is generally at least weakly unsteady; rapid area variations in the supra glottic space may produce localized jets [42] and the restriction of the glottic aperture produces a local acceleration. Consequently flow in the trachea is turbulent, posing more severe computational demands on laryngotracheal and tracheal simulations.

2.4.1 Transitional and turbulent flow models

Direct numerical simulation (DNS) numerically solves the NS equations without introducing any turbulence model. This indicates that all the scales, both spatial and temporal, of the turbulence must be resolved. It is the ideal case if there are enough computational resources

available. Typically it requires a higher order spatial discretization schemes and explicit temporal integration to help reduce the incurred numerical errors [136]. However, in STAR-CCM+, only second-order central-differencing scheme with boundedness is used, along with second-order implicit temporal discretization, which has been shown to produce a reasonable but not fully verifiable confidence of accuracy to meet the demanding standards for full DNS in most cases. Therefore, this method is called quasi direct numerical simulation (qDNS) in STAR-CCM+ [137, 138].

A popular alternative to DNS is LES, in which the larger scale unsteady features of turbulent flow are simulated, but the fine scale turbulence is modelled by an approximation. Still less accurate are models in which all of the turbulent fluctuations are modelled and the flow is assumed steady, or at most varying in time but slowly relative to turbulence timescales. These models are termed RANS, when the large scale flow is assumed steady, or unsteady RANS (URANS), where the large scale flow is permitted to be unsteady, but over longer timescales than the modelled turbulence.

The difference between turbulence modelling in LES versus that in RANS models is that for LES, a spatial filtering is applied to the equation rather than a temporal averaging in the case of RANS. Thus in LES, each of the variables is decomposed into a filtered component, that which is resolved by the mesh, and a sub-grid value, which has a spatial wavelength too small for the mesh to resolve. The rationale for LES modelling derives from Kolmogorov's theory of the self-similarity in turbulent flows [139], which suggests that it should be possible to explicitly solve only the large eddies, which contain most of the turbulent energy, and to model the small eddies by using a subgrid-scale (SGS) model. STAR-CCM+ provides three SGS models to represent the unresolved turbulent length scales: Smagorinsky, Dynamic Smagorinsky, and Wall Adapting Local Eddy (WALE). Within this study, the WALE SGS model is picked due to its flexibility in handling wall-bounded flows and the transition regime, with a reasonable computational cost for LES.

Turbulence scales

Determining appropriate modelling for turbulent flows requires a basic understanding of the length scales in a turbulent flow. From Kolmogorov's theory, the length scales depend on the kinematic viscosity and the rate of turbulent energy dissipation. To determine the turbulent energy dissipation, it is usual to separate out the fluctuating components of the flow from the steady components, since most flows (as in those modelled here) are assumed either steady or relatively slowly varying in time.

The temporal mean of any flow property f can be defined as:

$$\bar{f} = lim_{T\to\infty}\frac{1}{T}\int_{t}^{t+T} f(x,y,z,t)dt \tag{2.23}$$

where T represents the averaging time period and numerically, this integral form can be converted to discrete form:

$$\overline{f(x,y,z,t)} = \frac{1}{N}\sum_{i=0}^{N} f_i(x,y,z,t) \tag{2.24}$$

where N means the number of samples considered within the time period T and i is the element counter. The fluctuation of f can be expressed as:

$$f^{'}(x,y,z,t) = f(x,y,z,t) - \overline{f(x,y,z,t)} \tag{2.25}$$

The variance of $f^{'}$ will be in the form:

$$\begin{aligned} Variance(f^{'}) =& \overline{f'(x,y,z,t)^2} \\ =& \overline{\Big((f(x,y,z,t) - \overline{f(x,y,z,t)})\Big)^2} \\ =& \overline{f(x,y,z,t)^2} - \overline{2f(x,y,z,t)\overline{f(x,y,z,t)}} - \Big(\overline{f(x,y,z,t)}\Big)^2 \\ =& \overline{f(x,y,z,t)^2} - \Big(\overline{f(x,y,z,t)}\Big)^2 \end{aligned} \tag{2.26}$$

Numerically, the variance of $f^{'}$ will be defined as:

$$Variance(f^{'}) = \frac{1}{N-1}\left[\sum_{i=1}^{N} f_i^2 - \left(\frac{1}{N}\sum_{i=1}^{N} f_i\right)^2\right] \tag{2.27}$$

The means of quantifying the accuracy of CFD simulation results can be achieved by comparing the mesh element size and time step to the smallest scale within the bulk of flow.

Kolmogorov scales are the smallest scales in turbulent flow and at this scale flow will dominates by viscosity and the turbulent kinetic energy will dissipate into heat. The calculation of Kolmogorov length scale need to obtain the turbulent dissipation rate first. As pointed out by Delafosse et al.[140], the turbulent dissipation rate is defined as:

$$\begin{aligned}\epsilon =& \nu\{2\left(\overline{\left(\frac{\partial u_1^{'}}{\partial x_1}\right)^2} + \overline{\left(\frac{\partial u_2^{'}}{\partial x_2}\right)^2} + \overline{\left(\frac{\partial u_3^{'}}{\partial x_3}\right)^2}\right) + \overline{\left(\frac{\partial u_1^{'}}{\partial x_2}\right)^2} + \overline{\left(\frac{\partial u_2^{'}}{\partial x_1}\right)^2} + \overline{\left(\frac{\partial u_1^{'}}{\partial x_3}\right)^2} \\ &+ \overline{\left(\frac{\partial u_3^{'}}{\partial x_1}\right)^2} + \overline{\left(\frac{\partial u_2^{'}}{\partial x_3}\right)^2} + \overline{\left(\frac{\partial u_3^{'}}{\partial x_2}\right)^2} + 2\left(\overline{\frac{\partial u_1^{'}}{\partial u_2^{'}}\frac{\partial u_2^{'}}{\partial u_1^{'}}} + \overline{\frac{\partial u_1^{'}}{\partial u_3^{'}}\frac{\partial u_3^{'}}{\partial u_1^{'}}} + \overline{\frac{\partial u_2^{'}}{\partial u_3^{'}}\frac{\partial u_3^{'}}{\partial u_2^{'}}}\right)\}\end{aligned} \tag{2.28}$$

where $u_1^{'}$, $u_2^{'}$ and $u_3^{'}$ represents the fluctuating component of velocity vector and ν is the kinematic viscosity.

Once obtained the dissipation rate, the Kolmogorov length scale can be calculated by equation 2.29 :

$$\eta = \left(\frac{\nu^3}{\epsilon}\right)^{\frac{1}{4}} \tag{2.29}$$

At the same time, the Kolmogorov time scale can be expressed as:

$$\tau_\eta = \left(\frac{\nu}{\epsilon}\right)^{\frac{1}{2}} \tag{2.30}$$

2.4.2 Definition of simulation

In this work, there are two separate studies of the flow in the trachea. The first considers the effect of glottic aperture on inspiratory flow in the normal trachea, whilst the second concerns flow in pathological tracheas, where external compression by a retrosternal goitre results in a deviated and constricted trachea. The first study includes the entire supraglottic airway, including the nasal airway to provide realistic tracheal inflow. This study is conducted primarily using an unsteady laminar flow simulation, without engaging an LES model, despite the elevated Reynolds number. The second study applies LES modelling to pathological geometries without nasal airway attached.

In both cases, simulations are compared with qDNS results, whilst the first (glottic aperture) study also includes comparison with experimental data from a separate study. The relative accuracy of different modelling approaches can thus be compared. Both studies are assumed the flow density as constant and using segregated implicit unsteady solver.

2.4.3 Spatial convergence

A similarly meshing strategy is applied for tracheal modelling as used for the nasal cavity, with the combination of polyhedral mesh in the core and prism layer mesh near the wall. Especially, for LES model, a y+ value less or equal to 1 is sufficient to ensure the first layer of the cell is located within the laminar sub-layer. For pathological trachea geometries, the most demanding case (referred to as T15 in the later chapter) is selected to test for convergence (as the most constricted geometry, this provides the strongest flow jet and should represent the most complicated flow behaviour) and the mesh statistics for both complete airway and pathological trachea can be found in appendix A.6 and A.7.

In order to investigate the dependence of the flow on the computational resolution, the trachea geometry of 10 degrees glottis at flow rate 50 L.min^{-1} is considered. First of all, the spacial

convergence is conducted in a systematic manner and shown in table 2.4:

Simulation	1	2	3	4	5	6	7
Flow model	Laminar	Laminar	Laminar	Laminar	Laminar	LES	qDNS
Mesh elements (million)	1.8	2.2	2.9	4.6	6.5	11.2	14.6
Total pressure loss Inlet - outlet (Pa)	107.6	107.8	108.7	109.4	110.0	118.3	118.5
Relative error (%)	9.2	8.3	8.3	7.7	7.2	0.2	0

Table 2.4: Mesh independence checks for trachea simulations with nasal cavity attached.

Table 2.4 displays 7 different meshes. From the table we can see that simulation 3 has a decent converged result if simulation 7 is used as the reference, but with much fewer mesh elements, which reduced from 14.7 million to 2.9). Simulation 3 can be considered sufficiently accurate for measuring pressure loss purposes, given the uncertainty in the source image data, leading to appreciable computational time-saving.

2.4.4 Temporal convergence

Results were obtained for time steps ranging from 5×10^{-4} s up to 5×10^{-3} s; likewise, these showed that a 1×10^{-3} s time step to be sufficient to ensure relative accuracy over 95%. Keep using the qDNS simulation result as the reference value, we can find the relative errors of various time steps as shown in the table. From this we can conclude that the temporal resolution is secondary to spatial resolution, in that comparable errors are found for all of the time steps tested.

Simulation	a	b	c	d	e	f
Time step (ms)	5	2	1	0.5	0.2	0.1
Total pressure loss Inlet - outlet (Pa)	109.7	109.8	108.7	108.5	108.4	107.7
Relative error (%)	7.4	7.3	8.3	8.4	8.5	9.1

Table 2.5: Temporal resolution effect on the overall mean total pressure loss of laminar model simulation.

2.5 Laryngo-tracheal boundary conditions

Subjects with healthy trachea are simulated with nasal cavity attached to ensure a realistic upstream flow profile. Figure 2.11a shows the healthy subject laryngotracheal flow simulation uses the same half sphere as the inlet boundary as previously used for nasal cavity simulation. Extrusions are applied to the bronchial outflow tracts as the outflow boundary.

The inlet and outlet boundaries of pathological tracheal geometries use simple extrusion as shown in figure 2.11b, since the imaged region is normally of such limited extent to exclude some or even all of the supraglottic airway. In these flow simulations, the inlet also uses a specific mass flow inlet boundary type and the outlet is pressure outlet with zero static pressure.



(a) (b)

Figure 2.11: Figure a shows the boundaries for healthy subject laryngotracheal flow simulation, while figure b shows the boundaries for pathological laryngo-tracheal flow simulation.

Multiple flowrates are studied on complete airway geometries that range from 20 L.min^{-1} to 80 L.min^{-1} with 10 L.min^{-1} as the interval. There is no heat and water model applied on the laryngotracheal flow study. For pathological geometries, flowrate of 392 ml.s^{-1} (23.5 L.min^{-1}), corresponding to the peak flow rate for a half sinusoidal inhalation of duration 2 s at a tidal volume of 500 ml, using LES with the WALE sub-grid scale model in STAR-CCM+. Other flow rates (30, 40 and 50 L.min^{-1}) were also simulated for T15.

2.6 Definition of flow metrics

Reynolds number

The definition of Reynolds number is the ratio of inertial force over viscous force. The formula of calculating mean Reynolds number on the cross-sectional plane is:

$$Re = \frac{\rho \bar{U} d_H}{\mu} \tag{2.31}$$

where ρ is the fluid density, $\bar{U}$ is the mean velocity of the cross-sectional plane, d_H is the

hydraulic diameter the geometry and μ is the dynamic viscosity. The hydraulic diameter is used to represent the characteristic length of the flow within non-circular tubes or channels and the formula is:

$$d_h = \frac{4A}{P} \tag{2.32}$$

where A is the cross-sectional area of the flow and P is the associated perimeter.

Within the nasal cavity, the Reynolds number of each half cavity is calculated individually while the bilateral cavity Reynolds number a sum of mass flow weighted value of left and right cavity Reynolds number, as shown below:

$$Re_{Bi} = Re_L \cdot \frac{\dot{m}_L}{\dot{m}_L + \dot{m}_R} + Re_R \cdot \frac{\dot{m}_R}{\dot{m}_L + \dot{m}_R} \tag{2.33}$$

where Re_{Bi} represests the bialteral cavity Reynolds numnber and Re_L as well as Re_R are the Reynolds number of left and right cavity separately. $\dot{m}_L$ and $\dot{m}_R$ are the mass flow of left and right cavities.

Vorticity and wall shear stress

The vorticity of the flow field is represented by ω which is the curl of the flow velocity $\mathbf{u}$ with the form of $\omega = \bigtriangledown \times \mathbf{u}$. The wall shear stress is defined as:

$$\tau_\omega = \mu(\frac{\partial u_i}{\partial x_j} + \frac{\partial u_j}{\partial x_i})n_j \tag{2.34}$$

where u_i and u_j are the velocity components, n_j is a component of the wall normal vector.

Pressure loss and resistance

The ideal airway would deliver fully conditioned air at a negligible energy cost to the lungs. Instead, it is necessary for the respiratory muscles to expend work, known as the work of breathing, in order to deliver air to the alveolar gas exchange surface in the lung. In normal restful breathing, most of the effort required to move air occurs during inspiration and is accounted for by the work required to overcome surface tension and expand the alveoli. The airway surface resistance is generally a smaller component of the total work and is accounted for primarily by the nose, the glottis and the early generations of airway branching. Considered by itself, the contribution to airway resistance of the normal trachea is negligible. As air flows through a conduit, the product of total pressure and flow velocity over a cross-section is equal to the mechanical energy flux which can be evaluated by measuring the dissipation rate along the flow axis direction. Thus an appropriate means to quantify the energy cost of a portion of the airways is the total pressure loss across the corresponding region. Within this study, a surface average report is created and used to calculate both the total pressure and static pressure on the cross-sectional planes:

$$P = \frac{\int_i^n P_i dA_i}{\int_i^n dA_i} \tag{2.35}$$

where i is the face identifier, n is the total amount of the faces of each cross-sectional plane, A is the area and P is pressure. Similar as this area averaged calculation of pressure loss, the mass flow averaged calculation of pressure loss can avoid the artefact effect of calculation of flow measures such as total pressure loss or resistance, especially in the flow recirculation region. The formula is in the similar form as equation 2.35 but with an added weight factor which is mass flowrate on each surface cell centre:

$$P_{mf} = \frac{\int_i^n w_i \cdot P_i dA_i}{\int_i^n w_i \cdot dA_i} \tag{2.36}$$

where P_{mf} is the pressure on each cross-sectional plane with mass flowrate weighted. w_i is the weight factor which is equal to the mass flowrate on each surface cell of the cross-sectional plane.

The unit flowrate pressure loss is defined as the ratio of total pressure loss to the corresponding flowrate. This is also named as resistance and is commonly used by clinician while assessing the nasal cavity patency, which with the formula shown:

$$R = \frac{PL}{Q} \tag{2.37}$$

where PL is pressure loss and Q is flow rate.

similarly as the bilateral cavity Reynolds number, the bilateral pressure loss and resistance are also weighted by the mass flow split ratio between left and right cavities.

Energy flux and dissipation calculation

The changes in energy flux along the cross-sectional planes represents the energy required to drive the flow though the geometry. The instantaneous energy flux on a specific plane is defined as:

$$E_i = \int_S (\mathbf{u} \cdot \mathbf{n})[P_s + \frac{1}{2}\rho|\mathbf{u}|^2]dS \tag{2.38}$$

where $\mathbf{u}$ is the velocity vector, ρ is the flow density, P_s is the static pressure and $\mathbf{n}$ is the normal vector of the cross-sectional plane. The first term within the round bracket represents the velocity normal component of the cross-sectional plane and the term within square bracket is total pressure. The surface integral over the product of these two terms indicate the energy flux through the associated planes. The total energy loss within a volume formed by plane i and j can be calculated by formula:

$$\Delta E = (E_i - E_j) \tag{2.39}$$

On the other hand, the energy lost of the fluid can also be evaluated by calculating the dissipation rate of the fluid as shown by formula 2.40:

$$\epsilon_{total} = \nu\{ \left[\left(\frac{\partial(u)}{\partial(x)} \right)^2 + \left(\frac{\partial(v)}{\partial(y)} \right)^2 + \left(\frac{\partial(w)}{\partial(z)} \right)^2 \right] + \left(\frac{\partial u}{\partial y} + \frac{\partial v}{\partial x} \right)^2 + \left(\frac{\partial u}{\partial z} + \frac{\partial w}{\partial x} \right)^2 + \left(\frac{\partial v}{\partial z} + \frac{\partial w}{\partial w} \right)^2 \} \tag{2.40}$$

For RANS turbulence model, the velocity contains two components which are the field mean component ($\bar{u}$) and fluctuating component ($u^{'}$), then the dissipation rate can be evaluated as laminar or turbulent dissipation separately.

Relative humidity and moisture content level

In the case of the nasal airways, besides the axial resistance through the cavity, the way air is directed and divided in the cavity is examined in this work in order to quantify the effects of geometry on the patterns of flow. Whereas the energy cost of flow delivery may be thought of as the primary metric, there are important secondary costs that can also be measured. Firstly, the degree to which the nasal airways accomplish warming and humidification are important measures which can be reflected by the increase in temperature and relative humidity (RH).

RH depends on the temperature and is normally defined by either the ratio of water vapor partial pressure to the equilibrium vapor pressure or the ratio of actual water vapor dry mass mixing ratio ω to the saturation mixing ratio ω_s at the corresponding temperature and pressure. The equation of calculating relative humidity used in this study is:

$$RH(\%) = 100 * \frac{\omega}{\omega_s} \tag{2.41}$$

This is equation is used for setting the boundary conditions. However, a re-defined term that used for describing the humidity level of the flow within nasal cavity is introduced and named

as moisture content level to the alveolar condition. The fully saturated wet air at 37°C can be guaranteed by every healthy subject when the flow reaching alveolar location (except extreme conditions). Then the Moisture Content (MC) level can be calculated by the following formula.

$$MC(\%) = 100 * \frac{\omega}{\omega_{37^{\circ}\mathrm{C}}} \tag{2.42}$$

where ω indicates the mass fraction of H2O at local temperature and $\omega_{37^{\circ}\mathrm{C}}$ represents the fully saturated mass fraction of H2O at 37°C.

Fanning Drag coefficient and Poiseuille number

As described by Muzychka et al. [141], steady laminar flow in a long duct is governed by the balance between pressure gradient and viscous dissipation:

$$\underbrace{\nabla p}_{\text{pressure}} = \underbrace{\mu \nabla^2 \vec{V}}_{\text{friction}} \tag{2.43}$$

A simple scale analysis of the above equation give for the left hand side:

$$\frac{\Delta P}{L} = \mu \frac{V}{L_{char}^2} \tag{2.44}$$

where L_{char} is some appropriate characteristic length scale, e.g. the hydraulic diameter. Applying similar order of magnitude analysis to the wall shear stress we get:

$$\vec{\tau} \sim \mu \frac{V}{L_{char}} \tag{2.45}$$

Introducing the non-dimensional Fanning friction factor, as shown:

$$f = \frac{WSS}{0.5 * \rho \bar{u}^2} = \frac{\tau}{\frac{1}{2}\rho V^2} \tag{2.46}$$

and dropping the numerical factor $\frac{1}{2}$ for simple order of magnitude analysis:

$$f \sim \frac{\tau}{\rho V^2} \sim \frac{\mu}{L_{char}} \times \frac{1}{\rho V^2} \sim \frac{1}{Re_{L_{char}}} \tag{2.47}$$

So that we can expect:

$$f \cdot Re_{L_{char}} \sim 1 \Longrightarrow f \cdot Re_{L_{char}} = C, \text{a constant.} \tag{2.48}$$

For a cylindrical tube, the solution is readily found to be:

$$f = \frac{16}{Re_d} \tag{2.49}$$

For more complex duct shapes (assumed with uniform cross-section), the value of the constant varies. It can be computed analytically for simple shapes since with a constant pressure gradient, the equation 2.43 reduces to a constant right-hand side Poisson equation that can be transformed into Laplace's equation (the analogous relation for heat transfer is considered in previous study [142]). In all cases, a perimeter-averaged wall shear stress can be computed, from which the Fanning friction factor can be deduced.

Defining the Poiseuille number as:

$$Po = f \cdot Re \tag{2.50}$$

according to Muzychka et al. [141] and this varies from 12 to 24 for long duct but with constant cross-section.

However, for developing flows, the wall friction is determined by the momentum balance in the boundary layer, which for steady flow is that between inertia and friction forces, i.e:

$$\underbrace{\rho\vec{V}\cdot\nabla\vec{V}}_{\text{inertia}} = \underbrace{\mu\nabla^2\vec{V}}_{\text{friction}} \tag{2.51}$$

Under this situation, the Poiseuille number is considerably higher due to the developing boundary layer effect. Also as discussed by Muzychka et al [141], boundary layer development is slower in a duct than in an external flow due to the acceleration effect of the growing boundary layer; consideration of this leads to the generally accepted relation:

$$L_h = 0.011 D_h Re_{D_h} \tag{2.52}$$

where L_h is the hydrodynamic entrance length; D_h is the hydraulic diameter. The effect of boundary layer development is to enhance Poiseuille number, with the degree of enhancement dependent on a reduce duct length scale:

$$L^+ = \frac{L/D_h}{Re_{D_h}} \tag{2.53}$$

As an indication, for a rectangular channel, a value of L+ of O(0.01) can double the value of Po (figure 7 [141]).

Film coefficient

In heat transfer, the heat film coefficient is defined as the ratio between the heat flux $\dot{Q}$ and the driving force of the heat (temperature difference):

$$\dot{Q} = hA\Delta T \tag{2.54}$$

where A is surface area where the heat transfer takes place, ΔT is the temperature difference between the fluid temperature and the solid surface temperature and h is the heat transfer film coefficient. Convective heat transfer occurs in the presence of a temperature difference

between a moving fluid and at least part of a surface bounding the flow. In the same way that there is a velocity boundary layer between the (zero) net velocity at the wall and the flow velocity at some distance from the wall, there is a thermal boundary layer in convective heat transfer.

In analogy to the heat transfer, the mass transfer film coefficient can be defined in similar terms:

$$\dot{n} = h_c A \Delta c_A \tag{2.55}$$

where $\dot{n}$ is the mass transfer rate, h_c is the mass transfer film coefficient, A is the surface area where the mass transfer takes place and Δc_A is the mass concentration difference between the fluid and the solid surface.

Dimensionless parameters: Nusselt number and Sherwood number

To be able to quantify the relative importance of convective versus conductive heat transfer across a boundary, the Nusselt number (Nu) then is introduced:

$$Nu = \frac{hL}{k} \tag{2.56}$$

where h is the convective heat transfer coefficient and L is the characteristic length, k is the thermal conductivity of the fluid. A Nusselt number close to one typically indicates a laminar flow, while a larger Nusselt number normally corresponds to turbulent flow with more active convection. The choice of characteristic length L depends on whether this is a developing boundary layer or fully developed flow, the hydraulic diameter is typically used.

The analogous mass transfer Nusselt number is named as Sherwood number (Sh): the ratio of the convective mass transfer to the rate of diffusive mass transport. The corresponding formula

is:

$$Sh = \frac{h_c L}{D} \tag{2.57}$$

where L is characteristic length, D is mass diffusivity and h_c is the convective mass transfer film coefficient.

Chapter 3

Geometry and airflow in congested and decongested nasal cavities.

This chapter presents the results of a study of nasal cavity geometry and inspiratory airflow in the normal state and after application of a topical decongestant. For simplicity, we will refer to the normal state as congested and refer to the post-decongestant application state as decongested. Computational fluid dynamics is applied to determine detailed patterns of airflow in 10 subjects nasal airways in both congested and decongested states.

In the first part of this chapter, the methods of analysis are illustrated as they are applied to a subject specific geometry. In the second part, the analyses illustrated for the subject specific case are presented for the whole cohort, both to illustrate the range of inter and intra subject variability and to test the significance of the changes associated with decongestion. Bilateral (20) and unilateral (40) geometries, including congested and decongested geometries, are shown separately. The significance of the findings and ancillary results are then discussed and presented.

3.1 Subject specific analysis of nasal airflow

For the subject specific geometry (subject D) considered below, we will present the results in the following sequence:

1. the location of the series of interrogation planes used for comparative analysis;
2. the anterior to posterior nasal cavity cross-sectional area distribution;
3. the anterior to posterior variation in Reynolds number;
4. illustrations of the flow field;
5. wall stress maps;
6. effects of flow rate on metrics such as total pressure, resistance and friction factor.

3.1.1 Definition of planes

From anterior to posterior, the nasal cavity is separated into a series of sections separated by cross-sectional planes at the nostril (Nos), nasal valve (NV), vestibule, anterior septum (AS) and posterior septum (PS). The particular cross-sectional planes defined for this study applied to the given subject (D) as shown below, figure 3.1, where the figure also indicates the anatomical features used as key landmarks. The region between the anterior septum and posterior septum is divided into four equal sub-regions by planes labelled: 1V, 2V and 3V. As shown by figure 3.1, there is another set cross-sectional planes are generated and ideally it is perpendicular to the geometrical centerline of the cavity, which is indicated by the red dashed line in the figure. Although the dimension of each nasal cavity is not the same, the anatomical features of nasal cavity are fairly consistent. To standardize the analysis for all the nasal cavities, the intranasal centerline distance is normalized between 0 and 1, as labelled in the figure.

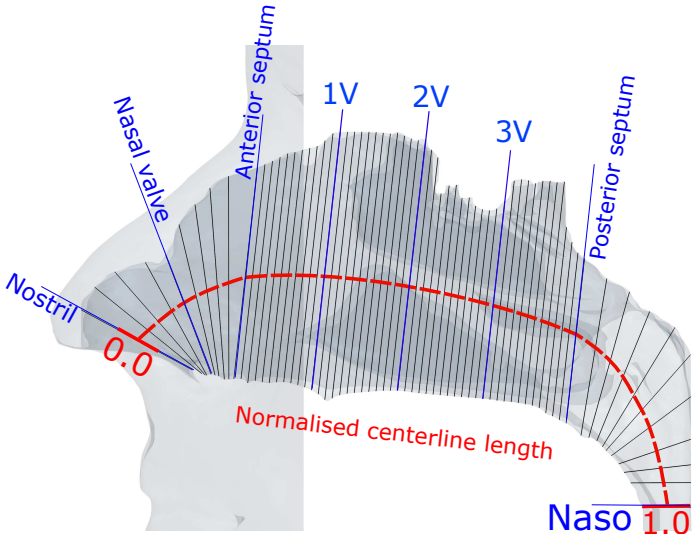


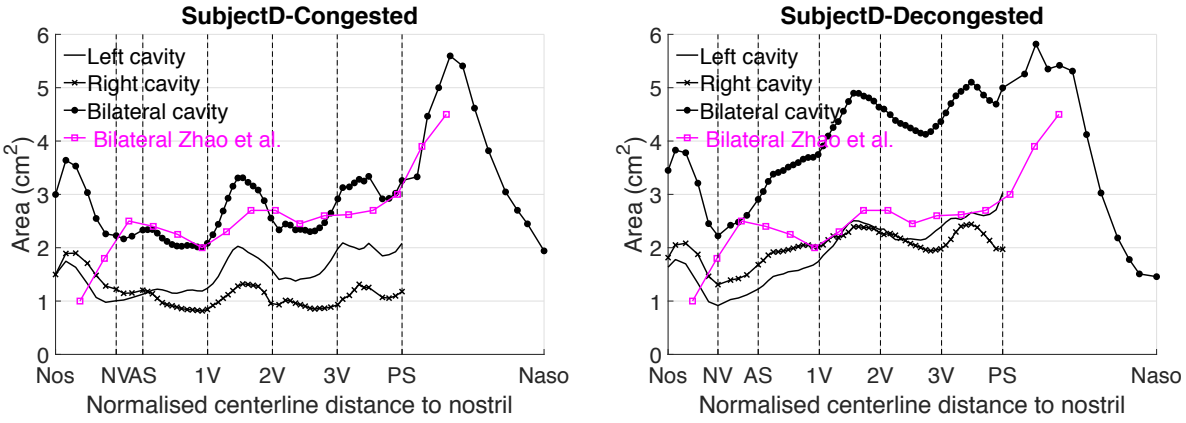
Figure 3.1: Subject D congested cavity geometric view that rendered by STAR-CCM+. Blue lines are planes that defined according to anatomical landmarks and the red dashed line is an indication of nasal cavity centerline within normalized value between 0 and 1. The grey lines are the projection view of cross-sectional slices along the cavity centerline.

3.1.2 Cross-sectional area variation

For this subject, the corresponding cross-sectional area (CSA) distributions are plotted in figure 3.2 for both congested and decongested nose; note that the separation of left and right CSA only extends to the posterior septum. Figure 3.2a is the cross-sectional area distribution under congestion, while figure 3.2b shows the same but in the decongested condition. It appears that whereas the nasal cavity area from nostril to nasal valve is barely altered, the gross effect of decongestion occurs from the anterior septum through the turbinate region, increasing the whole cavity cross-sectional area by more than 50%.

Furthermore the results indicate that decongestion does not simply equalize areas on each side of the nose: a finding emphasized by the results from the whole cohort as shown later. For this subject the increase in cavity CSA (and correspondingly volume) is significantly greater on the right than on the left side; moreover the degree of cross-sectional area dominance of the left cavity over the right cavity is completely altered by decongestion.

In the case of this subject, the point of minimum CSA (CSA_{min}) in the right cavity does not occur at the nasal valve in the congested state, but is located posteriorly at location 1V; by contrast decongestion clearly establishes the nasal valve as the CSA_{min} location for both sides. The magenta line in figure 3.2 shows the cross-sectional area measurements from Zhao et al [2] over 22 healthy subjects during resting breathing. It can be seen that the measurements for this subject are comparable with Zhao et al's results, although the way of defining cross-sectional planes are considerably different in the anterior nose, where Zhao et al. use purely vertical (coronal) planes rather than angled normal to the flow direction (refer to figure 2 of Zhao et al. [2]). Comparison of our complete data set with the results of Zhao et al. are shown later.



(a) (b)

Figure 3.2: The horizontal axis represents the normalised centerline distance and labelling with the anatomical markers that defined previously. Those abbreviations are: Nos = nostril plane, NV = nasal valve plane, AS = anterior septum plane. 1V = first vertical plane, 2V = second vertical plane, 3V = third vertical plane and PS = posterior septum plane. The magenta line in the figure shows the results from Zhao et al [2]. For both congested (left figure) and decongested (right figure) cavities, the unilateral and bilateral cavity cross-sectional area distribution are plotted and compared with Zhao et al. results.

3.1.3 Reynolds number variation

Using the definition of hydraulic diameter, equation 2.32, and taking mean velocity as the flow rate divided by CSA, the variation in Re for congested and decongested cases is shown in figure 3.3. Note the large difference in Reynolds number regimes between the anterior cavity, up to the head of the middle turbinate at location 1V approximately (Re values of order 1000

at the nasal valve), and the fully turbinated region from 1V to the posterior septum (Re of order 500). For a simple pipe of diameter d, Reynolds number expressed in terms of flowrate reads as:

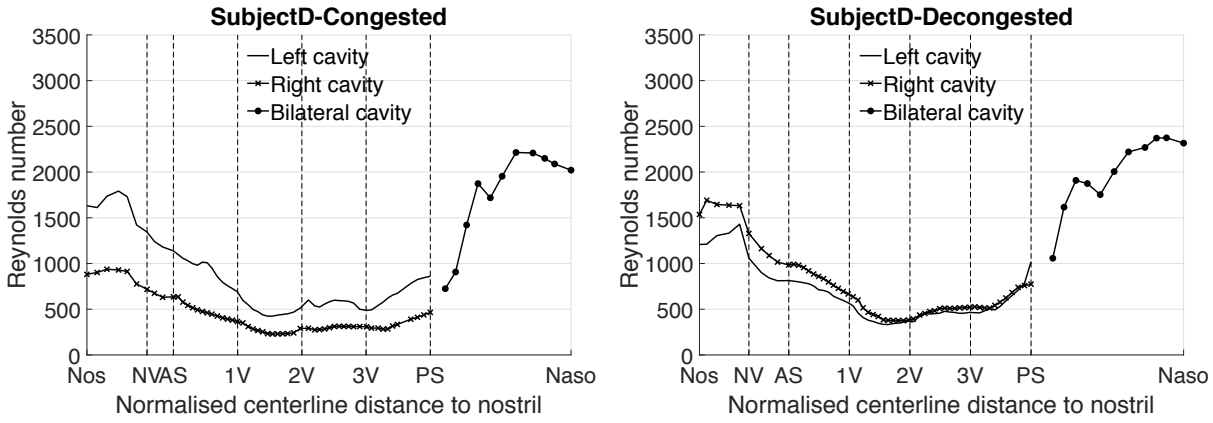
$$Re = \frac{\rho Q}{d\mu} \tag{3.1}$$

and so for a given flowrate, an increase in cross-sectional area would consequently reduce the Reynolds number. However for nasal airways, where mean velocity is defined as $\frac{Q}{CSA}$ and the hydraulic diameter is used in place of diameter, Reynolds number is computed as:

$$Re = \frac{4\rho Q}{\mu P} \tag{3.2}$$

Thus, although the CSA is significantly increased by decongestion, the perimeter change in the main cavity, approximately the sum of the product of cavity height and passage width is much less altered, and the effect of decongestion on Reynolds number is slight.

In the case of this subject, the major effect due to decongestion of the right cavity is that it also lowers resistance there, significantly increasing the flow on that side. In fact in the turbinated region between plane 1V and PS, the figure 3.3b shows an increase in Reynolds number in this region for the right cavity, suggesting that the increase in flow on this side more than compensates for the increased D_h; there is a slight decrease in Reynolds number on the left.

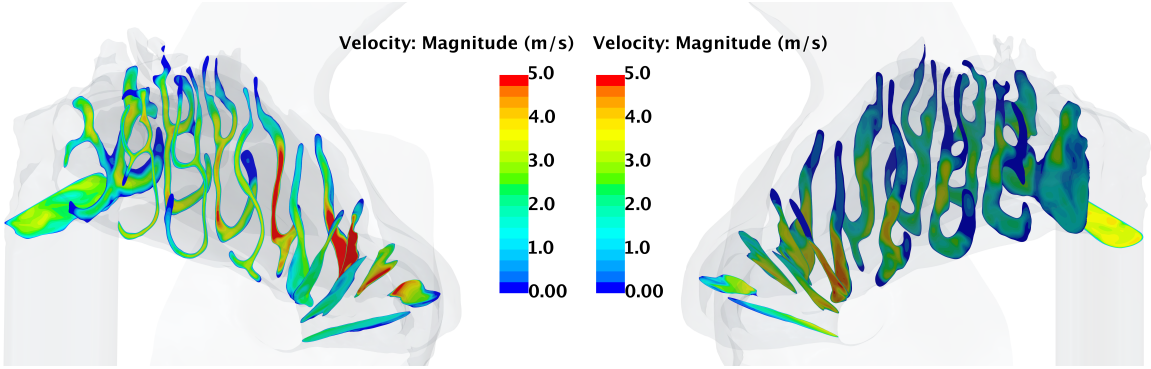


(a) (b)

Figure 3.3: Decongestion effect on Reynolds number variations of subject D at flowrate of 30 L.min^{-1}.

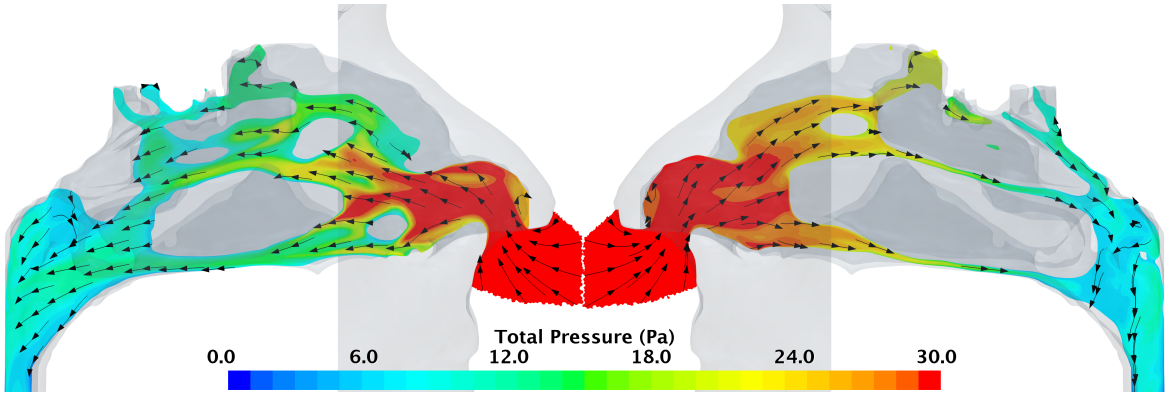
3.1.4 Flow field variation

The velocity field before and after decongestion is compared in figure 3.4, in which the congested cavity is shown on the left and the decongested cavity is shown on the right. Prior to decongestion, the left cavity has considerably higher flow speeds than the right side cavity; in fact the mass flow left-right split in the congested case is 66%-34%. After decongestion, the left-right flow split is 47%-53% so that the flow speed in the right cavity then exceeds that of the left cavity. Overall from the figure, it is clear that the volume expansion in the cavity posterior to the nasal valve caused by decongestion leads to the reduction of velocity magnitude under the same flowrate. Moreover, the figure also shows that the volume expansion after the nasal valve induced by decongestion (figure 3.2) not only lowers flow speed but reduces flow in the superior cavity, leading to recirculation regions in the anterior cavity in both sides (figure3.4 and figure 3.5).

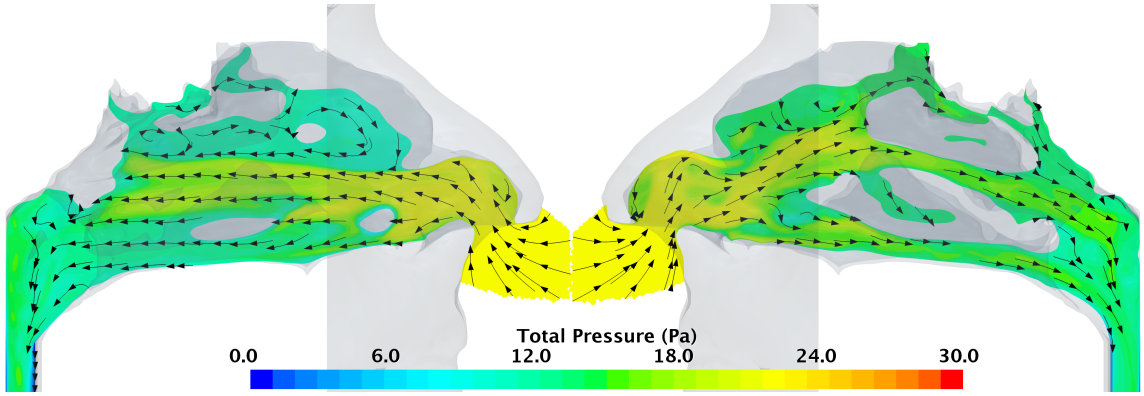


(a) (b)

Figure 3.4: Subject D cavity cross-sectional planes view of velocity field at flowrate of 30 L.min^{-1}. Figure 3.4a is congested cavity and figure 3.4b is the decongested cavity.



(a)



(b)

Figure 3.5: Subject D sagittal plane view of total pressure distribution at flowrate of 30 L.min^{-1} for both congested and decongested cavities. Figures on the left are representing the left cavity while the right side means the right cavity. Same sagittal plane is taken on each side of the cavity before and after decongestion.

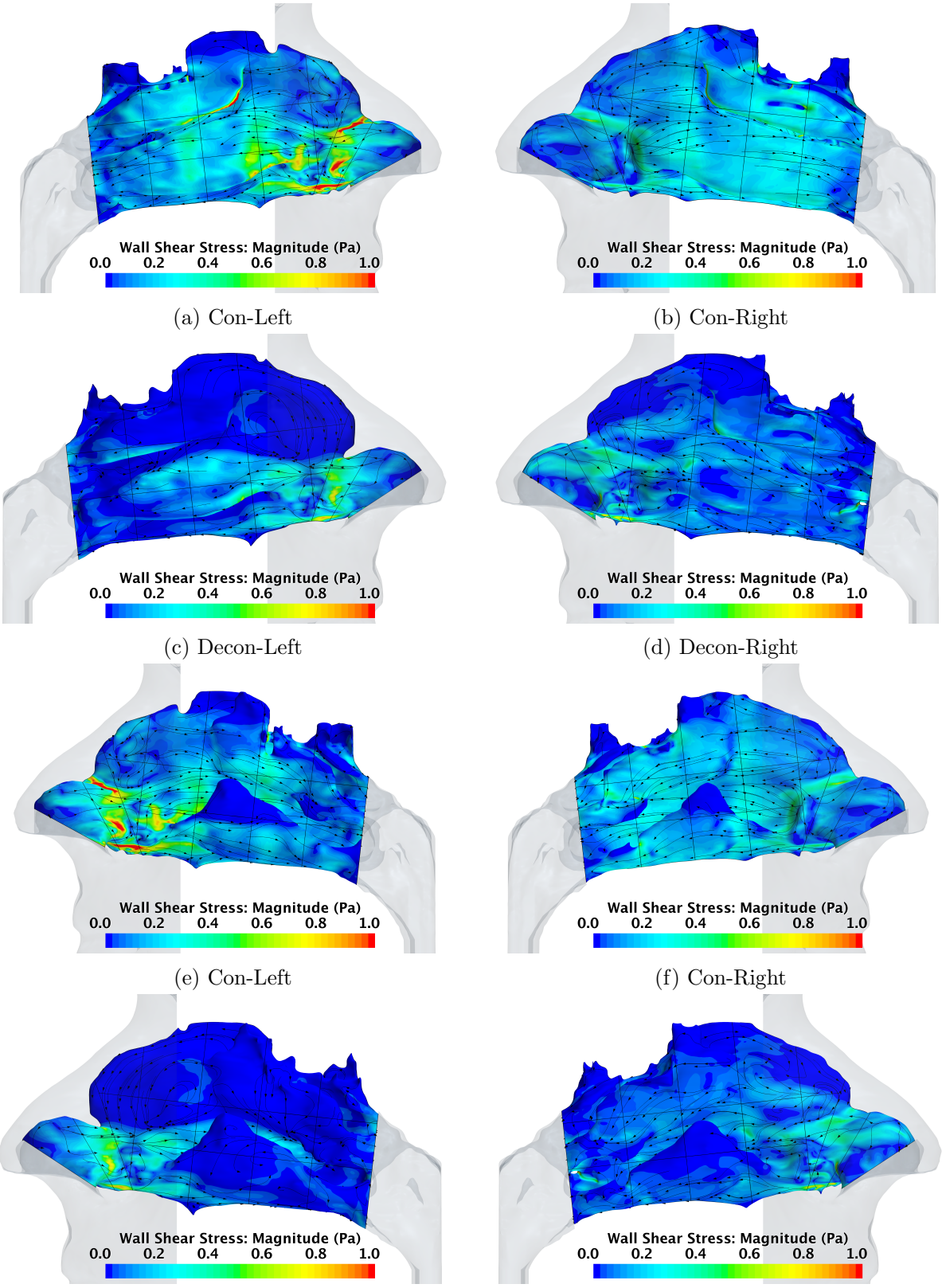
The total pressure distribution on the same sagittal planes as described for the velocity field

are shown in figure 3.5, with superimposed arrows indicating the flow direction. Cavities under both congested and decongested conditions both indicate a rapid loss of total pressure across the nasal valve. In the congested case, the magnitude of total pressure loss is clearly far greater, owing to the reduced CSA in the cavity. For decongested case, areas of recirculation area evident in the anterior cavity, owing to the increased area into which the inspired air discharges.

3.1.5 Wall shear stress distributions

The wall shear stress (WSS) distributions on the cavity surface are compared in the following sequence of images: (1) figure 3.6 (a-d), views of the turbinates as they would be exposed by removing the septum, with left vs right cavities compared reading across the page, and with upper pair corresponding to the congested nose and the lower pair to the decongested nose; (2) figure 3.6 (e-h), views of the outer cavity wall in the same order as for (a-d); (3) figure 3.7 (a-d), the final pair showing the views of the septal surface, again in the same order, is discussed later.

Considering the first set of views which show the inferior and middle turbinates, high shear stress values occur both at the nasal valve and at the head of the turbinates where the nasal valve flow jet impinges (figure 3.6a and figure 3.6b). WSS values are noticeably larger in the congested left cavity than for the right cavity, due to asymmetric mass flow split. For the decongested nose, the results show the WSS is relatively lower over both sides of the cavity (figure 3.6c and figure 3.6d), as expected. However, it is also evident from the surface streamlines that there are extensive recirculation zones in the decongested cavities, compared to the more unidirectional flow for the congested cavity.



(a) Con-Left (b) Con-Right

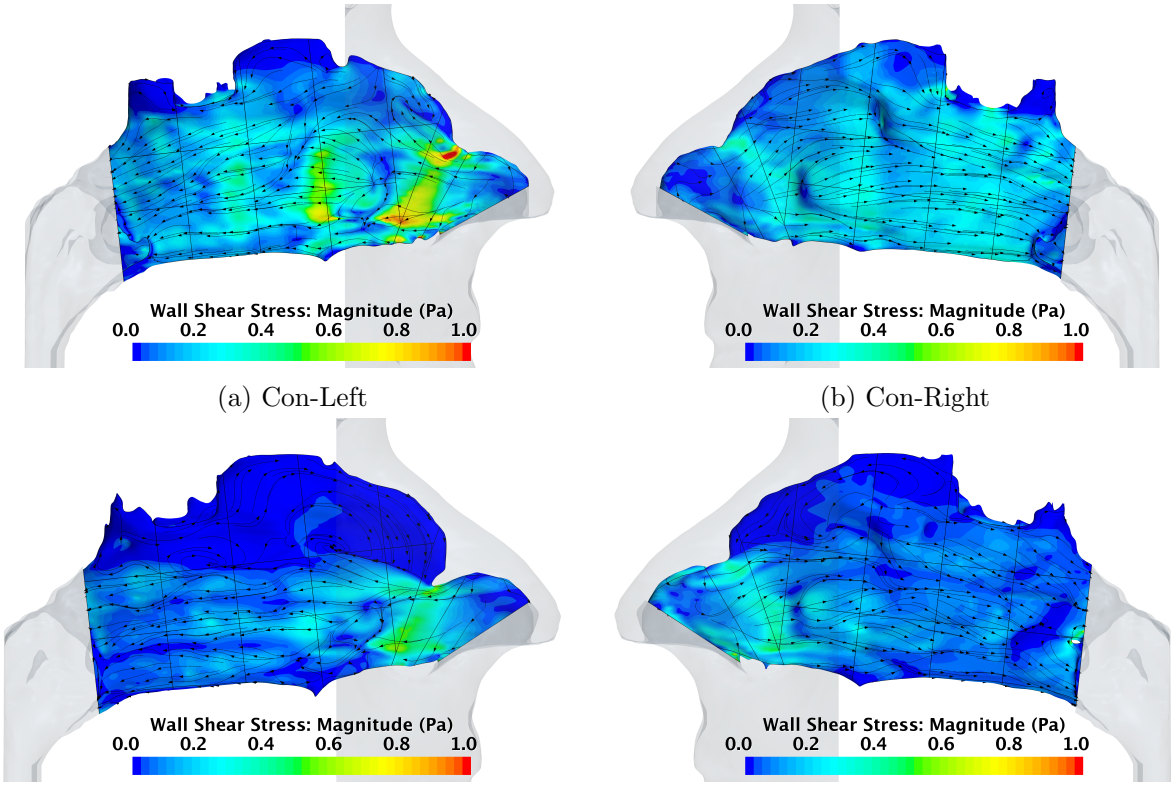
(c) Decon-Left (d) Decon-Right

(e) Con-Left (f) Con-Right

(g) Decon-Left (h) Decon-Right

Figure 3.6: Subject-D congested VS decongested WSS distribution on turbinates. Figure 3.6a-3.6d are the turbinates views that with the removal of septum, while figure 3.6e-3.6h are the turbinates that viewed from outside of the turbinates.

Figure 3.6e to figure 3.6h shows the same pattern as before, but now viewing left and right nasal cavity surfaces from the same side as the maxillary sinus(which is removed and the ostium closed). Finally, the WSS distributions on the cavity septum, figure 3.7, again shows that the highest values all tend to locate at the nasal valve region of both sides before and after decongestion. Comparing all three views of WSS in congested and decongested cavities, and particularly this last septal surface view, one can also see a marked change in the inferior to superior cavity flow distribution as a consequence of decongestion.



(a) Con-Left (b) Con-Right

(c) Decon-Left (d) Decon-Right

Figure 3.7: Subject D congested VS decongested WSS distribution on septum. Figure 3.7a and 3.7b are the congested left and right cavity separately, while the lower pair are the decongested cavities.

3.1.6 Effect of flowrate

Pressure loss and resistance

The effects of changes in flowrate were studied for both congested and decongested cavity for subject D. The increase of flow rate has a minor but consistent effect on the flow split between left and right side cavities, table 3.1. From the results, the left nose airflow dominates that on the right, taking approximately 70% of inhaled air to the 30% on the right. However, the decongestion changes the dominance which makes the left nose airflow takes only 47% while 53% on the right.

Flowrate	Con-L(%)	Con-R(%)	Decon-L(%)	Decon-R(%)
15 L.min^{-1}	69	31	47	53
20 L.min^{-1}	68	32	47	53
25 L.min^{-1}	67	33	47	53
30 L.min^{-1}	66	34	47	53

Table 3.1: Mass flow split ratio with various flow rate.

Nasal airway resistance (NAR) is generally defined as the static pressure loss experienced by air flowing from nostril to nasopharynx per unit of volumetric flowrate, and is typically expressed in terms of Pa.(L.min^{-1})$^{-1}$. However static pressure depends on the local flow speed through the Bernoulli relation, so that changes in static pressure consequently do not reflect the energy dissipated in overcoming frictional resistance. Total pressure loss rather that static pressure loss is a better reflection of the total energy lost and NAR is defined here in terms of the total pressure loss.

As shown in the figure 3.8, the total pressure loss increases from approximately 7 Pa at 15 L.min^{-1} to 20 Pa at 30 L.min^{-1} (figure 3.8a), i.e. doubling the flowrate increases pressure loss

much faster than proportionately. Resistance (figure 3.8c), which would remain unchanged if pressure loss were linearly proportional to flowrate has increased, though only by approximately a third. Comparing each of the unilateral cavities separately figure 3.9a and figure 3.9e, the far greater flowrate in the left cavity alters the form of the pressure loss: the graph corresponding to the left cavity shows a pronounced loss associated with the dissipation of the jet issuing from the nasal valve. This feature is absent on the right, where the lower flow leads to a more gradual patterns of loss.

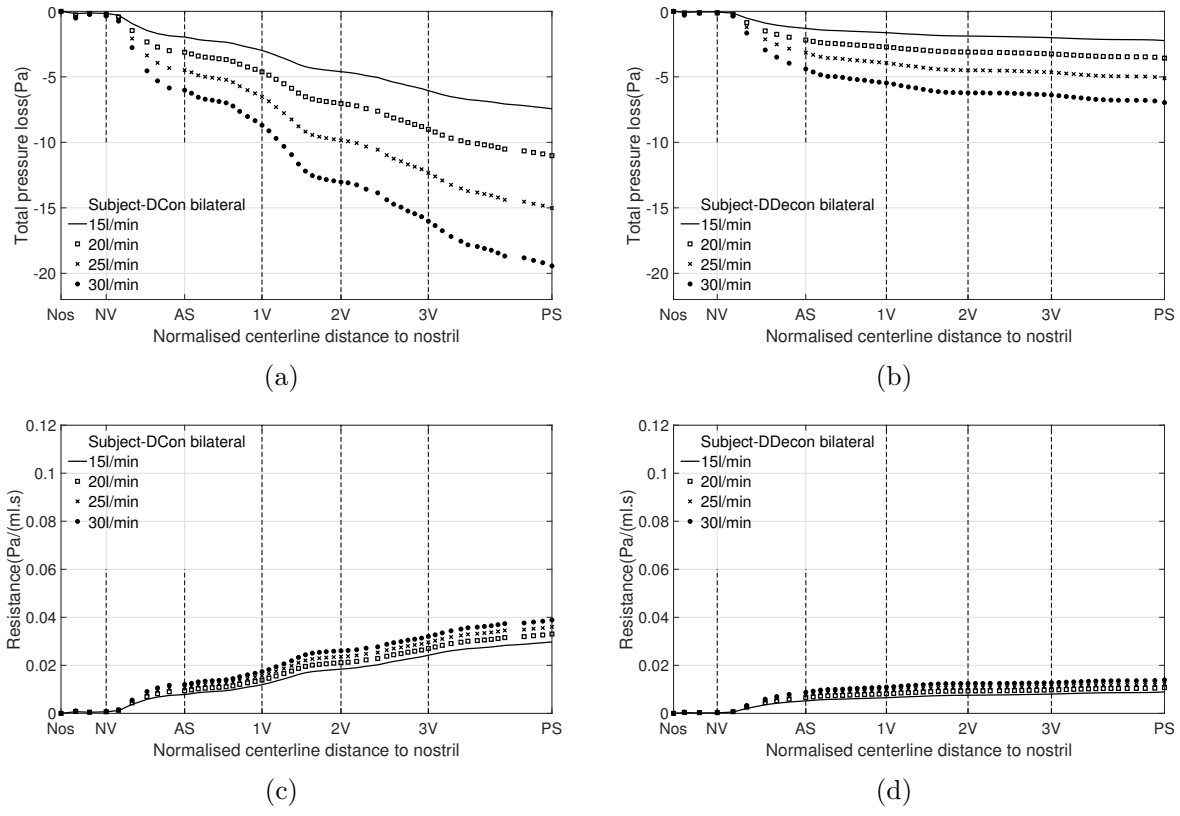


Figure 3.8: Bilateral cavity pressure and resistance distribution comparison before and after decongestion with multiple flowrates. Figure a shows the total pressure loss across the cavity from nostril plane until the posterior septum. Similarly, figure b shows the same results but after decongestion. Correspondingly, resistance is plotted for congested and decongested cavities as shown in figure c and d separately.

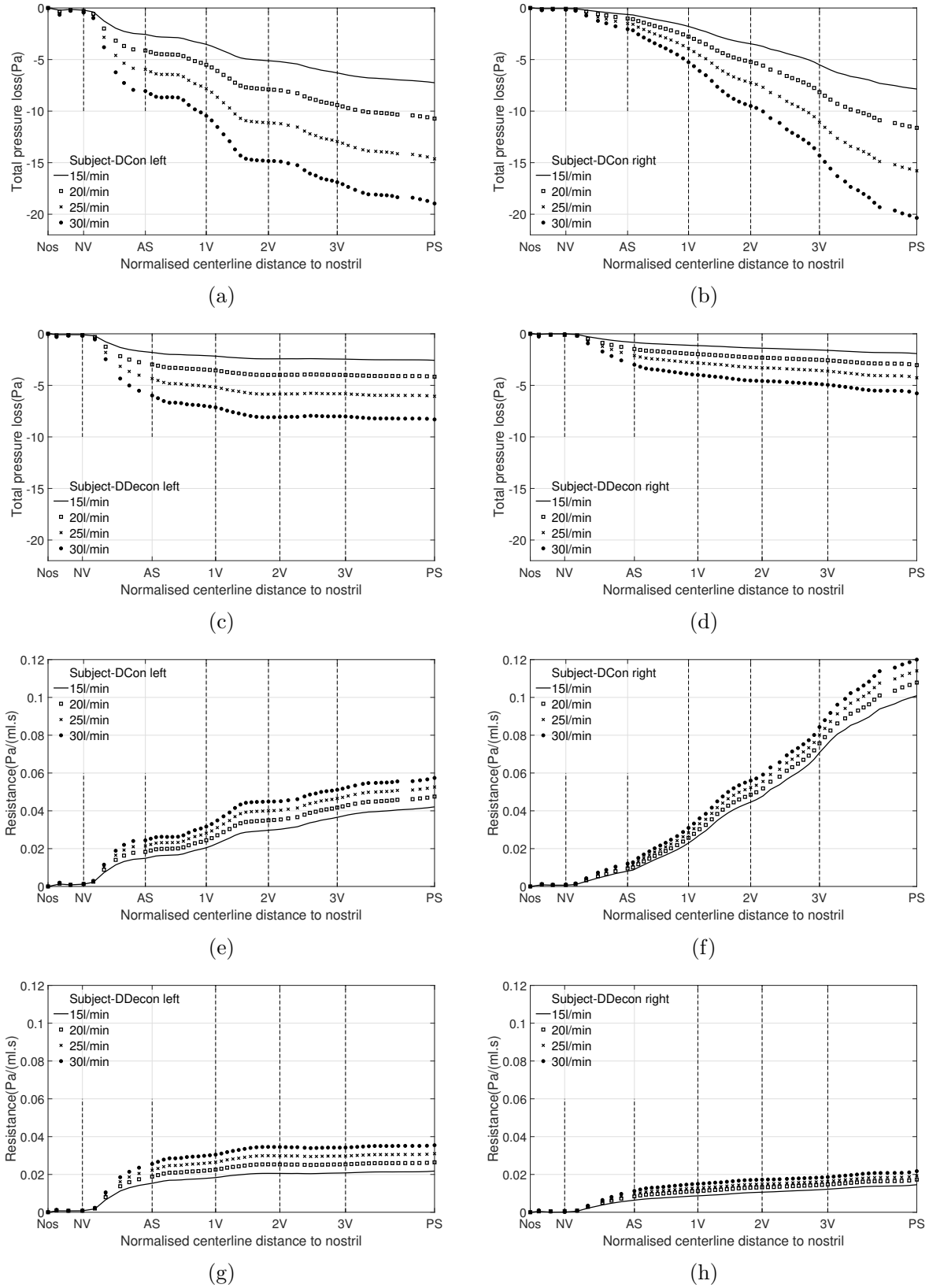


Figure 3.9: Left and right cavity pressure and resistance distribution. Figure a-d show the distribution for total pressure loss on each single side of the cavity with flow rate raising from 15 to 30 L.min^{-1}. Resistance distribution is displayed by figure e-f in the same way as total pressure loss.

Comparing both figure 3.8 and figure 3.9 decongestion for this case reduces the overall total pressure loss by about two-thirds compared with that of the congested results. Similar ratio also can be found from the comparison of resistance distribution. Figure 3.9 show the actual total pressure loss, as well as resistance, are reduced extensively due to the expansion of the cavity on both sides. Effects are more pronounced for the right cavity, which has a much higher mass flow ratio than in the congested state. The effect of decongestion on the left cavity resistance is also evident though not as significant as for the right cavity.

For comparison, figure 3.10 shows the static pressure distributions for subject D before and after congestion applied, illustrating how the Bernoulli effect locally masks the drop in total pressure.

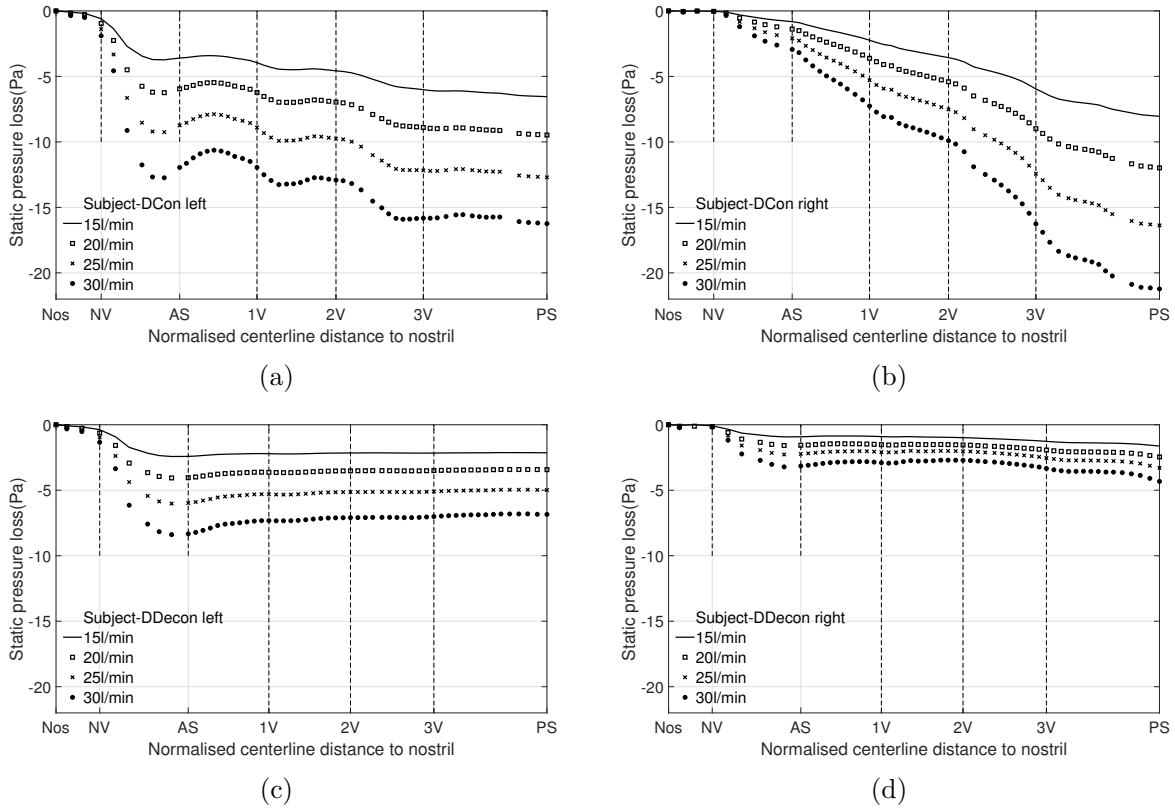


Figure 3.10: Static pressure distribution across the cavity with multiple flowrate on each single side of the cavity. Figure a-b are the results under congested states and c-d are the results after decongestion.

From the plot 3.10a we can see that flow in the congested left cavity is more complex compared

with the right cavity, there are two times that pressure recovery occurred for all different 4 flowrates. The first time is located within plane AS and 1V, while the second time is within plane 1V and 2V. Between plane AS and 1V is where the beginning of the head of middle turbinate, this direct impingement of flow into the turbinate head will lead to the increase of the local static pressure. However, in the same location of right cavity, the static pressure plot does not show the similar trend which is because the highly asymmetric mass flow split ratio between left and right cavity. Comparing figure 3.10a and3.10c it shows that due to the vast expansion of left cavity after plane NV after decongestion (figure 3.2a), the flow in the decongested left cavity of subject D shows much simpler profile than that of the congested state. In addition, due to the expansion of right cavity as well after nasal valve, the static pressure loss in the decongested right cavity is much smaller than that under congested condition, although the decongestion right cavity has higher mass split ratio compared with the congested condition.

Frictional loss and Poiseuille number

The Fanning drag coefficient (f) is defined as the ratio between WSS and the dynamic pressure, equation 2.46. Figure 3.11 illustrates the bilateral f factor and the Poiseuille number variations along the centerline from nostril to posterior septum, with the left pair in figure 3.11 for the subject D in the congested condition and the right pair are the results for decongested cavity. For the Fanning drag coefficient, decongestion lowers the coefficient slightly and reduces the anterior to posterior variations; increasing the flowrate significantly lowers the frictional factor. On the other hand, the Poiseuille number plots show very similar distributions for congested and decongested cavities. Looking at the values of $f \cdot Re$ for both bilateral and unilateral cavities (figure 3.13), values for the Poiseuille number are generally between approximately 18 to 30 for the posterior cavity. Large variations in Poiseuille number corresponding to changes in flowrate are confined to the anterior portion of the nose. This suggests the posterior, turbinated region of the nose corresponds more closely to an established duct flow (for which the Poiseuille number would be independent of flowrate), whilst the anterior part shows a very different friction coefficient behaviour, due to rapid flow development and possibly due to the presentence of jet flow through the nasal valve.

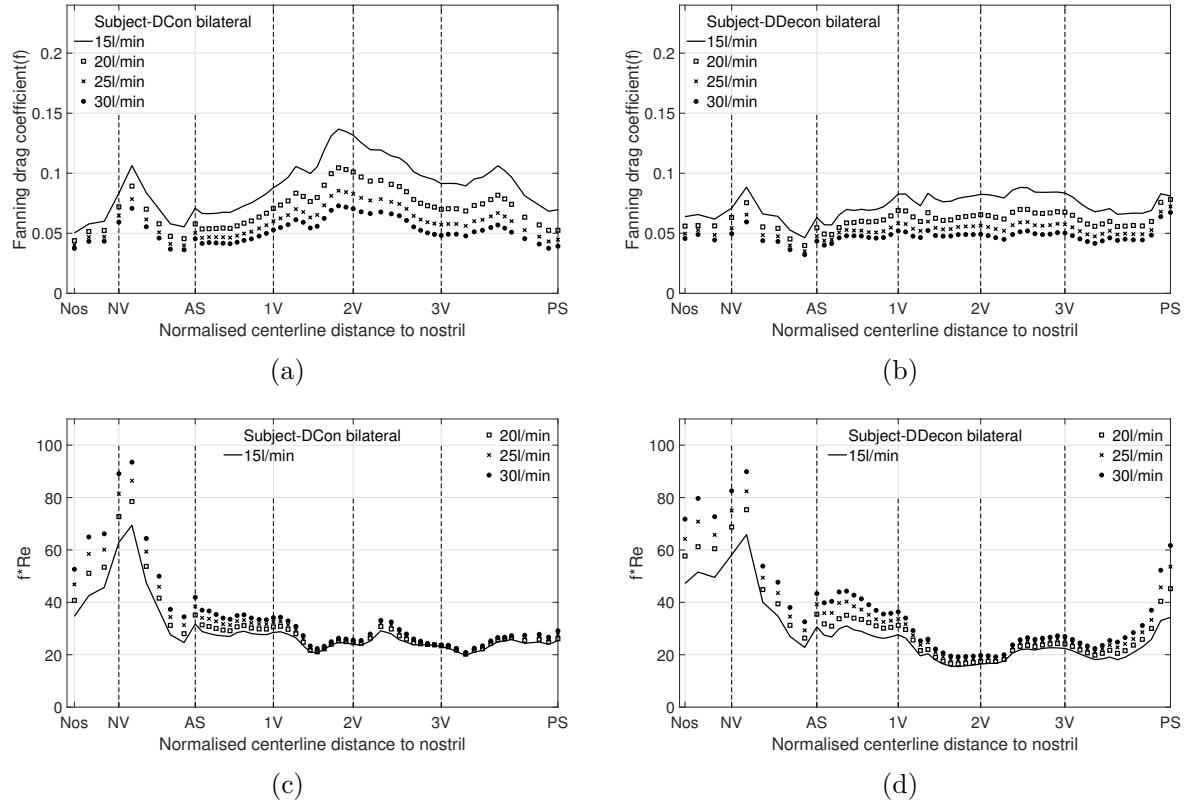


Figure 3.11: Decongestion effect on bilateral cavity Fanning drag coefficient and Poiseuille number with multiple flowrate studied. The left pair show the results for congested cavities, while the right pair are for decongested cavities.

It has shown that the decongestion cavity tends to have both smaller value and fewer variations of the Fanning drag coefficient for all the four flowrates being studied here. However, the Poiseuille number distribution for decongested cavities shows slightly pronounced variation across the cavity, although the values are fairly consistent with that of the congested cavities. This might due to the more complex velocity profiles of decongested cavities that due to the wider cross-sectional area caused by decongestion expansion.

If we analyze each half nose individually, the corresponding plots are shown in figure 3.12 and 3.13. It can be seen that, for congested cavity, both the Fanning drag coefficient and Poiseuille number of right cavity show more fluctuations than the left cavity that due to the larger variations of the cross-sectional area distribution (figure 3.2). Although the cross-sectional area of both sides of the cavity are not constant from anterior to posterior and also the velocity

profiles are unknown, this analogy to duct flow by analyzing the Fanning drag coefficient and Poiseuille number shows that the behaviour of the posterior part of the nasal cavity are fairly similar as the duct flow, contrary to the anterior part of the nasal cavity. Furthermore, the decongestion cavity has more regularised distribution of both Fanning drag coefficient and Poiseuille number, especially for under lower flowrate (15 L.min^{-1}).

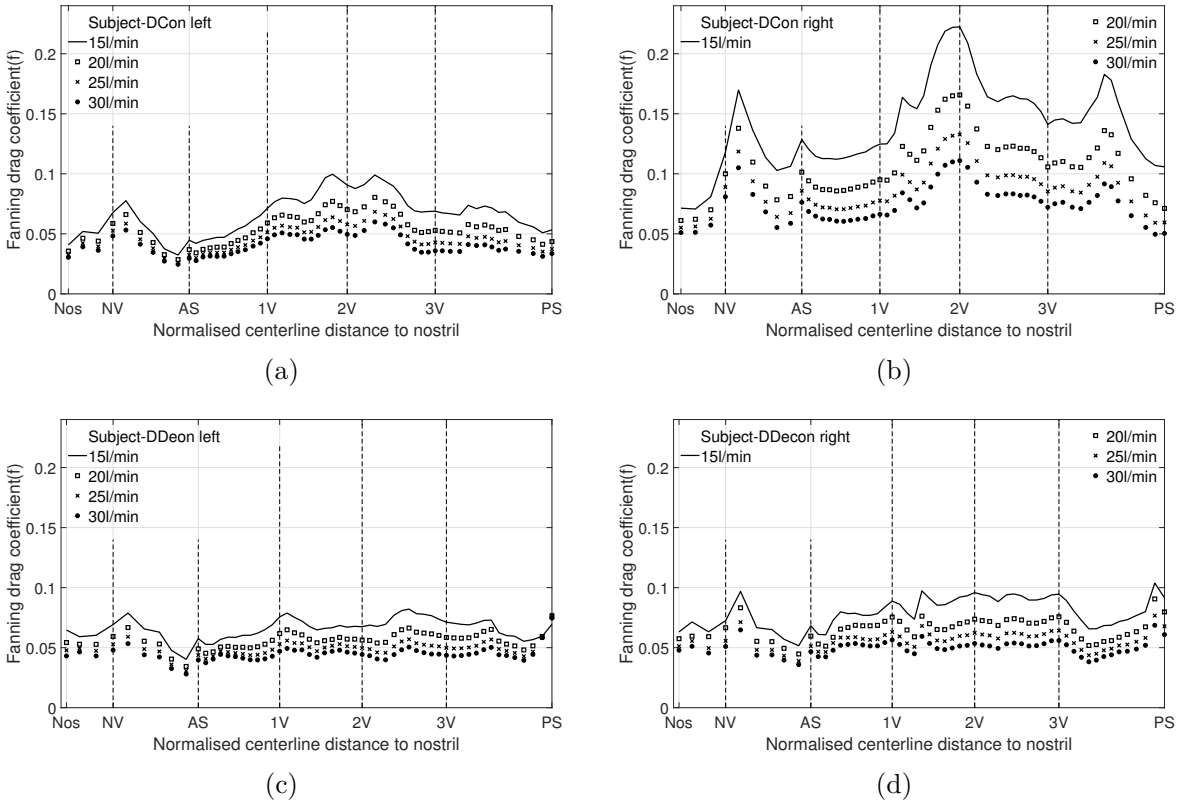


Figure 3.12: All the plots show the Fanning drag coefficient distribution along the cavity centerline of subject D. For each single plot, it shows the comparison with multiple flowrates. Figure 3.12a and 3.12c are the results for congested cavity and figure 3.12b and 3.12d are for decongested cavity.

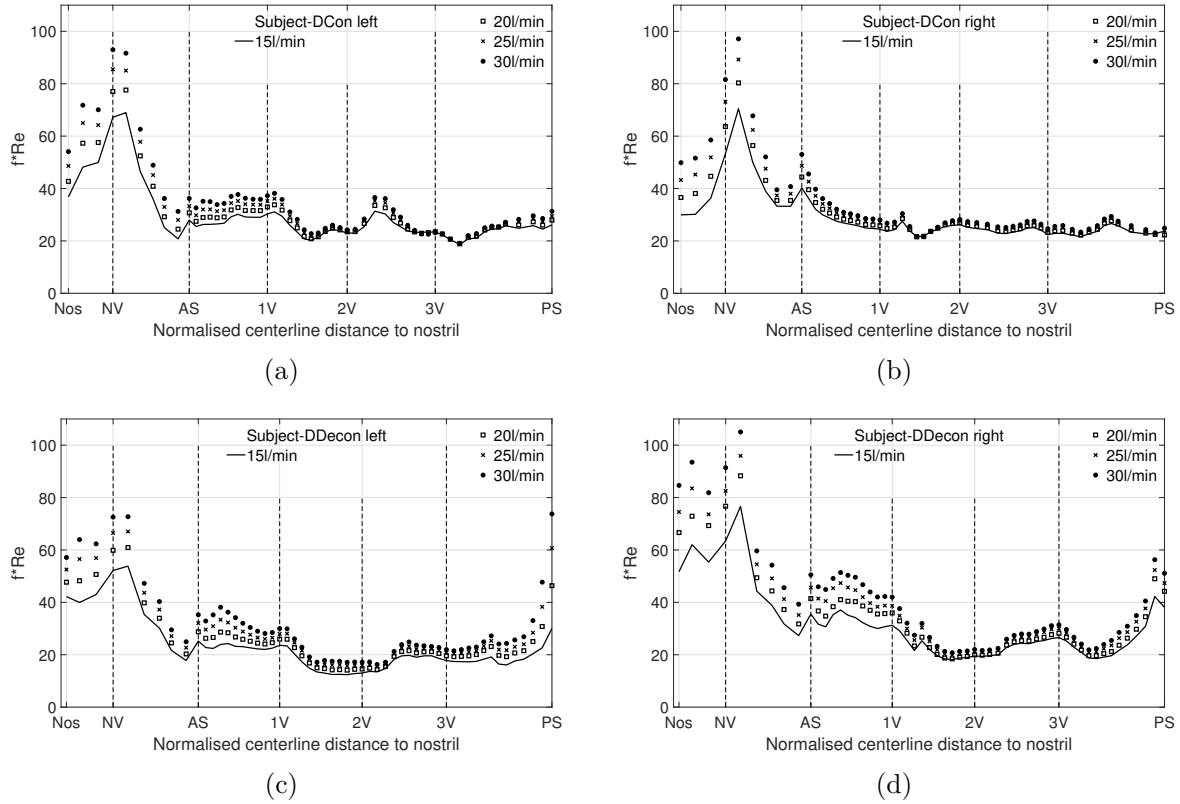


Figure 3.13: All the plots show the Poiseuille number distribution along the cavity centerline of subject D. For each single plot, it shows the comparison with multiple flowrates. Figure 3.13a and 3.13c are the results for congested cavity and figure 3.13b and 3.13d are for decongested cavity.

3.2 Bilateral nasal cavity geometric and flow analysis

3.2.1 Geometry comparison

The study cohort size is 10, with two sets of data for each subject corresponding to their normal state (labelled as congestion), and that after application of a decongestant, labelled decongestion. The effect of decongestion on nasal cavity surface area, volume and surface area volume ratio (SAVR) are tested for significance using the Wilcoxon signed-rank test [143]. This is a non-parametric test, meaning it does not assume a form for the data distribution. The null hypothesis for paired data set is that the differences have a distribution centered about zero. With only 10 subjects, testing for normality would be somewhat questionable. Whilst paired

t-testing could be applied more confidently to the unilateral data (assuming 20 independent half nasal cavities), for the most part we rely on the Wilcoxon signed-rank test to compare metrics for the two states.

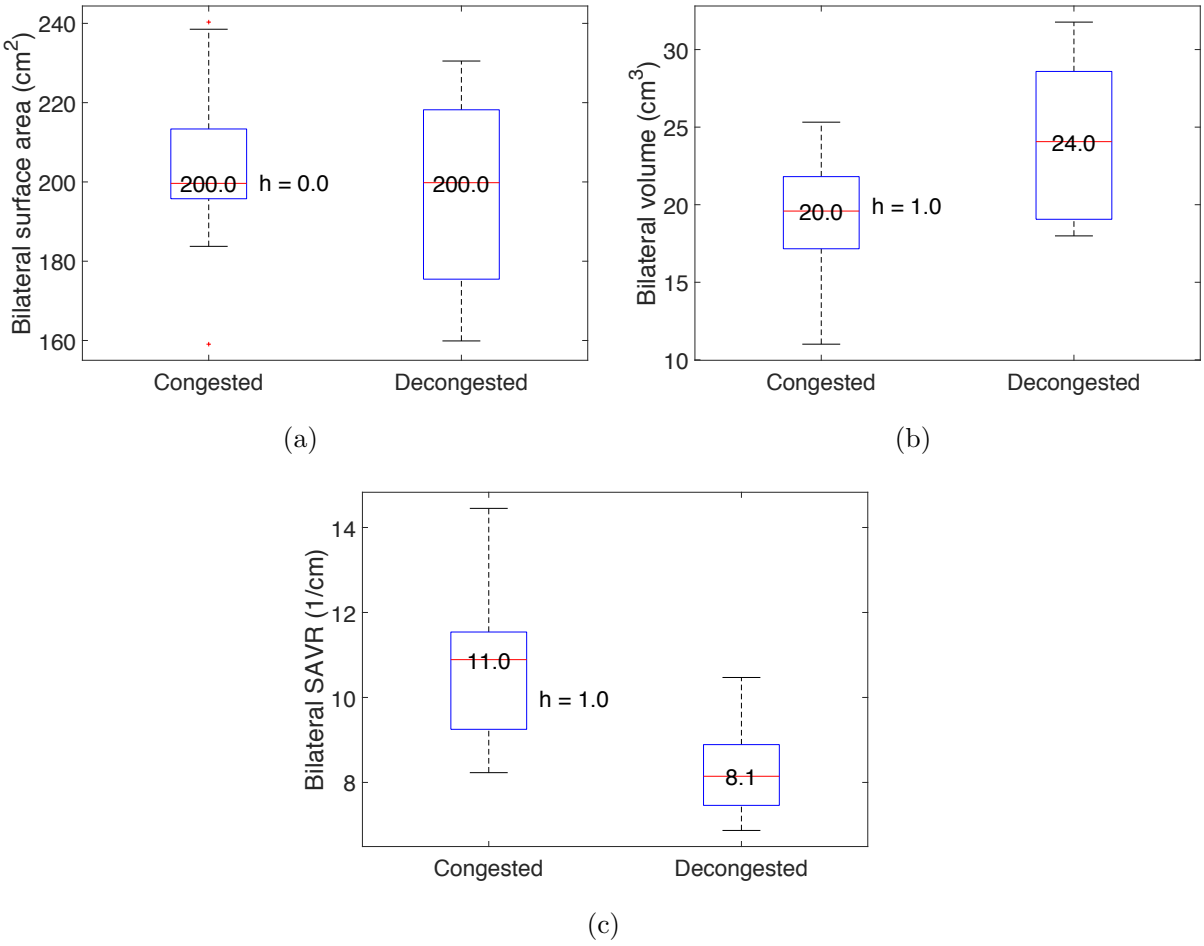


Figure 3.14: This figure shows the decongestion effect on geometric changes by showing the results of Wilcoxon signed-rank test. Reading from a to c, plots show comparisons for: bilateral area, bilateral volume and bilateral SAVR separately.

Concerning SAVR, this is defined as the cavity surface area over the cavity volume. It is a useful metric to assess the effect of decongestion on the cavity geometry, particularly in relation to the ability of the cavity wall surface to transfer heat and moisture to the cavity interior volume. The flux of heat and water through the wall is limited by the temperature and concentration gradients at the surface, so that reduction of SAVR will tend to reduce transport, and vice versa for increases in SAVR. Figure 3.14 displays box plot of surface area, cavity volume and SAVR

before and after decongestion. The median is shown by horizontal red line in the figure and the top, lower edges of the box indicate the one and three quartile limits respectively. In addition, the results of Wilcoxon signed-rank test are also attached in the figure by showing the value of 'h' only. The logical value of 'h = 1' indicates that the test rejects the null hypothesis that there is no statistic difference of its median value at the 5 % significance level. For simple and easy to read, the specific value 'p' will not be shown on each of the boxplot, instead I will labelled with 'h = 1' for significant cases and 'h = 0' for insignificant cases. Thus figure 3.14a shows that the surface area change is not significant (h=0) after decongestion. However, the cavity volume and SAVR comparison from figure 3.14b and figure 3.14c indicate the significant difference (h = 1) with p value of 0.0039 and 0.0020 individually. The raw data of the corresponding geometric measures can be found from table B.1 of appendix B.1.

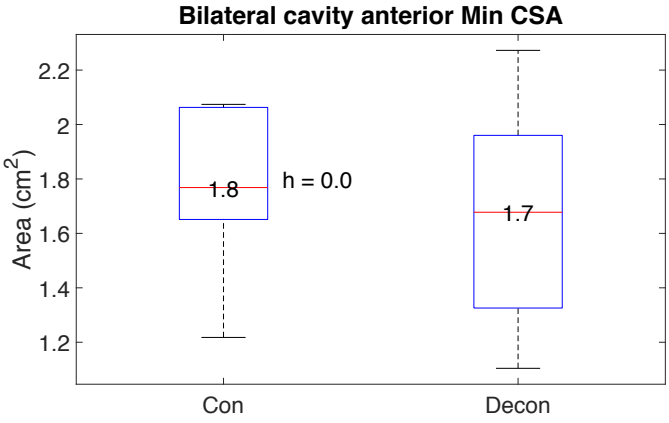


Figure 3.15: Anterior cavity minimum cross-sectional area comparisons for congested and decongested cavities, with h value shown for application of the Wilcoxon signed-rank test; h = 0 means the null hypothesis has been accepted.

Apart from being commonly treated as the first valve between atmosphere and lungs, the nasal valve contains multiple components: septal cartilage (which is rigid), inferior portion of the superior lateral cartilage (which has some mobility), the erectile tissue of the nasal septum and inferior nasal concha head [144]. The change of nasal valve might cause significant effect on the manner of directing inhaled air. Figure 3.15 shows the minimum anterior cross-sectional area before and after decongestion distribution by box plot and the median after decongestion is reduced from 1.8 cm^2 to 1.7 cm^2. The corresponding Wilcoxon signed-rank test shows there

is no significant difference with a value of h = 0.

Internally, the human nasal cavity normally contains three turbinates. From inferior to superior, the turbinates direct the inhaled air flow across the largest possible surface area of the mucosa. Based on the anatomical landmarks proposed by ENT surgeon Dr. Cetto, the nasal cavity between the anterior septum and posterior septum can be divided into three sections: top, middle and lower cavity. These sections are defined intentionally to capture each turbinate separately. The SAVR variations of top, middle and lower sections of the nasal cavity cohort under both congested and decongested conditions are demonstrated by figure 3.16. Although the median of top cavity SAVR shows some difference (from 13 to 11) after decongestion, the difference is not statistically significant within the level of 5 %. However, the SAVR of middle and lower sections does show significant difference before and after decongestion, with p values of p = 0.004 for the middle and p = 0.002 for the lower cavity. Note that, figure 3.16 shows that top section of the cavity has the larger SAVR median than the other two sections, no matter whether during congested or decongested conditions.

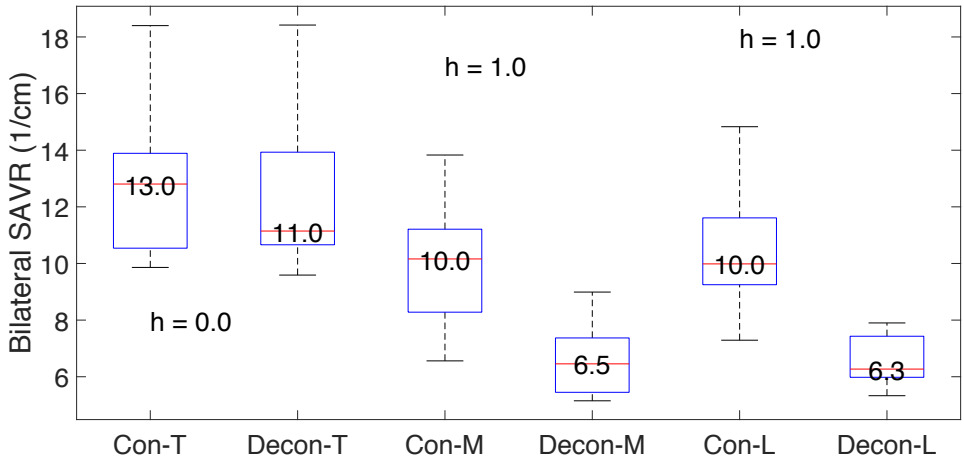


Figure 3.16: Bilateral significance test of top, middle and lower cavity SAVR before and after decongestion.

As have been defined previously, figure 3.1, the normalized distance of each characteristic plane to nostril plane are listed in table 3.2. Although each nasal cavity has a different length,

their normalized anatomical features location are similar and as shown in the table. 'Nos', 'NV','AS','1V','2V','3V','PS' and 'Naso' represent cross-sectional planes at nostril, nasal valve, anterior septum, 1V, 2V, 3V, posterior septum and nasopharynx separately. It shows the maximum standard deviation (SD) of these planes is less than 5% (plane PS).

Plane	Nos	NV	AS	1V	2V	3V	PS	Naso
Mean	0	0.1179	0.1832	0.3165	0.4498	0.5831	0.7164	1
SD	0	0.0262	0.0410	0.0359	0.0347	0.0375	0.0437	0

Table 3.2: This table shows the mean location of each plane of all the subjects in the second row and the third row lists the SD of each plane accordingly.

Figure 3.17 compares the intranasal cross-sectional area distribution of both congested and decongested cavities. The origin point of lateral axis represents the location of nostril plane and it ends up at the position of nasopharynx plane (as defined in figure 3.1). Furthermore, there are also several reference dash lines vertically that corresponds to the planes previously defined from table 3.2. As can be seen the mean nasal valve area is reduced slightly due to the decongestion. The area expansion after nasal valve of decongested cavities on average is much more pronounced than that of the congested cavities. This is due to the erectile structure within the cavity thus the decongestion will significantly increase the intranasal volume. Meanwhile, the congestion will make the cavity cross-sectional area after nasal valve (as shown in the figure 3.17 between AS and 1V dash lines) even smaller than the NV area on average. Apart from that, the maximum cross-sectional area is still located around the posterior septum where the two cavities joined as one for both congested and decongested cavities. The decongestion changes the way of how the mean cross-sectional area between plane 'AS' and '1V' grows, at which the head of inferior turbinate located. In general, after the nasal valve, the decongestion effect will roughly increase the cavity cross-sectional area 1.5 times larger until it reaches the posterior septum.

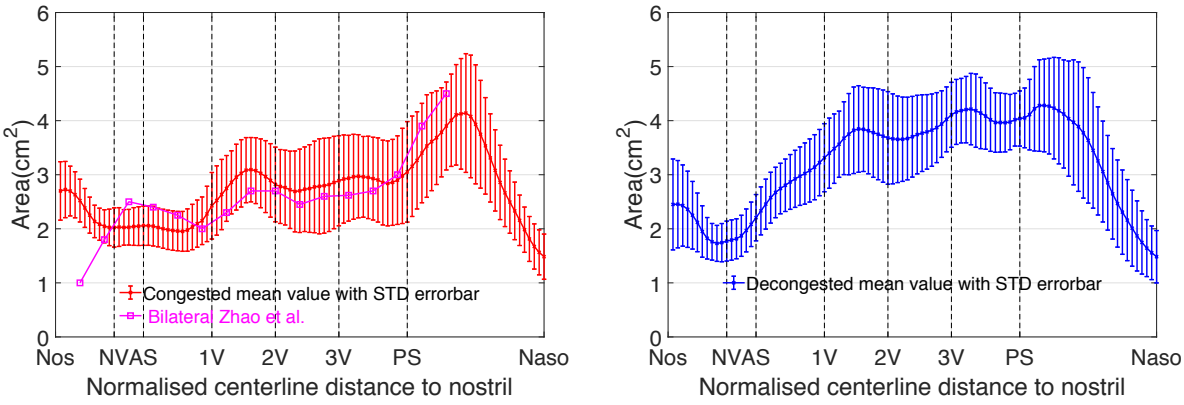
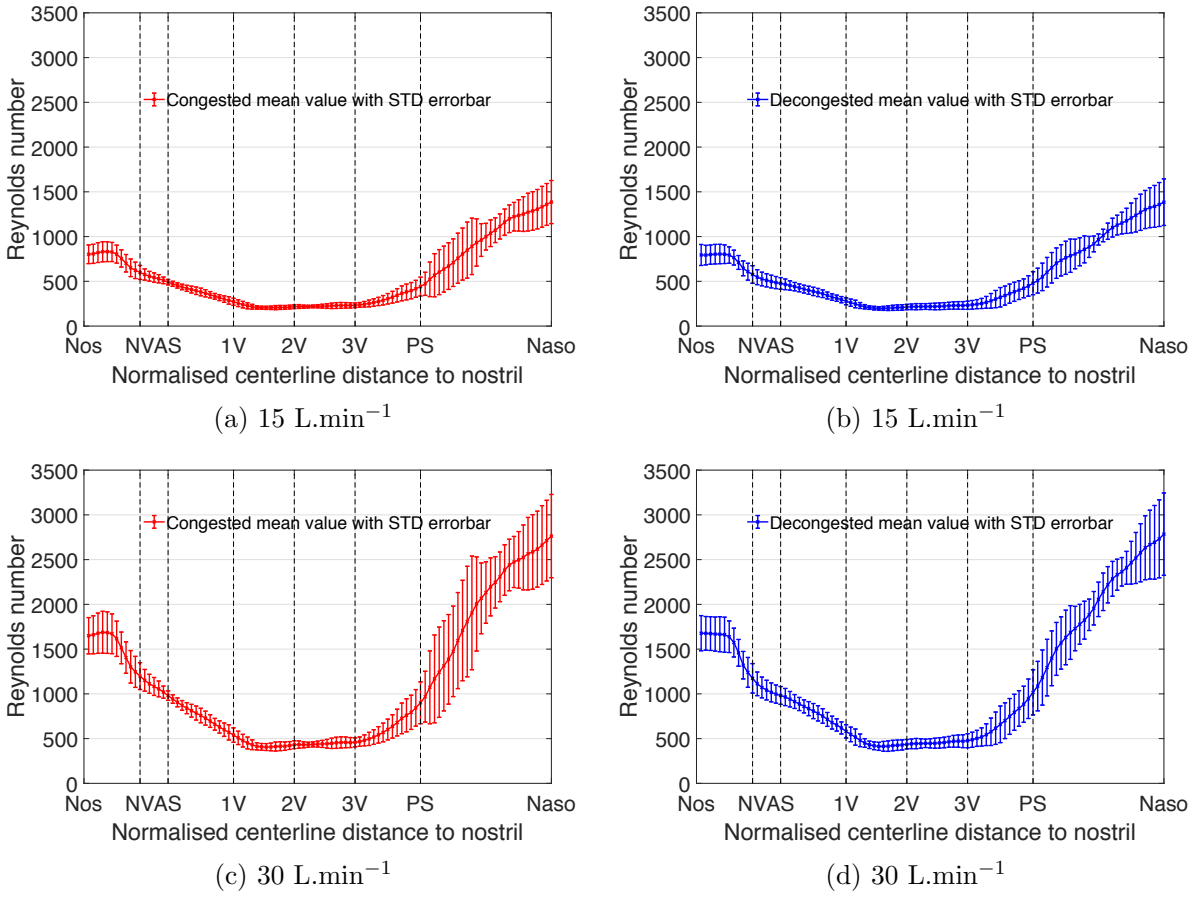


Figure 3.17: Comparison between congested and decongested bilateral cross-sectional area distribution with one standard deviation error bar. Red line represents the mean value of cross-sectional area distribution among all the congested cavities and blue line shows the results for decongested cavities. Zhao et al.'s results are plotted together with the congested cavities plot.

3.2.2 Reynolds number

Two different flowrates are simulated for all the nasal cavities: 15 L.min^{-1} for resting breathe and 30 L.min^{-1} for light exercise breathe. Figure 3.18 plots the mean Reynolds number distribution along the centerline over all the subjects with one standard deviation as error bar. From the figure, we can see that the mean Reynolds number for both congested and decongested nasal cavities at flowrate of 15 L.min^{-1} is below 2000 across the whole cavity. There are two peak values that are located at anterior and posterior individually. One of the peak is due to the narrow cross section at nasal valve and the other peak is due to the small cross-sectional area that caused by the base of the tongue at nasopharynx. Although the mean Reynolds number of 30 L.min^{-1} at the nasopharynx region are over 2000 for both congestion and decongestion, more than 80% of the cavity still have the mean Reynolds number below 2000. As was seen there is a pronounced increase of cross-sectional area of decongestion cavities after nasal valve, however Reynolds number between congestion and decongestion cavities for both flowrates show similar value. This is likely caused by the extreme irregular shape of the cavity cross sections which will lead to similar hydraulic diameter and induced an insignificant change of Reynolds number after decongestion compared with that of the cross-sectional area variation as explained earlier

for the single case.



(a) 15 L.min^{-1} (b) 15 L.min^{-1}

(c) 30 L.min^{-1} (d) 30 L.min^{-1}

Figure 3.18: Mean Reynolds number comparison. Left pair (red line) represent the congested cavity and right pair (blue line) represent the decongested cavity.

3.2.3 Flow partitioning: top, middle and lower

As has been described above, the definition of top, middle and lower cavity do not have physical barriers across these sections vertically. Thus the flow can freely go through each section. Figure 3.19 displays the mean mass flow split ratio of top, middle and lower sections of all the cavities.

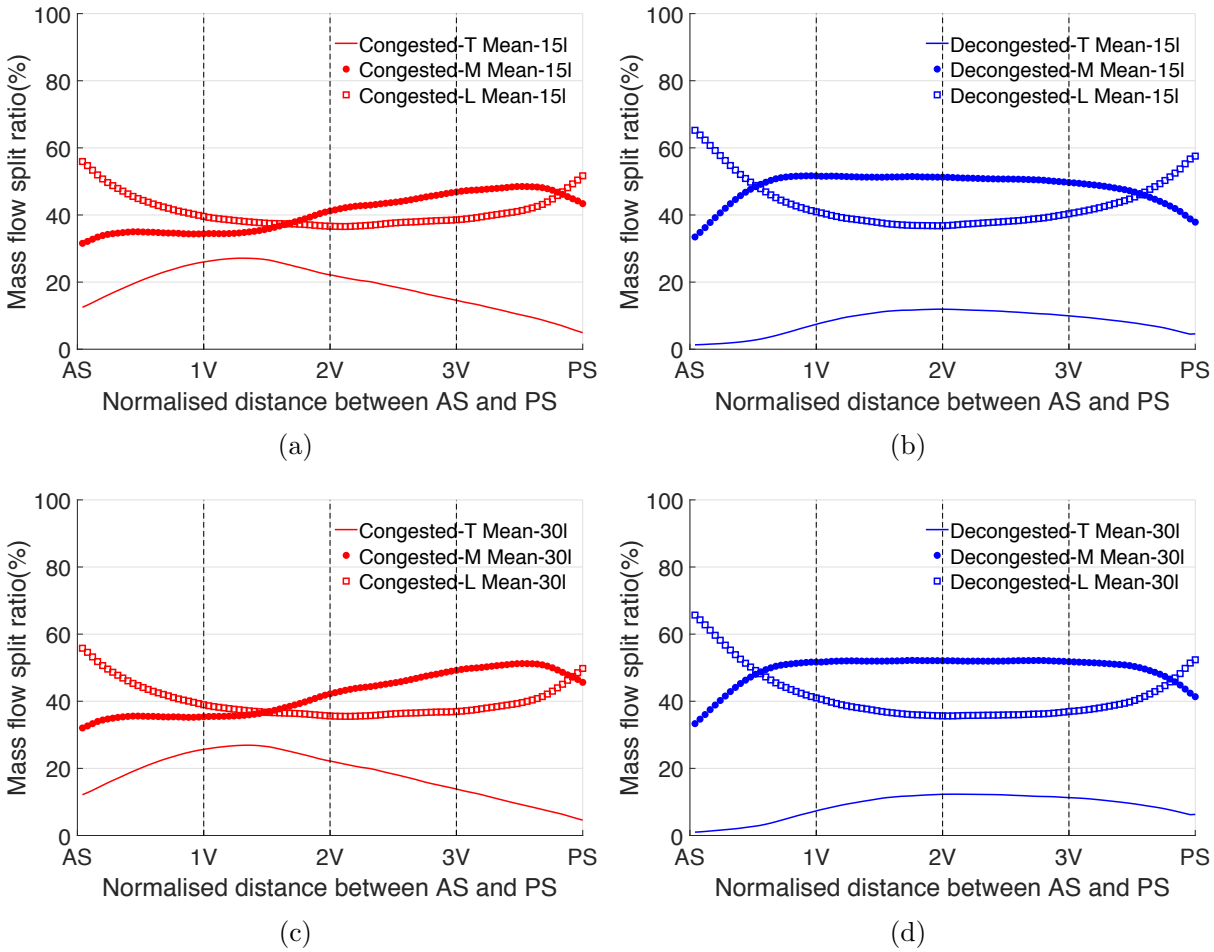


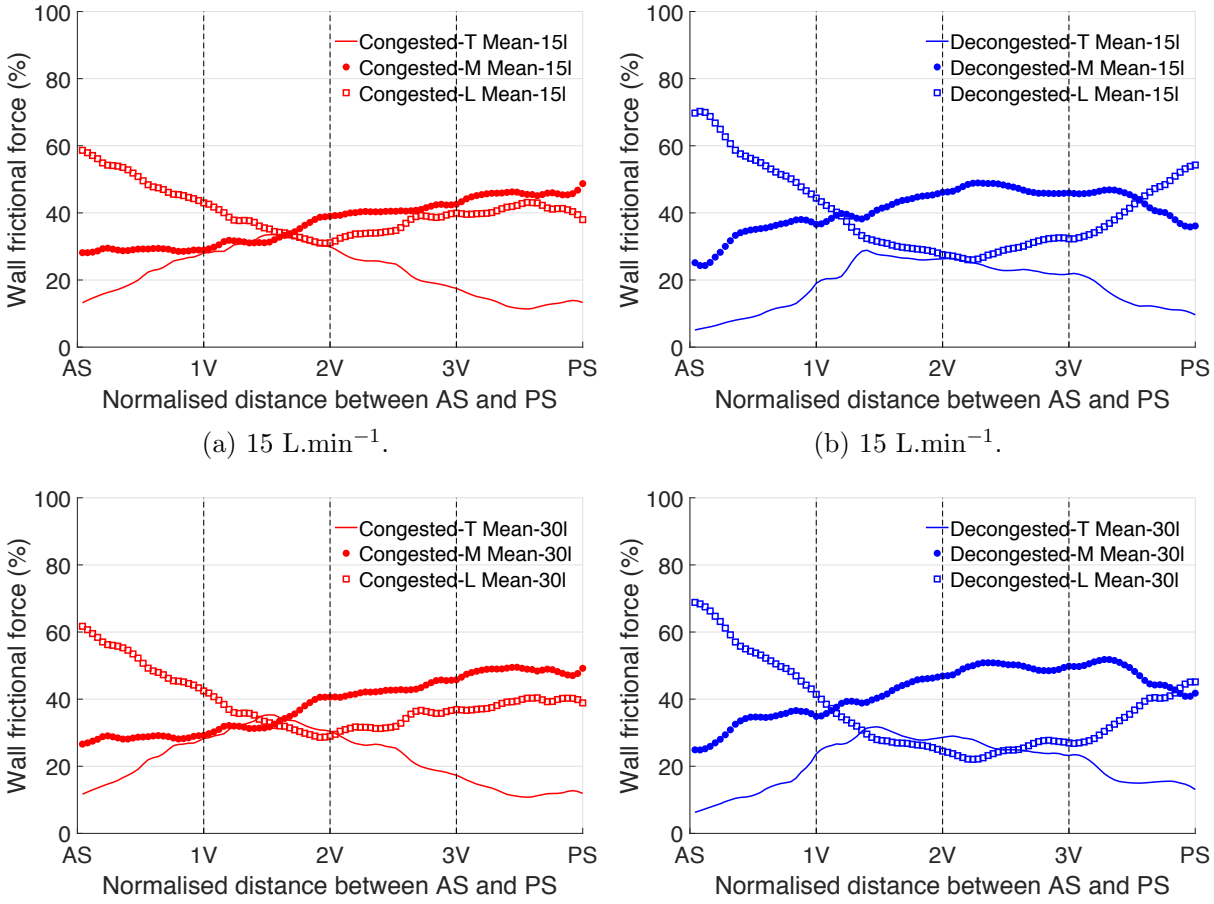
Figure 3.19: Decongestion effect on the mass flow split ratio over top, middle and lower regions of all the bilateral cavities. Each line represents the mean value of the 10 subjects and two flowrates are compared: 15 and 30 L.min^{-1}.

Firstly, comparing figure 3.19a and figure 3.19b we can see that decongestion will change the mass flow split ratio: top cavity will have much less portion of the mass flow than that of the congested cavities on average, meanwhile, the mass flow that go through the middle cavity will increase, but the portion of mass flow go through the lower cavity region will keep nearly unchanged. Similar patterns also can be found after the flowrate is doubled (30 L.min^{-1}). The relatively narrower anterior section of congested cavities will drive more flow into the top cavities after flow pass nasal valve compared to that of the decongested cavities. Moving posteriorly, for congested cavities, the mass flow split ratio of the middle cavity starts to increase after '1V' and before '2V' at which the head of middle turbinate located. However, in the same region of decongested cavities, the immediate expansion of cavity CSA after nasal valve will direct the

flow earlier split into middle and lower sections of the cavity. Last but not least, either the cavity is under congested or decongested conditions, the mass flow split ratio will nearly keep the same if only simply double the inlet flowrate, although the higher flowrate tends to have more distinguishable split pattern among top, middle and lower sections of the cavity.

Similarly, figure 3.20 shows the surface friction force distribution ratios along the cavities defined by the product of WSS and surface area. Figure 3.20a and 3.20c show that the increase of flowrate does not affect the surface frictional force distribution of the mean value for all the cavities, while the geometry change that caused by decongestion will alter the split patterns significantly. As can be seen from the plot, the decongestion will make the middle cavity suffer more resistance than the lower part within the pure turbinates region that defined by plane 1V and PS. In addition, the decongestion also slightly reduces the portion of frictional force in the superior cavity that due to larger CSA in general of decongested cavities. Specifically, among these three sections (top, middle, lower) of the cavity, it shows that from anterior to posterior, the surface frictional force within the middle section is consistently high (though it is slightly increasing across the cavity) no matter what the condition of the cavity is, except the lower cavity that has the largest portion of the total frictional force in the anterior cavity (before the middle region between 1V and 2V). As we have seen the head of the inferior turbinate located around plane 1V (figure 3.1), thus the flow stream will get redirected after it passes plane 1V, shown by figure 3.19. In other words, this will lead to the alteration of frictional force split as well that the middle cavity starts to replace the lower cavity as the most resistive section of the cavity proportionally. In the decongested lower section of the cavity, the surface frictional force from plane AS to PS plane has larger variations than that of the congested cavity. In addition, the considerable difference of surface frictional force distribution can be found from the middle section of the nasal cavity: first of all, after decongestion the surface frictional force starts to increase proportionally immediately after anterior septum plane, but it only starts to increase after the location between plane 1V and 2V of congested cavity. On the other hand, at plane AS, the decongestion effect can increase the lower section surface frictional force around 10% proportionally, that mainly contributed by the reduction of the friction force from top

section. This is mainly attributed to the decrease of the mass flow into the superior turbinate (figure 3.19). In summary, within the cavity range considered here (from plane AS to PS), in the anterior quarter of the cavity, over half of surface frictional force is contributed by the lower section. However, in the rest three-quarter of the cavity posteriorly, the middle section starts to take over the lower section and becomes the most resistive region.



(a) 15 L.min^{-1}. (b) 15 L.min^{-1}.

(c) 30 L.min^{-1}. (d) 30 L.min^{-1}.

Figure 3.20: Flow rate and decongestion effect on frictional force split ratio among top, middle and lower sections of nasal cavity.

3.2.4 Pressure loss and resistance

Total pressure is the sum of the static pressure and dynamic pressure. Total pressure is often used as an indication of the flow energy, although energy flux might be more direct. However total pressure is in general more difficult to measure, so that experimental nasal airway resis-

tance is defined in terms of static pressure changes. Plots of mean total pressure and static pressure distributions along the nasal cavity centerline are shown in figure 3.21 and figure 3.23 respectively. Comparing figure 3.21a and figure 3.21c, it can be seen that not only the overall mean total pressure loss for the congested cavity will be approximately tripled if the flowrate is doubled, but also that the higher flowrate is likewise associated with higher variations of total pressure loss among all the congested cavities.

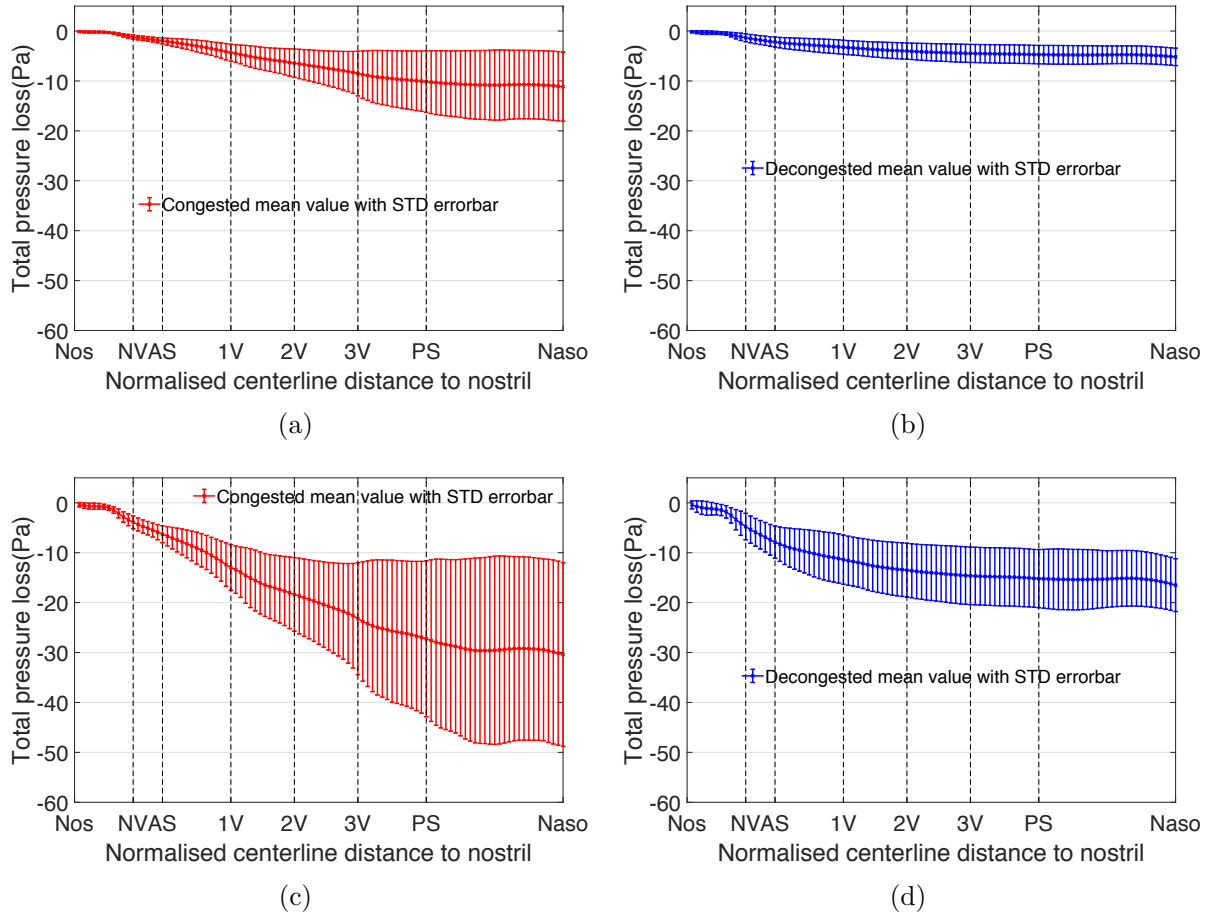


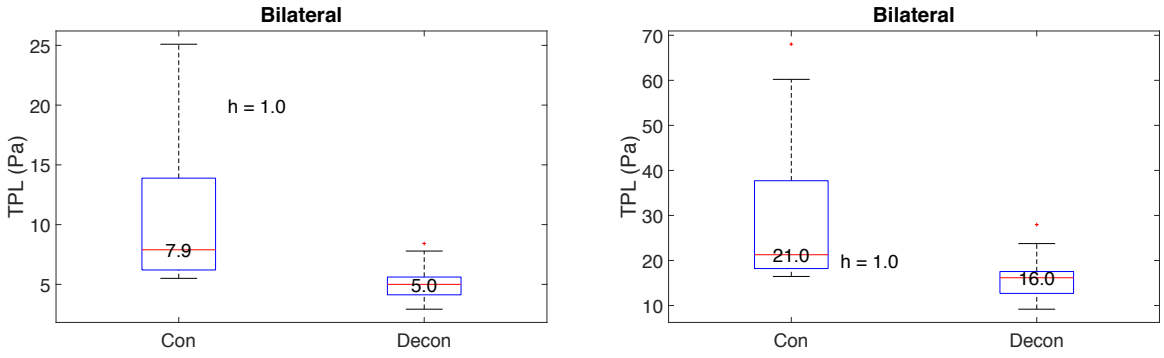
Figure 3.21: Intranasal cross-sectional plane averaged total pressure distribution along the cavity. Figure 3.21a and 3.21b show the results of 15 L.min^{-1} and 3.21c and 3.21d are the results for 30 L.min^{-1}.

For the decongestion cavities, the distributions are markedly different, with far smaller pressure losses in the cavity from anterior to posterior septum. Median overall total pressure losses at 15 L.min^{-1} are reduced approximately 38% by decongestion (from 7.9 Pa to 5.0 Pa). At 30

L.min^{-1}, total pressure losses are reduced by decongestion by approximately 25% (from 21 Pa to 16 Pa).

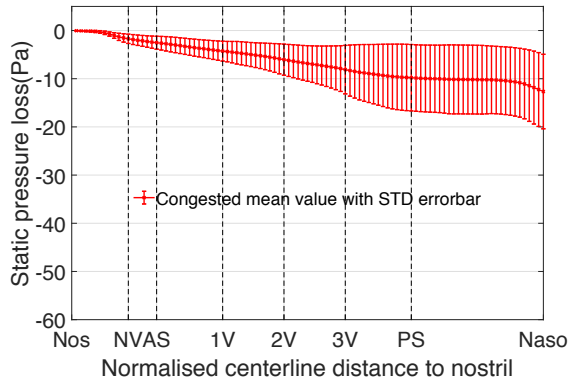
For the total pressure loss distribution from anterior to posterior, it shows that contribution of total pressure loss within the congested cavities are more evenly distributed within the range of NV and PS which is due to the consistency narrow CSA of the cavity, no matter the lower or higher flow rate (figure 3.21a and 3.21c). However, after the cavity being decongested, the total pressure loss is more concentrated anteriorly of region between NV and 2V (figure 3.21b and 3.21d) for both flowrates.

Box plot comparisons of the total pressure loss for congested and decongested cavities are shown in figure 3.22. Both for lower and higher flowrates, the geometry changes due to the decongestion are seen to significantly reduce total pressure loss.

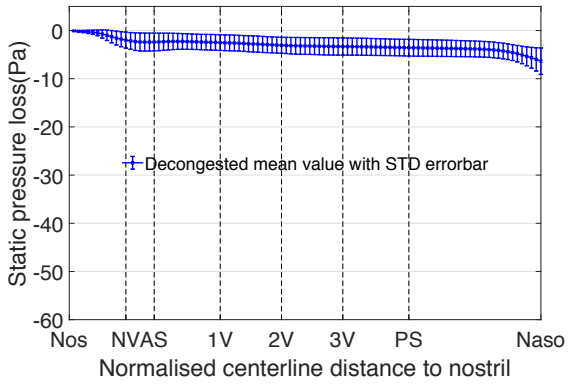


(a) 15 L.min^{-1} (b) 30 L.min^{-1}

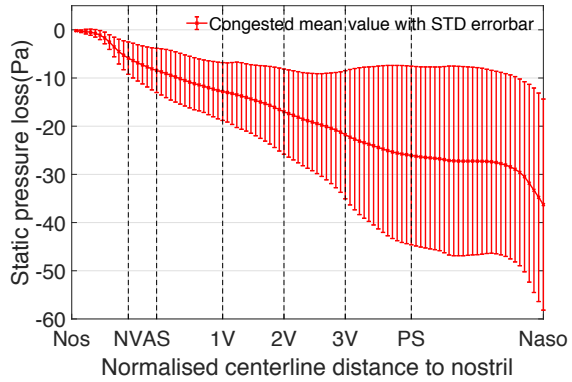
Figure 3.22: Significance test between congested and decongested cavity of total pressure loss. Left figure shows the result of 15 L.min^{-1} and right figure is the result of 30 L.min^{-1}.



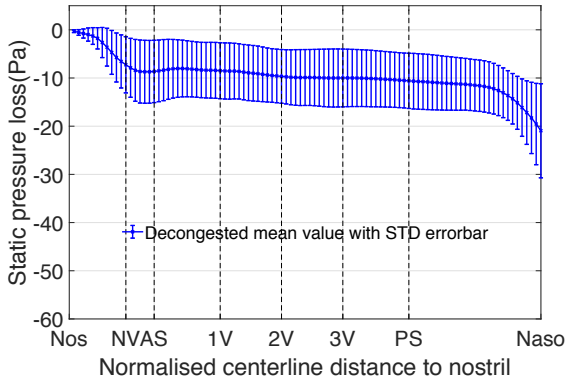
(a) 15 L.min^{-1}.



(b) 15 L.min^{-1}.

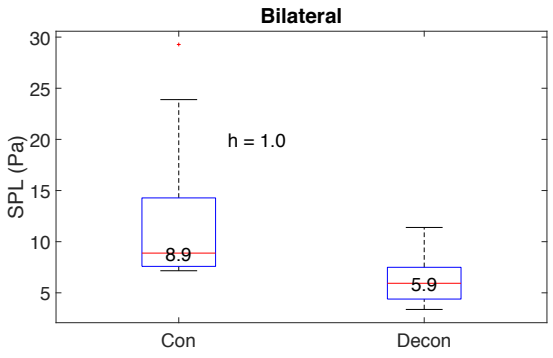


(c) 30 L.min^{-1}.

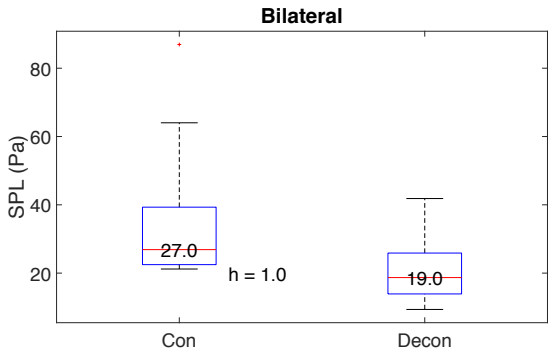


(d) 30 L.min^{-1}.

Figure 3.23: Intranasal cross-sectional plane averaged static pressure distribution along cavity centerline with two different flow rate as label in the figure.



(a) 15 L.min^{-1}



(b) 30 L.min^{-1}

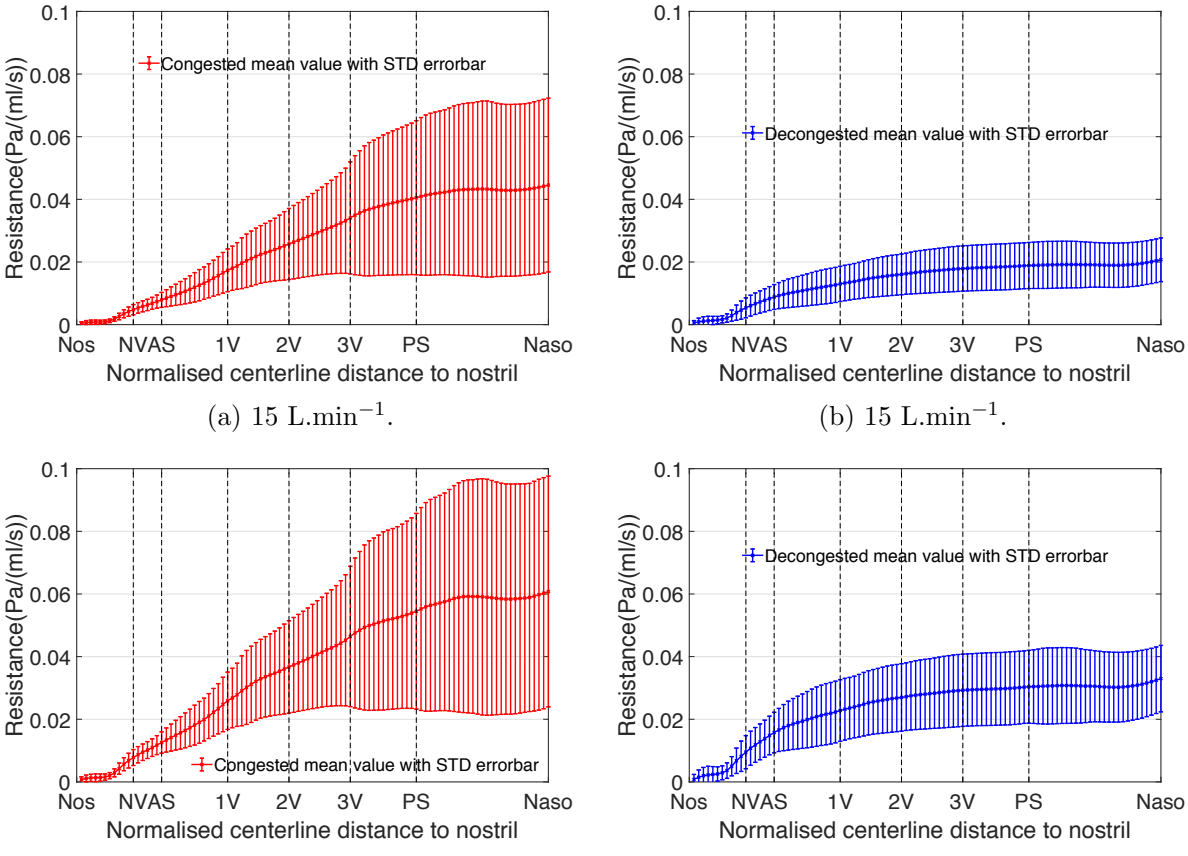
Figure 3.24: Significant test of static pressure loss between congested and decongested cavity. Left figure shows the flow rate at 15 and right is 30 L.min^{-1}

Considering the plots of static pressure for the decongested cavities, the rapid drop in pressure from nostril to NV and the slight pressure recovery between NV and anterior septum are char-

acteristic of a jet entering the cavity downstream of the valve. The effect is more noticeable at higher flowrates, with the median static pressure loss (SPL) rising from 5.9 Pa to 19 Pa for the decongested cavity.

In the decongested cavity, static pressure drops little in the enlarged cavity, but then drops again rapidly in the nasopharynx, where the CSA reduces.

By contrast, for the decongested cavity, the rate of static pressure loss is considerably more uniform. There is a slightly greater loss rate around the nasal valve, and a marked decrease in rate of loss in the enlarged CSA downstream of the posterior septum and before the contraction in the nasopharynx.



(a) 15 L.min^{-1}.

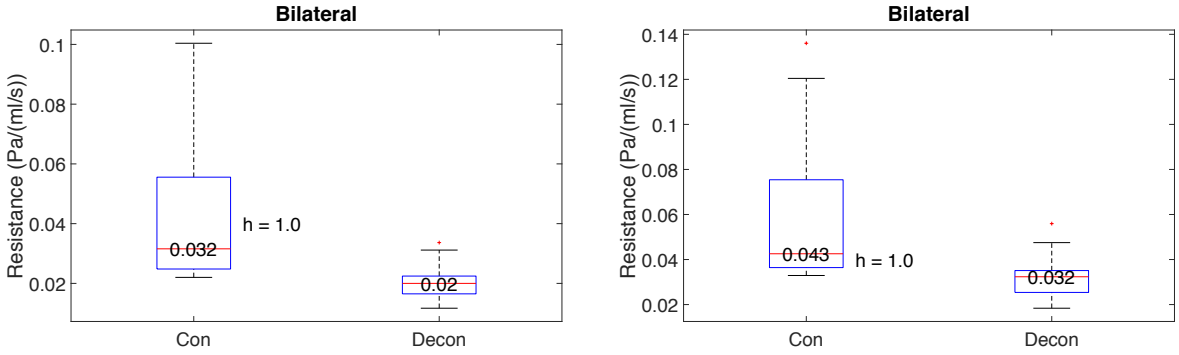
(b) 15 L.min^{-1}.

(c) 30 L.min^{-1}.

(d) 30 L.min^{-1}.

Figure 3.25: Intranasal cross-sectional plane averaged resistance distribution along cavity centerline. The solid line is the mean value among all the subjects considered and the errorbar is the value of one standard deviation.

Resistance is one of the often used index for clinicians, figure 3.25 and 3.26 show the intranasal resistance distribution with multiple conditions and the cavity total resistance significance test between congested and decongested cavities. As expected from the definition of resistance that the distribution suppose to have the same characteristic as the total pressure loss as well as the significance test results.



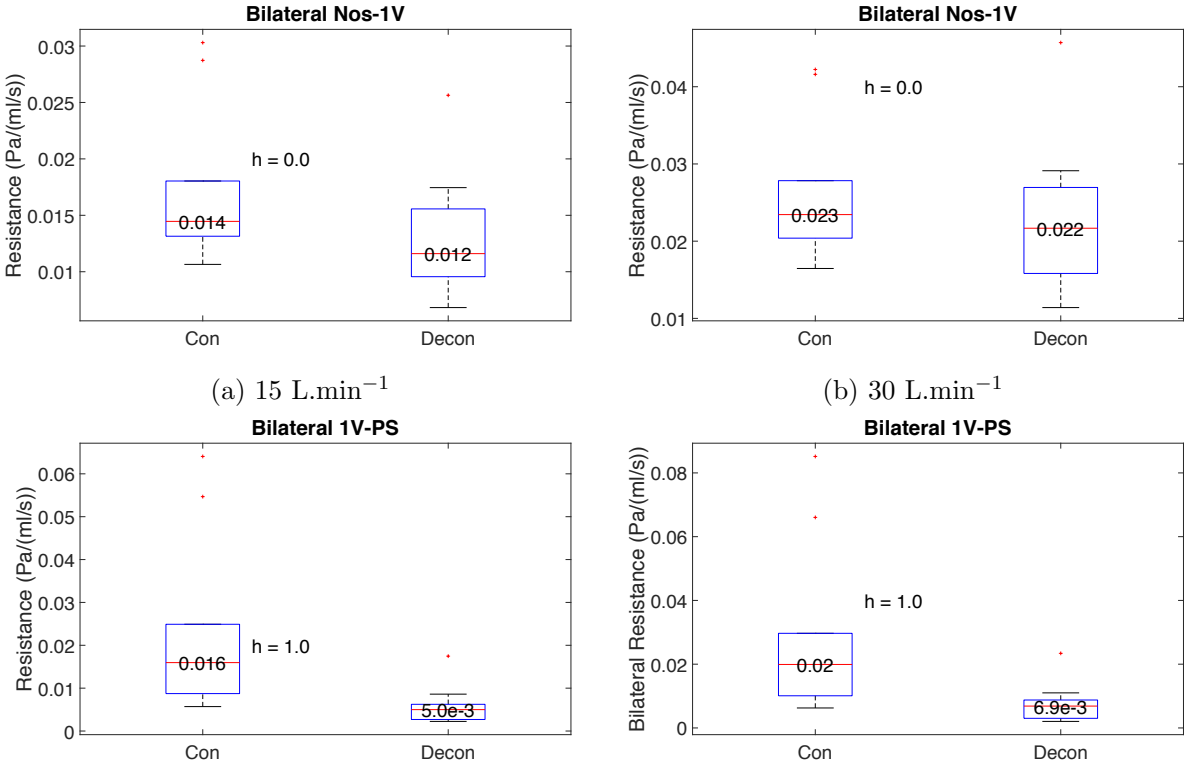
(a) 15 L.min^{-1} (b) 30 L.min^{-1}

Figure 3.26: Significance test of cavity total resistance between congested and decongested conditions. Left figure shows the result of flow rate 15 L.min^{-1} and right figure is the result of flow rate 30 L.min^{-1}.

The preceding analysis describes the nasal cavity flow anterior to plane 1V as displaying the character of the flow in a converging-diverging nozzle due to the existence of nasal valve (especially for decongested cavities). Conversely the posterior part of the cavity before plane PS, which is more or less the pure turbinates region, point to different characteristics for congested and decongested cavities.

Referring back to the area distribution, whilst the CSA increases in both congested and decongested cavities, the increase is more dramatic in the decongested cavity. This suggests investigating separately the airway resistance within the anterior part of the cavity (between nostril and plane 1V) and the posterior part (between plane 1V and PS) rather than the overall resistance. This allows the effect of changing flowrate and changing of geometry (by decongestion) on the resistance to be considered separately anteriorly and posteriorly. From figure 3.27, changes in the anterior resistance are not significant statistically, for either flowrate. However,

the median posterior cavity resistance is reduced by approximately three times and clearly significant.



(a) 15 L.min^{-1} (b) 30 L.min^{-1}

(c) 15 L.min^{-1} (d) 30 L.min^{-1}

Figure 3.27: Anterior and posterior nasal airway resistance. Upper left right pair: anterior resistance. Nos-1V denotes nostril (Nos) to approximate location of anterior head of middle turbinate (plane 1V), Lower left right pair: posterior resistance. 1V-PS denotes plane 1V to posterior septum (PS).

3.2.5 Friction coefficient and Poiseuille number

The figure 3.28 plots the mean distribution of Fanning drag coefficient and Poiseuille number of all the subjects, it does not only compare the difference before and after decongestion but also shows the effect of doubling the mass flowrate. From the plot we can see that the Fanning drag coefficients for under both flowrates are following similar trends but the lower flowrate tends to have larger variations both inter subject (higher SD value) and intra subject (higher mean values) than the higher flow rate. The Poiseuille number distribution in the anterior

cavity shows more variation and larger values compared to that of the posterior cavity due to the developing flow profile.

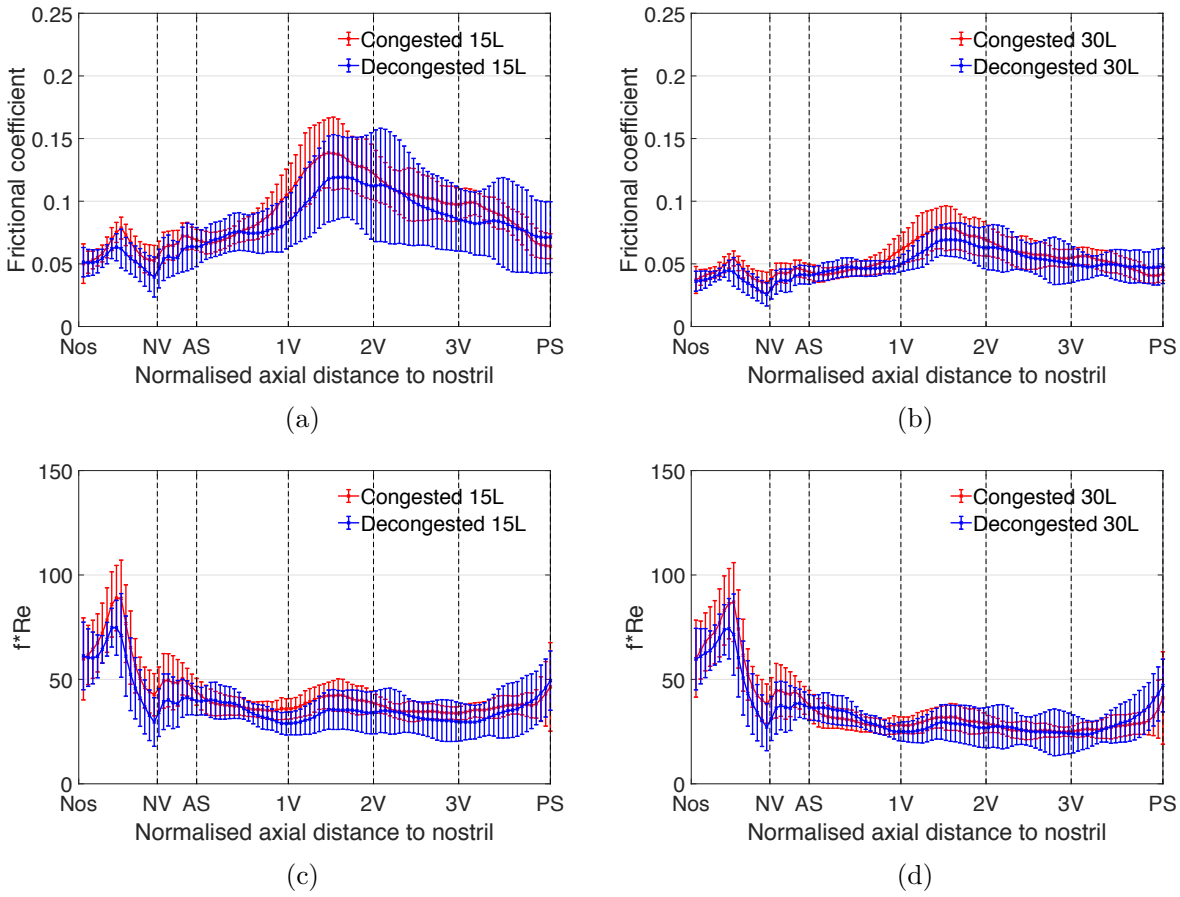
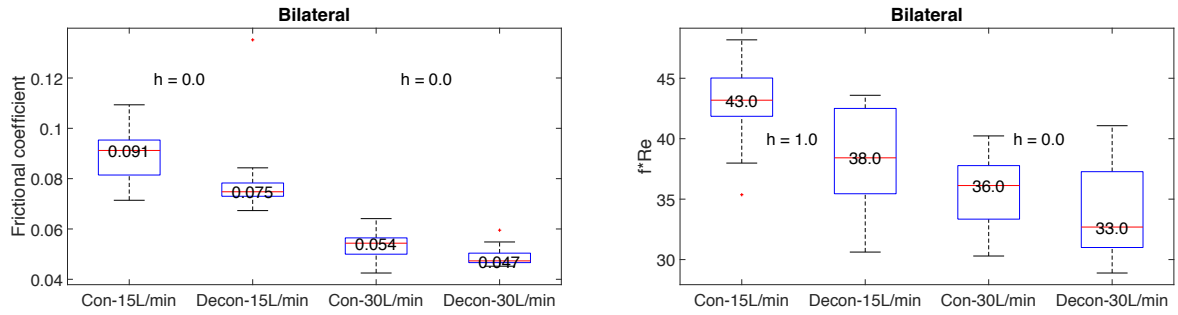


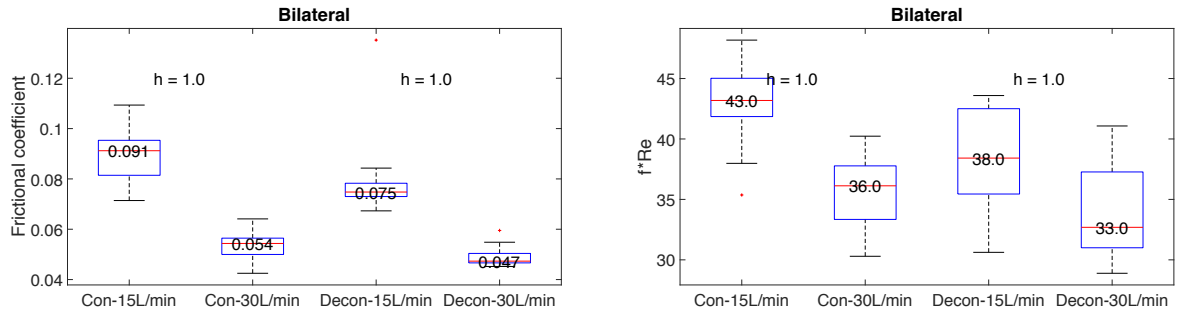
Figure 3.28: Effects of decongestion and change of flowrate on frictional coefficient and Poiseuille number distribution. Figure 3.28a and 3.28b are the frictional coefficient distribution and figure 3.28c and 3.28d are the Poiseuille number distribution under two flowrates as labelled.

The Wilcoxon signed-rank test compares the mean Poiseuille number over the whole cavity before and after decongestion as well as multiple flowrates.



(a) (b)

Figure 3.29: Decongestion effect on bilateral cavity mean Fanning drag coefficient and Poiseuille number.



(a) (b)

Figure 3.30: Flow rate effect on bilateral cavity mean Fanning drag coefficient and Poiseuille number.

From figure 3.29 we can see that the decongestion only shows significant statistic difference on the cavity mean Poiseuille number at lower flowrate 15 L.min^{-1}. On the contrary, the change of flowrate does have a statistically significant effect on both frictional coefficient and Poiseuille number of both congested and decongested cavities.

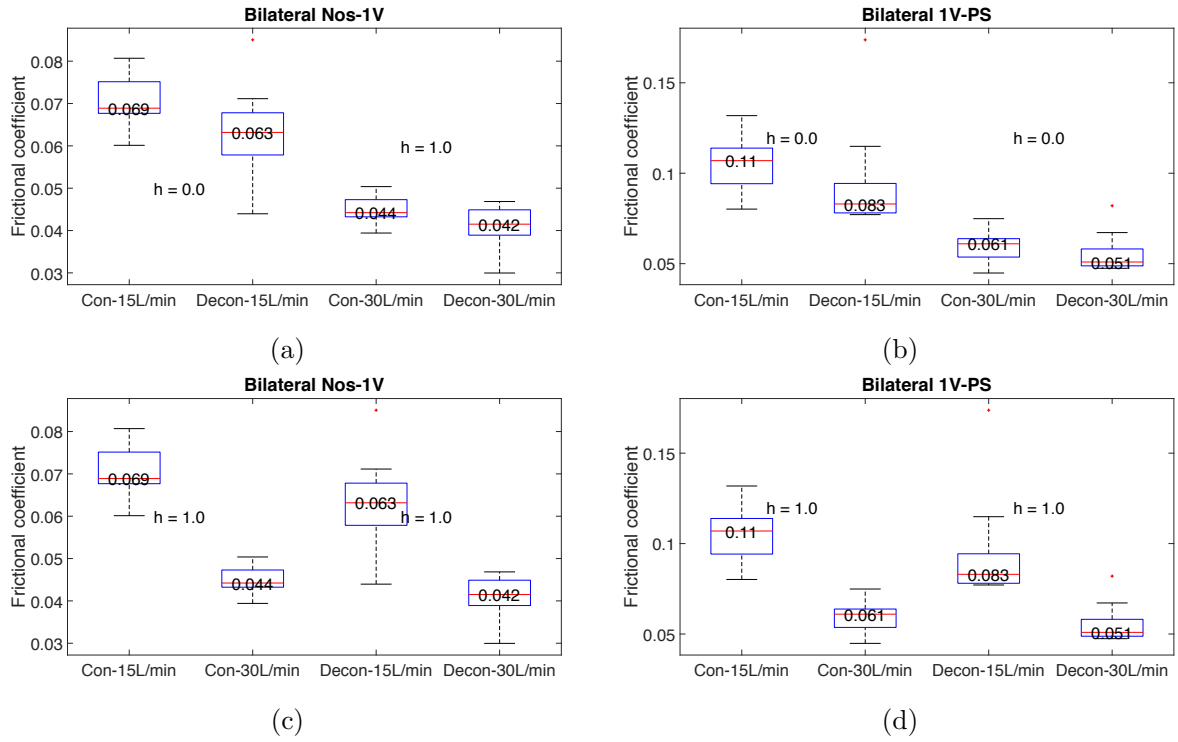


Figure 3.31: Decongestion and flow rate effects on the anterior and posterior part of the cavity for Fanning drag coefficient. 'Nos-1V' means the cavity region defined by nostril plane and 1V plane and the corresponding plot shows the value that averaged with this region. '1V-PS' defined the same way but by plane 1V and PS. Figure 3.31a and 3.31b are the test of decongestion effect, while the lower pair are the test of the effect of change of flowrate.

The plots in figure 3.31 show that the changes in friction coefficient due to decongestion are generally not significant - most likely the changes are too small for the number of individuals to be statistically significant at the 5% level - except for the anterior nose at high flow rates (figure 3.31a). By contrast, the changes in frictional coefficient due to increased flowrate are significant throughout the cavity for both the congested and decongested geometry (figure 3.31c and 3.31d).

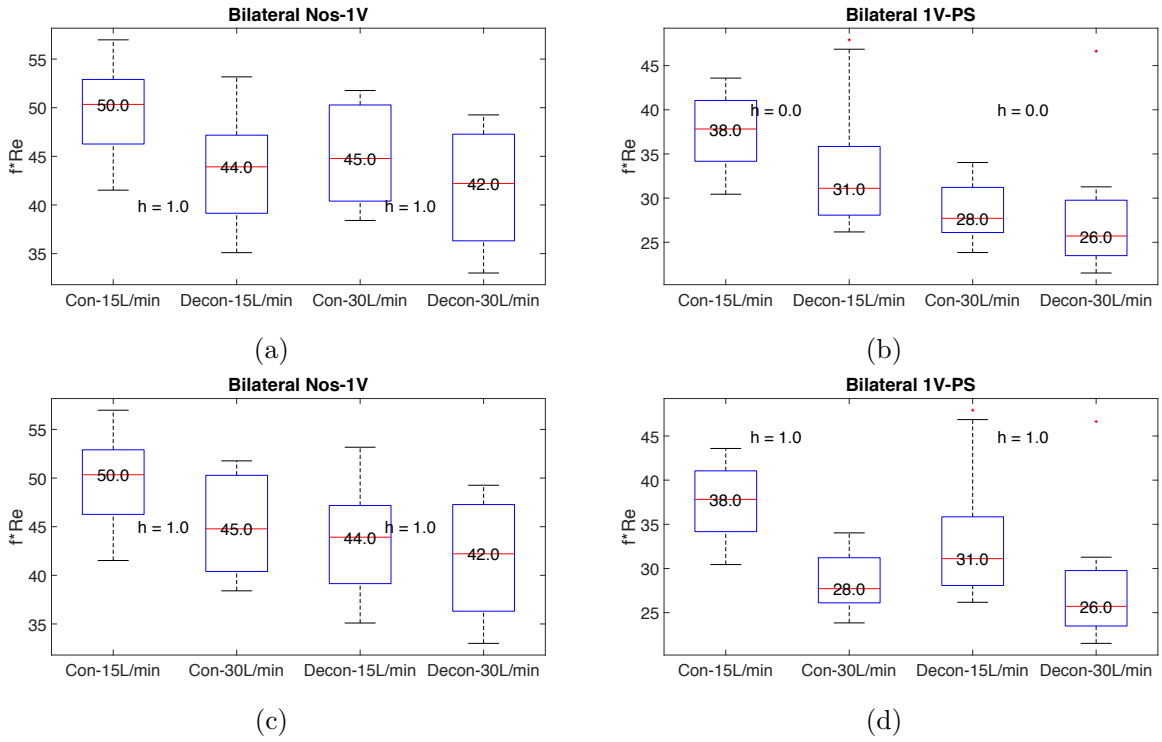


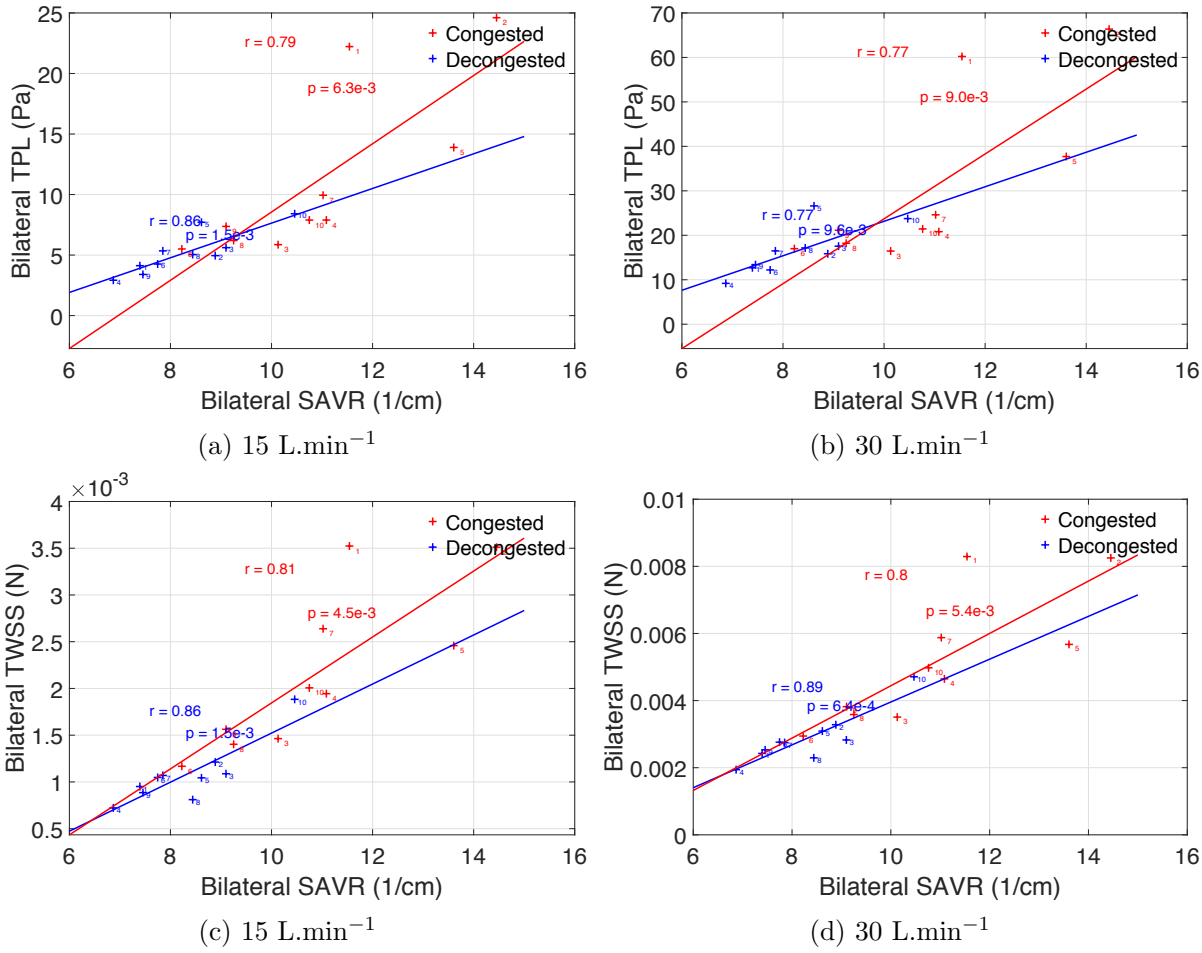
Figure 3.32: Decongestion and flow rate effects on the anterior and posterior part of the cavity for Fanning drag coefficient. 'Nos-1V' means the cavity region defined by nostril plane and 1V plane and the corresponding plot shows the value that averaged with this region. '1V-PS' defined the same way but with plane 1V and PS.

Similar as figure 3.31, figure 3.32 shows the same comparison but with Poiseuille number. The results show that the decongestion only has statistically significant effect on the anterior cavity of the Poiseuille number for both lower and higher flowrates, however, the change of flowrate does show significant difference both in the anterior and posterior cavity at the level of 5% statistically for both congested and decongested cavities.

3.2.6 Correlation analysis

Linear regression is used to examine the correlations between geometric measures and physical quantities. Within this study, the Pearson correlation coefficient (r) with an absolute value over 0.8 is categorized as 'strong' and less than 0.8 but greater than 0.6 is treated as 'moderate' and less than 0.6 is considered 'not evident'.

Evaluating the correlations of the anterior minimum cross-sectional area (CSA) against with all the other physical quantities: total pressure loss, static pressure loss, total WSS, none of them show evident correlations (figure B.1). Furthermore, the conclusion is not going to change after doubling the flowrate either. Those findings are expected because anterior minimum CSA is just local geometric measures while the physical quantities such as total pressure loss are measured over the whole cavity, thus it is reasonable that no strong (even moderate) correlations can be found.



(a) 15 L.min^{-1} (b) 30 L.min^{-1}

(c) 15 L.min^{-1} (d) 30 L.min^{-1}

Figure 3.33: Bilateral SAVR, TPL and TWSS.

The surface area volume ratio is a vital parameter that indicates the balance between volumetric flow and the mucosal surface area available for exchange. Higher area volume ratios indicate a relatively narrower cavity. The overall total pressure loss (TPL) has contributions from both the jet dissipation loss and from the WSS. Figure 3.33a shows that the decongested cavities

have a lower SAVR, lower TPL and a slightly stronger correlation between total pressure loss and SAVR than that for the congested cavities. However the difference in correlation strength becomes smaller by doubling the flowrate as shown in figure 3.33b. Likewise, strong correlations can be found between SAVR and total surface WSS under two different flowrates (figure 3.33c and figure 3.33d).

3.3 Unilateral nasal cavity geometric and flow analysis

3.3.1 Geometric comparison

As is known, under quiet breathing, air reaching the nasopharynx will have undergone the bulk of the air conditioning required to match alveolar conditions, but the relative contribution from each side of the cavity varies depending on the different morphologies. This suggests grouping all the half cavities into two categories, either by left and right sides or by flow dominant and non-dominant sides. The flow dominant, or simply dominant side of each subject is defined at the congested condition as the cavity that carries over half of the total mass flowrate. Table 3.3 lists each subject's dominant side under congested condition (normal condition) with value one and this labelling will be kept after applying topical decongestion.

Subject name	A	B	C	D	E	F	G	H	I	1
Left	0	0	1	1	0	0	0	1	1	1
Right	1	1	0	0	1	1	1	0	0	0

Table 3.3: Dominant side of nasal cavity with value one and non-dominant side identified by value zero.

As expected, from table 3.3 it can be seen that the dominant side of the cavity is not consistent among different subjects: either left or right side can be the dominant side of the cavity.

Table B.4 in appendix B.3 lists all the area and volume values of each unilateral cavities, but the box plot with the Wilcoxon signed-rank test results (figure 3.34) can give more direct

comparison.

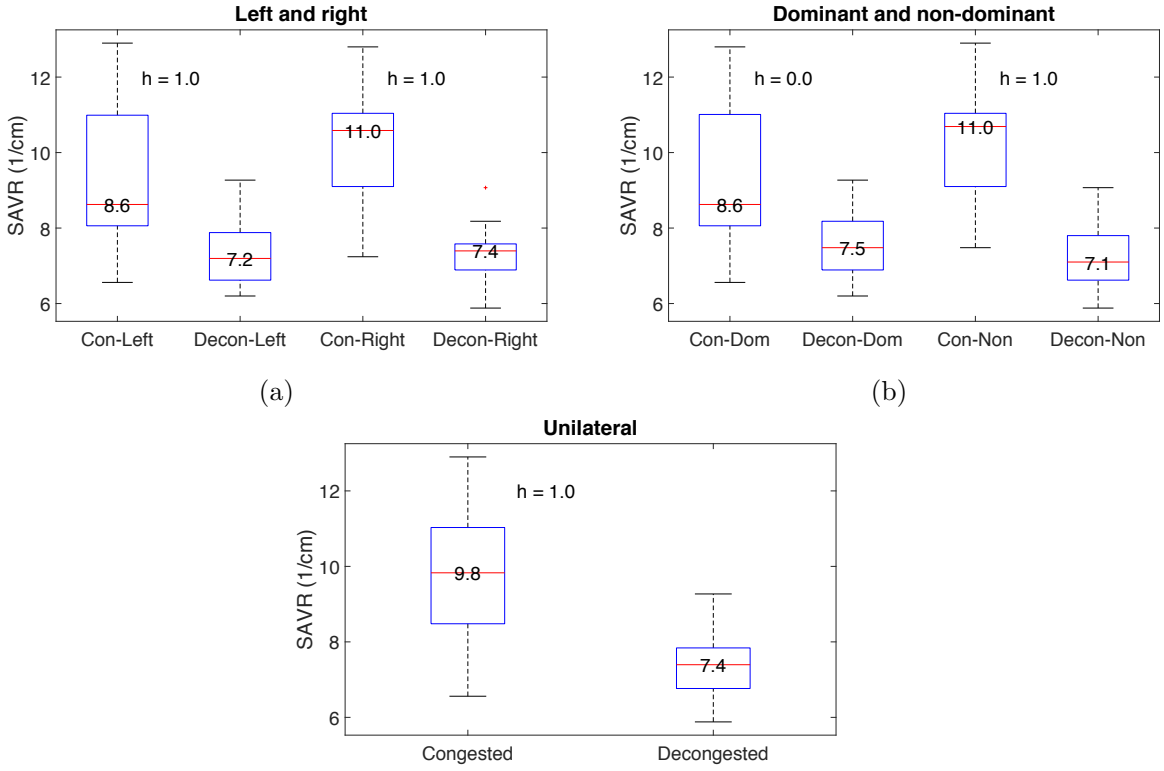


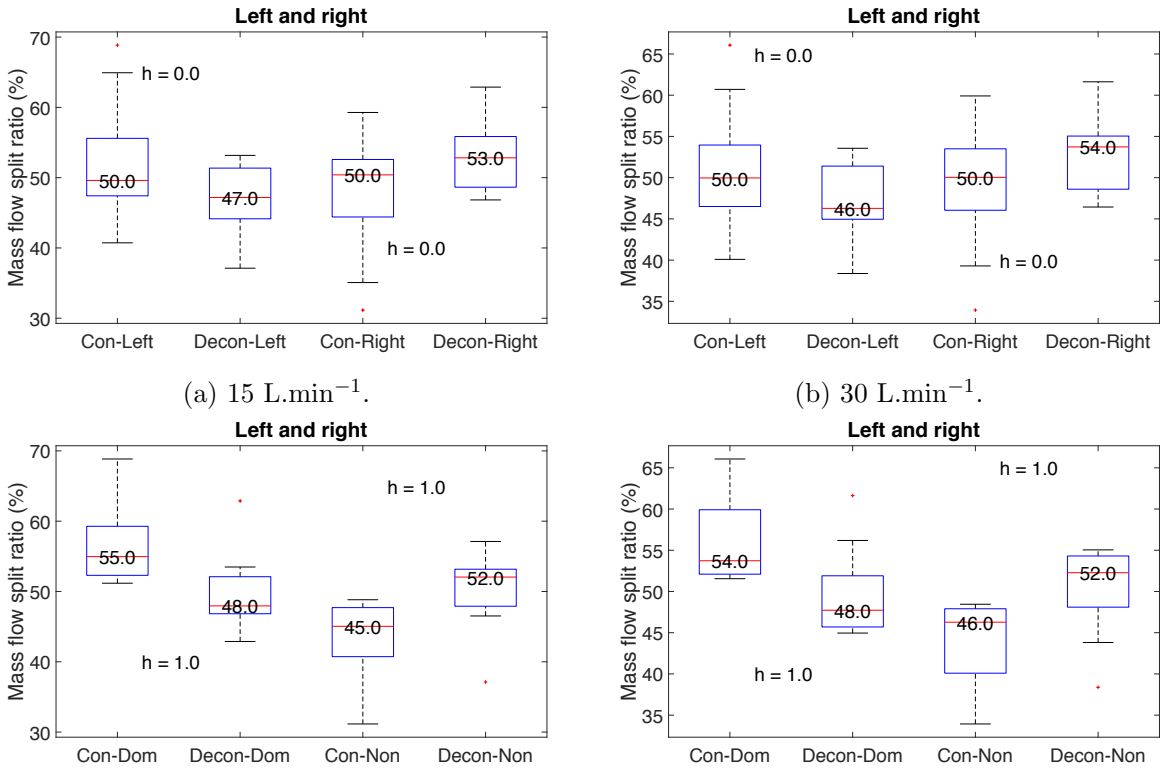
Figure 3.34: Unilateral SAVR before and after decongestion comparison.

Plot 3.34a compares the SAVR of left and right cavity and of dominant and non-dominant side of the cavity before and after the decongestion. It can be seen that the SAVR of left cavity after decongestion is significantly reduced (h = 1, p value of 0.037). Same conclusion for right cavities as well but with smaller p value (3.9e-4). Conducting the same analysis on dominant and non-dominant side, it shows that the decongestion only has a statistically significant effect on the SAVR of the non-dominant side of the cavity (h = 1, p = 0.002). The dominant side of the cavity does not show significant difference before and after decongestion. This is because the non-dominant half cavities are more expandable than the dominant side of the cavities. In addition, if each of the half cavity is treated as an individual object, it also shows that the decongestion effect is statistically significant on the SAVR of unilateral cavities.

3.3.2 Flow partitioning: left and right

This section compares the mass flow split between different sides of the cavity. Firstly comparing the changes of mass flow split between left and right cavity after decongestion. Figure 3.35a shows that there are no significant changes after decongestion for both left and right cavities of total flowrate at 15 L.min^{-1} and this conclusion is not altered by simply doubling the total mass flowrate (figure 3.35b). Secondly however, if the grouping rules are changed to dominant and non-dominant sides, the results obtained are as shown in the following plots: figure 3.35c and figure 3.35d. From these plots, decongestion is found to significantly change the mass flow split ratio of dominant and non-dominant sides for both lower and higher flowrates, rendering the flow split between the two halves more equal.

Summing up, these findings indicate that the decongestion can shift the dominance of the half cavities. In other words, firstly there is no bias of the flow split over left and right side after decongestion, and secondly decongestion reduces dominant/non-dominant asymmetry. This suggests treating each single half cavity as an individual entity for flow analysis.



(a) 15 L.min^{-1}.

(b) 30 L.min^{-1}.

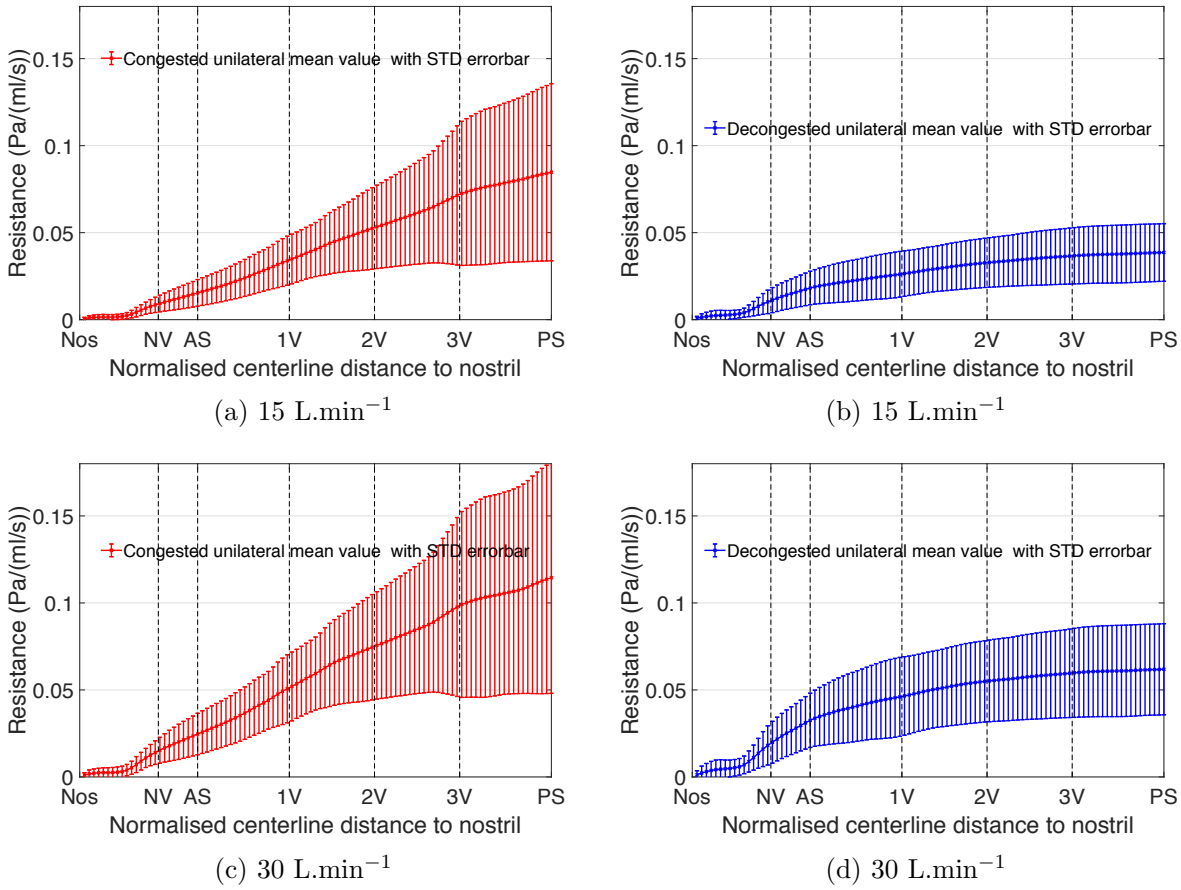
(c) 15 L.min^{-1}.

(d) 30 L.min^{-1}.

Figure 3.35: Decongestion effect on mass flow split ratio between left and right cavity, or dominant and non-dominant side.

3.3.3 Resistance

Due to the asymmetric mass split ratio of the cavity for different subjects, the resistance might be a better metric rather than pressure loss for investigating the decongestion effect on unilateral cavities. Figure 3.36, it shows that decongestion not only reduces the mean unilateral total resistance (about half), but also reduces the dispersion level of the resistance (smaller SD) from nostril to posterior septum.

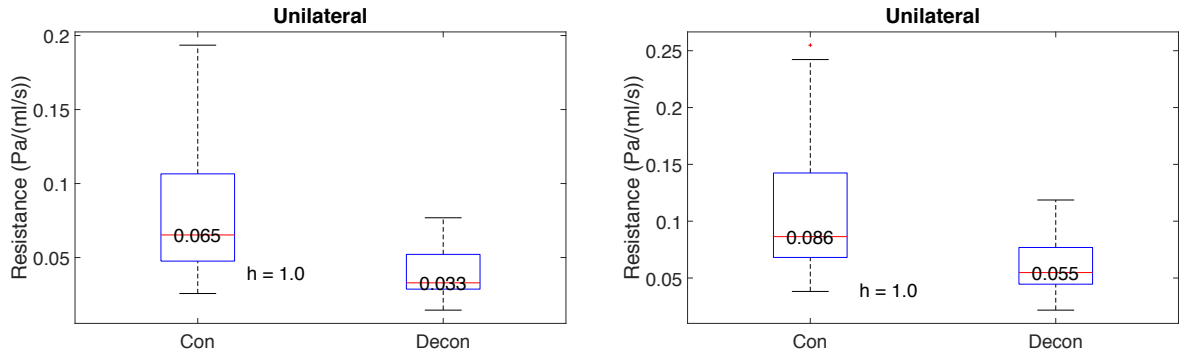


(a) 15 L.min^{-1} (b) 15 L.min^{-1}

(c) 30 L.min^{-1} (d) 30 L.min^{-1}

Figure 3.36: This figure shows the unilateral resistance distribution across the cavity for both congested and decongested cavities of two flowrates. Red line represents the congested cavity and blue line represents decongested cavity.

In quantitative terms, box plots of resistance values show that for both lower and higher flowrates, the geometry change by decongestion reduces the median resistance (at 15 L.min^{-1}) by approximately half with high statistical significance (now given a dataset twice as large as for the bilateral comparisons). Results for the higher flowrate (figure 3.37b) likewise shows significant reduction due to decongestion, although the median reduction is less than that at lower flowrate. The decreased effect at higher flowrate is because the nasal valve contributes proportionately more to flow loss in the decongested cavity at higher flowrate.

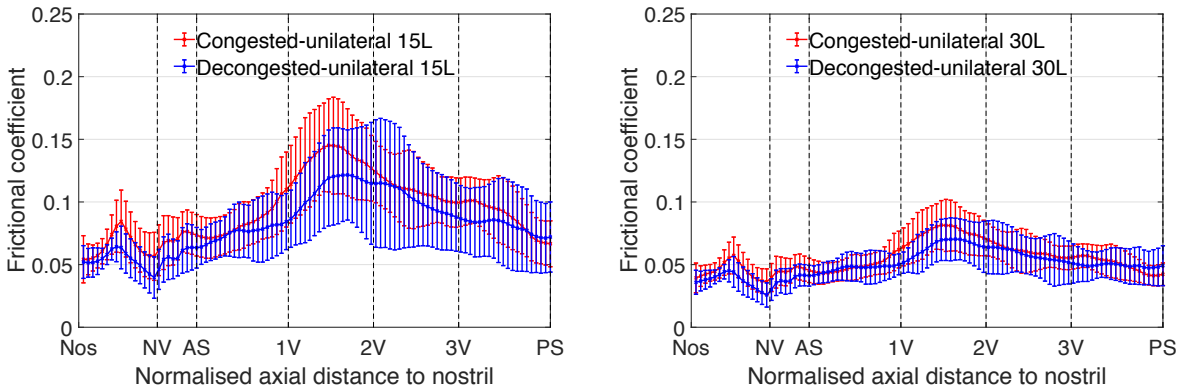


(a) 15 L.min^{-1}. (b) 30 L.min^{-1}.

Figure 3.37: Unilateral total resistance before and after decongestion at two flowrates. Median values and significance test results for comparisons are overlaid.

3.3.4 Friction coefficient and Poiseuille number

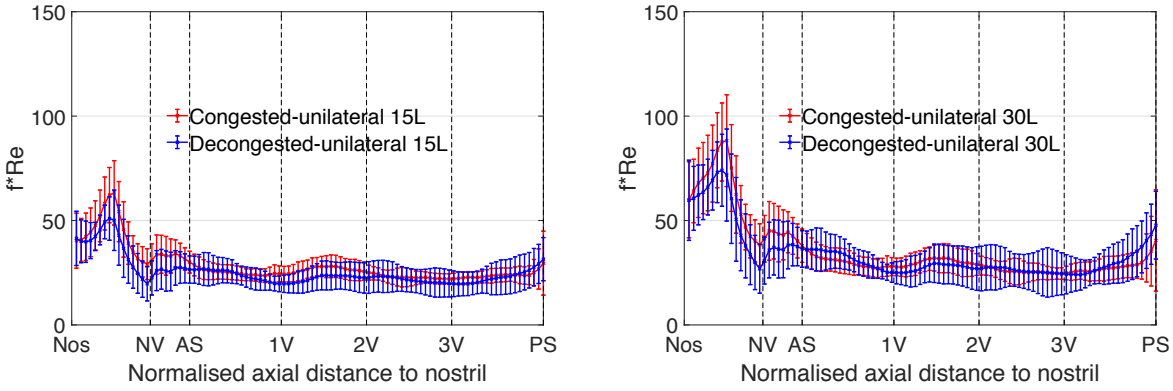
Plots in figure 3.38 show the Fanning drag coefficient values along the cavity centerline from nostril to PS under two different flowrates. It shows that increase the flowrate proportionally will not change the Fanning drag coefficient distribution but could reduce its value. However, it is not the same for Poiseuille number. Double the flowrate can only increase the Poiseuille number slightly, except in the anterior part of the cavity. This is attributed to the disturbance of turbinates of the cavity, which will make the flow constantly developing and never will get a fully developed profile.



(a) 15 L.min^{-1}. (b) 30 L.min^{-1}.

Figure 3.38: Fanning drag coefficient distribution along the cavity centerline from anterior to posterior at two flowrates of congested and decongested cavities.

The decongestion effect seems to have an even smaller effect on both the frictional coefficient and Poiseuille number, as can be seen the small offset between the red and blue lines of each plot.



(a) 15 L.min^{-1}. (b) 30 L.min^{-1}.

Figure 3.39: Poiseuille number distribution across the cavity for both congested and decongested cavities at two flowrates.

Frictional coefficient and Poiseuille number of each unilateral cavity are averaged over the whole cavity and the significance test of these mean values is conducted between congested and decongested cavities, as well as between lower and higher flowrates. The results are shown in figure 3.40. Figure 3.40a shows that at both lower and higher flowrates, the difference of Fanning drag coefficient between congested and decongested cavities are statistically significant, although the difference of its median is not very different. However, for Poiseuille number, the difference are significant both statistically and the change of its value (figure 3.40b). Similarly, the comparison between groups of lower and higher flowrate, shows statistically significant difference on frictional coefficient of both congested and decongested cavities as well as the Poiseuille number of decongested cavities. However, there is an exception of the Poiseuille number of congested cavities (figure 3.40d).

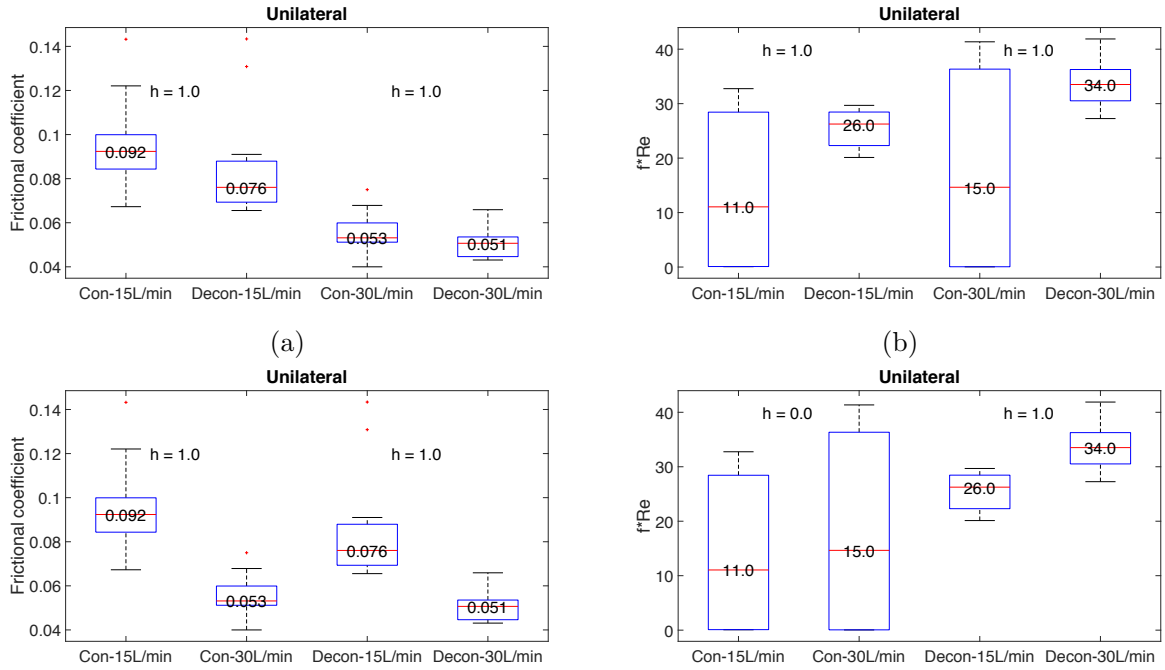


Figure 3.40: Effects of decongestion and of flowrate on the cavity mean value of both Fanning drag coefficient and Poiseuille number. In the top pair figure 3.40a and 3.40b, results are compared between congested and decongested cavities at the same flowrate for Fanning drag coefficient and Poiseuille number separately, while the lower pair figure 3.40c and 3.40d, the results are paired to aid comparison of the flowrate effect for the same state (congested or decongested) on same quantities.

Instead of averaging the Fanning drag coefficient and Poiseuille number over the whole cavity, there are two different subregions are defined by plane Nos and 1V and by plane 1V and PS. Conducting the same analysis as described above, figure 3.41a and 3.41c show that both the geometry change by decongestion and the increased flowrate will reduce the frictional coefficient of the anterior part of the cavity and the difference are statistically significant. However, in the posterior part of the cavity, except the decongestion effect at higher flowrate shows no statistic difference, the others comparison all shows the same conclusion as the anterior cavity.

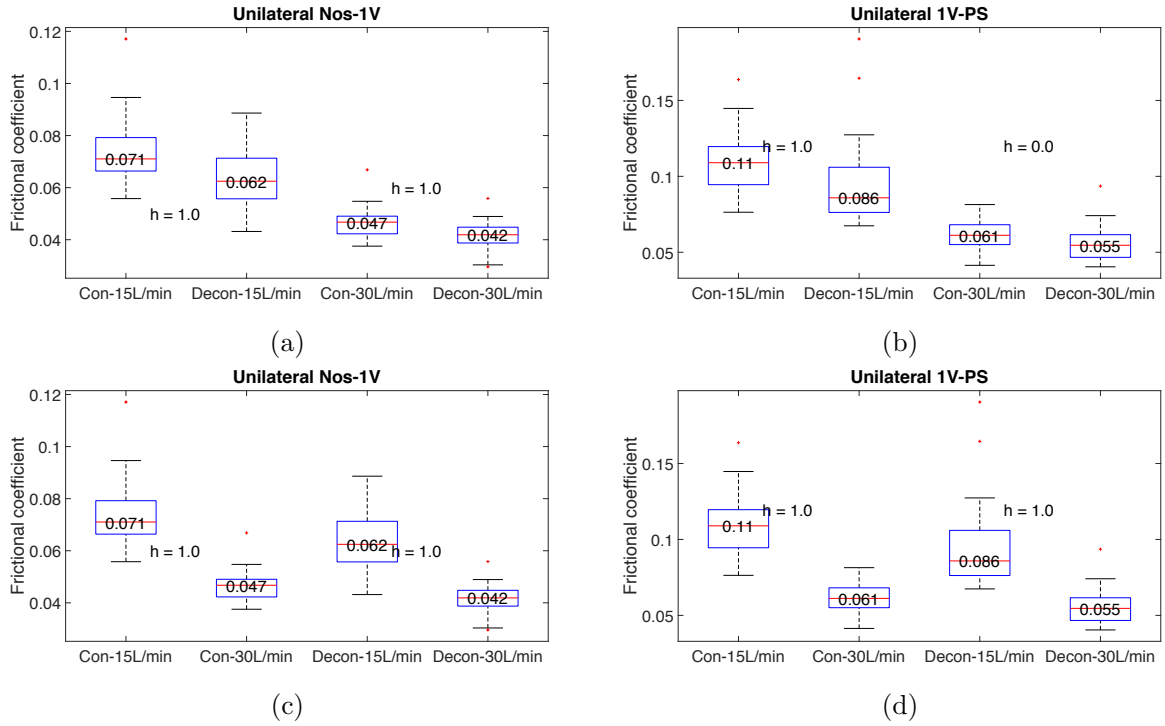


Figure 3.41: This figure computed friction coefficient results arranged to facilitate comparisons of effect size. Top pair (a and b): comparing effect of decongestion on friction coefficient for anterior nose (Nos-1V) and for posterior nose (1V-PS) at the same flowrate. Lower pair (c and d): comparing effect of flowrate on friction coefficient for anterior nose (Nos-1V) and for posterior nose (1V-PS) under the same geometric states (congestion or decongestion). This is a breakdown of the results from figure 3.40.

Results for the Poiseuille number are shown below. Considering first the top pair, although decongestion increases the median Poiseuille number more than twice that for the congested cavities, the difference is nearly but not quite significant at the 5% level in the anterior nose. For the posterior nose, the increase in Poiseuille number associated with decongestion is likewise more than twice and is significant.

Flowrate is found to have much less effect on the Poiseuille number, particularly for the posterior nose, where the median value only increases by about a quarter. This suggests the posterior part of the nose shares some of the characteristic of a fully developed duct flow, where one would expect no change in Poiseuille number with flowrate. There are of course differences in that the posterior nose is not a duct of constant cross-sectional form, but this suggests the flow may be approximated rather crudely as such.

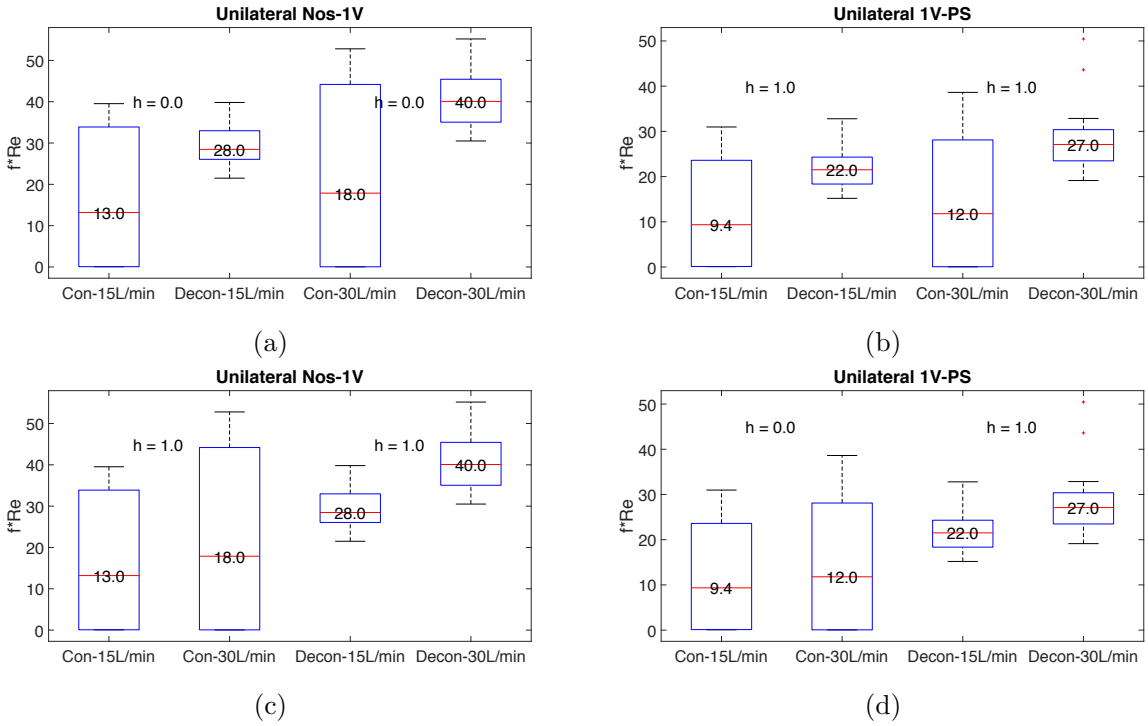
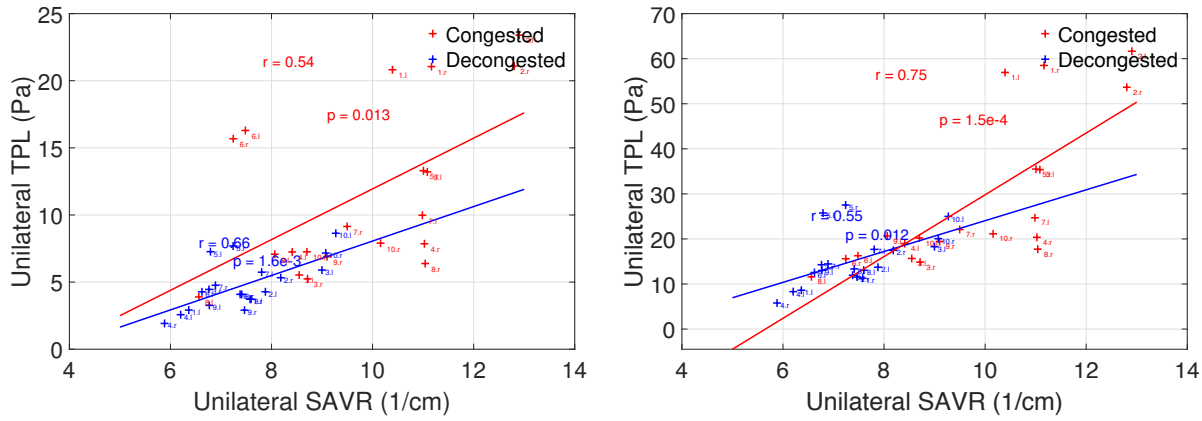


Figure 3.42: Figure 3.42a is the comparison of decongestion effect size n mean Poiseuille number at same flowrate. Unilateral cavity results are partitioned into anterior region (between nostril and 1V) and posterior cavity (between 1V and PS). Figure 3.42c and 3.42d compare the effect of flowrate on Poiseuille number for the same geometry.

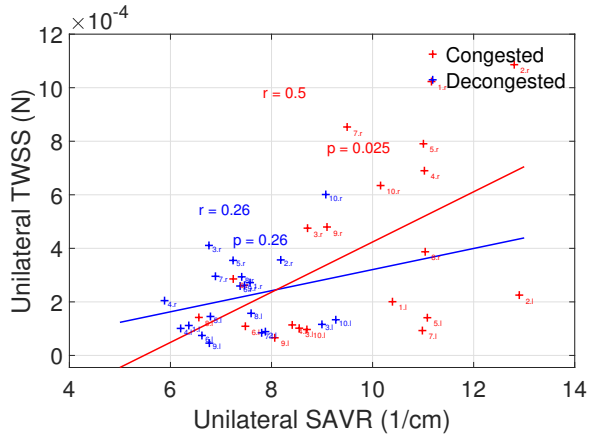
3.3.5 Correlation analysis

The unilateral correlations of anterior minimum CSA with other flow measures (TPL, TWSS) do not show evident correlations ($r < 0.6$) as shown in append ix B.4, same as the bilateral cavities. However, the SAVR shows moderate correlations with total pressure loss, whilst total wall shear stress shows a degree of association but weak correlation. Figure 3.43 shows that under both lower and higher flowrates, the congested cavities generally have stronger correlations than that of the decongested cavities.

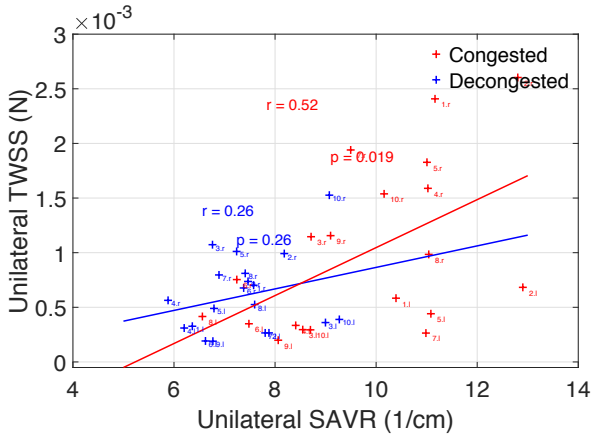


(a) 15 L.min^{-1}

(b) 30 L.min^{-1}



(c) 15 L.min^{-1}



(d) 30 L.min^{-1}

Figure 3.43: Correlations of SAVR to TPL and TWSS. The top pair shows the correlations of SAVR to TPL at both lower and higher flowrates, while the lower pair is the same but for correlation between SAVR and TWSS.

Chapter 4

Heat and water transport in congested and decongested nasal cavities.

For most subjects at rest, the nasal airways process all inspired air, providing a large proportion of the total heat and moisture required to match conditions in the tissues of the lung. Habitual oral breathing bypass the filtration, humidification and heating provided by the nose. It leads to undesirable reduction of physiological function, including increased water loss (42% greater [145]) and increased rates of upper respiratory tract infections [146].

In this chapter, we apply computational modelling to investigate the process of heat and moisture exchange during inhalation. The same 10 individual subjects for which airflow analyses were performed in chapter 3 are again considered, to compare the effects of flowrate and decongestion on the heat and water transport performance. As in chapter 3, detailed patterns are first presented for a single individual geometry before presenting the results for the entire cohort.

A major source of uncertainty in modelling heat and water transport in the nose is the appropriate boundary condition, particularly the spatial extent of the water exchange surface and the capacity of the mucosal surface to supply adequate water. This aspect has been discussed in chapter 2, and it is important to bear in mind that the results presented here are associated

with the boundary condition described in that chapter.

For the cohort analyses, results are presented where possible in terms of the relevant dimensionless parameters as defined in chapter 2, namely the Nusselt number for heat transfer and Sherwood number for mass transfer. In reporting the whole cohort results the bilateral data are presented first before considering the unilateral data.

4.1 Subject specific analysis of heat and water transport within nasal cavity

As for the flow analysis, results are first shown for the subject specific (subject D) geometry and these results are presented in the following order:

1. First, both heat flux and water flux maps on the cavity inner surface are displayed to review the characteristic patterns;
2. Secondly, at the anatomical similar locations within the cavity, the present computational results for this subject are compared with previous experimental work by others;
3. Next, the effect of different inflow conditions, including both the change of flowrate and the change of ambient condition, on the air conditioning performance are considered.

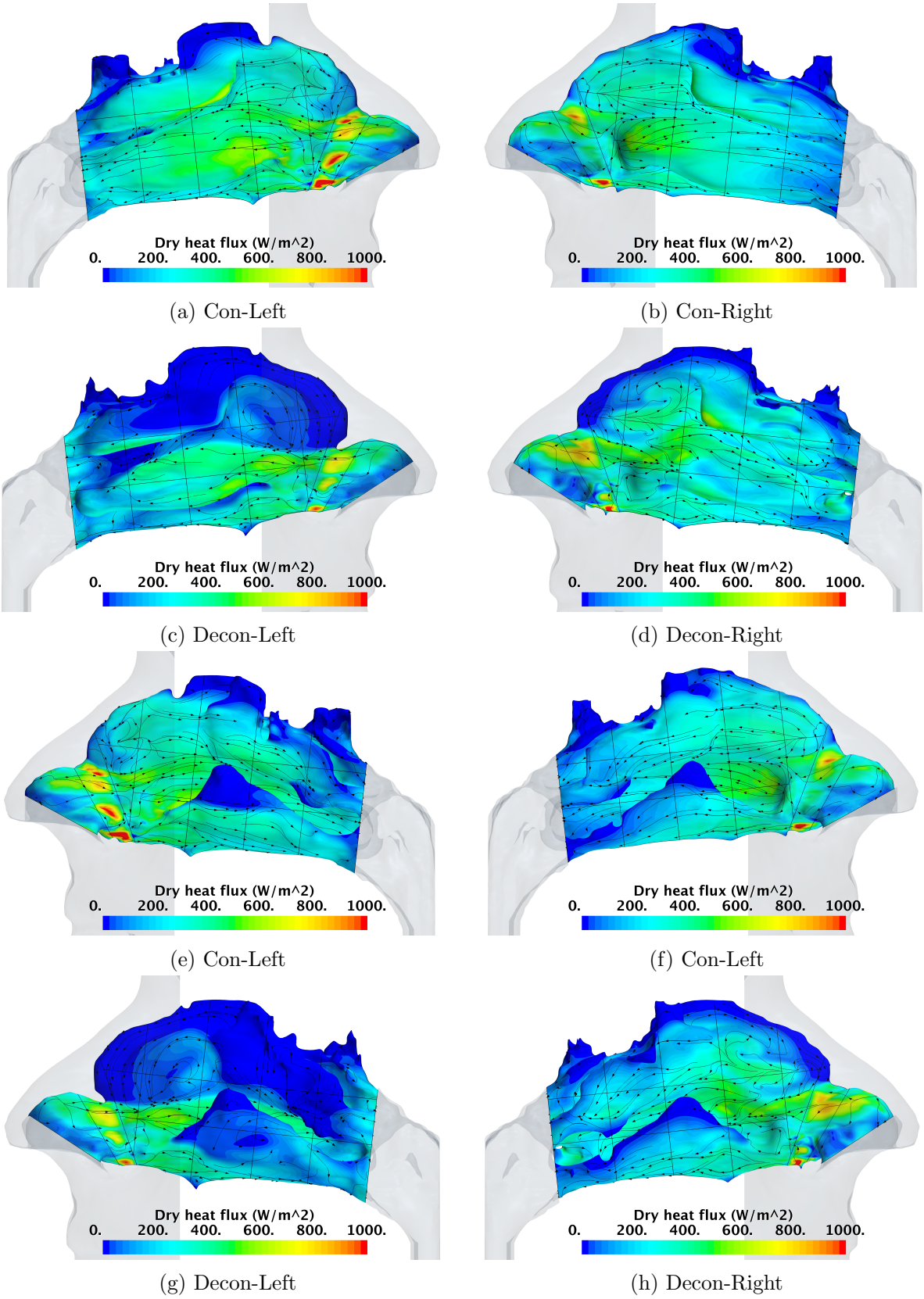
4.1.1 Surface maps of dry heat exchange

Two heat flux exchange processes occur during the conditioning process of inhaled air: warming the air requires heat input firstly to raise the air temperature and secondly to supply the heat required to evaporate water from the mucosal surface. We can consider the heat required purely to increase the air temperature as the dry heat flux. The dry heat flux is driven by the surface temperature gradient at the mucosal surface. The latent heat flux (is an evaporative

heat flux during inspiration and condensative heat flux during expiration) that is associated with water vapor exchange.

Maps of the dry heat flux on the cavity, showing the expected turbinates are displayed and compared before and after decongestion in figure 4.1. The cavity exposed by removal of the septum is shown by views a, b, c, d; whilst views e to h map the heat transfer from the side of the maxillary sinus (which is excluded from the simulation). Comparing with the flow computations, in particular with the wall shear stress predictions of figures 3.6 and 3.7, there is clearly a strong association between regions of high wall shear stress and high heat transfer, particularly in the anterior nose nasal valve and head of the turbinates. This applies whether or not the cavity is under congested and decongested conditions.

The superimposed surface streamlines on the heat flux maps show the recirculation region in the anterior superior part of the cavity, most evident on the left side. Although decongestion lowers mean flow speed in the nose, it also affects the left/right balance of flow split. For this subject, the expansion of the right cavity is largely offset by the greatly enhanced flow there, so the net effect of decongestion on right cavity dry heat flux is negligible; by contrast the effects on the left cavity of volume expansion are magnified by the reduction in flow due to rebalancing of the left/right flow split (figure 4.1c).



(a) Con-Left (b) Con-Right

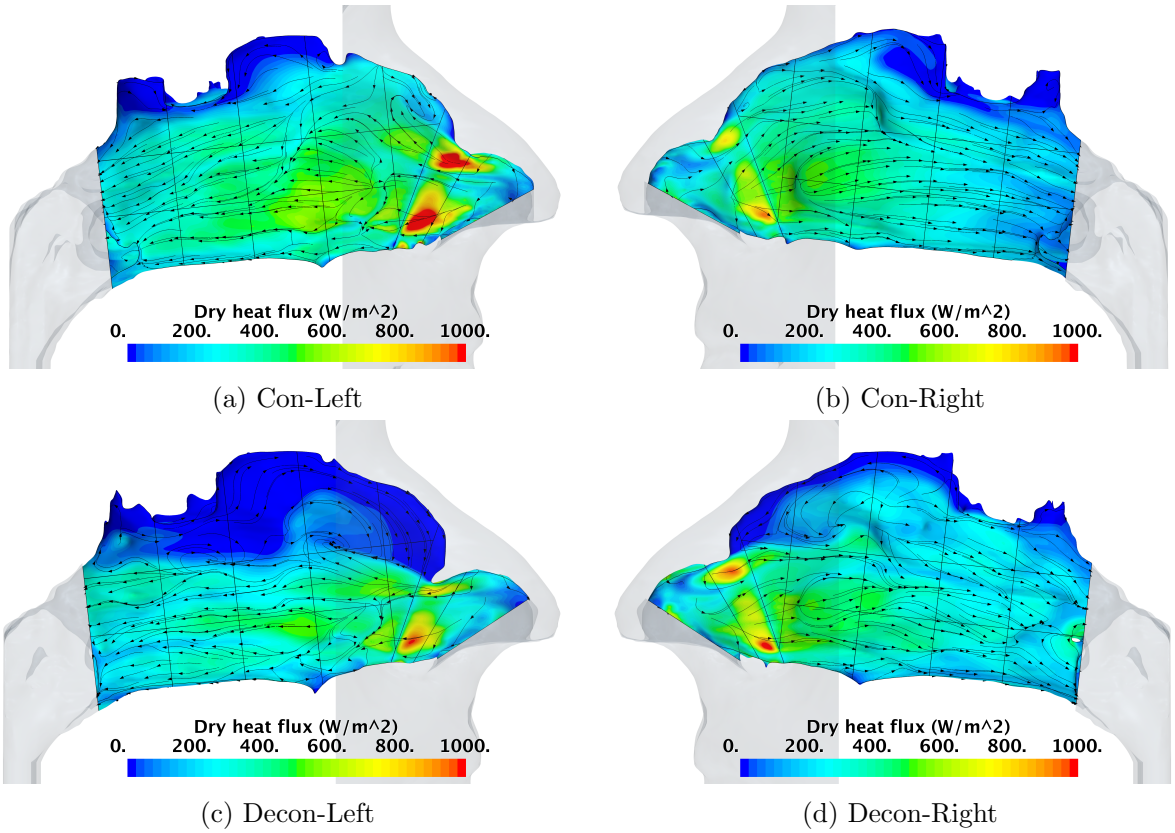
(c) Decon-Left (d) Decon-Right

(e) Con-Left (f) Con-Left

(g) Decon-Left (h) Decon-Right

Figure 4.1: Comparison of dry heat flux for left and right noses of subject D, with superimposed surface streamlines indicating the near wall flow direction. Figure 4.1a-4.1d are organized so that left and right column views correspond respectively to the left and right cavities; the top pair compare left and right for the congested cavities and the lower pair are for the decongested cavities; in these four views (a to d), the septum has been removed to expose the turbinates. Similarly, figure 4.1e-4.1h also show the dry heat flux on the cavity surface, but viewed from the opposite (maxillary sinus side, but with the sinus removed).

Figure 4.2 shows similar distributions as describe above (figure 4.1), but now viewing the septal surfaces on each side. As expected, the higher dry heat flux exchange also occurs around the nasal valve. In general, we can see that although the decongestion effect does not change the region around nasal valve as the greatest heat exchange surface per unit area, there is a marked reduction due to decongestion on the left and little change on the right (due to the flow rebalancing as mentioned). In addition, there is marked similarity with the corresponding WSS (figure 3.7) maps as well.



(a) Con-Left (b) Con-Right

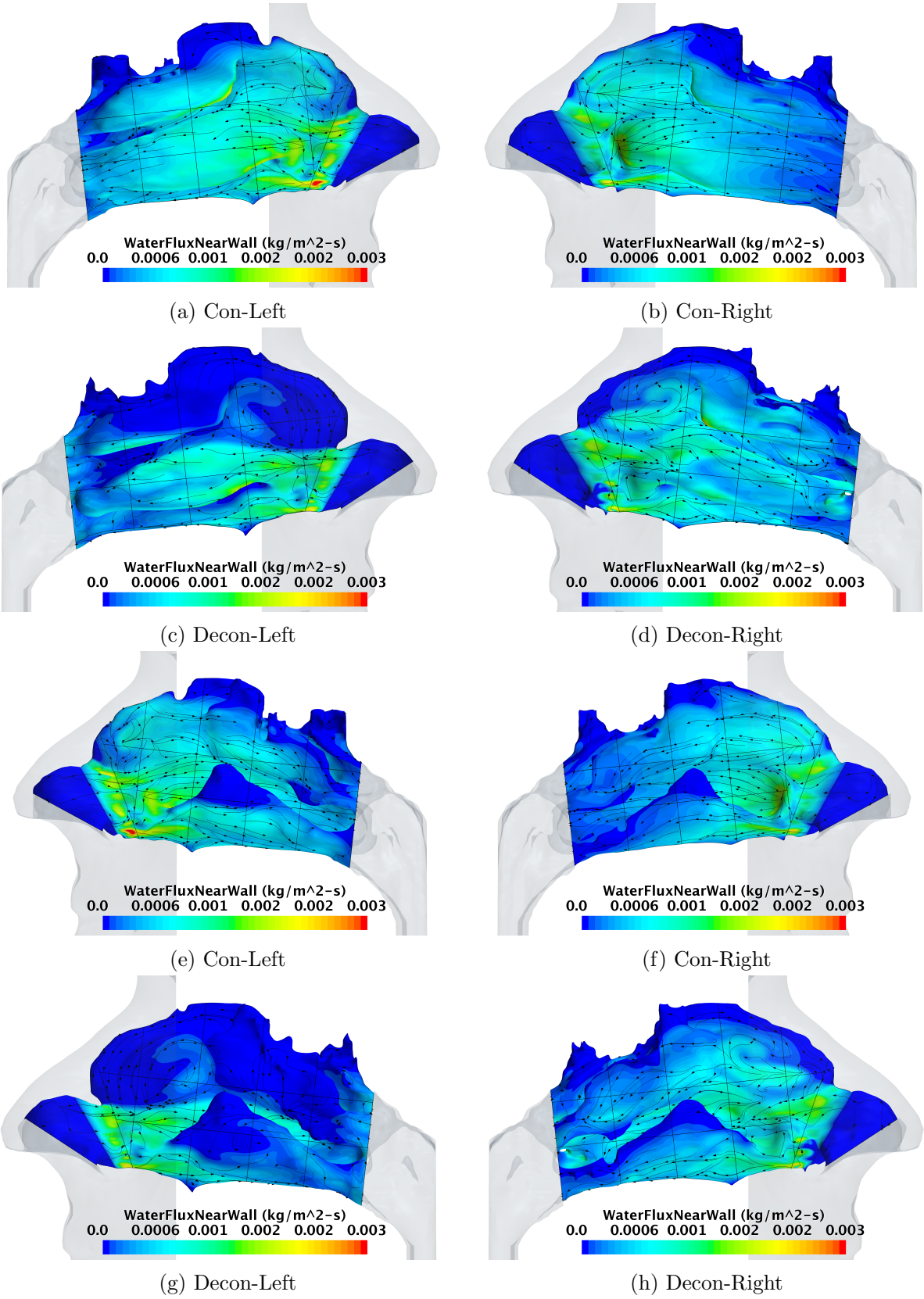
(c) Decon-Left (d) Decon-Right

Figure 4.2: This figure shows the dry heat flux map on the cavity septum surface between congested and decongested cavities. Again, sub-figure 4.2a on the left side represents the congested left cavity surface with the view of septum. Similarly, the top right corner (sub-figure 4.2b) represents the congested right cavity septum view. Furthermore, sub-figures 4.2c and 4.2d show the same quantity with the same view but for decongested cavities.

4.1.2 Surface maps of water exchange

The water flux on the surface is governed by equation 2.18 and 2.19, from which it is evident that the surface water flux depends not only on the gradient of water concentration in the

flow near the surface but also on the surface temperature of the cavity and of the air. This is because the warmer the air, the greater is its water carrying capacity. Referring back to the water exchange boundary condition discussed in chapter 2 (figure2.8d), there is no water flux in the nostrils. The water flux map on the cavity surface shown in figure 4.3 and 4.4 indicate that the regions of highest burden of water exchange are around the nasal valve, but are also distributed over the surface of the turbinates, and again with high values at the anterior and inferior portions of the turbinates, corresponding to regions of elevated shear stress. As noted above, for the left cavity decongestion greatly reduces flow speeds (figure 3.4), lowering water transport, however, the reduction in flow to the superior part of the left cavity renders its ineffective for this task. The rebalancing of flow for the right cavity compensates for volume changes, and so the effects are reduced on that side.



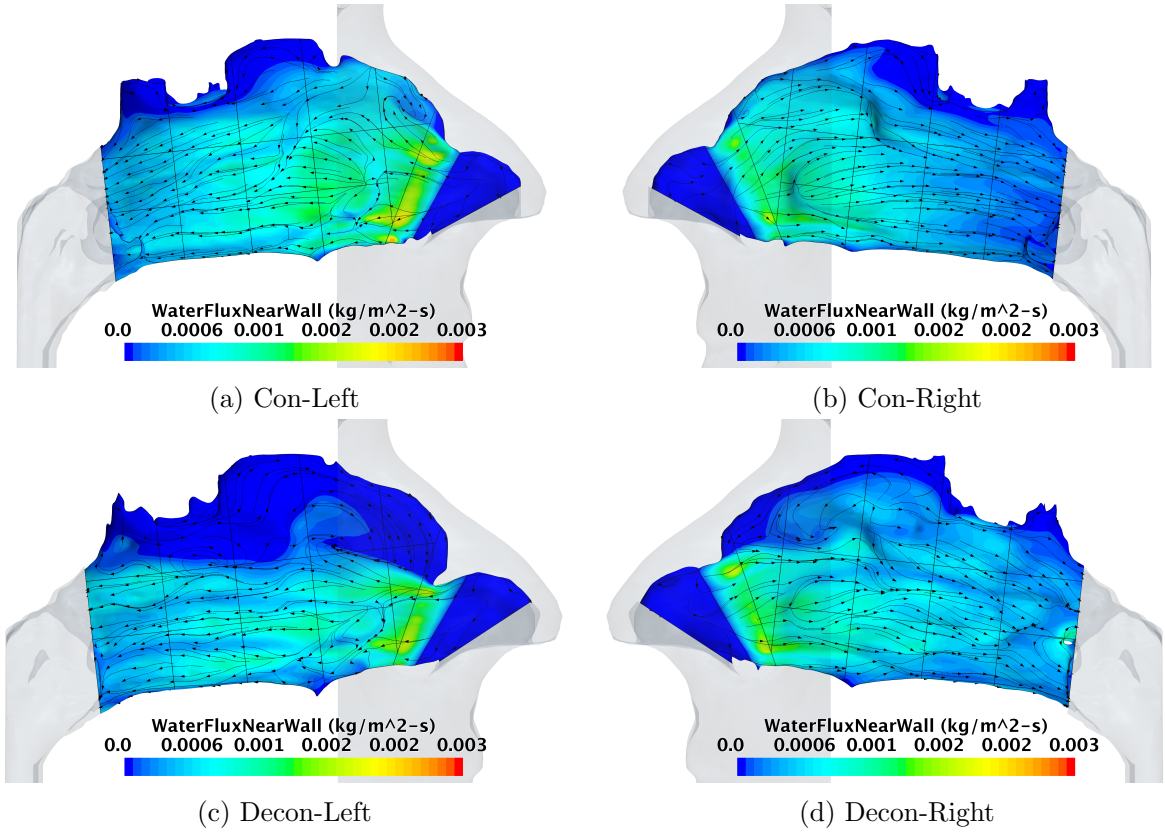
(a) Con-Left (b) Con-Right

(c) Decon-Left (d) Decon-Right

(e) Con-Left (f) Con-Right

(g) Decon-Left (h) Decon-Right

Figure 4.3: Comparison of surface water flux values between congested and decongested cavities of subject D. Sub-figures a and c compare the left cavity with the septum removed to expose the turbinates. Correspondingly, sub-figures b and d compare congested and decongested right cavities. Sub-figures e to h display the surface water flux on the cavity turbinate, but with the view from the outside of the turbinates.



(a) Con-Left (b) Con-Right

(c) Decon-Left (d) Decon-Right

Figure 4.4: The surface water flux distribution on the cavity septum are shown here. The patterns of water flux seen on the turbinated wall in the previous views are broadly similar to those on the septal surfaces.

4.1.3 Comparison with previous studies.

Both Ingelstedt et al. [147] and Rouadi et al. [77] measured the air temperature and relative humidity within nasal cavity during inspiration that shows 31-34°C and 90-95% separately. More recently, Keck et al. measured the temperature and humidity profile at multiple positions within nasal cavity at room temperature 25°C, 35% relative humidity at quiet breathing [1, 69, 70].

We refer to the three positions used for measurements of Keck et al [70] namely the nasal valve (1.5 cm), anterior turbinate (2.5 cm) and nasopharynx (6.0 cm) separately. At the anatomically similar locations for the subject D congested simulation, the temperature and relative humidity are listed in table 4.1 and compared with the data of Keck et al.. Note that the experimental

values from Keck et al. are measured by a single probe point at the specific location which can not be precisely defined; in order to effect a reasonable comparison, the values computed from the present simulation results are taken from the anatomically similar locations but using a cross-sectional plane averaged value rather than from a single point.

Subject D congested	Nasal valve	Anterior turbinate	Nasopharynx
Temperature(°C)	29	31	32
Relative humidity(%)	60	75	90
Keck et al. experiment	Nasal valve	Anterior turbinate	Nasopharynx
Temperature(°C)	28.9±2.3	30.3±1.6	32.6±1.5
Relative humidity(%)	69.0±6.5	78.7±7.2	90.3±5.3

Table 4.1: Simulation results at anatomic similar locations as Keck et al. [1].

Table 4.1 shows that the present simulation results are consistent with those of Keck et al. measurements. In the absence of measurements for the precise geometry of the selected subject, this provides at least a measure of confidence in the heat and water modelling proposed for this study.

4.1.4 Effect of different flowrates

After validating the reliability of the simulation methodology, in this section we study the effect on heat and water exchange for different flowrates at the same ambient condition (same temperature and relative humidity). The effect of flowrates on temperature, moisture content, heat film and mass film coefficients for the bilateral cavity are shown in figure 4.5. Four flowrates are considered, from 15 L.min^{-1} to 30 L.min^{-1} with a constant incremental of 5 L.min^{-1}. The first sub figure (a) shows how the cross-sectionally averaged mean temperature plotted along the cavity centerline increases from anterior to posterior. The effect of increasing flowrates is to reduce the mean temperature, such that flow reaching the posterior septum (plane PS) reduces

in temperature from nearly 32°C to 30.3°C (figure 4.5a). Similar trends can also be found in the plots of moisture content level (figure 4.5b).

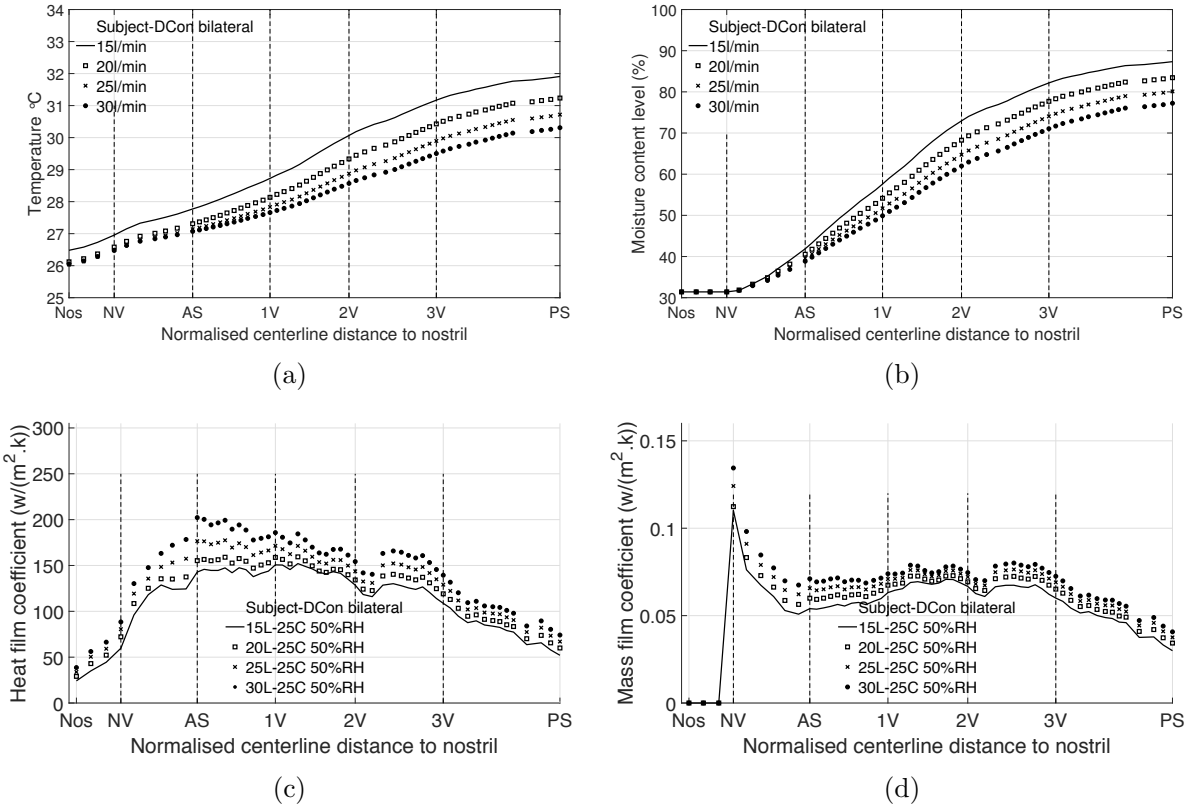


Figure 4.5: Effect of flowrate on the distribution of temperature, water content level, heat film coefficient and mass film coefficient, plotted along the cavity centerline of subject D congested cavity.

The reduction in temperature rise of air passing through the nasal cavity shows that the efficiency of exchange cannot match the increased need for heating and humidifying that due to the increase of volume flow. Figures 4.5c and 4.5d, show that increasing the flowrate significantly increases the film coefficients, signifying an increase in efficiency of the exchange process. The increased heat and mass film coefficients induce a higher gradient between the core flow and the cavity surface that will lead to the higher demand of heat and water exchange during the nasal conditioning process. Consequently, the total amount of heat and water exchange does increase markedly with the increase of flowrate. It is the case though, however this is not enough to fully cope with the added volume flow.

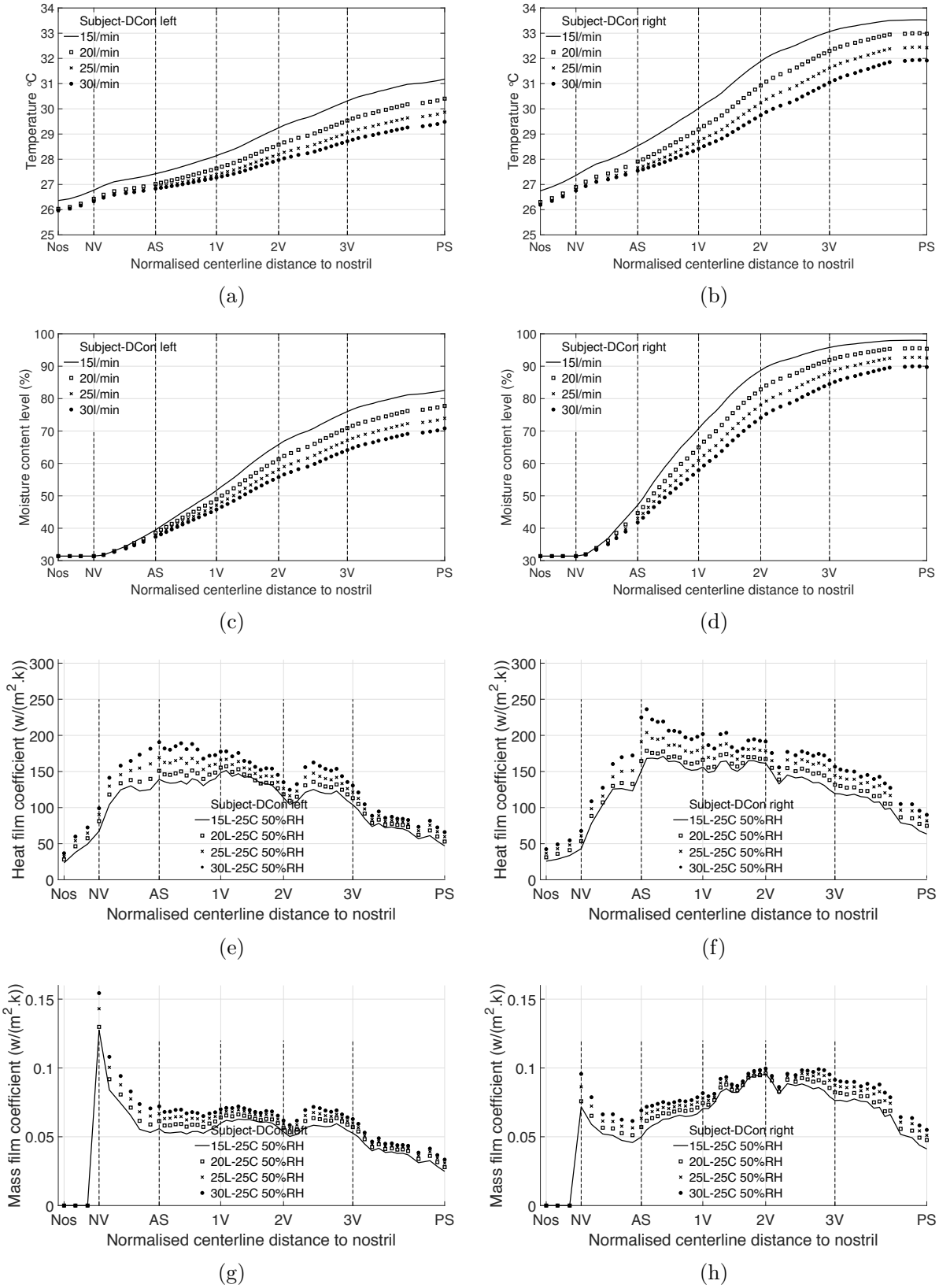


Figure 4.6: This figure shows the distributions for the same quantities as figure 4.5, but plotted in the left and right cavity individually of congested cavity of subject D. Figures on the left are representing the left cavity and figures on the right side represent those for the right cavity.

The distribution of the same heat transfer quantities considered above, but now within the left and right cavities individually are shown in figure 4.6. Overall the distributions are similar to those that for the bilateral cavity. However, the bilateral data obscures the differences in flowrate and geometry in the separate cavities, so it is of interest to study these individually and to gauge the differences in performance of the two sides, figure 4.6a and 4.6b. Note particularly that the flowrate legend for these unilateral cavity plots indicate the bilateral cavity mass flowrate, whereas the actual flowrate through each cavity must be deduced from the left/right flow split ratio given in table 3.1, and are not to be taken as half of the bilateral flowrate.

It can be seen that, for this particular case (congested subject D cavity), there is a marked difference in performance, with the right cavity achieving much higher temperature as well as moisture content level at plane PS for a given total mass flowrate than that for the left cavity. However it is also the case that the right cavity processes less air than that processed by the left cavity (31% VS 69%), refer to figure 3.2a also.

Comparison of the unilateral intranasal heat and mass film coefficient distribution along the cavity centerline, figure 4.6e-4.6h, indicates higher performance for the right cavity, particularly for water in the posterior part. The higher airflow in the left cavity however manifests in higher mass film coefficient in the anterior part. These trends agree with the slightly higher Fanning drag coefficient found for the right cavity compared with that for the left (figure 3.12a and figure 3.12b) which is particularly marked at the lower flowrate, and the same difference in levels can be seen on the WSS surface maps for the congested state.

4.1.5 Effect of different ambient conditions

In addition to considering the effects of increasing flowrate, it is of interest to examine the effect of changing flow conditions (temperature and relative humidity) under the same flowrate. Results are shown in figure 4.7. Following the same convention, the bilateral cavity distribution of temperature, moisture content level and film coefficients will be described first. As the

relative humidity is not the true reflection of the air humidity, the conversion from RH to absolute humidity is listed in table 4.2:

Temperature (°C)	Relative humidity (%)	Absolute humidity (g.m^{-3})
25	50	11.5
25	35	8.1
15	50	6.4
5	10	0.68
Alveolar: Temperature (°C)	Relative humidify (%)	Absolute humidity (g.m^{-3})
37	100	44

Table 4.2: Convertin of relative humidity to absolute humidity.

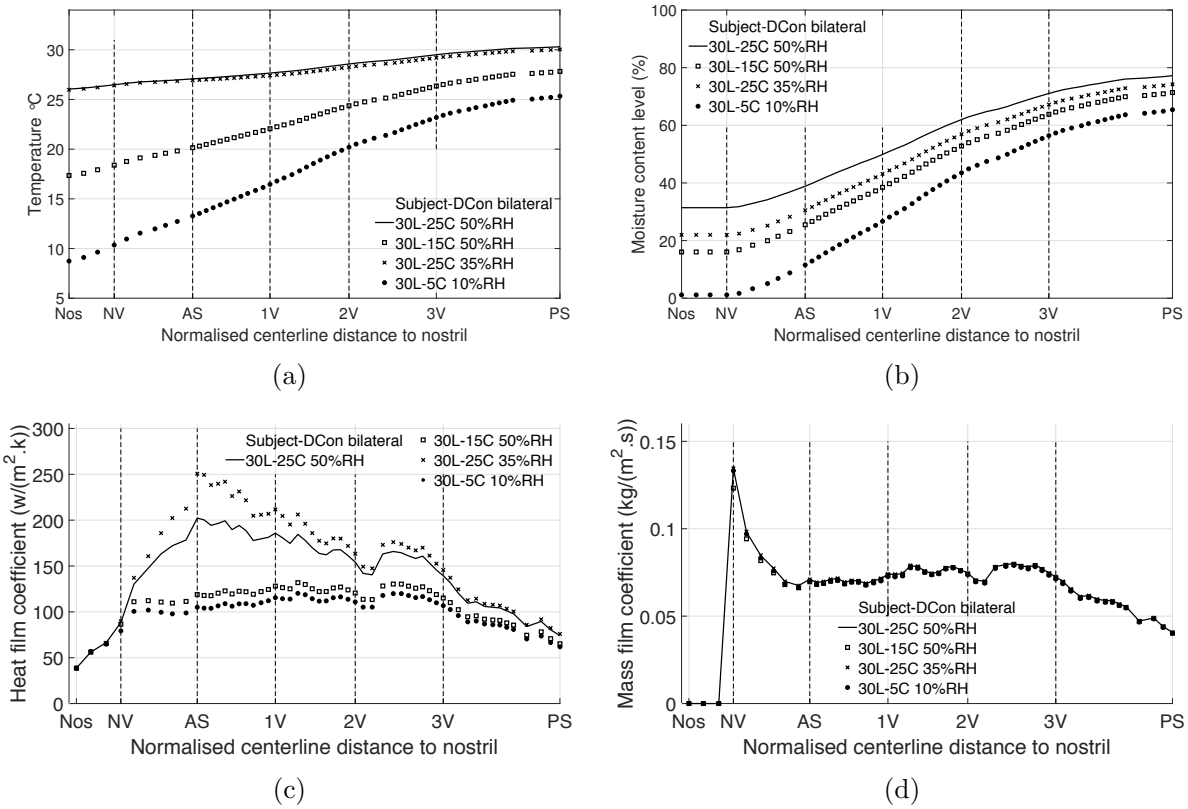


Figure 4.7: This figure shows the intranasal distributions of multiple measurements of the bilateral subject D cavity. Following the reading orders are: temperature, moisture content level, heat film coefficient and mass film coefficient respectively.

Unsurprisingly, the results indicate that the nose achieves higher values for water content with reduction in the demand posed by the external environment, with cold, dry air requiring greatest net added water. Overall, despite the broad range of ambient conditions, the nasal cavity conditions the inhaled air to a remarkable degree by the time it reaches plane PS. Interestingly, while the heat film coefficient shows considerably large variations (as was observed previously for varying flowrate), in this comparison where flowrate is constant, the mass film coefficient barely changes for the different ambient conditions.

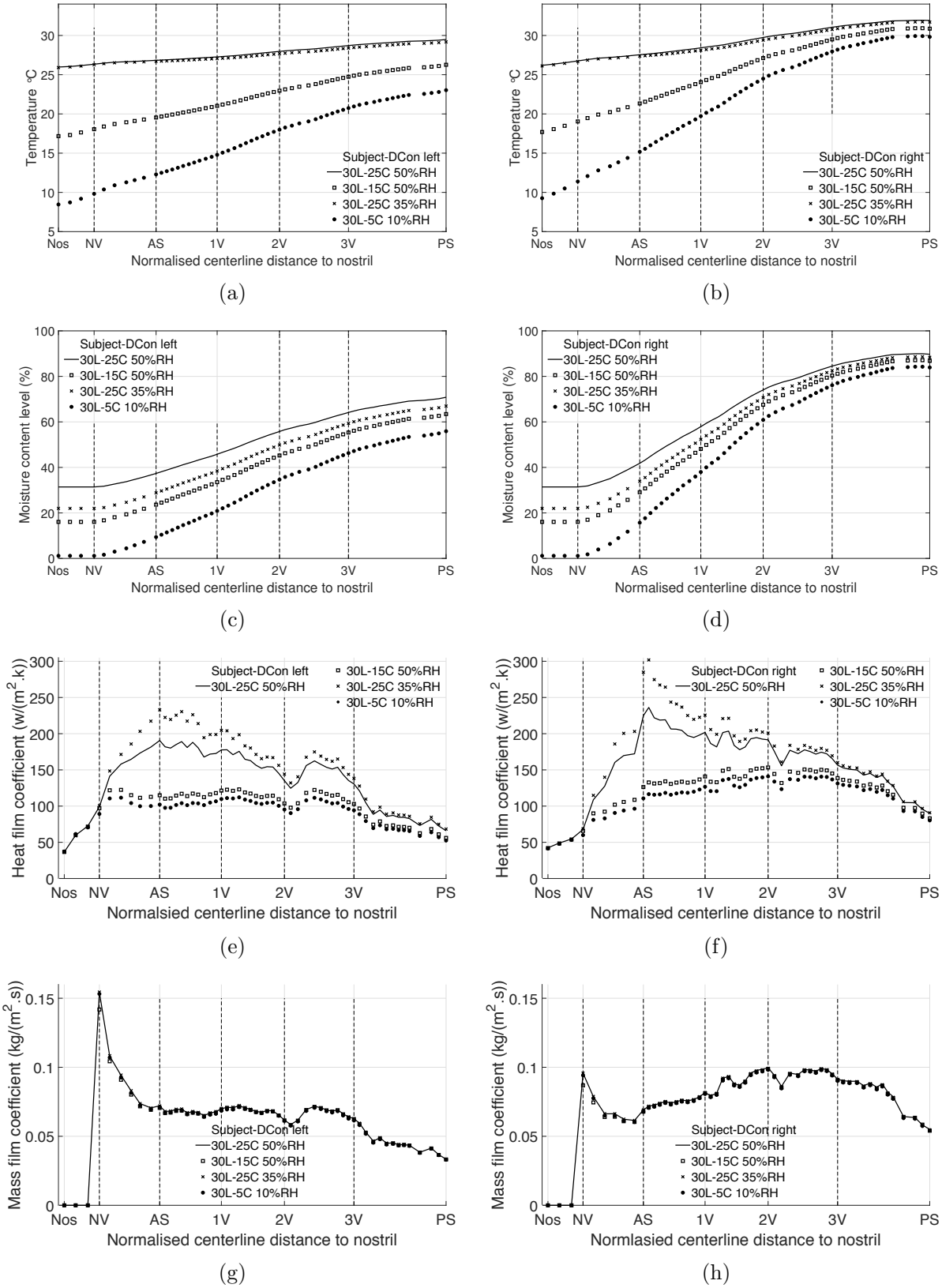


Figure 4.8: Unilateral temperature, moisture content level, heat and mass film coefficient distribution along the cavity centerline. Figures on the left column (a,c,e,g) represent the left cavity while figures on the right column (b,d,f,h) represent the right cavity.

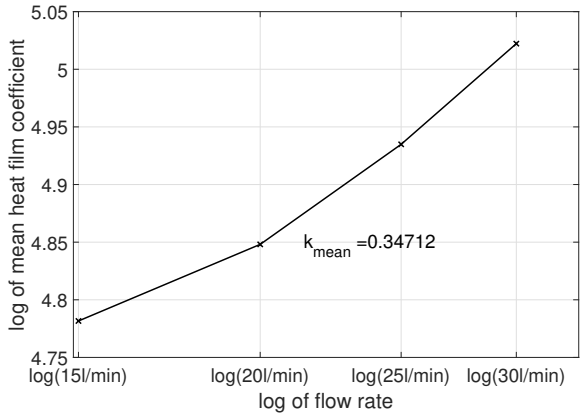
Considering the results in more detail, most of the features have seen at varying flowrates are reappearing. The temperature of the inspired air as it reaches the posterior septum for the left cavity (figure 4.8a) is again markedly lower at all ambient conditions than that for the right cavities (figure 4.8b). This is expected given that carrying double the flowrate effectively doubles the exchange requirements. Now for varying ambient conditions, we observe that the difference in performance is most marked for the conditions that most heat and water demanding, i.e., cold dry air (5°C, 10% RH).

Similar to the results for varying flowrates, it appears that both the heat film coefficient and the mass film coefficient in the posterior part of the cavity is slightly higher for the right side (figure 4.8f) than that for the left side (figure 4.8e). Again, it is worth comparing with the flow results, where we can observe the slightly higher Fanning drag coefficient that was found for the right cavity compared with that for the left, figure 3.12b and figure 3.12a, also compare with the WSS surface maps for the congested state.

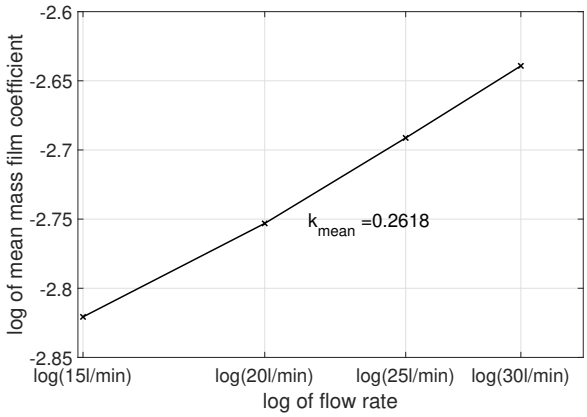
Likewise for the anterior nose for this subject, especially between nasal valve and anterior septum, WSS, Fanning factor and both heat and mass film coefficients all are somewhat larger for the high flow side, i.e., values of left cavity higher than the right cavity.

In summary, these results for the unilateral cavities reveal significant differences that correspond with the differences in flowrate and passage width of the left and right cavities. Note particularly the difference in the anterior versus posterior mass film coefficient distributions between the left and right cavities. The mass transfer may be regarded as more important than the heat transfer because the latent heat of water evaporation (or condensation) has strong effect on the nasal cavity membrane surface.

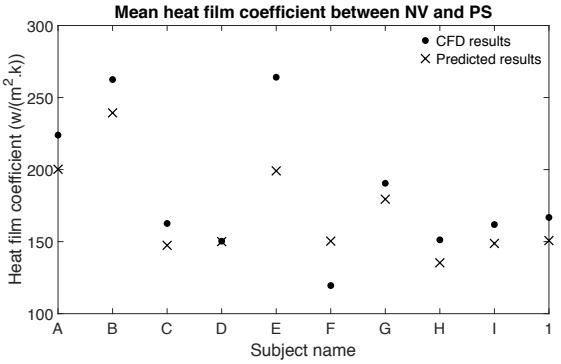
4.1.6 How similarly do results scale with flowrate for other subjects?



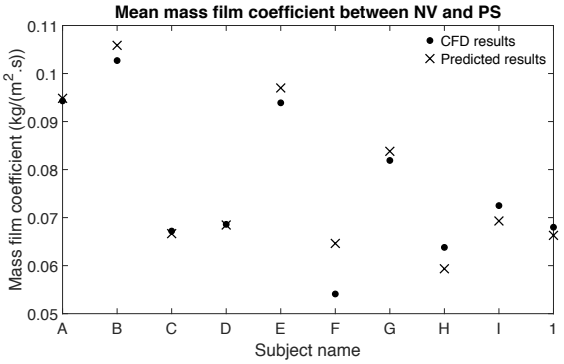
(a) Bilateral log mean heat film coefficient VS log flow rate



(b) Bilateral log mean mass film coefficient VS log flow rate



(c)



(d)

Figure 4.9: Figure a shows the log of flowrate versus log of mean heat film coefficient of the bilateral cavity for subject D, whilst figure b shows the same but for mass film coefficient. Figure c and d apply the mean gradient calculated from the curves shown in figures a and b to predict the corresponding values for the other subject geometries.

Before considering the cohort results in detail, it is of interest to compare the effect of increasing the flowrate on heat and water exchange for the cohort, using results from subject D as a scaling factor. First by plotting the log relationship between flowrate and film coefficients, figure 4.9a and figure 4.9b, a power law exponent may be deduced, with values as shown on the plots. Then the scaling deduced from subject D was applied to the results for each of the cohort (in the congested state) at the lower flowrate to predict the corresponding value at higher (double) flowrate. Figure 4.9 shows the predicated results of other subjects by using this log mean gradient overall predictions are quite good, with the mean of 170 and standard deviation of

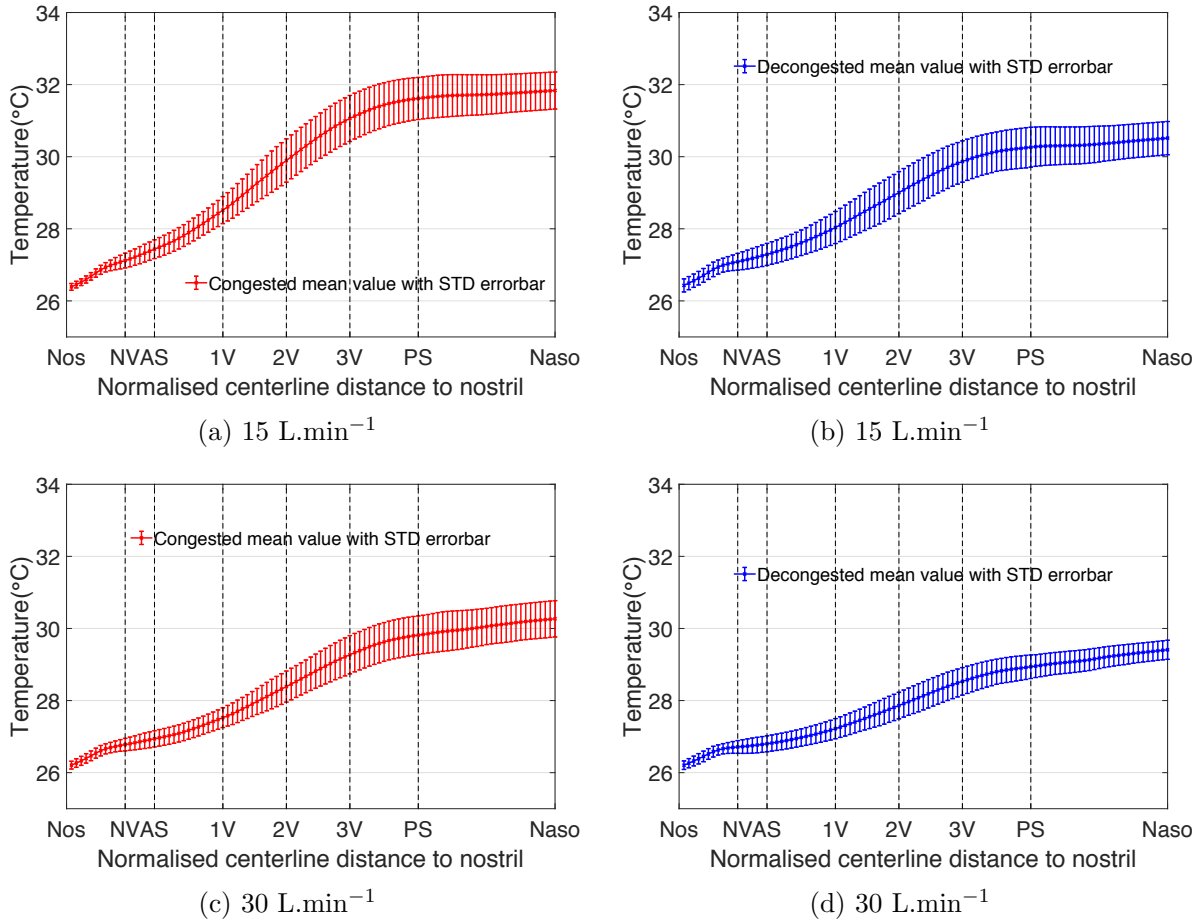
33 for heat film coefficient and mean of 0.078 and standard deviation of 0.016 for mass film coefficient, particularly for the mass film coefficient.

4.2 Bilateral heat and water analysis

4.2.1 Temperature and moisture

In this section we compare the results for the whole cohort, beginning with the temperature distribution along the cavity centerline from nostril to nasopharynx. The average temperature profile, plotted along the centreline from anterior to posterior and the limits for one standard deviation are shown in figure 4.10. Reading from left to right, the upper pair shows the effect of decongestion for lower flowrate, whilst the lower pair performs the same comparison at the higher flowrate. The results show the mean temperature at nasopharynx for the congested cavities to be roughly 1°C higher than that for the decongested noses with the specified external temperature and humidity. Both congested and decongested noses show a higher rate of temperature increase in the anterior cavity (up to plane 2V), tailing off slightly at 3V and more rapidly further towards the nasopharynx.

Between the region of plane PS and the plane Naso, the temperature increase is minor, showing reduced efficiency of heating in the posterior part (after plane PS) of the cavity. Similar trends are also observed for the higher flowrate. However, the driving temperature difference is also reduced, so that a fairer measure of effectiveness would be the heat transfer coefficient, to be discussed later. Naturally, the higher flowrate leads to slightly lower conditioned temperature of both congested and decongested cavities at the nasopharynx, showing that the increase in heat flux is unable to compensate for the increase in volumetric flow.

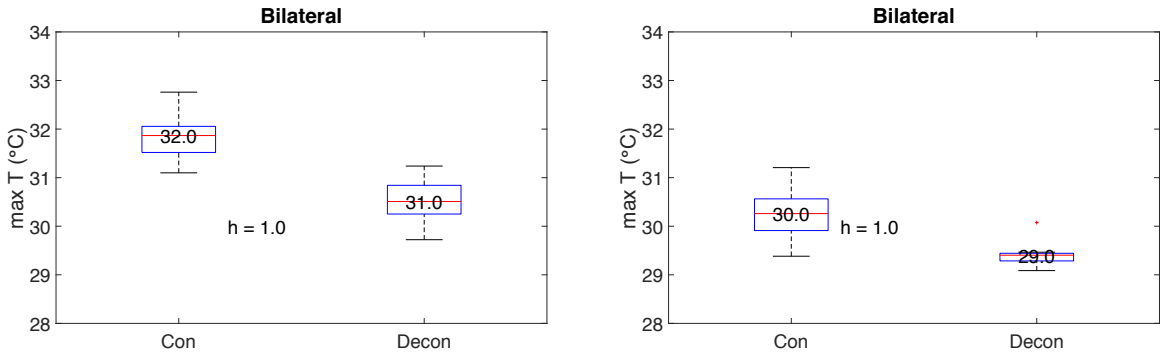


(a) 15 L.min^{-1} (b) 15 L.min^{-1}

(c) 30 L.min^{-1} (d) 30 L.min^{-1}

Figure 4.10: Mean temperature and one standard deviation bilateral temperature distribution for all 10 subjects from anterior to posterior of the cavity. Left are for subjects in congested state and right for decongested conditions. Upper pair are for the lower flowrate and lower pair for higher flowrate. For reference, inhaled air is at 25°C and 50% relative humidity.

Significance testing applied to the hypothesis that decongestion does not alter the temperature at the nasopharynx shows rejection to very high level of certainty, (figure 4.11), whether under lower or higher flowrates. Thus although the decrease of median value is only of an order of 1°C, decongestion significantly alters nasal heat transfer and thus the conditioning performance.



(a) 15 L.min^{-1} (b) 30 L.min^{-1}

Figure 4.11: This figure compares the temperature at the nasopharynx plane between congested and decongested cavities. Appling the Wilcoxon singed-rank test shows the significant changes due to decongestion. Figure on the left is for a flowrate of 15 L.min^{-1} and on the right for a higher flowrate at 30 L.min^{-1}.

Table 4.3 calculates the ratio between increased inflow temperature at the nasopharynx plane and the difference between inflow and alveolar temperature (37 °C) for both lower and higher flowrates. The results in the table can be used to indicate how much the air can be conditioned when the air reaches the nasopharynx proportionally to the alveoli condition. It shows that on average the decongestion can affect the air conditioning efficiency of the cavity more than 11% at lower flowrate and slightly lower (7%) for higher flowrate. This is might due to the higher temperature gradient at high flowrate will enforce the conditioning process which makes the difference between congested cavity and decongested cavity less distinguishable.

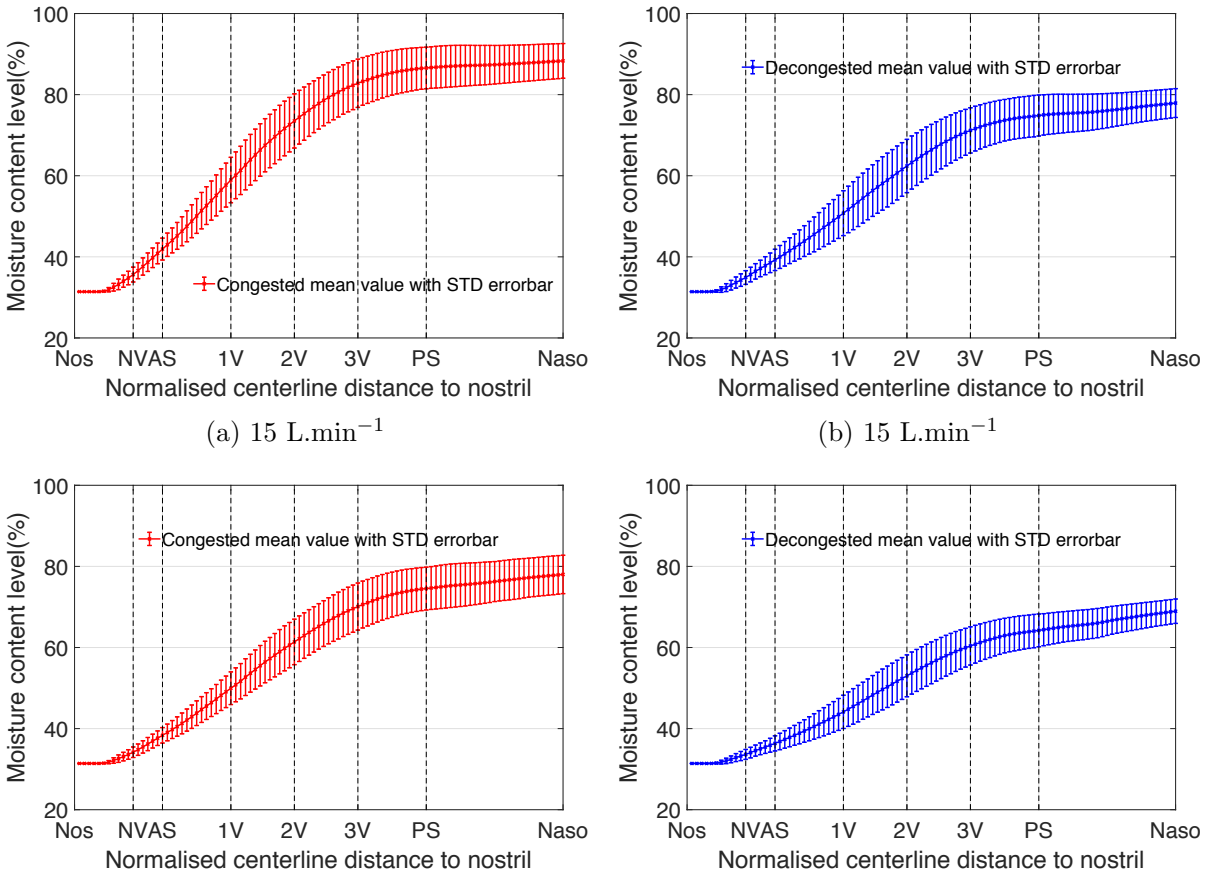
Flowrate (L.min^{-1})	Congested (%)	Decongested (%)
15	57	46
30	44	37

Table 4.3: This table lists the ratio between inflow temperature at the nasopharynx plane of the cavity over the difference between inflow temperature and alveoli temperature.

Figure 4.12 shows the moisture content for congested and decongested noses separately. On average the congested cavities humidify the inspired air 10% more than that achieved by the decongested noses. In addition, similar to the heating profile when the air flow through the

cavity, over 90% of the humidifying process will be finished within the anterior 60% of the cavity.

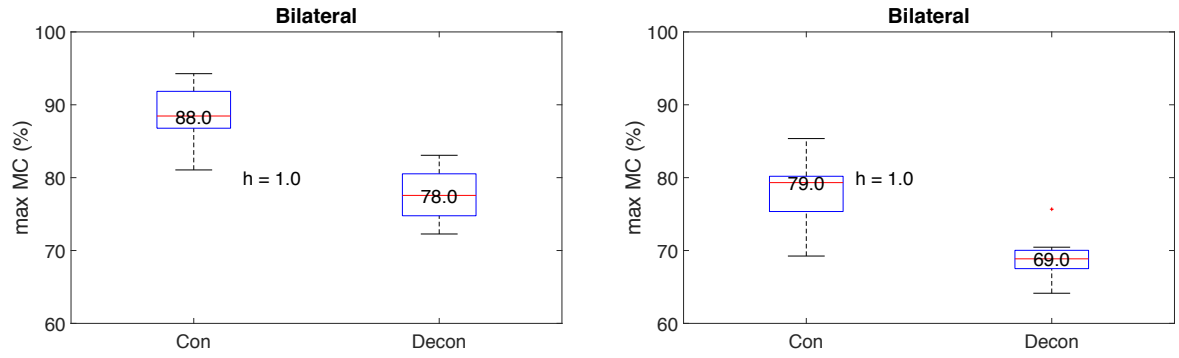
Comparing the same geometry under different flowrates, increasing the flowrate also drops the moisture content level at the nasopharynx plane. Decongestion is found to significantly reduce the nasal cavity's capability to perform humidification of air reaching the nasopharynx for both lower and higher flowrates, as shown in figure 4.13.



(a) 15 L.min^{-1} (b) 15 L.min^{-1}

(c) 30 L.min^{-1} (d) 30 L.min^{-1}

Figure 4.12: Mean moisture content level of all the subjects distribution from anterior to posterior part of the cavity. Figure a to b are comparing the decongestion effect of flowrate at 15 L.min^{-1}, while figure c to d are the same but with the flowrate doubled.



(a) 15 L.min^{-1} (b) 30 L.min^{-1}

Figure 4.13: Nasopharynx plane moisture content level between congested and decongested cavities are tested by Wilcoxon singed-rank test at two flowrates. The results for both flowrates show that there is significant decrease statistically of moisture content level at nasopharynx plane after decongestion.

In summary, for all the healthy subjects considered here, either congested or decongested, on average, the anterior section of the cavities show a high conditioning efficiency for both heating and moistening. Moreover, the decongestion effect will reduce the nasal cavity conditioning efficiency about 10% and has a statistic significant effect.

4.2.2 Heat and moisture transfer coefficients analysis

As shown above, both the temperature and moisture content level are nearly unchanged after plane PS, thus in this section, we only conduct the non-dimensional parameter until plane PS. Firstly, the heat film coefficient as well as its non-dimensional version are calculated and discussed. Secondly, the mass film coefficient and Sherwood number are addressed in a similar manner.

Heat film coefficient and Nusselt number

By comparing the mean heat transfer film coefficient (figure 4.14a-4.14b) of all the subjects between congested and decongested noses as well as different flowrates, the results show that the congested cavities have larger values intranasally for both higher and lower flowrates. But

the decongested cavities tend to have relative less variations under two flowrates by viewing the range of one SD errorbar. The relatively even distributed heat film coefficient across the main cavity (between plane AS and PS) indicates the effectiveness of heat exchange of the cavity is fairly consistent. The heat film coefficient starts to drop gradually after plane 2V which is due to the lower temperature gradient. Figure 4.14b shows that doubling the flowrate does not change the pattern of the intranasal heat film coefficient distribution, although the actual values are being increased due to high heat exchange demanding. Nusselt number as the so called non-dimensional heat transfer coefficient, the mean distribution for all the subjects are plotted in figure 4.14c and 4.14d for lower and higher flowrate separately. The values of Nusselt number across the cavity always less than 50 even for the higher flowrate.

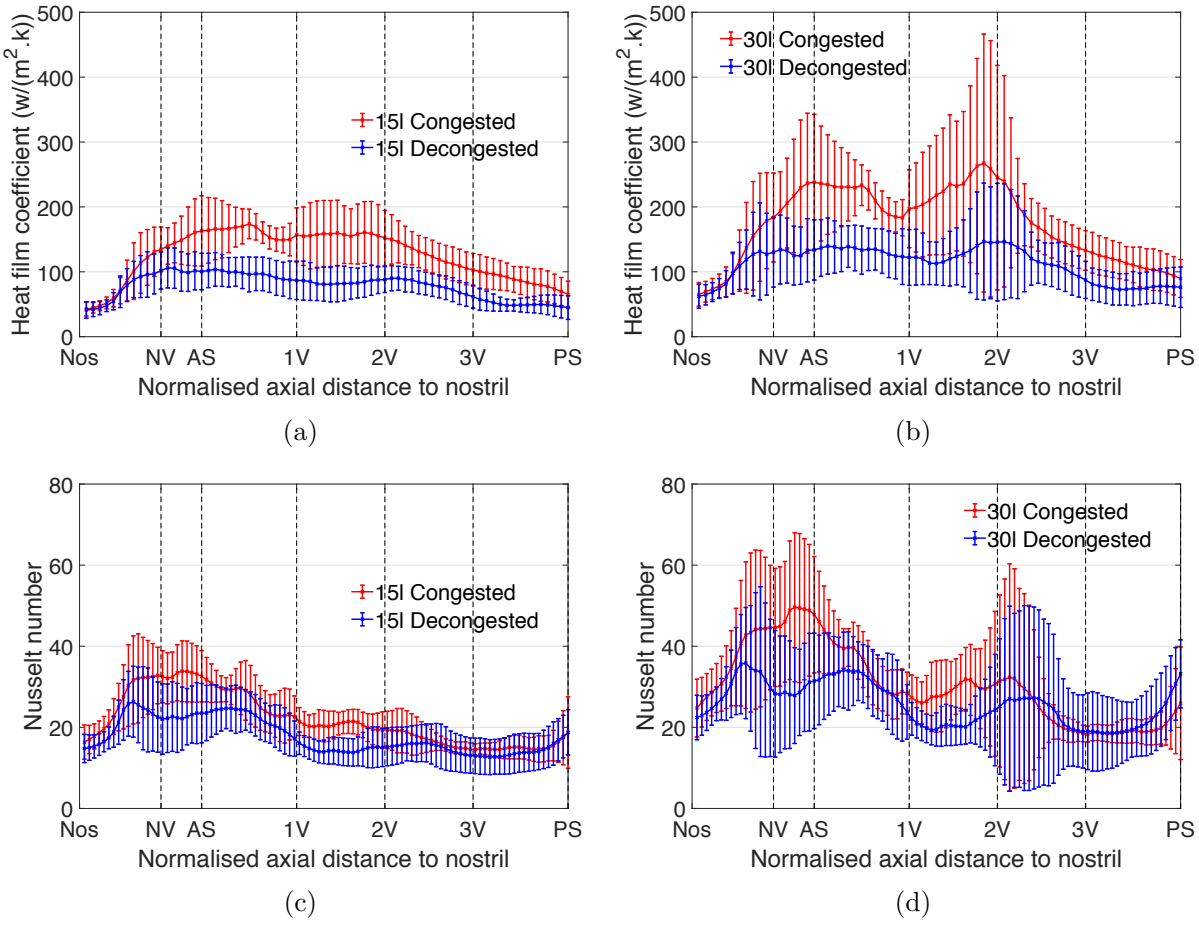


Figure 4.14: Bilateral heat film coefficient and Nusselt number distribution between congested and decongested cavities as well as different flowrate.

As for the flow results in chapter 3, we now consider separately the mean heat film and Nusselt

number values for the anterior nose (plane Nos-1V) and for the posterior nose (plane 1V-PS), figure 4.15 and figure 4.16. From Figure 4.15a, it shows that the decongestion considerably lowers the mean value of heat film coefficient in the anterior cavity for both higher and lower flowrates, resulting in a decrease of about one third of the median that from 122 to 82 for low flowrate and 177 to 111 for higher flowrate and also with the high values for significance. Similar results can be get as well in the posterior part of the cavity (figure 4.15b). By contrast, figure 4.15c to 4.15d show that increasing flowrate significantly increases heat film coefficient, roughly about one third for the anterior cavity while a little less in the posterior cavity.

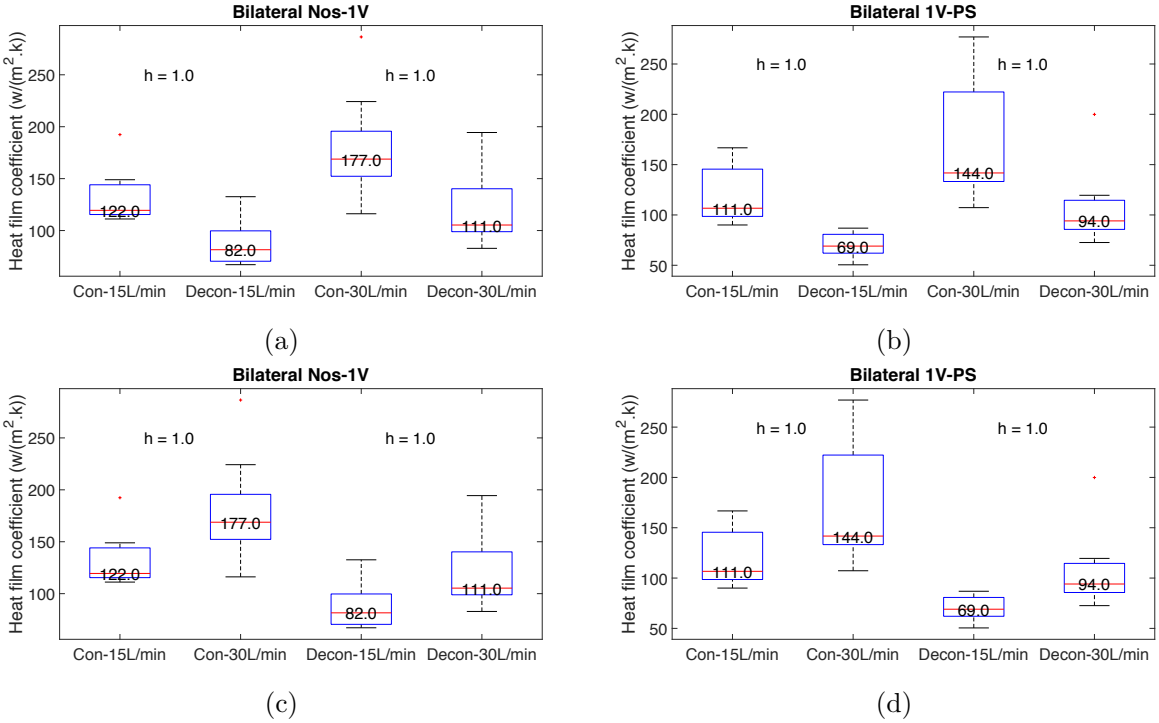


Figure 4.15: Heat film coefficient box plots for the anterior cavity (plane Nos-1V) and for the posterior cavity (plane 1V-PS). The upper pair (a,b) compares effect of decongestion at a given flowrate and the lower pair (c,d) compares the effect of flowrate for give state (congested or decongested).

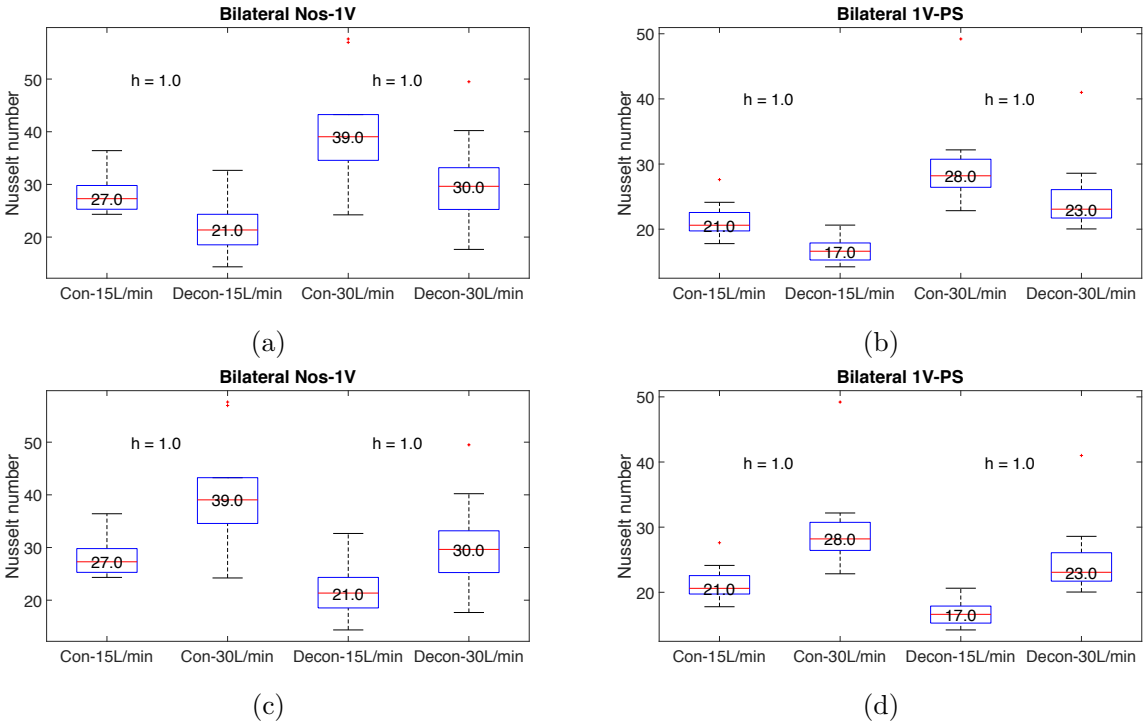


Figure 4.16: Decongestion and flowrate effect on mean Nusselt number within anterior (between plane Nos and 1V) and posterior (between plane 1V and PS) separately. Figure a and b are the test of decongestion, whilst c and d are for the flowrate change test.

Figure 4.16 shows the results of conducting the same test on Nussult number. The same conclusion applies that both decongestion and flowrate alter the mean Nusselt number of both the anterior and posterior cavity to a statistically significant degree, with decongestion lowering the Nusselt number, whereas increasing flowrate increases Nusselt number.

Flowrate ($L.min^{-1}$)	Congested Nos-PS h ($W.m^{-2}.K^{-1}$)	Decongested Nos-PS h ($W.m^{-2}.K^{-1}$)	Congested Nos-PS Nu	Decongested Nos-PS Nu
15	125.4	78.0	24.6	19.2
30	174.0	112.1	34.6	27.4
Flowrate ($L.min^{-1}$)	Congested Nos-1V h ($W.m^{-2}.K^{-1}$)	Decongested Nos-1V h ($W.m^{-2}.K^{-1}$)	Congested Nos-1V Nu	Decongested Nos-1V Nu
15	130.6	87.8	28.7	22.1
30	179.3	119.8	40.6	30.3
Flowrate ($L.min^{-1}$)	Congested 1V-PS h ($W.m^{-2}.K^{-1}$)	Decongested 1V-PS h ($W.m^{-2}.K^{-1}$)	Congested 1V-PS Nu	Decongested 1V-PS Nu
15	121.2	70.2	21.3	16.8
30	169.8	106	30	25.1

Table 4.4: This table lists the mean heat film coefficient and Nusselt number for the cohort subjects of different geometry regions, e.g., the whole nasal cavity (between plane Nos and PS), anterior cavity (between plane Nos and plane 1V), posterior cavity that defined by plane 1V and PS.

	Nos-PS	Nos-1V	1V-PS
Congested h_{30}/h_{15}	1.4	1.4	1.4
Decongested h_{30}/h_{15}	1.4	1.4	1.5
Congested Nu_{30}/Nu_{15}	1.4	1.4	1.4
Decongested Nu_{30}/Nu_{15}	1.4	1.4	1.5

Table 4.5: This table shows the mean heat film coefficient ratios of different geometric partitions between the higher and lower flowrates.

As has been used in chapter 3, the local partition of the whole nasal cavity can be divided into anterior and posterior cavities that separated by plane 1V. Table 4.4 lists the mean heat film coefficient and Nusselt number of all the subjects within different geometric regions of the cavity. And table 4.5 shows the associated ratios of the results between high and lower flowrates. The results from table 4.4 indicate that no matter within which partition of the cavities, the decongestion would reduce the corresponding heat film coefficient and Nu number. Furthermore, it also shows that increasing flowrate can lead to the increase of mean heat film coefficient and Nu number for all three geometric partitions. In addition, as expected from the intranasal distribution results of heat film coefficient across the cavity, the anterior part of the cavity has a slightly higher value than that of the posterior cavity. The ratio of the cavity mean heat film coefficient within different partitions (whole cavity, anterior cavity and posterior cavity) of the cavity between higher flowrate and lower flowrate shows are the same with value 1.4, except for decongested posterior cavity of value 1.5. Similar ratio also also being calculated for Nu number and it shows the same results as heat film coefficient.

Subject	Con-15 $\frac{f}{Nu}$	Decon-15 $\frac{f}{Nu}$	Con-15 $\frac{f}{Sh}$	Decon-15 $\frac{f}{Sh}$	Con-15 $\frac{f}{St_h}$	Decon-15 $\frac{f}{St_h}$	Con-15 $\frac{f}{St_m}$	Decon-15 $\frac{f}{St_m}$
A	0.0039	0.0044	0.0092	0.0096	0.99	1.18	1.98	1.09
B	0.0032	0.0035	0.0085	0.0087	0.98	1.02	2.08	0.95
C	0.0036	0.0035	0.0086	0.0080	0.94	0.90	1.96	0.84
D	0.0038	0.0040	0.0084	0.0087	1.01	1.06	2.03	0.99
E	0.0039	0.0055	0.0088	0.0103	0.95	1.01	1.83	0.94
F	0.0027	0.0037	0.0066	0.0085	0.70	0.98	1.53	0.91
G	0.0041	0.0036	0.0098	0.0085	1.00	0.90	1.97	0.84
H	0.0036	0.0040	0.0094	0.0089	1.08	1.09	2.36	1.02
I	0.0048	0.0077	0.01	0.0159	1.06	1.40	2.01	1.30
1	0.0031	0.0033	0.0083	0.0088	0.97	1.11	2.12	1.03
Mean (15)	0.0037	0.0043	0.0088	0.0096	0.97	1.07	1.98	0.99
Mean (30)	0.0016	0.0018	0.0042	0.0044	0.83	0.90	1.96	0.84

Table 4.6: The ratios of friction coefficient over multiple quantities, i.e, Nusselt number, Sherwood number, both heat and mass Stanton number. All the ratios are using the mean values of the whole cavity of each quantity. The last row gives the mean ratio of flowrate at 30 L.min^{-1} directly, without showing each value of every subjects. Ideally, the ratio between frictional coefficient and Stanton number is 2 for laminar flow.

Table 4.6 lists the ratios between frictional coefficient and others, i.e., NU, Sh, St for heat and mass. It shows that after doubling the flowrate the mean cavity ratio between f and Nu (or Sh) nearly reduced half (45%) of that at 15 L.min^{-1}, while the ratio between f and St is not varying much. Very roughly, this indicates that the heat or mass transfer of the whole cavity behaves in a similar manner as the fully developed duct flow, which the $\frac{f}{Nu}$ and $\frac{f}{Sh}$ are only a function of Reynolds number and $\frac{f}{St}$ is constant. This measurements of great interest to be further applied in the analysis with larger sample size, i.e., far larger than 10 subjects.

Mass film coefficient and Sherwood number

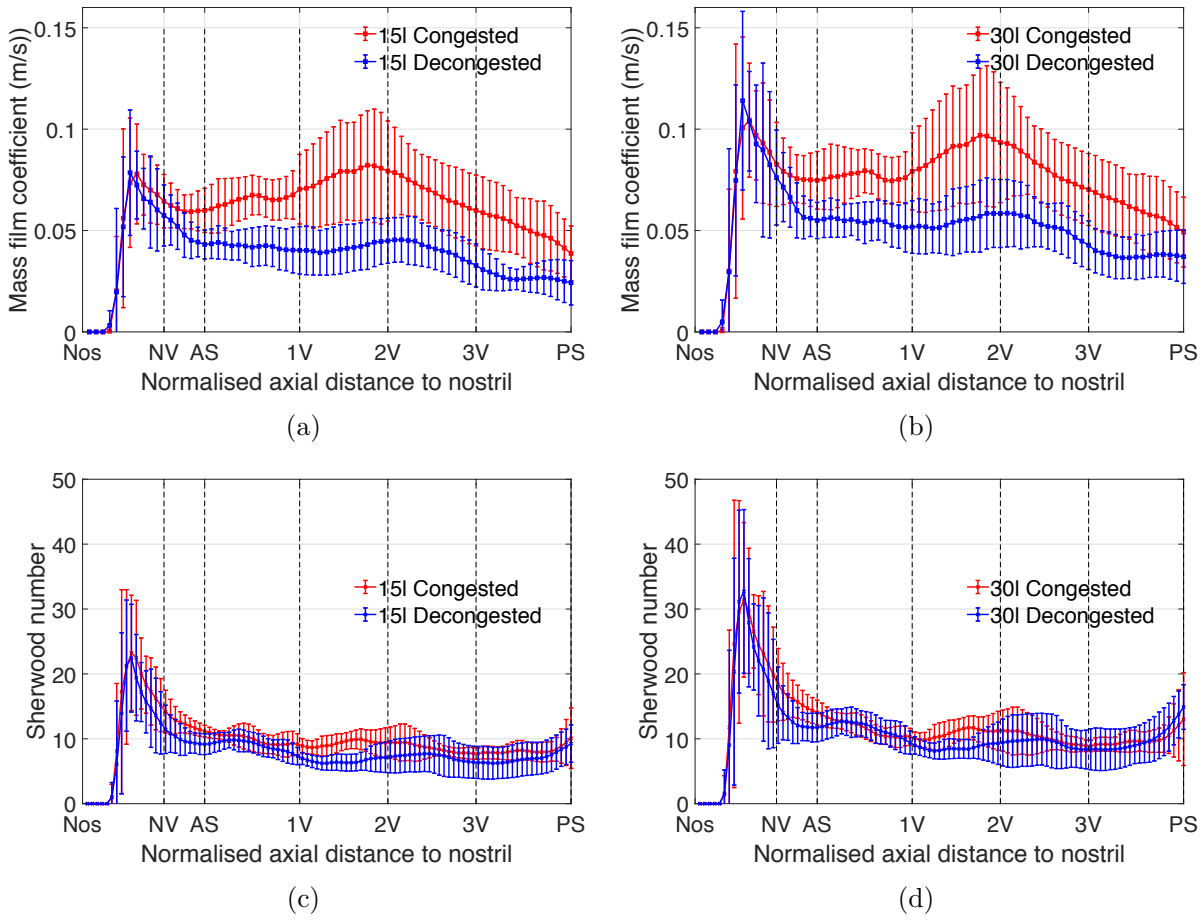


Figure 4.17: Mass film coefficient and Sherwood number between congested and decongested cavities under both higher and lower flowrates. The upper pair (a,b) are the intranasal mass film coefficient distribution along the cavity centerline, while the lower pair are the same but for Sherwood number.

Mass film coefficient is an appropriate quantity to evaluate the transfer efficiency of the moisture from the surface to the cavity volume. Figure 4.17a shows the distribution of mass film coefficient across the cavity. From the figure, one can observe that the expansion of cavity CSA by decongestion will reduce the mass film coefficient. Doubling the flowrate (figure4.17b), shows similar distributions with slightly higher value. The two maxima points of the mass film coefficient in the plot are located at around the nasal valve and plane 2V separately. The higher value at the nasal valve is because of the high moisture gradient caused by temperature gradient, which drives the moisture vapor transport. The second maxima point is weaker and

may reflect the narrower passages in this area for the congested noses.

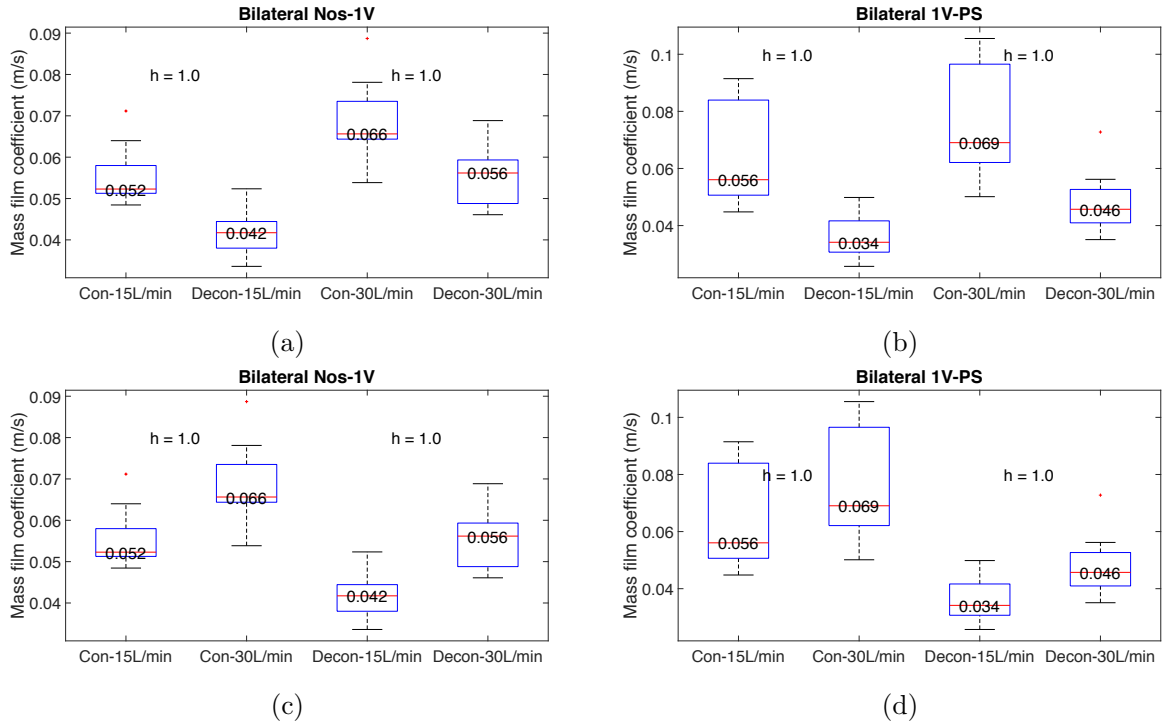


Figure 4.18: Bilateral mean mass film coefficient, within anterior part (between plane Nos and 1V) and within posterior part (between plane 1V and PS), Wilcoxon singed-rank test, before and after decongestion as well as before and after increase of flowrate, are distributed by this figure.

The corresponding intranasal Sherwood number distribution across the cavity appears fairly consistent after plane AS for both congested and decongested cavities of two different flowrates. Referring back to the definition of Sherwood number, this implies that the increase in characteristic length due to decongestion, compensates for the reduction in mass film coefficient in much of the cavity.

Again, the significance test is applied to the mass film coefficient and Sherwood number as well as shown in figure 4.18 and figure 4.19. It shows that no matter in the anterior or posterior cavity, the decongestion will reduce the mass film coefficient and to a statistically significant effect. In other words, the decongestion can reduce the efficiency of moistening of the cavity both in the anterior and posterior part. Figure 4.18c and 4.18d compare the increase of flowrate effect on the mass film coefficient of the nasal cavity under same state (congested or decongested). The

results show that increase of flowrate will lead to a higher cavity moisture exchange efficiency, although the eventual moistening conditions are not being improved, refer to figure 4.12.

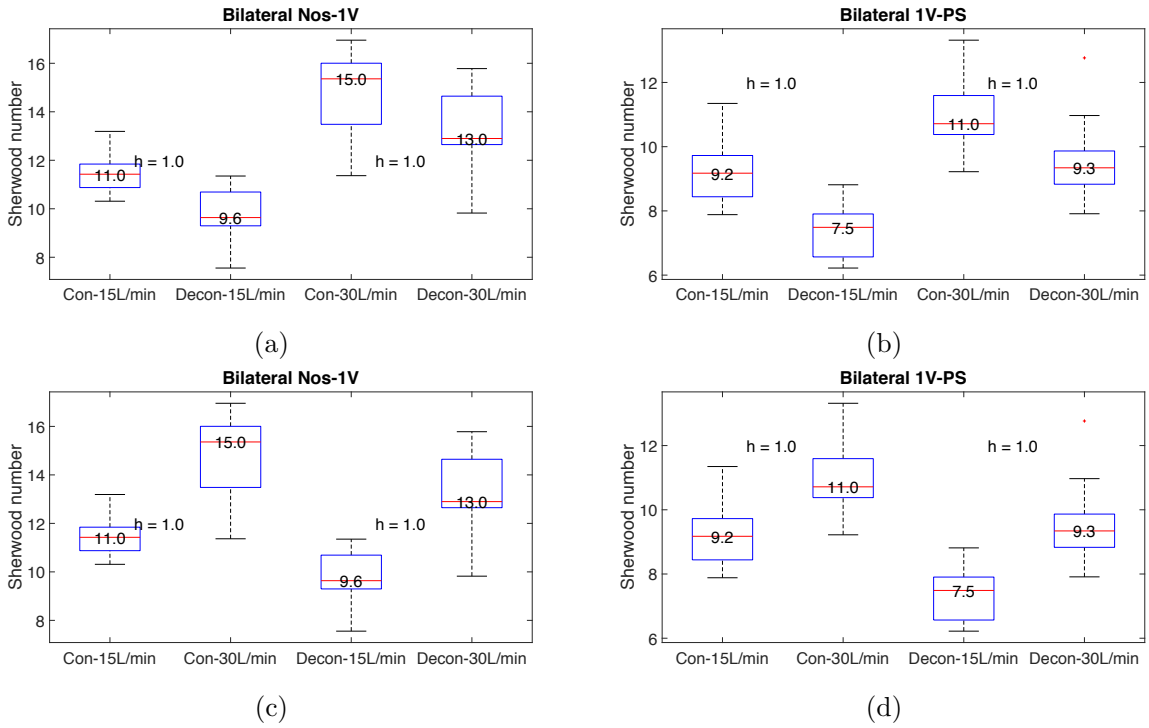


Figure 4.19: This figure distributes the same test results as figure 4.18, but for quantity Sherwood number instead.

As can be seen from figure 4.18 and figure 4.19, it shows that statistically both the geometry change (by decongestion) and flowrate change (doubled) will have the significant effect on the mean value of both mass film coefficient and Sherwood number within the anterior and posterior part of the cavities. From table 4.7 we can see that the decongestion will also reduce the mass film coefficient just like the effect on heat film coefficient described above and increase of flowrate will also increase the moistening efficiency. The ratio of increase on mass film coefficient by doubling the flowrate is around 1.3 (table 4.8) for all the three geometric divisions (whole cavity, anterior and posterior cavity). The Sherwood number also behaves in the same manner as the Nusselt number. This means double the flowrate only increase the mass transfer efficient a third, which is slightly lower than that for the heat transfer efficiency (nearly half) from table 4.5.

Flowrate ($L.min^{-1}$)	Congested Nos-PS h_c ($m.s^{-1}$)	Decongested Nos-PS h_c ($m.s^{-1}$)	Congested Nos-PS Sh	Decongested Nos-PS Sh
15	0.061	0.039	10.2	8.5
30	0.073	0.052	12.6	11.3
Flowrate ($L.min^{-1}$)	Congested Nos-1V h_c ($m.s^{-1}$)	Decongested Nos-1V h_c ($m.s^{-1}$)	Congested Nos-1V Sh	Decongested Nos-1V Sh
15	0.056	0.042	11.4	9.8
30	0.070	0.056	14.9	13.3
Flowrate ($L.min^{-1}$)	Congested 1V-PS h_c ($m.s^{-1}$)	Decongested 1V-PS h_c ($m.s^{-1}$)	Congested 1V-PS Sh	Decongested 1V-PS Sh
15	0.065	0.036	9.3	7.4
30	0.077	0.048	10.8	9.7

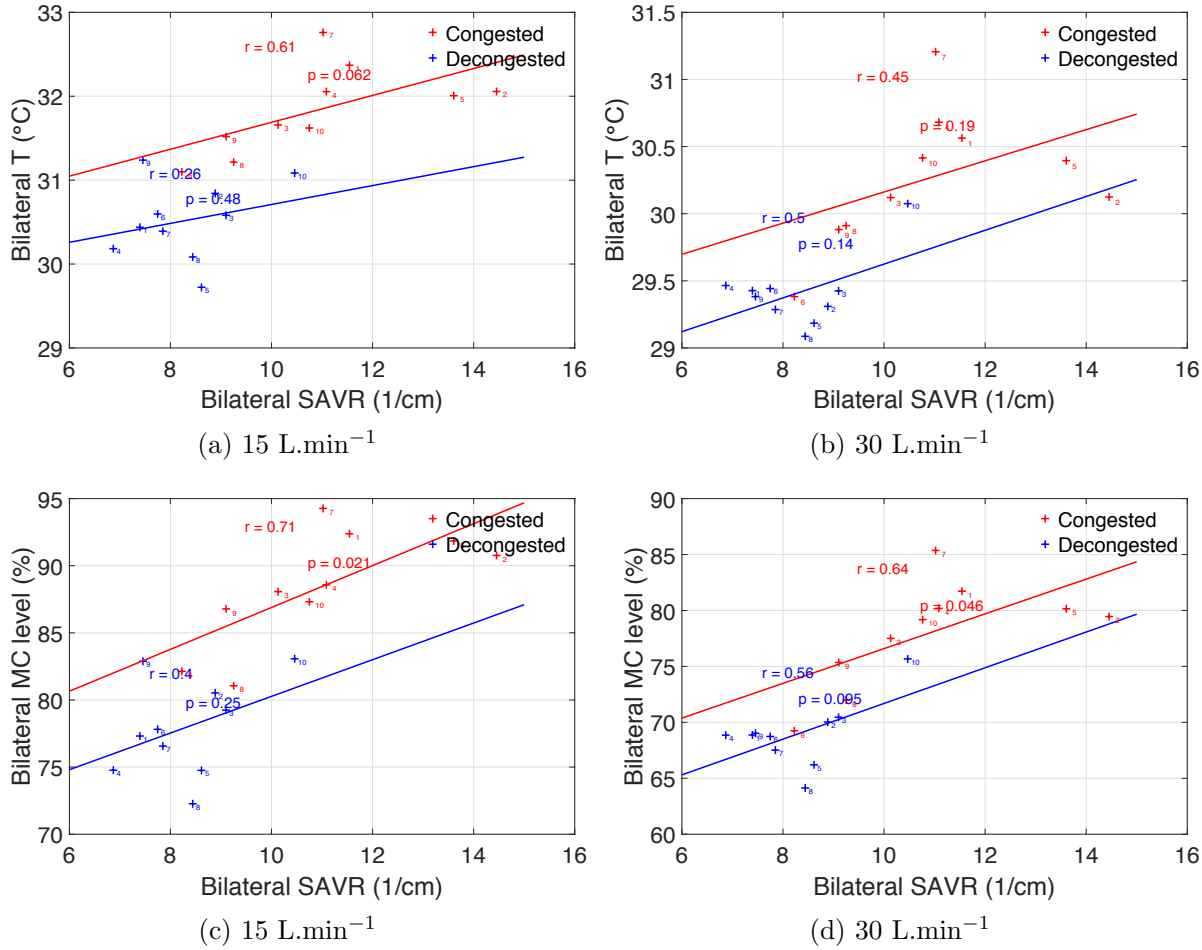
Table 4.7: This table lists the mean mass film coefficient at different flowrates of the same geometric partitions as described in table 4.4.

	Nos-PS	Nos-1V	1V-PS
Congested h_{c30}/h_{c15}	1.2	1.3	1.2
Decongested h_{c30}/h_{c15}	1.3	1.3	1.3
Congested Sh_{c30}/Sh_{c15}	1.2	1.3	1.2
Decongested Sh_{c30}/Sh_{c15}	1.3	1.4	1.3

Table 4.8: This table shows the mass film coefficient ratio between higher and lower flowrates within three geometric partitions: whole cavity (Nos-PS), anterior cavity (Nos-1V) and posterior cavity (1V-PS).

4.2.3 Correlation analysis

In the section, the correlations are tested between not only previous defined geometric measures, but also with air conditioning related quantities such as the nasopharynx temperature (T) and moisture content level (MC), total amount heat flux transferred (THF) and total amount water flux transferred (TH2OF).



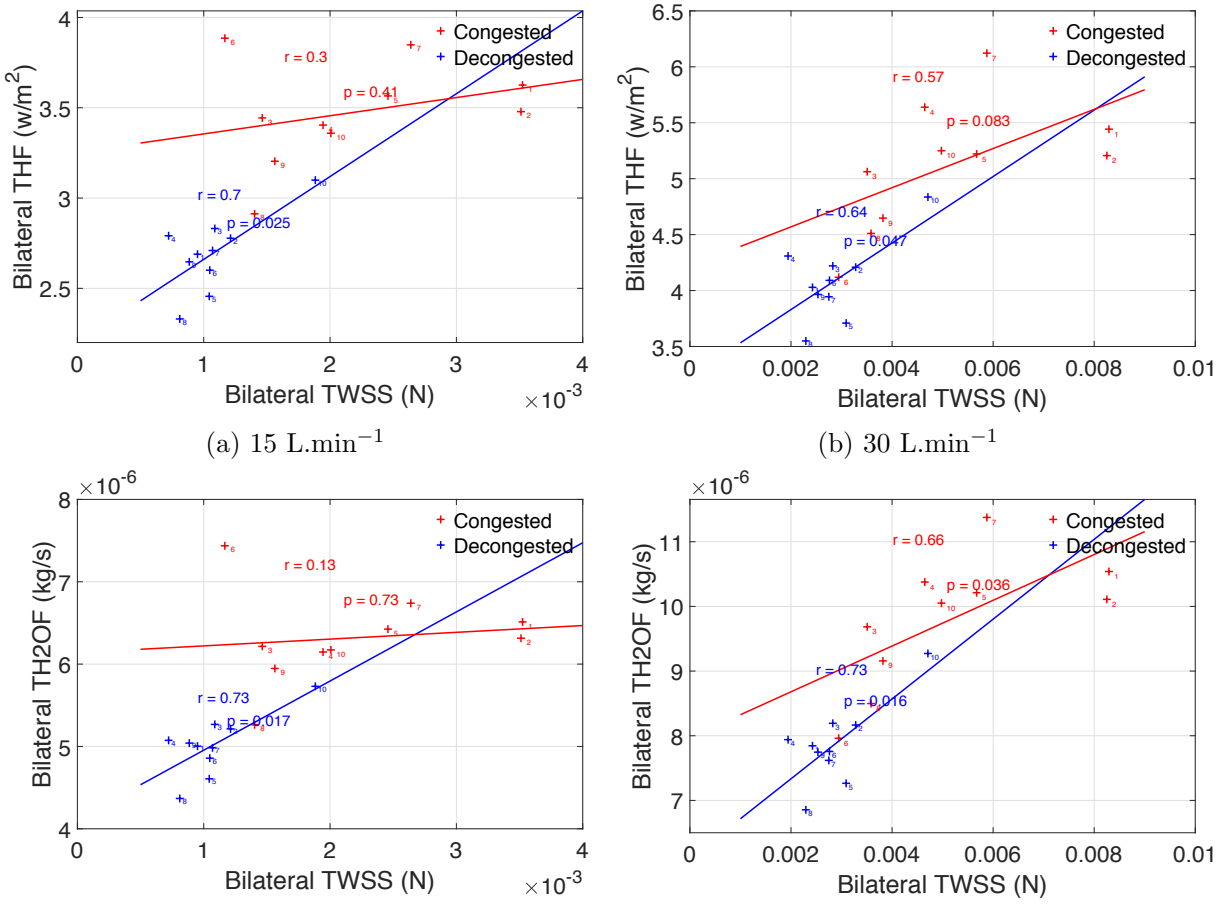
(a) 15 L.min^{-1} (b) 30 L.min^{-1}

(c) 15 L.min^{-1} (d) 30 L.min^{-1}

Figure 4.20: Figure a shows the correlations between bilateral SAVR and temperature at nasopharynx plane. Figure b shows the correlations between bilateral SAVR and moisture content level at nasopharynx plane.

Firstly, the correlations of geometric measures to physical quantities are tested. The results shows that for congested cavities, there is a moderate correlation (r = 0.61) between SAVR and nasopharynx temperature at 15 L.min^{-1}, but not for decongested cavities (r = 0.26).

This correlation will get weaker after increases the flowrate twice that gives r of value 0.45 (figure 4.20b). Secondly, the correlations of bilateral moisture content level at the nasopharynx plane to the SAVR for different flowrates are shown in figure 4.20c. Similarly as the temperature, the SAVR and moisture content level correlation will also get slightly weaker after doubling the flowrate (figure 4.20d). As shown in appendix C.1, there was a lack of appreciable correlation between the cavity SAVR and the total amount of heat flux or total amount of water flux transferred. Additionally, as known from the previous analysis, both the dry heat flux and water flux maps show good association with the WSS maps. Investigating the correlations between total surface frictional force and total heat flux or water flux gives the following plots:



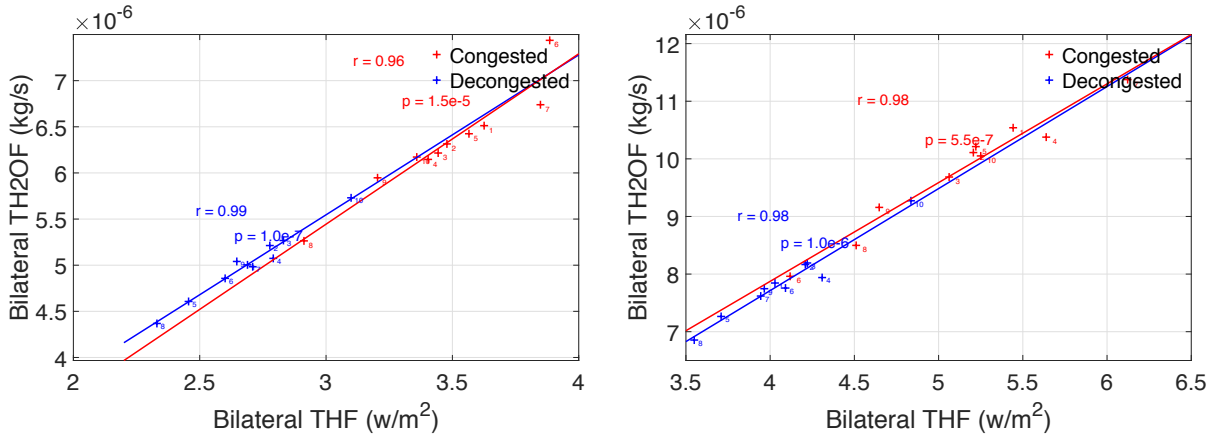
(a) 15 L.min^{-1} (b) 30 L.min^{-1}

(c) 15 L.min^{-1} (d) 30 L.min^{-1}

Figure 4.21: The correlation plots between surface total wall shear stress (TWSS) and both the total heat flux transferred and total amount of water transferred.

Figure 4.21 describes both congested and decongested cavities have better correlations with

total surface frictional force (represents by TWSS) to total heat flux transferred or total water flux transferred compared to that under lower flowrate (15 L.min^{-1}), except the congested cavities which show better correlations at higher flowrate. However, all the correlations shown by figure 4.21 are significant with 'p' values less than 5%, except those congested cavities under lower flowrate. In summary, there are no strong correlations between the cavity total wall shear stress with the total heat transferred or total moisture transferred. As have been exposed from the detailed maps analysis, it shows the heat and water transfer are associated with the distribution of WSS, but they are mostly concentrated on the anterior and inferior sections of the cavity. Thus the total amount of these measures (WSS, total heat and moisture flux) are not well correlated.



(a) 15 L.min^{-1} (b) 30 L.min^{-1}

Figure 4.22: Correlation between total heat flux and total water flux transferred under two flowrates.

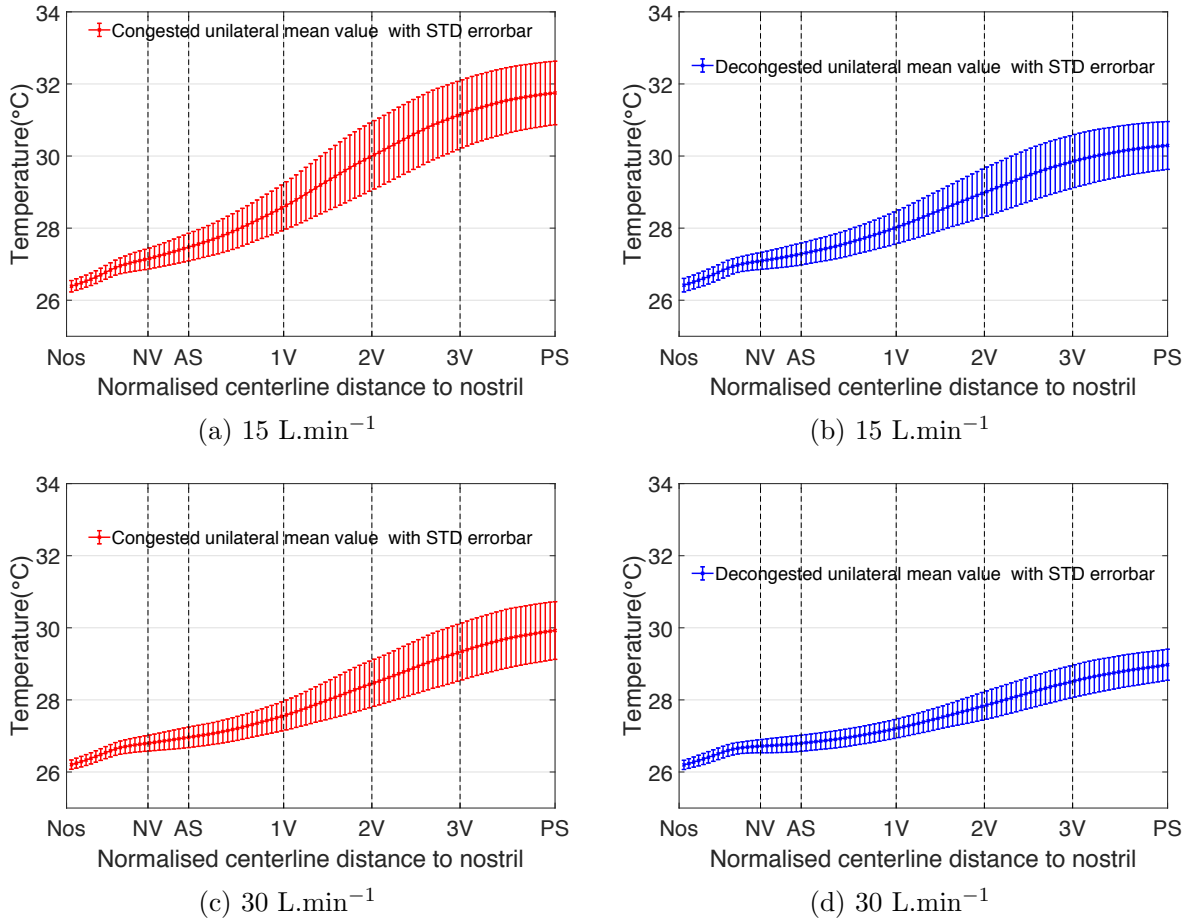
Unsurprisingly, the correlation between total heat flux and total water flux of the cavity from figure 4.22 shows that there is strong and significant correlation between the total heat and water flux of the cavity ($p > 0.9$). This is because the heat and moistening processes are happening at the same time and are coupled by the latent heat effect.

4.3 Unilateral heat and water analysis

After analyzing the results over the bilateral cavities, this section proceed the same analysis but over the unilateral cavities which extends the sample size from 10 to 20 of each state.

4.3.1 Temperature and moisture

Comparing the results from figure 4.23 to the bilateral plots (figure 4.10), we can see that the unilateral plot shows very similar distribution as well as the final conditioned state. Increasing flow or decongestion again leads to decreasing performance, to a significant level (figure 4.24).



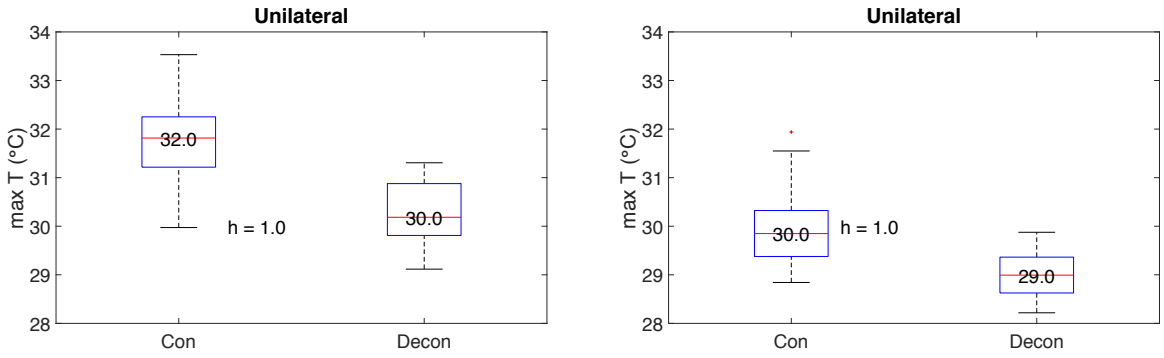
(a) 15 L.min^{-1}

(b) 15 L.min^{-1}

(c) 30 L.min^{-1}

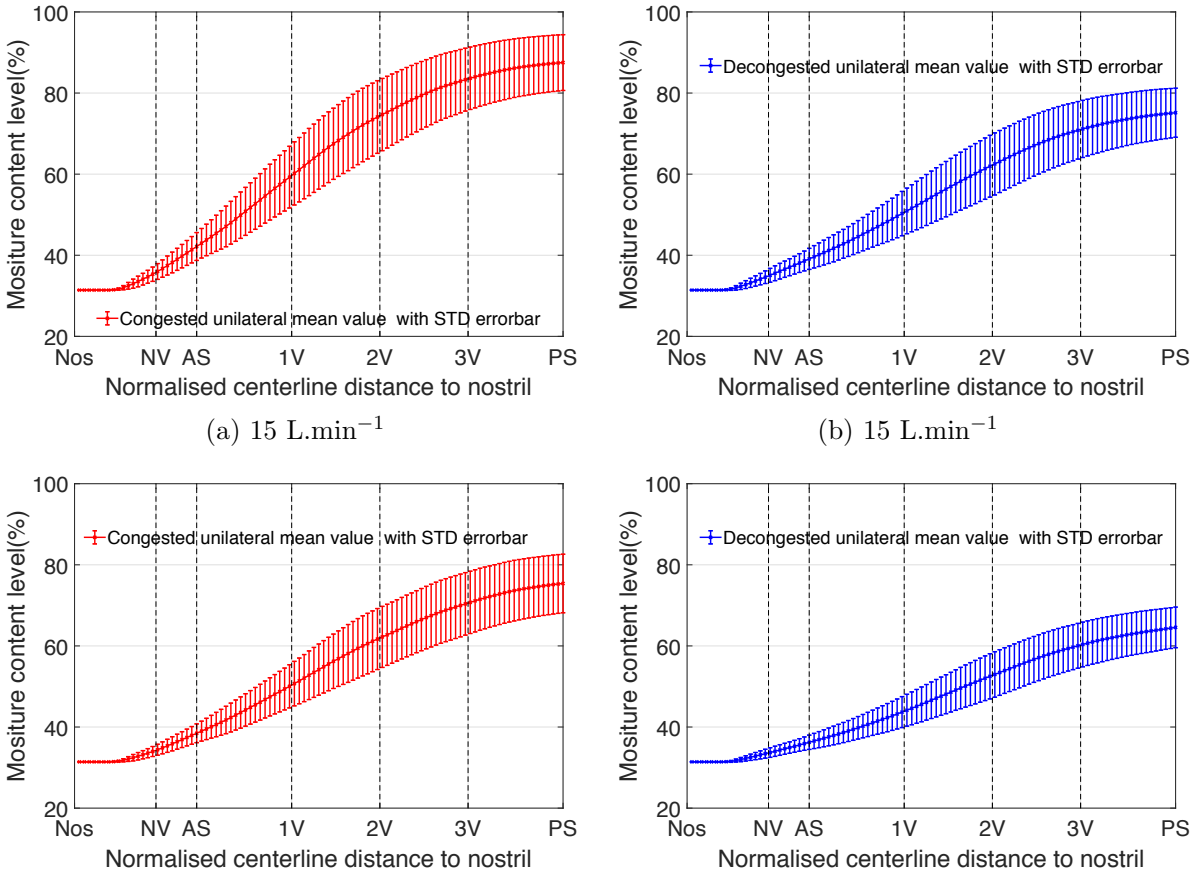
(d) 30 L.min^{-1}

Figure 4.23: Mean temperature distribution of all the unilateral cavities from nostril to posterior septum. The upper pair represents the results for lower flowrate (15 L.min^{-1}) simulations before and after decongestion, while the lower pair is the results for higher flowrate (30 L.min^{-1}). Note particularly the flowrate labelled represents the bilateral flowrate and the unilateral values need to deduce from the mass flow split ratio.



(a) 15 L.min^{-1} (b) 30 L.min^{-1}

Figure 4.24: Unilateral Wilcoxon signed-rank test for temperature at posterior septum plane before and after decongestion.



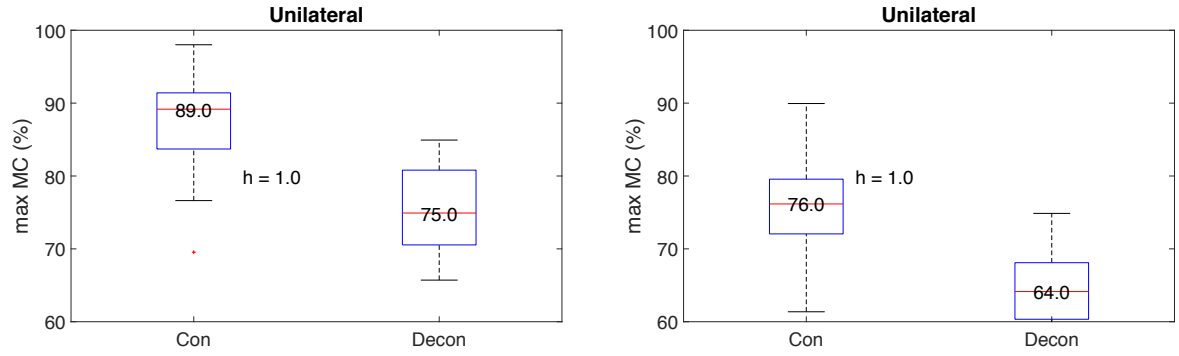
(a) 15 L.min^{-1} (b) 15 L.min^{-1}

(c) 30 L.min^{-1} (d) 30 L.min^{-1}

Figure 4.25: This figure, again, shows the same distributions but for quantity moisture content level for unilateral cavities.

Accordingly, the unilateral mean moisture content distribution also closely matches the bilat-

eral cavity results, confirming that decongestion will reduce the final (at posterior septum) conditioned value. Applying significance testing to the reduction in moisture content MC level, due to the decongestion effect for the unilateral cavity has the same conclusion as for that bilateral cavity. In summary, this shows again that there is no difference if we treat each half cavity as an individual object in a cohort study like this.



(a) 15 L.min^{-1} (b) 30 L.min^{-1}

Figure 4.26: Wilcoxon singed-rank test for the moisture content level at plane PS of unilateral cavitites.

4.3.2 Heat and moisture transfer coefficients analysis

For clarification, we should keep in mind that the mass flowrate number of unilateral legend indicates the value of bilateral cavity, and the actual values of each half noses need to be deduced based on the mass split ratio.

Heat film coefficient and Nusselt number

Figure 4.27 shows the heat film coefficient distribution from anterior nostril to PS plane at two different flowrates. Refer back to the same plot but for bilateral cavities, figure 4.14, we can observe that the mean unilateral distribution of heat film coefficient and Nusselt number are nearly identical to that of the bilateral results, except figure 4.27d shows obvious higher standard deviation for unilateral Nusselt number at higher flowrate (30 L.min^{-1}).

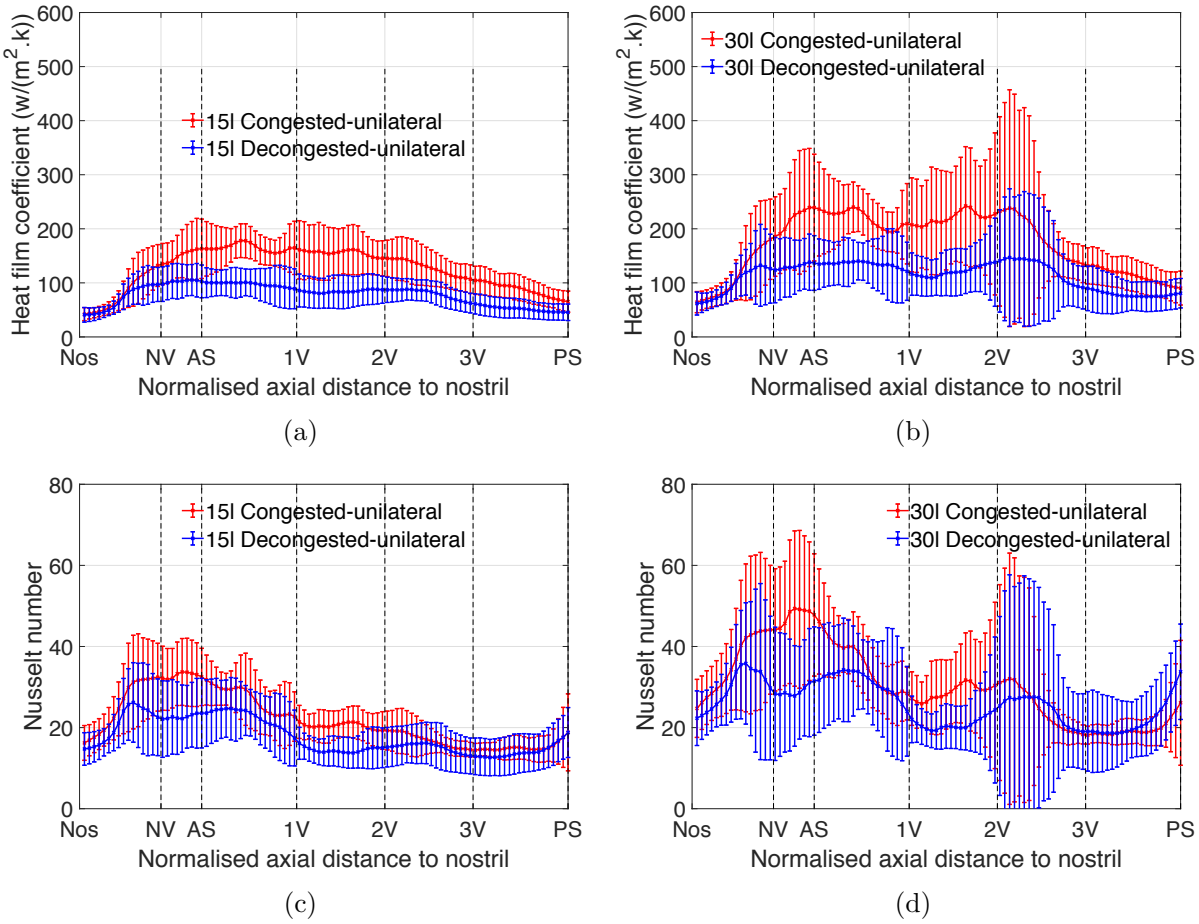


Figure 4.27: This figure shows the same distribution as figure 4.14, but this is for unilateral cavities instead. The upper pair (a,b) represent the heat film coefficient result, whilst the lower pair (c,d) are for the intranasal Nusselt number.

If we calculate the mean heat film coefficient between nostril and plane 1V and between plane 1V and plane PS, the effect of decongestion on unilateral cavities are shown in the first row of figure 4.28. Similarly, the change of flowrate effect on the mean heat film coefficient are shown in the second row of the same figure. The results compared to that of the bilateral cavity do not only share the same conclusion but also with very similar median values as well. Thus, we can conclude that no matter bilaterally or unilaterally evaluate the decongestion or flowrate change effect on the anterior or posterior part of the cavity of the heat film coefficient, it all have statistically significant difference, i.e., the decongestion will reduce the heating efficiency, while the increase of flowrate will increase the heating efficiency.

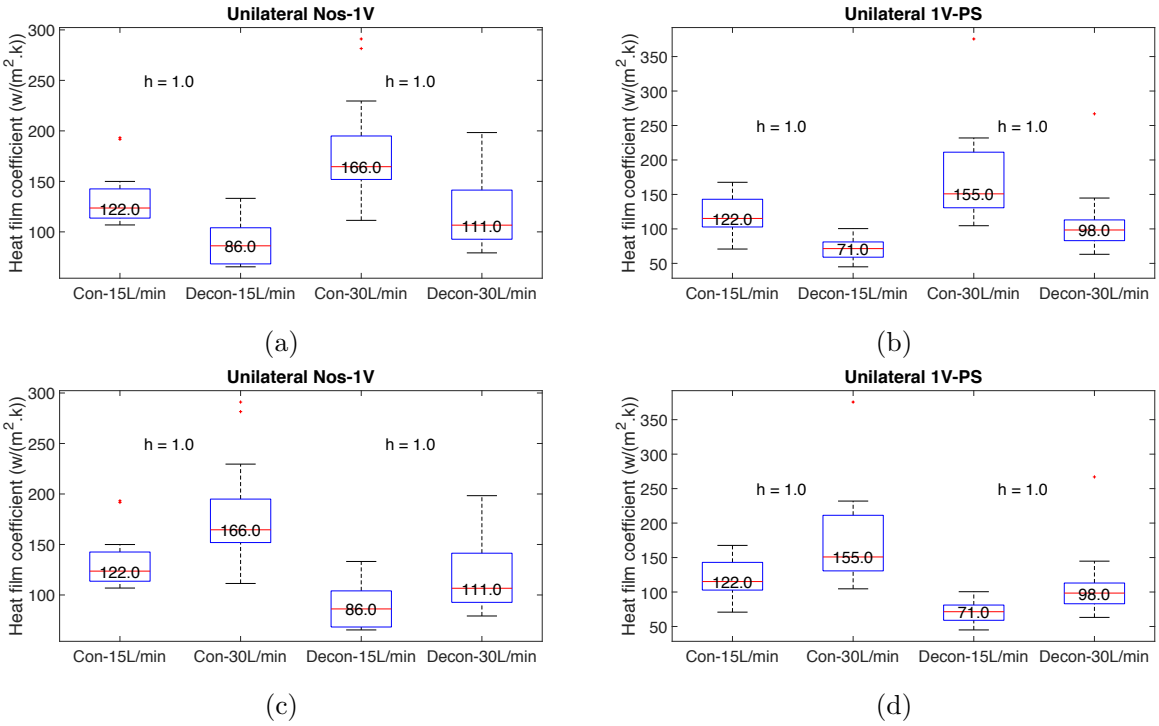


Figure 4.28: This figure shows the significance test results for the heat film coefficient for both the effect of decongestion and the effect of double the total mass flowrate. The upper pair (a,b) represent the effect of decongestion on heat film coefficient within both the anterior (between plane Nos to 1V) and posterior (between plane 1V and PS) cavity, while the lower pair (c,d) are the same but for the effect of doubling the total mass flowrate.

Figure 4.29 shows the significance test result for unilateral cavity of Nusselt number. Same as the bilateral results (figure 4.16), the decongestion will reduce the Nusselt number with statistic significance, whilst the increase of flowrate will increase the Nusselt number but also with statistic significance of both the anterior and posterior cavities.

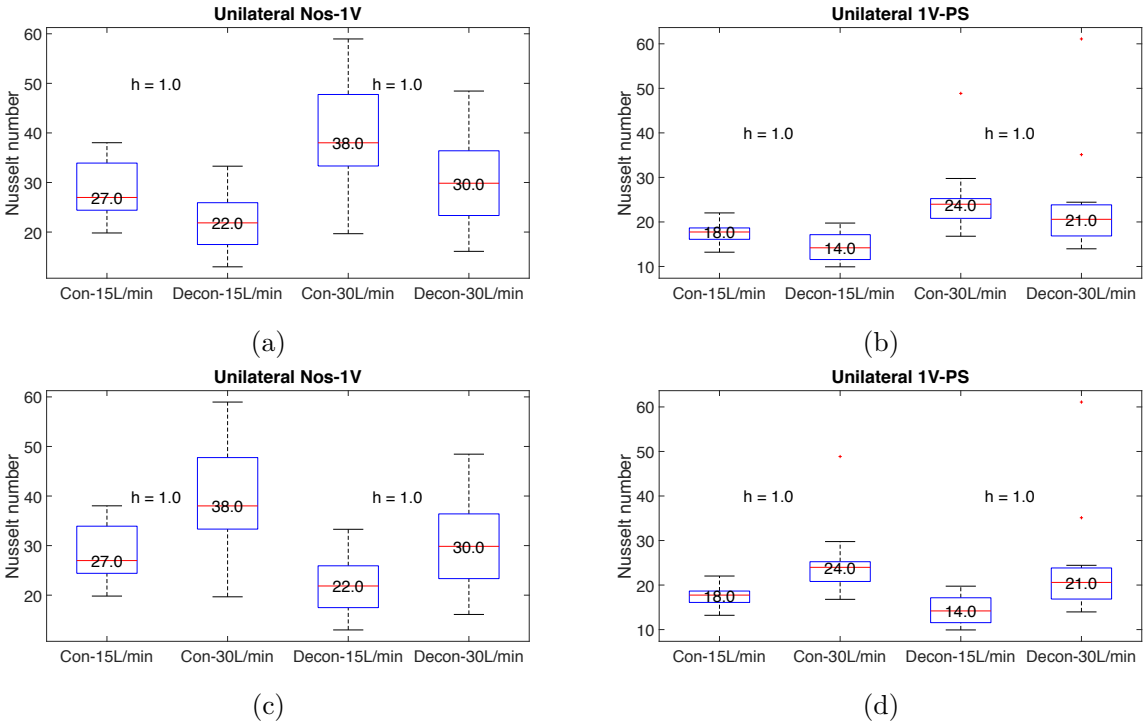


Figure 4.29: Decongestion and flowrate effect on the mean Nusselt number within anterior (plane Nos to 1V) and posterior (plane 1V to PS) cavity separately. The upper pair are for the effect of decongestion, while the lower pair are for the effect of change of flowrate.

Mass film coefficient and Sherwood number

Conducting the same analysis for mass film coefficient and Sherwood number as that for the bilateral cavity. Firstly, we can see the nearly identical mean intranasal distribution of both mass film coefficient and Sherwood number between unilateral cavities and bilateral cavities by comparing figure 4.17 and figure 4.30. Considering the statistic analysis for the unilateral cavity, we observed the same conclusion, although the values details are slightly different, comparing the results from figure 4.18 to 4.19 and figure 4.31 to 4.32.

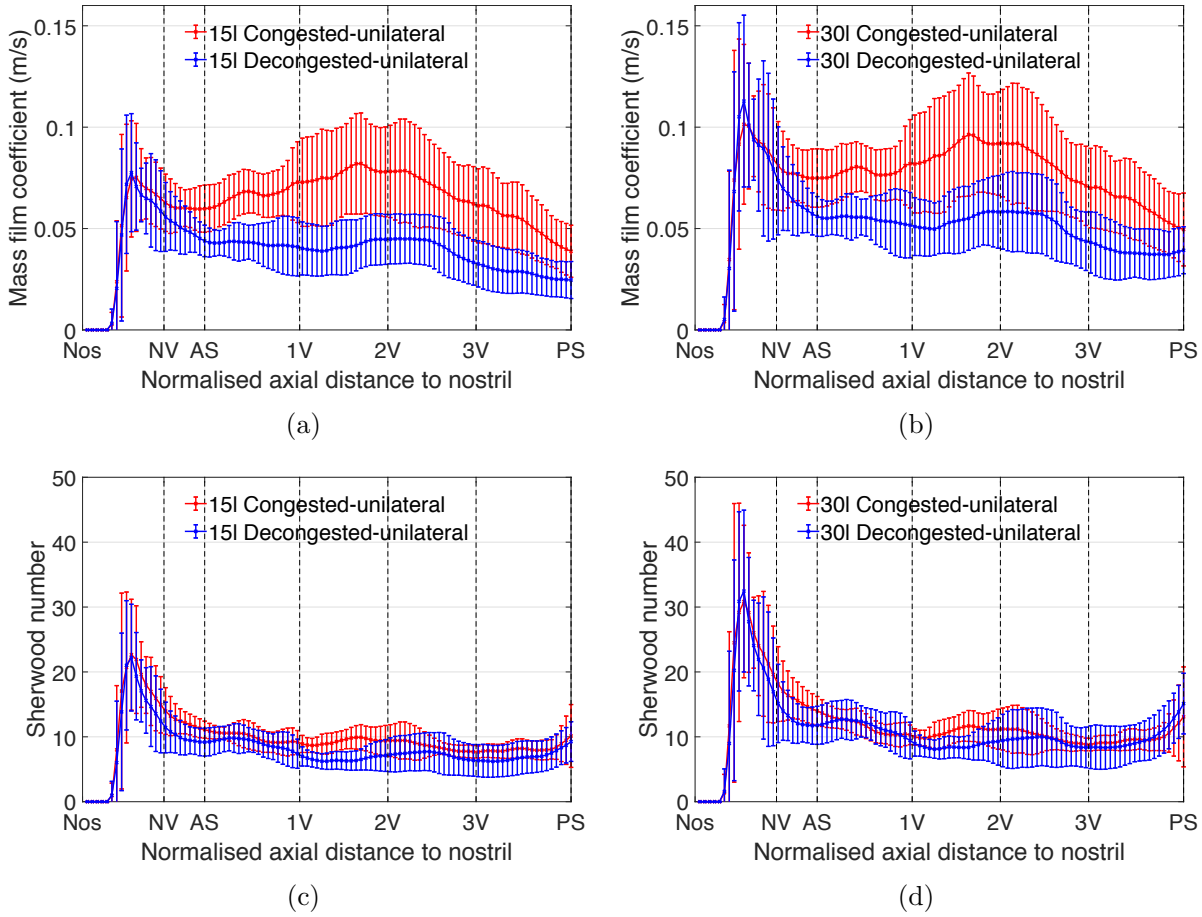


Figure 4.30: Unilateral cavities mass film coefficient and Sherwood number intranasal cavity distribution. Figure a and b are the mass film coefficient at lower and higher flowrates, while the lower pair (c,d) represent the Sherwood number at two flowrates.

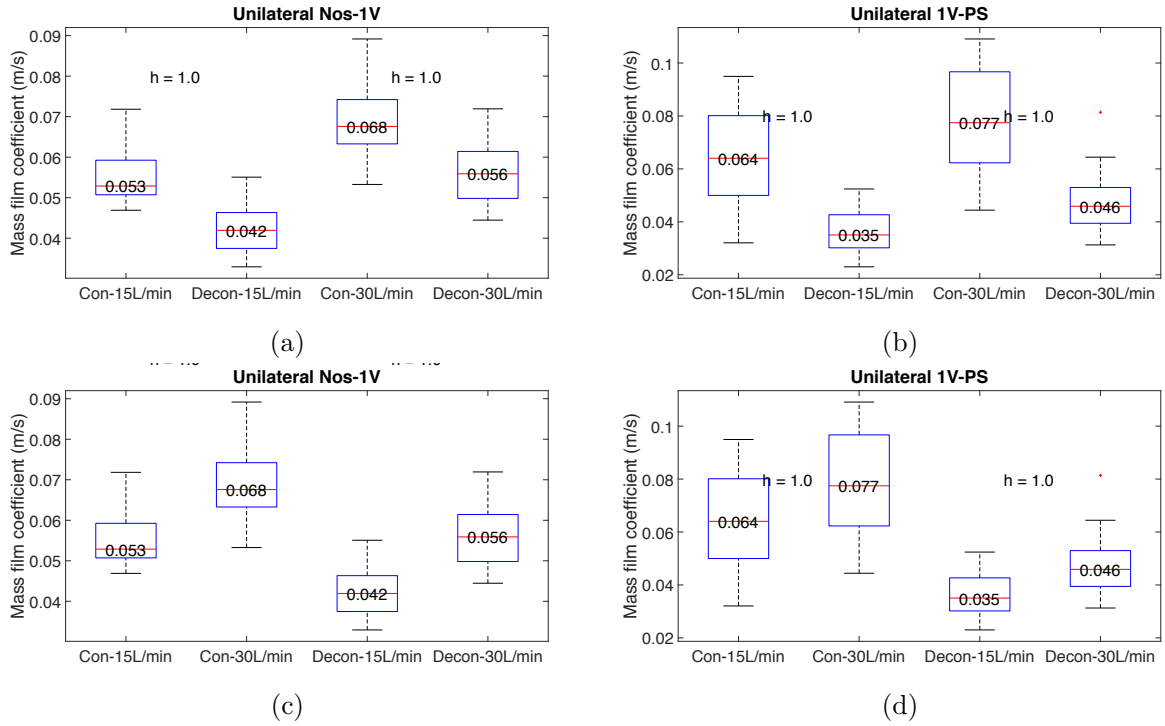


Figure 4.31: Unilateral mean mass film coefficient, within anterior part (between plane Nos and 1V) and within posterior part (between plane 1V and PS), Wilcoxon signed-rank test, before and after decongestion as well as before and after increase of bilateral flowrate, are distributed by this figure.

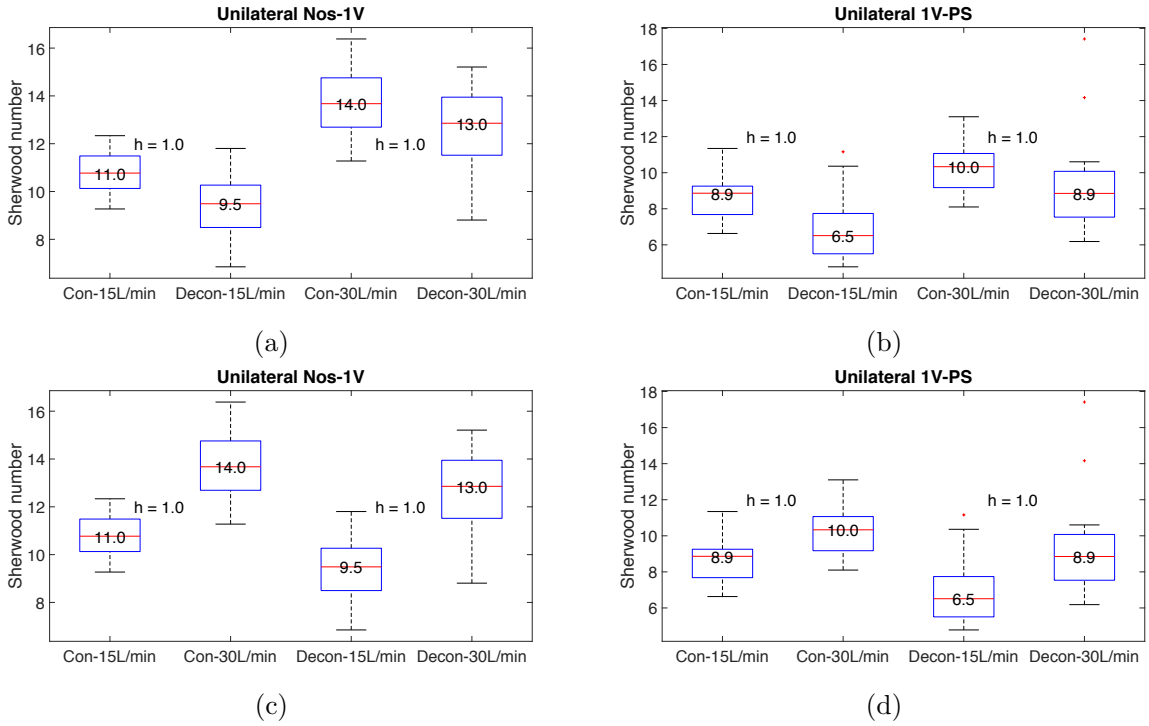
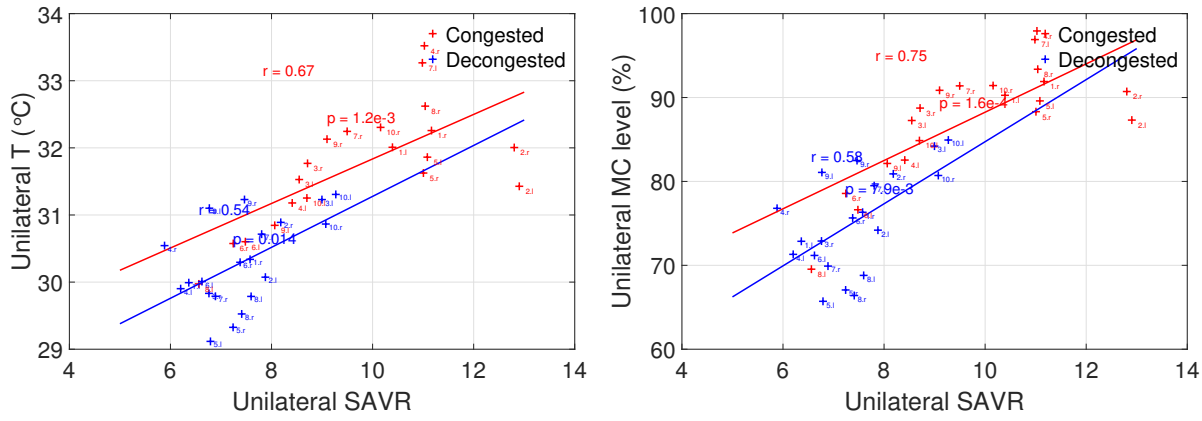


Figure 4.32: This figure shows the same results as figure 4.31, but for quantity Sherwood number instead.

4.3.3 Correlation analysis

As have been found that the bilateral correlation between SAVR and nasopharynx temperature does not show strong correlations. However, although it is also only moderate correlations between SAVR and conditioned temperature at posterior septum as well as the moisture content level, the unilateral cavity results in general have slightly higher correlations compared to that of the bilateral results. This might due to the unilateral results avoid the effect of asymmetric mass flow split ratio among left and right side cavities. With the doubled flowrate, the correlation factors get slightly weaker (figure C.2).

The unilateral cavity results about the correlations between total WSS and total heat and moisture transferred in figure C.3, it shows even weaker correlations compared with the results of bilateral cavity (figure 4.21).



(a) 15 L.min^{-1} (b) 15 L.min^{-1}

Figure 4.33: Unilateral correlations between SAVR and the conditioned temperature and moisture content level at posterior septum of both lower and higher flowrate.

Chapter 5

Laryngo-tracheal flow analysis

This chapter describes an investigation of inspiratory airflow through the larynx and into the trachea. The study considers how the flow behaviour and associated energy dissipation and pressure loss are affected by flowrate and by the reduction in glottis aperture respectively.

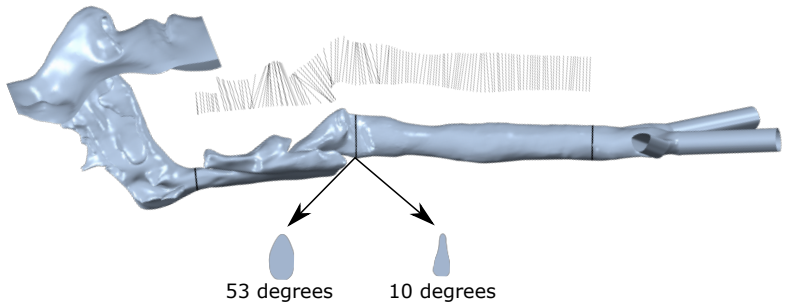
Even for complete normal anatomy, inspiratory flow in the larynx is complicated by the variations in upstream airway cross section (due to complex and soft tissues surrounding the tongue base and epiglottis) and by the changes in flow direction. The dominant flow feature is the laryngeal jet, which can significantly affect airway flow patterns as well as tracheal wall shear stress [16].

Before we get into the detailed analysis of the results, the geometry features and a set of predefined cross-sectional planes are introduced as shown in figure 5.1. From the figure we can see two different glottis shapes at the same location in the complete airway (distributed in figure 5.1a and shown by the cross-sectional plane). The geometry with small angle of glottis aperture (partly abducted) was achieved by manual modification from the full abducted complete airway (53 degrees glottis) by Dr. Lulu Ritchie, a trainee ENT surgeon, as described in her thesis [124]. Since the modification of the glottis geometry was performed directly on the original image segmentation, the process of translation to a surface mesh treated the modified

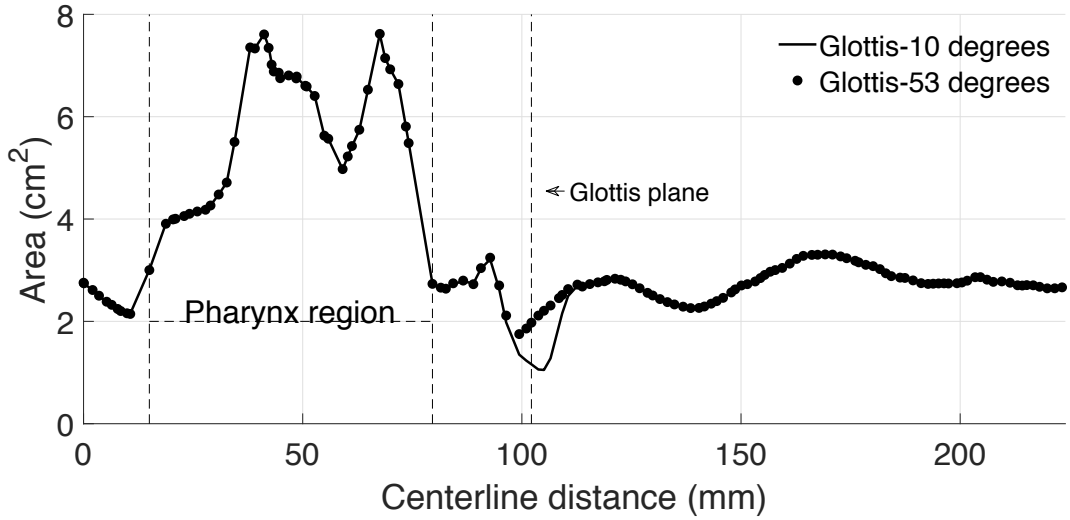
geometry as an entirely different object. Consequently, the necessary smoothing applied after exporting the STL surface mesh after the glottis modification introduced further minor differences beyond the modification region. These inadvertent geometry changes are not evident in the cross-sectional are plot, figure 5.1b. However, when considering the distribution of total pressure (figure 5.6) it should be remembered that these are the source of small differences between the two geometries in the pharynx region.

Considering the CSA variation in detail, figure 5.1b, the variation of the area distribution within the pharynx region (x = 15 mm and 80 mm) is caused by the redundant area after the truncation at the posterior of the oral cavity and at the esophageal opening.

Having introduced the geometries used for this study, the following sections present firstly, the validation of high resolution computational predictions by comparison with experimental results obtained by Dr. Lulu Ritchie. In her experiment, the measurements were taken in replica models of the same geometries, which were produced by rapid prototype manufacture [124]. Following validation of the high resolution computations, comparison is made for flow features resolved by different lower fidelity computational models and the predicted pressure losses. Flow features around the laryngeal jet are then displayed in detail and the associated effect on the surrounding tissues reflected by static pressure is analyzed. Next, the effect of a change of glottis aperture from fully abducted to partly abducted is considered. Finally the computational predictions of pressure loss obtained for both glottis apertures for different flowrates are discussed.



(a)



(b)

Figure 5.1: Figure a shows the complete upper airway geometry with detailed images that show the glottis cross-sectional plane of both 53 (fully abducted) and 10 (partly abducted) degrees. The predefined cross-sectional planes, each oriented normal to the geometric centerline are shown by the grey lines that above the surface rendering. Figure b shows the corresponding CSA distribution along the airway centerline from slightly below nasopharynx to just above the carina as marked by a solid black line on the surface rendering.

5.1 CFD and Experiment results

To perform a fair comparison with the experimental data, a configuration expected to yield a strong jet with associated large pressure loss was selected. The choice of a strong jet flow (partly abducted glottis aperture (10 degrees) at 50 L.min^{-1}), reflects the added complexity of higher Reynolds number where the range of turbulent length scales are greater and the computational demands correspondingly larger.

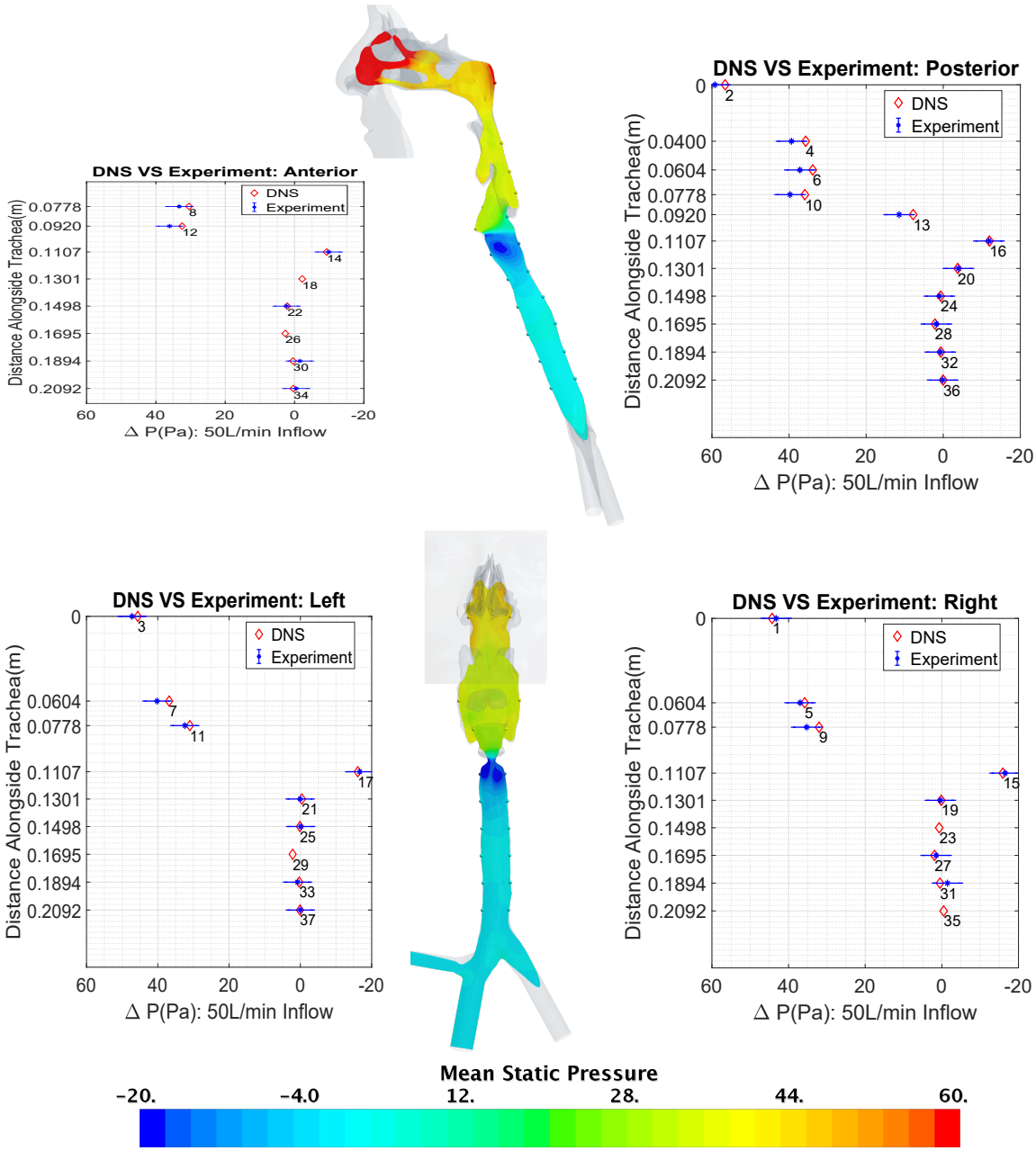


Figure 5.2: Mean static pressure of 10 degrees glottis between laminar simulation results and experimental results at flowrate of 50 L.min^{-1}. The blue dots with the margin bar of ± 3.5 Pa are the experimental results and the red dots are the simulation results. The scale of the vertical axis of each plot is the same as probe locations, as represented by the small dots, on each side of the airway. Value of 0 means the first probe location of each side separately.

Figure 5.2 shows the comparison of mean static pressure between experiment results and the qDNS results (refer to chapter 2 for qDNS description). In total 37 probes attached during

the experiment and these locations are identified by the small dots on the model rendering as shown in the figure 5.2. As can be seen clearly in the figure, the qDNS simulation results lies perfectly within the experimental error, marked for each data point by a ± 3.5 Pa margin bar.

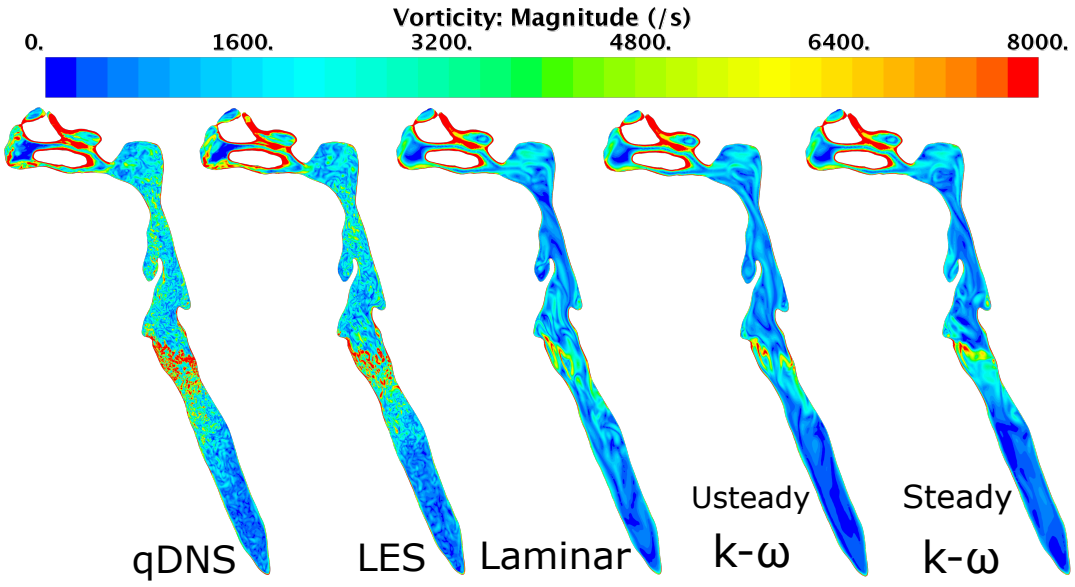


Figure 5.3: Comparison of different CFD models applied for flowrate of 50 L.min^{-1} to partly abducted glottis. Maps of vorticity magnitude are shown on the same sagittal plane for different turbulence models. Reading from left to right, the first two models feature highly resolved meshes: qDNS (15 million) and LES (11 million); the remaining three simulations use the same mesh which contains only 2.9 million elements.

It is recognized that qDNS needs extensive computational resources and is presently not practical if an answer is desired within a reasonable time span. Thus it is useful to find a balanced solution that can achieve certain accuracy but needs much less time compared to the qDNS. Figure 5.3 shows the CFD simulation results for various flow models applied to the partly abducted glottis airway, where vorticity magnitude is plotted, since this is a simple means to indicate distinct features in the flow. It can be seen that as the computational model is reduced both in the mesh density and temporal resolution, the flow details represented by vorticity are correspondingly extensively simplified. However the main jet structure is still evident even for the lowest resolution and least accurate flow model (namely the steady RANS model). From qDNS to laminar simulations, the mesh elements reduced from nearly 15 million to 3 million (the RANS simulations share the same order of mesh elements as laminar simulation), and the

temporal resolution reduces from 1×10^{-5} to 1×10^{-3} second.

The choice of flow model affects the overall total pressure loss between inlet and outlet. The results for the various turbulence models are listed in table 5.1:

Simulation name	Total pressure loss (Pa)	Relative error (%)
qDNS	118.5	0
LES	118.3	0.2
Laminar	108.7	8.3
Usteady k-ω	108.3	8.6
Steady k-ω	106.3	10.3

Table 5.1: Flowrate at 50 L.min^{-1} for partly abducted glottis (10 degrees). This table compares the overall total pressure loss of different flow models. The relative errors compared to qDNS simulation are shown in the right column.

Except the steady RANS simulation, all the rest have relative errors within 10%. The laminar simulation is picked, and used for further analysis rather than the unsteady RANS, since the laminar calculation is both faster and offers slightly better prediction, figure 5.3.

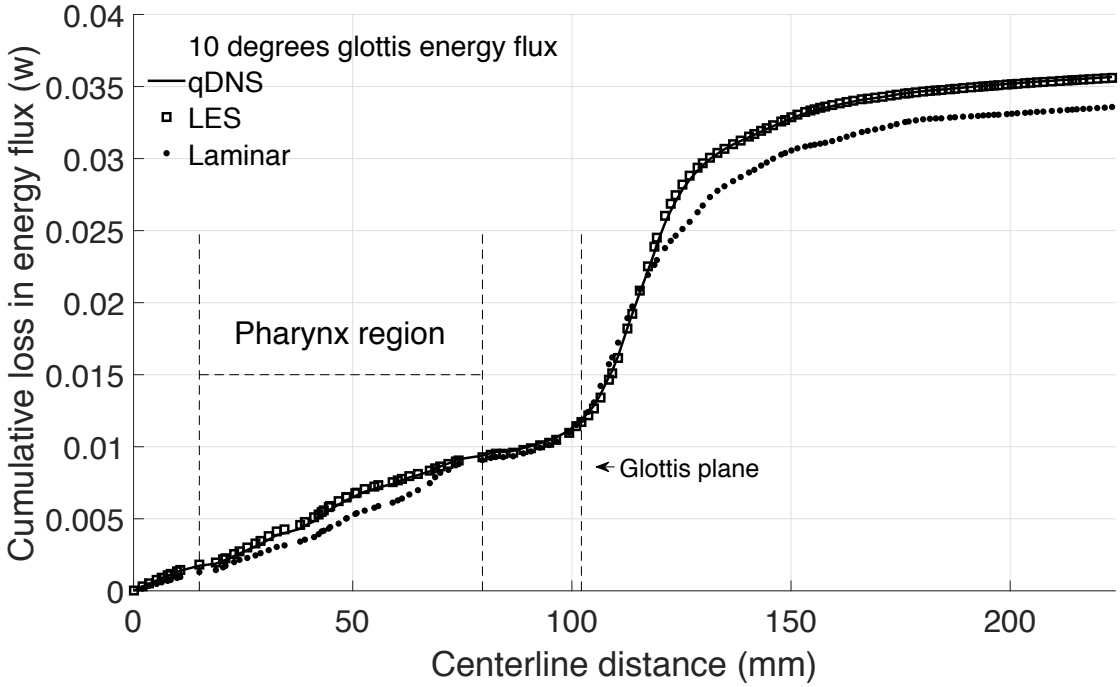


Figure 5.4: Cumulative losses in energy flux among qDNS, LES and laminar simulations.

Figure 5.3 shows both the qDNS and LES simulation capture much more flow structures (revealed by vorticity) compared to the laminar simulation results. All of flow models show the laryngeal jet after the constriction of glottis, but qDNS shows the finest details, whilst LES though similarly rich in features is slightly less detailed. Accordingly, figure 5.4 compares the cumulative energy flux losses along the airway centerline. From the plot we can see that the results of qDNS and LES are extremely similar, however, the laminar simulation has two obvious underestimations of energy loss before and after the glottis restriction. The overall underestimate of the energy flux losses is roughly 7% compared to the qDNS result.

In summary, it shows that LES is an alternative method to qDNS since it can effectively capture most of the flow features. However, for this study the unsteady laminar simulation was deemed to deliver results of acceptable accuracy. The much more coarser resolution of the unsteady laminar solver (100 times larger time step and one fifth mesh density compared to qDNS simulation) enabled a broad range of flowrates to be considered, with adequate accuracy (around 8%) to reveal the trends.

5.2 Effect of glottis aperture and flowrates

To study the effect of glottis aperture on the laryngeal jet, two different configurations are studied. Each of them is characterised by the angle of glottis aperture at its apex: in this study a 53 degree (fully abducted) and 10 degree (partly abducted) glottis is simulated, with aperture areas of 1.98 cm^2 to 1.16 cm^2 respectively, for a tracheal airway area of 2.64 cm^2 at the level of the first tracheal ring.

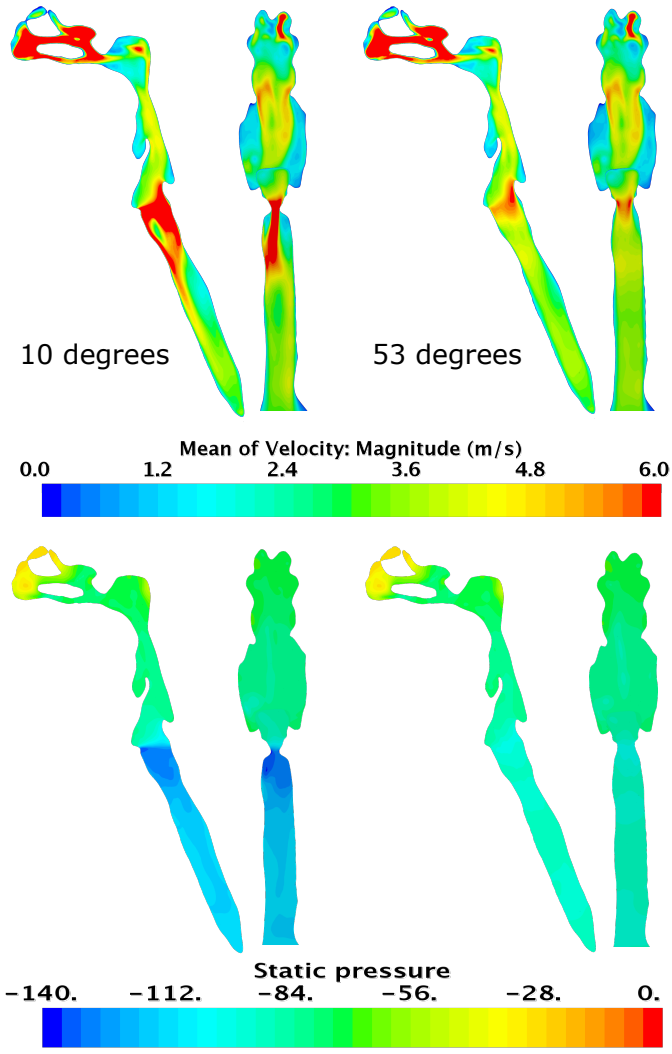


Figure 5.5: Left two views (above and below the velocity bar) show sagittal plane images of the 10 degrees glottis model.Right: same but for 53 glottis geometry. Both of them are viewed from the same sagittal planes with the mean velocity (top) and static pressure (bottom) are shown on the planes with the inlet static pressure preset as 0.

As shown in figure 5.5, the partly abducted glottis (10 degrees) geometry has a much stronger

jet compare to that of the fully abducted glottis (53 degrees) geometry. Accordingly, the normalized static pressure scalar scene indicates that the stronger jet will induce a larger static pressure drop (cause by local high velocity). This potentially can increase the risk of unexpected airway collapse,e.g., EILO [21].

Comparing the total pressure loss along the predefined cross-sectional planes, figure 5.6 first note that the rapid pressure drop at the beginning of the pharynx region is caused by the cross-sectional area increase. Secondly, the apparent fluctuations in total pressure in the pharynx are partly an artefact of the averaging procedure. Likewise the total pressure recovery after the glottis is again an averaging artefact, whereas static pressure partly recovers, the flow total pressure must decrease. The preceding energy flux plot (figure 5.4) is thus a more reliable indication of loss.

Further downstream of the glottis, the jet is dispersed and the flow reattaches, so that area averaging reflects the true flow total pressure. Thus comparing the difference in total pressure from the pharynx to the carina, it is evident that the reduction of glottis aperture can highly increase the total pressure drop across the restriction (nearly doubled with 40% area reduction.)

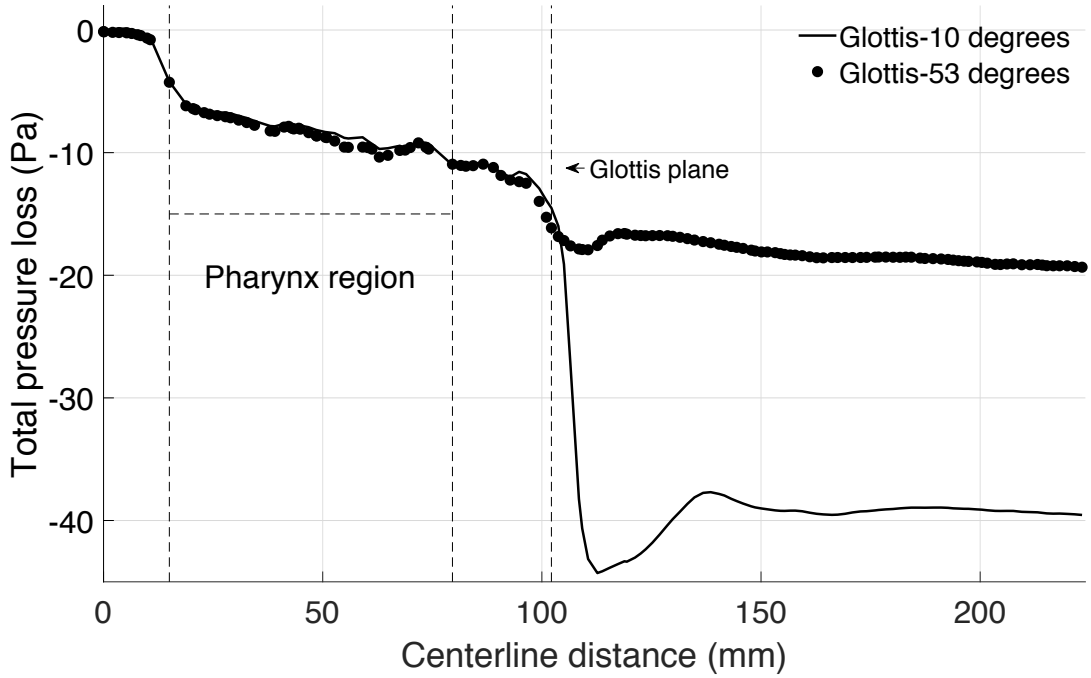


Figure 5.6: Total pressure loss distribution along the tracheal centerline of fully and partly abducted glottis at flowrate of 50 L.min^{-1}.

Figure 5.7 shows the comparison of resistance (defined in terms of total pressure loss) between two configurations of the glottis at 50 L.min^{-1}. By adopting a flowrate average of total pressure for each cross-section (see equation in chapter 2), the anomalies in total pressure can be removed leading to a sensible distribution of airway resistance. Note that for a fully abducted glottis, there is no abrupt transition in resistance from pharynx to the glottis. Further downstream, tracheal resistance is likewise negligible. By contrast, with reduced glottis area, a stronger and more persistent jet enters the trachea with associated energy dissipation extending over much of the tracheal length. Only towards the carina the rate of increase in resistance fall to negligible levels.

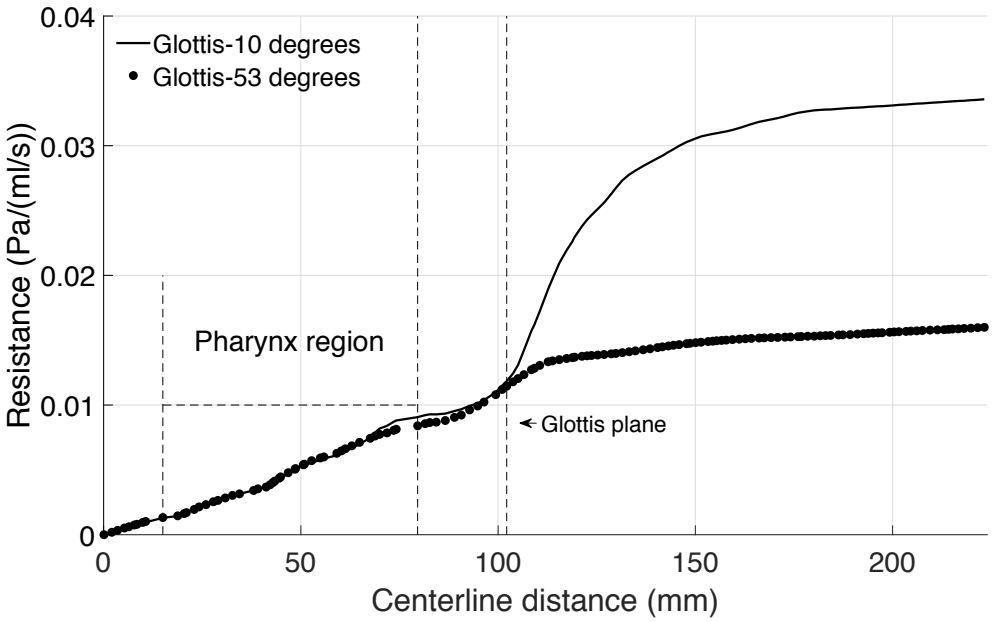


Figure 5.7: 53 and 10 degrees glottis resistance of flowrate 50 L.min^{-1}.

Figure 5.8 compares the total pressure losses along the centerline of the geometry of 10 degrees glottis with various flow rate from 20 to 80 l.min^{-1}. With the increasing of flowrate, although the overall total pressure loss is significantly larger, the pattern of pressure drop is remarkably similar.

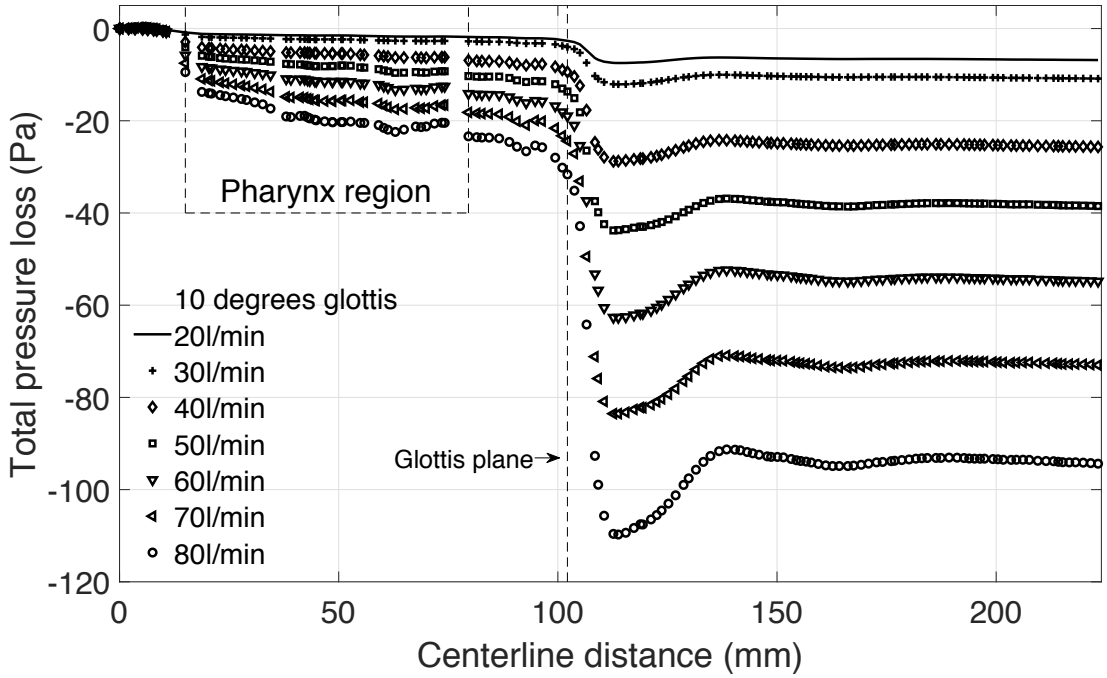


Figure 5.8: 10 degrees glottis total pressure loss variations with multiple flowrates.

From the plot (figure 5.8) it can be seen that the partly abducted glottis airway shows only about 10 Pa pressure loss at moderate breathing rate (30 L.min^{-1}) which is minor. However the pressure loss can increase dramatically while doing moderate exercise (flowrate at 80 L.min^{-1}). This level of pressure drop can potentially lead to exercise-induced partial closure of the vocal fold which can be mistaken as asthma. Thus the glottis aperture opening level need to pay attention during the clinical check cause the high possibility of airway collapse for patients who have a narrow glottis aperture.

From a fluid mechanics perspective, the glottis functions similarly to an orifice and the orifice loss of a constant cross-sectional ducts can be predicted approximately using the quadratic relationship between pressure loss and flowrate [148]. By plotting the log relationship of the total pressure loss against flowrate (figure 5.9). It shows at higher flowrates, a simple quadratic scaling of pressure loss with flow occurs, with exponent nearly 1.9.

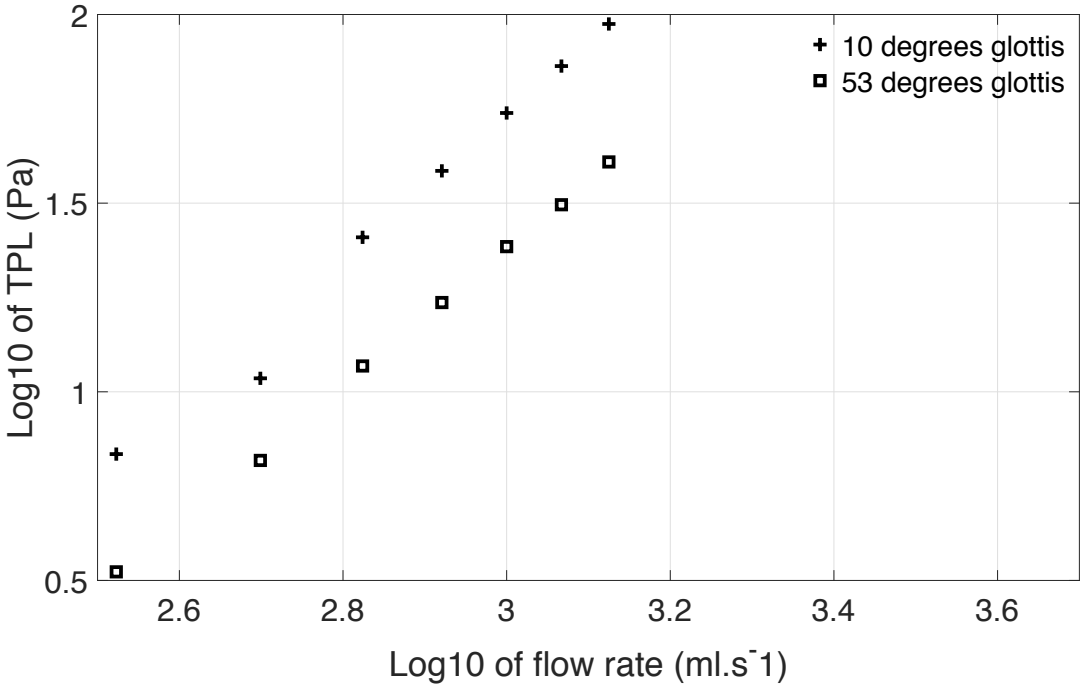


Figure 5.9: Log_{10} flowrate versus $\log_{10}$ total pressure loss.

Chapter 6

Tracheal stenosis flow analysis

Current objective methods assessing tracheal compression include: Computed Tomography (CT), Magnetic Resonance Imaging (MRI) and Lung Function Tests [149]. As high-resolution tomographic techniques develop, there are corresponding improvements in speed, accuracy, and ease with which tracheal compression can be imaged. Consequently, patients with these conditions sometimes undergo serial imaging to monitor disease progression.

Although routine interrogation of axial slices from a tomographic dataset may suffice for evaluating some airway abnormalities, several limitations are associated with single plane images, especially when displaying complex 3D relationships. The limitations of axial image evaluation can, however, be overcome with the aid of 3D reconstructed images from the original datasets. These provide not only a more anatomically meaningful display of complex structures but also allow more exact geometric quantification and the possibility for predictive analysis using computational fluid dynamics (CFD).

CFD has been applied for some time to predict airflow in the large airways, with computing power now sufficient to resolve the detailed flow dynamics [42, 150]. Processing the flow predictions provides measures such as pressure loss, resistance and wall shear stress which relate directly to patient symptoms [16, 45, 110, 151, 152, 153, 154]. Studies [155, 156, 157, 158] have

applied computational predictions to virtually model the effects of geometry modification on surgical intervention, with Chen et al pointing out the use of CFD to evaluate the effectiveness of tracheal surgery [114]. The potential scope for such applications is large, but our present, imperfect knowledge of the healing process, among other factors, means actual post-operative geometries may differ considerably from those intended; as yet relatively few studies have included models based on actual post-operative geometries.

This study describes the application of imaged geometries and computational methods to monitor disease progression from serial scans and the effect of surgical intervention. Image segmentation is used to produce a virtual 3D model, followed by computational simulation to estimate the associated tracheal airway resistance. However clinical imaging studies may exclude a portion of the airway; this can lead to inflow domain truncation affecting predictions; the mechanisms and functional consequences of this are discussed.

6.1 Material and Methods

6.1.1 Image Data

The pathological trachea used for this study was from a patient with a retrosternal goitre amongst other co-morbidities, particularly chronic obstructive pulmonary disease (COPD) [18]. The subject underwent several CT scans, due to complex medical history. Patient permission was obtained to analyze a series of clinical chest CT scans. Research and Ethics compliance was obtained from the local Joint Research Compliance Office reference 15SM2566. The data was analyzed using current American Thyroid Association (ATA) imaging test guidelines [159] for surgical intervention.

CT scans were obtained at quiet breathing before and after surgical intervention as follows,

where the prefix T denotes the intervening time in months between scans and the equipment used is given in parentheses:

- T0, (Phillips ICT 256), reconstructed as 1 mm thick slices;
- T4, (4 months after T0, Phillips Brilliance 64), reconstructed as 3 mm thick slices;
- T15, (15 months after T0, Phillips Brilliance 64), reconstructed as 2 mm thick slices;
- T23, (23 months after T0, Phillips Brilliance 16), reconstructed as 3 mm thick slices.

The in-plane resolution was 0.6 mm per voxel in all cases. The patient became symptomatic at T13, i.e., two months before the last pre-operative scan at T15. All three pre-operative scans were compared with a further CT scan (T23), two months following total thyroidectomy. Figure 6.1 shows a sagittal view of one slice for all the CT scans with the yellow marker at the minimum cross-sectional position, except T23.

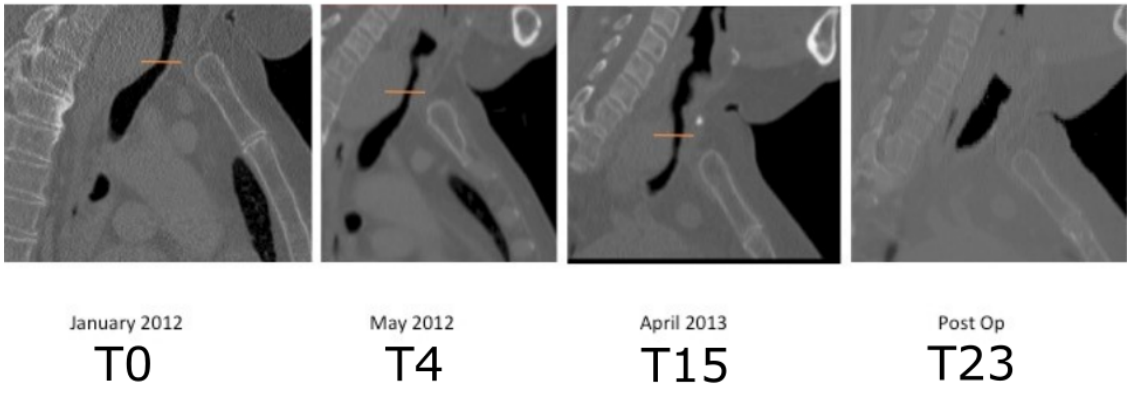


Figure 6.1: Sagittal view comparison corresponding to the point of maximal constriction in all scans. The yellow line in the picture indicates the location of minimum cross-sectional area (except T23).

Symptomatically, the patient had extreme difficulty taking every breath at T15, but reported total relief post thyroidectomy.

6.1.2 Airway Geometry Definition

Reconstruction of the tracheal lumen was performed using automated airway segmentations (Mimics Innovation Suite: Materialise, Technologielaan 15-3001 Leuven, Belgium), as illustrated in figure 6.2 for the T15 geometry.

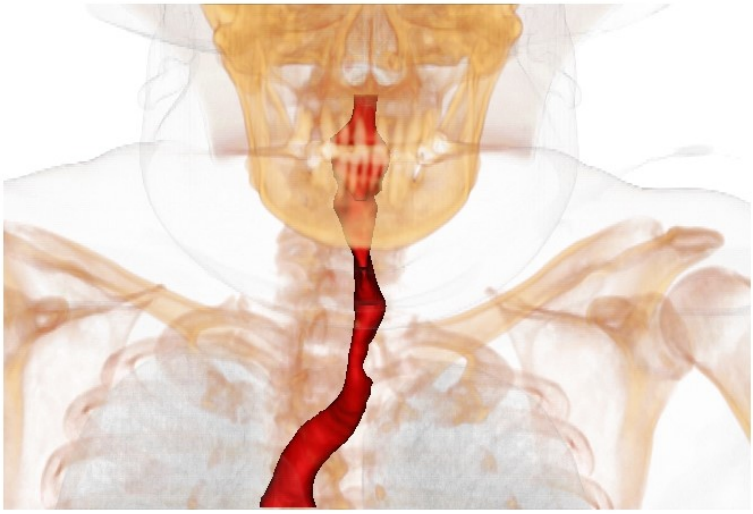


Figure 6.2: Volume rendering of the subject's anatomy at T15 showing the skeleton with a surface rendering of the segmented airway.

The overall length of the imaged portion of the airway varied depending on the scan protocol: T0 includes part of the trachea (below first trachea ring and above carina) whereas the other studies included a greater portion of the airway, either to the nasopharynx or to just below the carina, but not simultaneously both.

A trachea centerline was generated from the reconstructed airway volume using the Vascular Modelling Toolkit (VMTK) previously described [160]. An in-house MATLAB (R2016b, The MathWorks, Inc., Natick, MA, USA) code generated planes normal to the local centerline direction along the airway. The plane boundary was found where it intersected the surface geometry, allowing the cross-sectional area to be calculated, as described by Bates et al [150].

Tracheal airflow was calculated by CFD, using Star-CCM+ 11.04.012-r8 (Siemens Product Lifecycle Management Software Inc, Plano, TX, USA 75024) for both mesh generation and to solve the Navier–Stokes equations. Quasi-steady simulations were performed predominantly for a flow rate of 392 ml.s^{-1} (23.5 l.min^{-1}), corresponding to the peak flow rate for a half sinusoidal inhalation of duration 2 s at a tidal volume of 500 ml, using Large Eddy Simulation (LES) with the WALE sub-grid scale model in STAR-CCM+. Other flow rates (30, 40 and 50 l.min^{-1}) were also simulated for T15 to examine the feasibility of a power law fit for flow resistance. From previous studies [16, 110, 153, 161], LES as opposed to Reynolds-averaged Navier–Stokes (RANS) is the preferred CFD model to capture the jet structures emanating from the tracheal lumenal constriction [162]. It has been found that airway simulations may closely match experimental results for an airway, with observed differences attributed to limitations of mesh resolution [116, 163, 164]. The present computations were primarily performed on meshes of 3.8 million polyhedral elements, including wall prism layers with an averaged first layer height of 0.013 mm to 0.023 mm and time step 10^{-4} s. For all the simulations, both inlet and outlet section have been extended outwards by extrusion to avoid reverse flow effect at both ends. Simulations ran for 0.2 s physical time with the first 0.05 s discarded to allow any start-up transient to dissipate and results were averaged over the remaining period. A mesh independent study was also carried out and is shown in D.1.

6.2 Results and Discussion

6.2.1 Geometry

The area distribution curves show three pronounced minima, highlighted by larger markers (figure 6.3). From left to right these correspond to: (i) base of the tongue (associated with partial airway collapse as the subject was imaged in the supine position), (ii) glottis, (iii) the point of maximal tracheal compression. The scan data at T0 captures a relatively short region, approximately between the first tracheal ring and just above the carina. The T15 geometry also ends 9 mm above the carina, though includes the supra-glottic airway. Although scan

T4 includes the main bronchi, the area distribution does not extend to the origin since the definition of the tracheal centreline terminates before the carina.

Additional geometries were created as follows: (i) T15-S, where the airway section of T15 above the first tracheal ring is substituted by an extruded pipe; (ii) T4-L is an extension of the actual imaged airway T4, which did not include the larynx. To enable comparison of inflow disturbances, the missing supra-glottic airway was substituted for by that at T15, adjusted to ensure a smooth transition. To investigate the effect of inflow domain truncation associated with reduced field of view of the image data, additional studies were also performed on geometries denoted T4 and T15-S. Since the carina was not imaged in every one of the original data sets, anatomical landmarks in the image data were used to translate all area distributions to a common carina origin, with increasing negative distances corresponding to more superior locations. Figure 6.4 shows a rendering of the geometries used for CFD analysis.

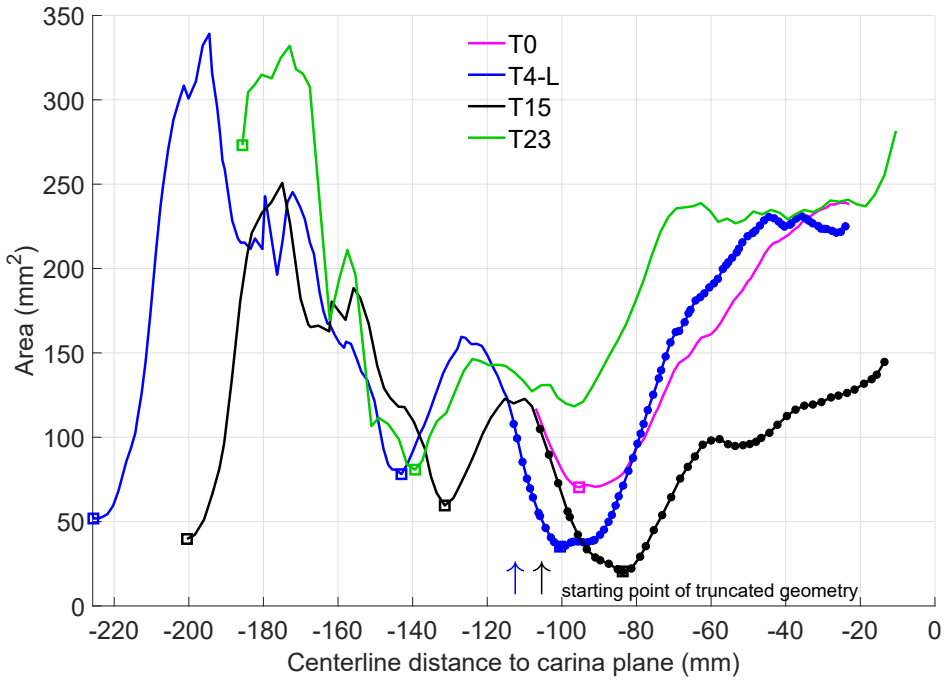


Figure 6.3: The cross-sectional area distribution for all the tracheal geometries within this research.

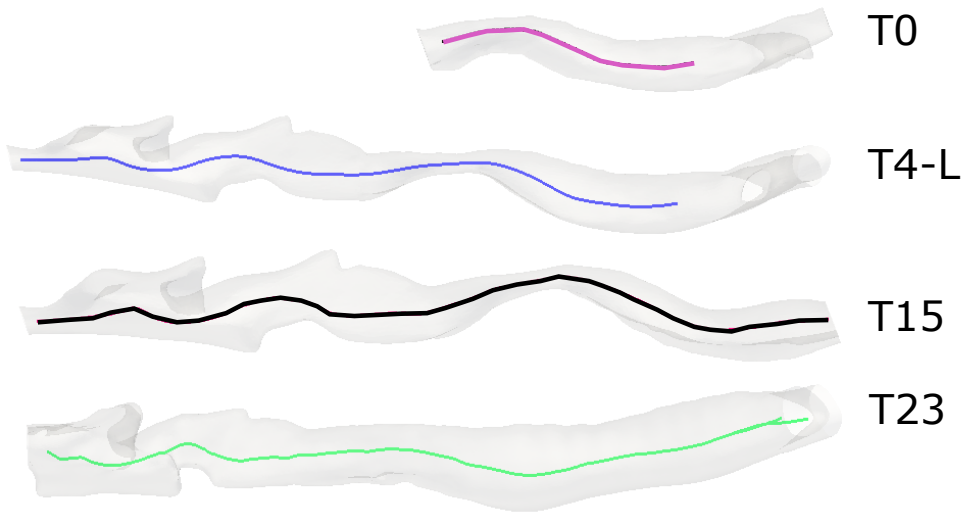


Figure 6.4: Geometries in sagittal orientation with centerline

The length of the constricted portion was defined as a contiguous segment with lumen cross-sectional area (CSA) reduced by 35% [165] or more compared to the first tracheal ring area, Table 6.1. The table shows that in the 15 months between the scans labelled T0 and T15, the minimum area reduced from 70.3 mm^2 to 20.5 mm^2 while the constriction length is not changing too much. The T15 constituting a constriction of 82.5% relative to first ring lumen and the minimum CSA for the pathological cases is displaced from its normal location at the glottis, but reverts to there post-operatively, table 6.1. The progressive change of compression that occurred after T4 corresponded with significant breathing difficulty reported by the patient.

CT scans	Constriction Length (mm)	Cross-sectional Area Minimum (mm^2)	Glottis Area (mm^2)	First Trachea Ring Area (mm^2)
T0	17.0	70.3	Not Available	Not Available
T4-L	32.0	35.2	84.1	148
T15	32.7	20.5	66.9	117
T23	0	80.8	80.8	146

Table 6.1: Geometric data of tracheal lumens. The percentage constriction is defined as the CSA ratio: $(CSA_{FirstRing} - CSA_{min})/CSA_{FirstRing}$ and is 82.5% for T15.

6.2.2 Flow Analysis

Air flowing through the airways loses energy due to viscous dissipation; this energy loss translates to the airway resistance component of the work of breathing. As outlined in D.2, the rate of energy loss can be described using an energy flux integral, defined as

$$E_{F,i} = \int_S (\mathbf{u} \cdot \mathbf{n})[P_s + \frac{1}{2}\rho|\mathbf{u}|^2]dS \tag{6.1}$$

where $\mathbf{u}$ is the velocity vector, ρ is the flow density, P_s is the static pressure and $\mathbf{n}$ is the unit normal vector of the cross-sectional planes that is perpendicular to the centerline; the slope at a point on a plot of E_F against distance from inflow indicates the local rate of dissipation. Energy dissipation can be considered to comprise two parts [17]: that required to overcome wall friction, and an excess due to flow non-uniformity. At first, a localized constriction increases the dissipation rate by raising wall friction; downstream where the geometry typically expands, a strongly non-uniform jet flow is produced that dissipates through internal shear layers, increasing losses. Likewise, where the trachea is significantly deviated, the turning required of the flow introduces bias, augmenting losses. Flow losses are commonly estimated from a combined application of pipe friction correlations and loss factors; an attempt to characterize idealized tracheal stenosis in terms of an appropriate loss factor has been applied previously [19]. Here the geometry is more complex and it is thus of interest to compare estimates based on simple loss factors with the results of computations, as discussed below.

Effect of Progressive Constriction on Inhalation Resistance and Energy Loss

Comparing T4-L and T15, the geometry of T15 is both highly compressed and deviated, which leads a shrinkage in axial length. Moreover, the progressive compression is associated with changes in the position of CSA_{min}. After thyroidectomy, case T23, the position of CSA_{min} reverts to its normal location at the glottis. The overall airway resistance at the prescribed flowrate of 23 l.min^{-1} for T15-Long, (0.68 Pa.ml^{-1}.s), scales (using an exponent of 1.96 as

described further) to 1.14 Pa.ml^{-1}.s (11.7 cm.H2O.l^{-1}.s), which is much in excess of the normal total airway resistance (let alone tracheal resistance), $\approx$ 1 cm H2O.l^{-1}.s [18].

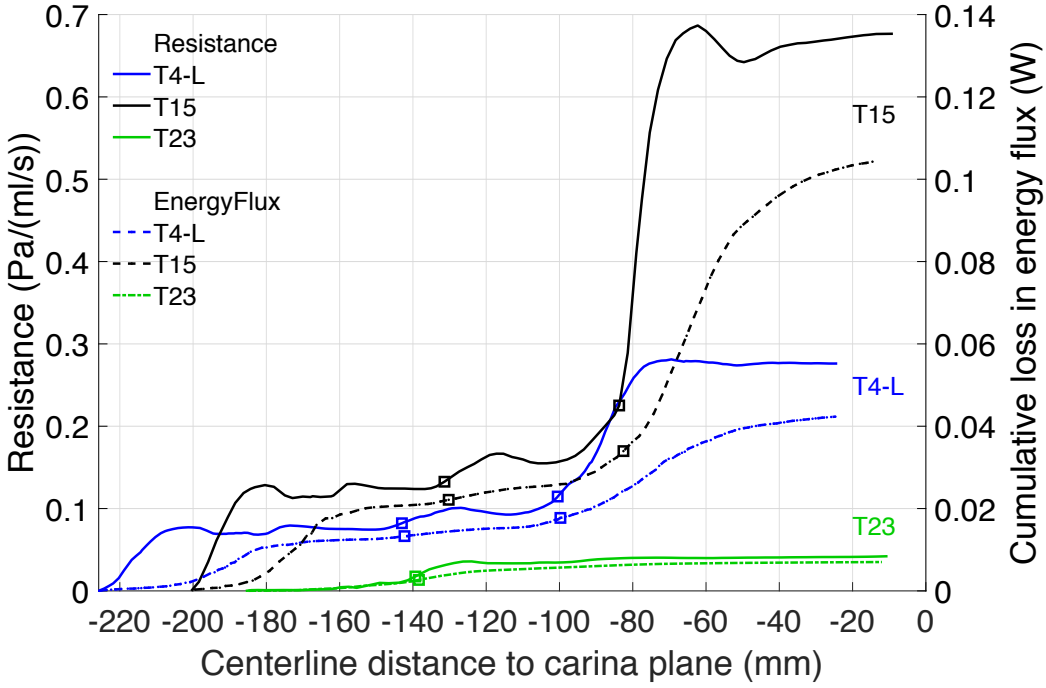


Figure 6.5: Resistance and cumulative energy flux of two pre-operative cases and the post-operative case. The extra maker of each line corresponds to the latter two locations of area minima as described above, namely the glottis and the most constricted region in the trachea.

For both T4-L and T15, resistance rises abruptly at two locations: the first due to the expansion of the area below the base of the tongue, and the second by the goitre compression below the glottis. Figure 6.5 shows there is also a small resistance increase within the range of $x = [-140 - 100]$, associated with the moderate increase in CSA after the glottis, figure 6.3. In both T4 and T15, the largest component of resistance occurs at the most restricted section of the trachea ($x = [-100 - 80]$), especially for T15. Overall, geometry T15 has a resistance about 2.4 times that of T4-L (details shown below and D.4).

However in T15 the contribution of tracheal compression is greater: downstream of the compression (figure 6.5, beyond position -100 mm), resistance increases by a factor of 3 between T4-L and T15, or almost matching the quadratic power: $(CSA_{min,T4}/CSA_{min,T15})^2$. The sud-

den drop in resistance where the lumen expands downstream of the compression is associated with the averaging of pressure across a larger area, whereas the actual energy dissipation occurs gradually as the jet breaks down and mixes. This can be seen by comparing the flow power loss curves, equation 6.1, right axes in figure 6.5. Localized reductions in flow resistance merely reflect averaging effects as the jet mixes, whereas flow power continuously reduces, providing a better means of assessing the energy cost of the constriction. In contrast, the resistance of the post-operative geometry is almost entirely attributable to the glottis, with the value of 0.05 $Pa.ml^{-1}.s$ closely matching normal and idealized tracheas [45, 116] adjusted for comparable flow rate. This indicates a clear objective surgical benefit from the perspective of fluid dynamic efficiency.

Insight into the fluid dynamic response to the airway lumen reduction between T4-L and T15 can be gained by comparing velocity distributions at selected planes, figure 6.6, in conjunction with volume renderings of vorticity, (indicating shear intensity, associated with energy loss). Plane G is defined at the glottis position, with three further planes at, after and further downstream of the CSA_{min} point. The vorticity rendering of figure 6.6 indicates energy dissipation upstream of Plane G (glottis) in both cases, corresponding to area expansion downstream of the tongue base. This is also shown in figure 6.5 and approximately mirrors the initial increase in resistance. Although not as significant as the losses associated with the compression, it shows the potential of postural airway collapse to augment resistance. (Note differences in the supra-glottic resistances of T4-L and T15 merely reflect the scaling required to fit the supra-glottic geometry of T15 onto T4).

At the respective CSA_{min} locations (plane labelled Min), both lumens are elliptical rather than circular, with the smaller lumen of T15 producing a stronger jet than in T4-L. Planes P1 and P2 of both T4 and T15 show highly asymmetric flow downstream of the constriction, caused by the complex geometric shape of the trachea; consequences of such flow non-uniformity have been discussed by Bates at al [150]. The considerably higher downstream vorticity in case T15 is also evident, signifying greater energy dissipation, figure 6.5.

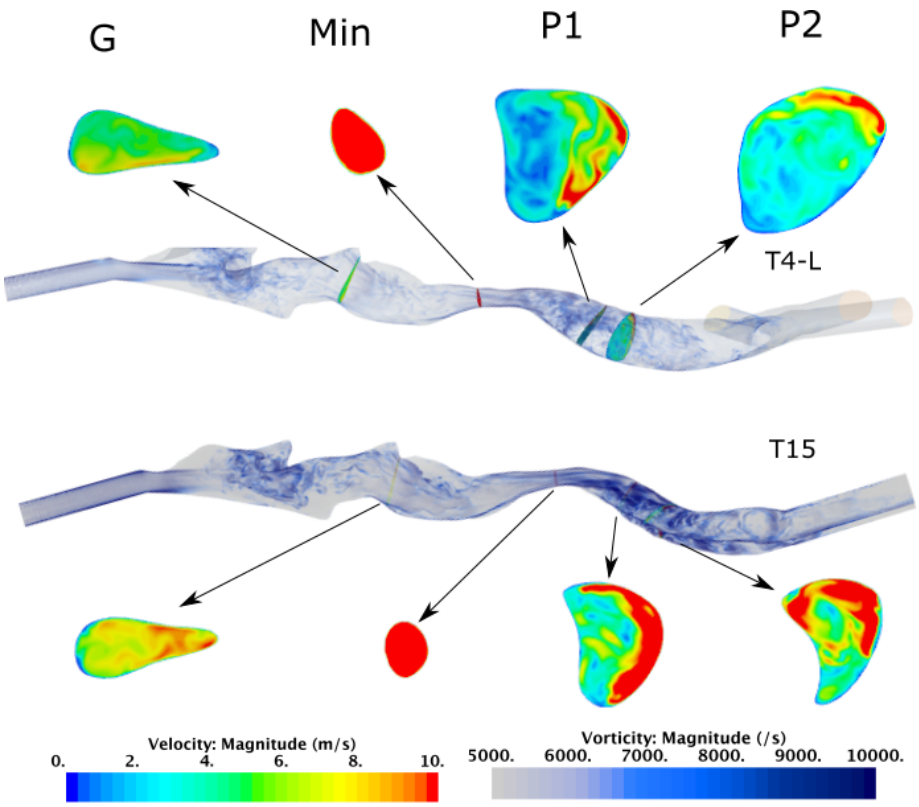


Figure 6.6: Jet structure: Top is T4-L and bottom is T15. Plane labelled as G and Min represent the planes located at glottis and minimum area position. Plane P1 means the first posterior plane after the jet and P2 is the second posterior plane further downstream.

Effect of Inflow Truncation: Upstream Boundary Moved Below Glottis.

Clinically acquired scan data may not encompass the whole airway. Consequently we have also computed flows for T4 and T15-S which are truncated below the glottis. Figure 6.7 compares the flow structure in the full and truncated T4 geometries (respectively labelled T4-L, T4), likewise in figure 6.8 for T15 geometries. Both truncated geometries are extended by several mean diameters at inlet using simple extrusion, to which a steady uniform inflow is applied. The locations of the cross-sectional planes are as in figure 6.6, except for the replacement of the glottis plane (G) by a sub-glottic inflow plane (SGI); the solution methodology is otherwise unchanged.

Truncating the geometry results in a more uniform inflow at plane SGI in both T4 and T15-S.

Truncation also removes the flow disturbances present in the full geometry, which result from upstream jet breakdown following constrictions at the tongue base and glottis, as shown by the vorticity volume renderings. In both cases, vorticity rendering shows jet breakdown to occur earlier in the full geometries; whilst greater persistence of the jet flow in the truncated geometries is shown by comparing the cross-sectional velocity distributions at planes P1 and P2. These results accord with findings regarding the influence of upstream disturbances in other studies[110, 166, 167].

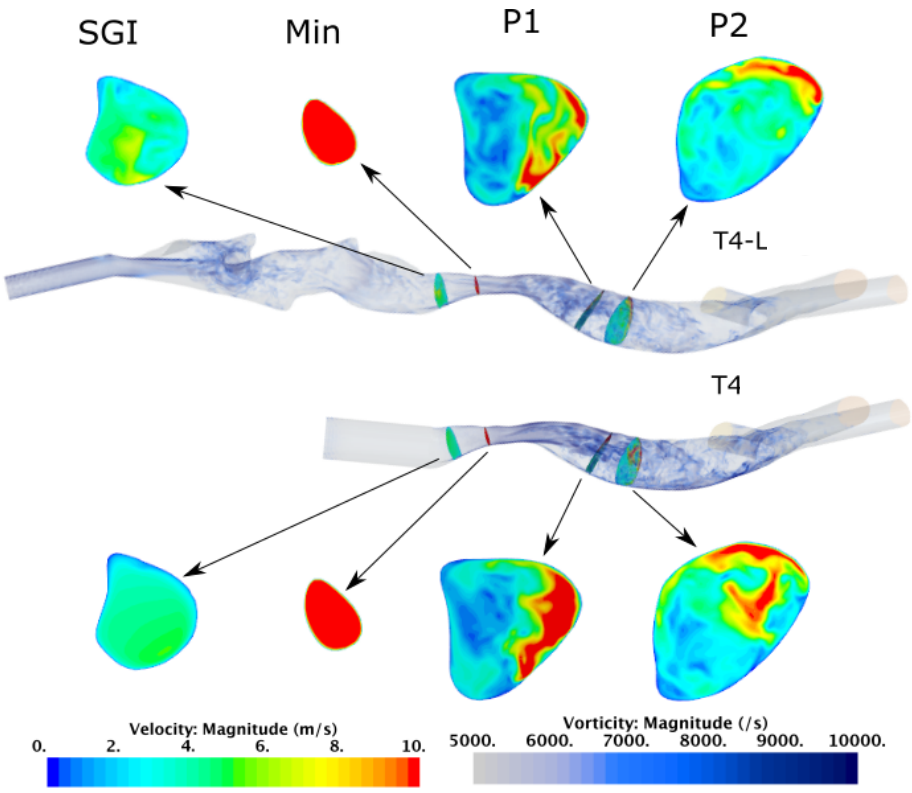


Figure 6.7: Jet structure of T4-L compared with T4-Short. Plane SGI means supraglottic inlet plane, the other three planes are as described above.

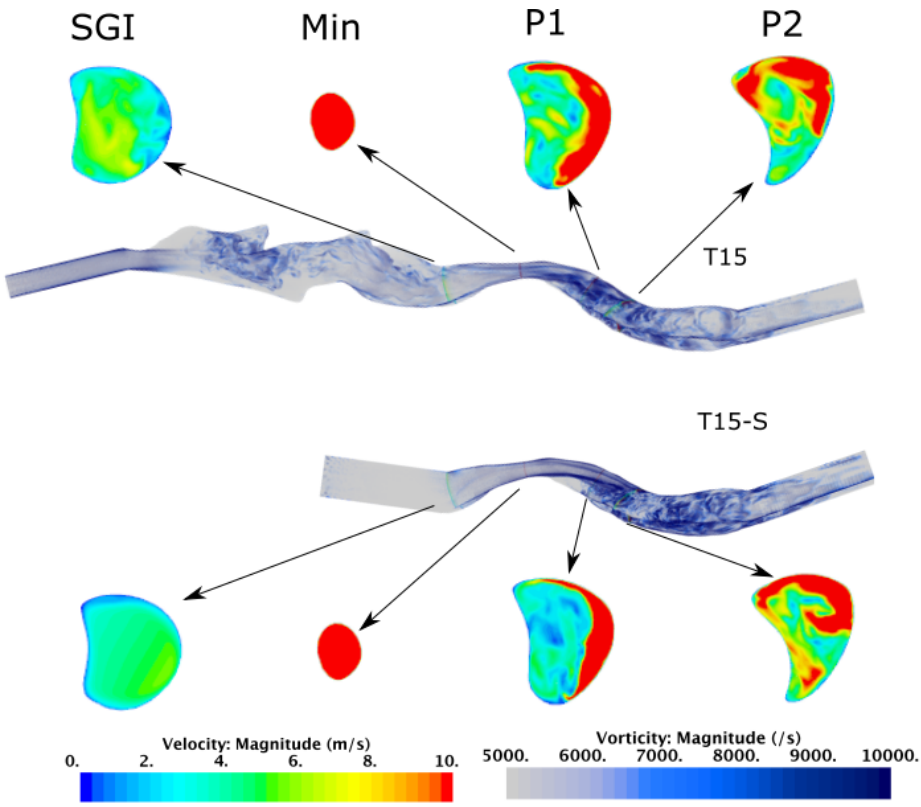


Figure 6.8: Jet structure of T15 compared with T15-S. Plane SGI means subglottic inlet plane while the other three planes as described above.

Truncation of the superior geometry has a significant effect on the pattern of inhalation energy loss, as seen in figure 6.9, which includes plots of cumulative changes in total pressure times volume flux integrated over the lumen, relative to a common origin at the site of truncation. Although the eventual accumulated losses within the same geometry range are similar, for the truncated geometry the rise in energy loss is delayed by approximately 10 mm compared to the full geometry. This mirrors the delay in the jet breakdown, observed in the vorticity renderings. Further downstream of the constriction, losses in the truncated geometry eventually surpass those in the full geometry (at around 20 mm upstream of the carina).

Corresponding plots for airway resistance are also shown in figure 6.9. Differences in airway resistance first become evident in the resistance curve overshoot approximately 70 mm upstream of the carina; after a further 10 mm downstream, the magnitude of the difference settles to an approximately constant offset. Despite the evident difference in the jet flow behaviour caused by upstream geometry truncation, the resistance associated with the constriction is only 7%

greater for the truncated case.

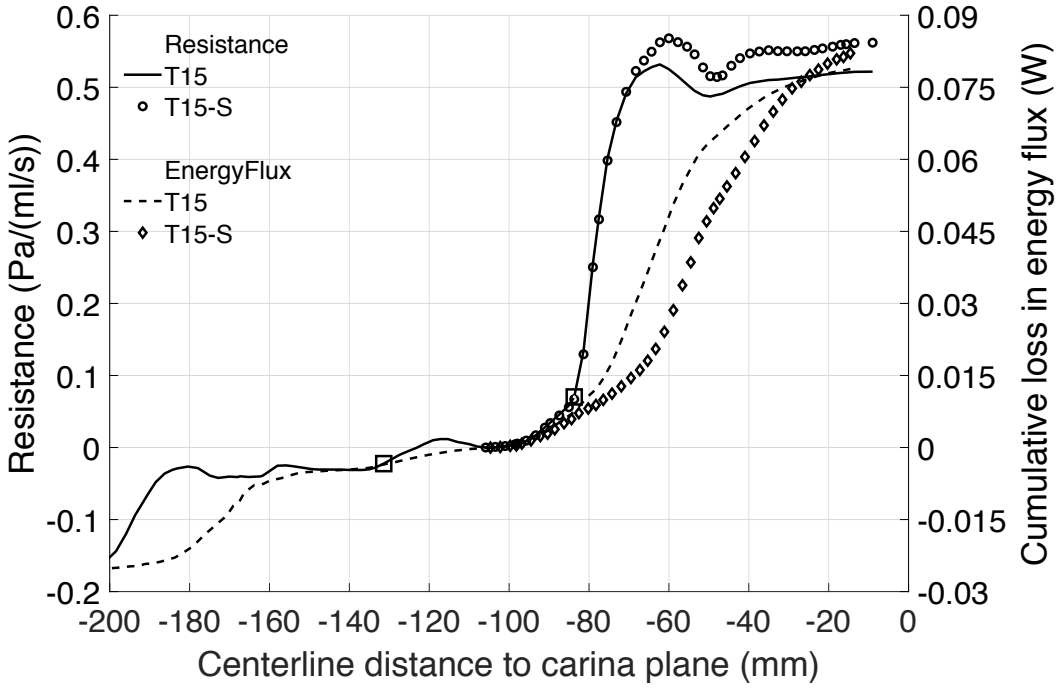


Figure 6.9: Resistance and energy flux plot for T15 and T15-S. The extra square marker represents the glottis and minimum point position.

To take this investigation one step further, another two extra geometries are generated based on the T15-S: T15-SG1 and T15-SG2. Both of them are made by adding an extra smaller extruder on top of the current extrusion used by T15-S and this structure will introduce more turbulence. Figure 6.10 shows the geometries and with the turbulence intensity scalar. As noted within the figure, the label 'TI-ref' which indicates that the way of calculating the turbulence intensity here is using a reference velocity rather than the conventional definition (details can be found in D.3). Table 6.2 lists the inflow constriction ratio referring to T15. As can be seen from the table, a natural glottis blockage ratio is 43% of the geometry within this study and T15-SG1 has almost the same blockage ratio while T15-SG2 is a bit over blocked.

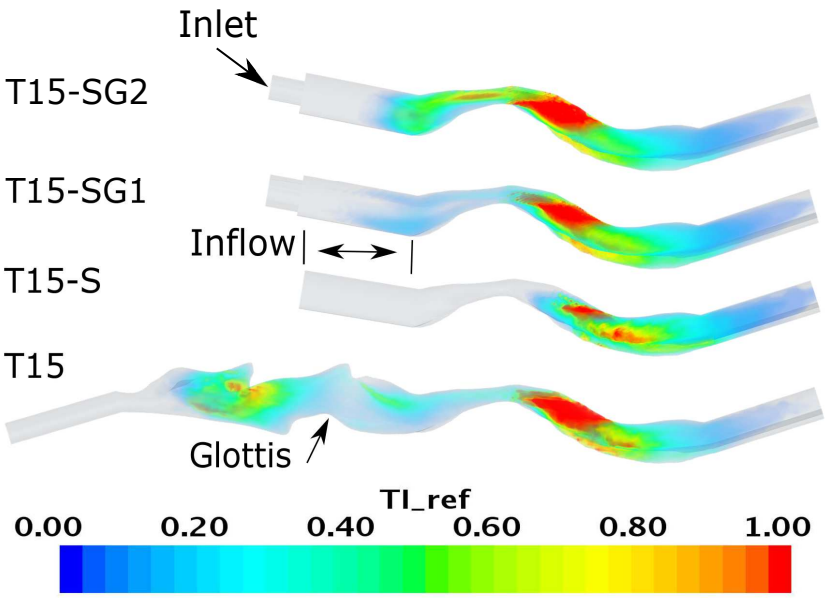


Figure 6.10: Turbulence intensity average on the T15 first tracheal ring mean velocity

	Glottis Area (mm^2)	First Trachea Ring Area (mm^2)	Inflow Constriction Ratio (%)
T15	66.9	117	43
T15-S	Not Available	Not Available	0
	Inlet Area (mm^2)	Inflow Cross-sectional Area (mm^2)	
T15-SG1	68.3	121	44
T15-SG2	38.2	121	68

Table 6.2: Geometric data for T15 and short cases

Table6.3 lists the turbulence intensity referred to the fist trachea ring mean velocity which gives an direct image of the relative turbulence intensity level compared to the natural glottis.

TI-ref (%)	Fist Trachea Ring (Inflow)	Minimum Section	Outflow
T15	15	21	16
T15-S	4e-6	3e-5	30
T15-SG1	10	12	24
T15-SG2	55	57	18

Table 6.3: Turbulence intensity value for all T15 geometries

As described above, the existence of inflow disturbance will cause the jet early breakdown downstream and slightly less energy loss that can attribute to the relatively weak jet. Figure 6.11 compares all the T15 short geometries with the T15 complete geometry. The black plot represents the same constriction ratio as the natural glottis shows close match with T15 plot. This indicates that although the way of generating inflow disturbance is different, the effect of pre-dissipated inflow on the behaviour of downstream energy loss is identical. Furthermore, by focusing on the T15-SG2 plot which has 25% more constriction than the natural glottis constriction shows that the rate of energy dissipation is larger than all the other geometries. In summary, we can closing story of the truncation effect on the overall tracheal resistance is minor by figure 6.12 and it is possible to get a fairly accurate energy loss prediction by simply adding the same constriction above the inflow to achieve the same inflow disturbance.

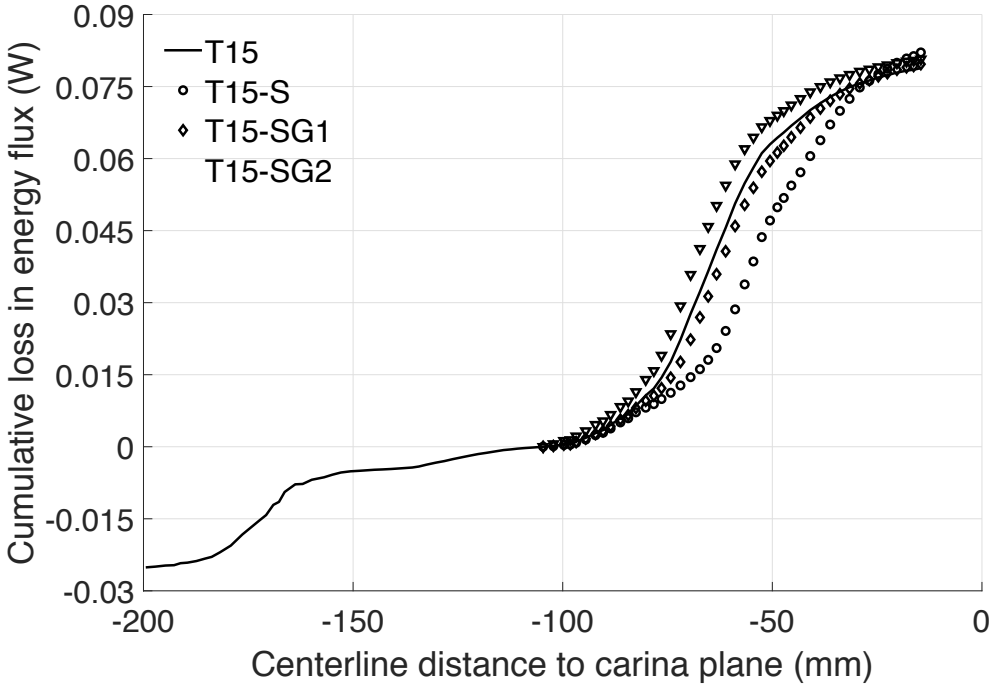


Figure 6.11: Energy flux comparison with various inflow conditions

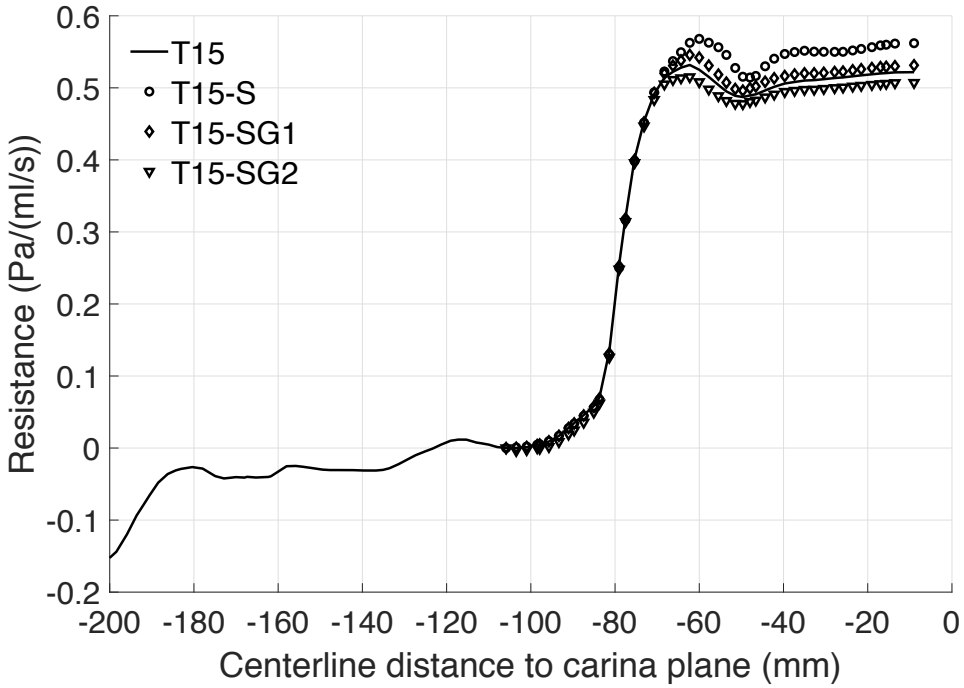


Figure 6.12: Resistance comparison with various inflow conditions

Inspiration Versus Expiration

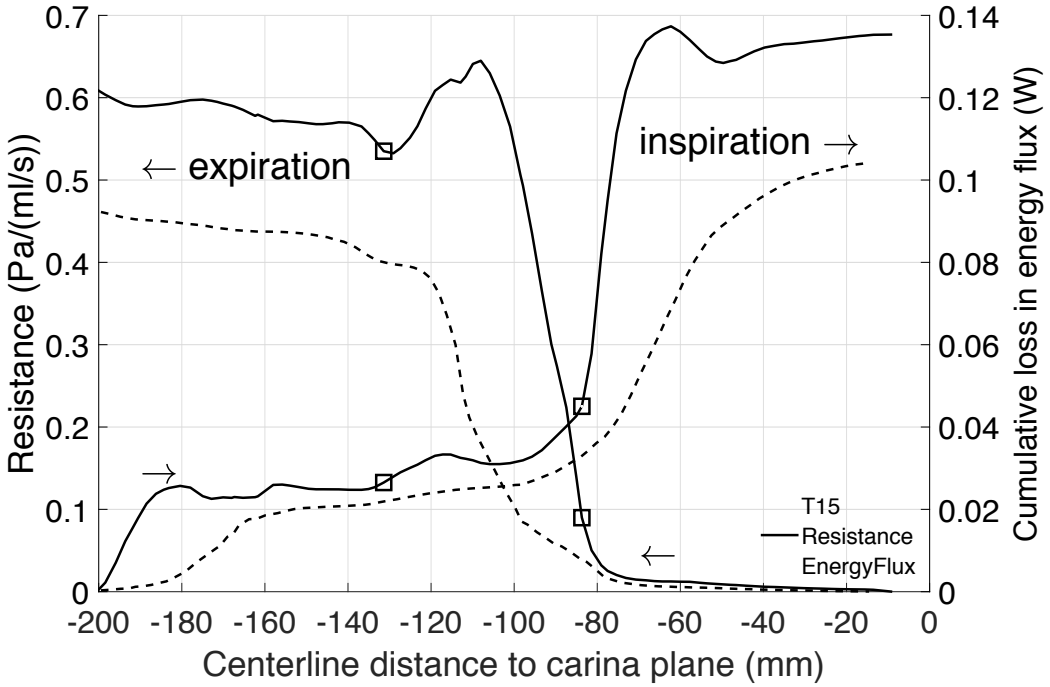


Figure 6.13: Resistance and energy flux plot for T15-Long at both inhalation and exhalation condition. The extra square marker represent the glottis and minimum point position.

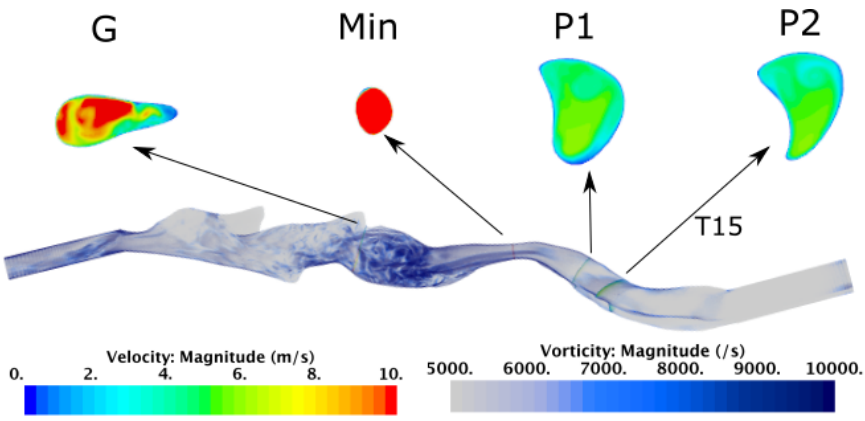


Figure 6.14: Jet structure of T15-Long exhalation.

Previous studies on tracheal airflow have placed greater emphasis on inspiratory rather than expiratory flow, but either can cause difficulties. Expiratory airway resistance and energy loss are compared with that during inspiration in figures 6.13. Losses associated with mixing of the expiratory flow entering the trachea from the bronchi (present in the T4 geometry) were

found to be minimal (of order 3%, D.4) suggesting that truncation above the carina (neglect of bronchi) minimally affects loss, although this is not expected to hold if bronchial stenosis were present.

During expiration, the flow traverses the airway area variation (figure 6.3) in reverse. For this subject area variations (from contraction to expansion) are approximately symmetric about respective minima. Reading the energy loss and resistance curves in figure 6.13 from right to left, following the expiratory flow direction, confirms the correspondence between area variation and loss. The rapid expansion inferior to the constriction, which resulted in the jet losses for inspiration, now presents simply a constriction to the returning flow, with minimal associated loss. On the other hand, the expansion in area superior to the constriction now creates a jetting of the expiratory flow directed through the glottis, evident in the vorticity and velocity plots of figure 6.14. The contribution of the constriction to airway resistance and to energy loss is similar for both inspiration and expiration. The supra-glottic area variation (from -200 mm to -130 mm), due to partial airway narrowing, contributes significantly to the inspiratory loss; expansion of the expiratory flow into the nasopharyngeal space would likely produce an additional loss if it were included.

Power Law Fit of Pressure Flow Relation

Both truncated and full geometries of the most constricted geometry T15 (82.5% constriction, see table 6.1) were tested for a range of inspiratory flow rates (table 6.4):

	Flow rate (l/min)	23.5	30	40	50
A	T15 Pressure loss between inlet and outlet (Pa)	276.8	446.5	774.5	1223.9
B	T15 Pressure loss between SGI and outlet (Pa)	206.8	331.9	582.3	911.3
C	T15-S Pressure loss between SGI and outlet (Pa)	223.6	357.6	616.3	950.9

Table 6.4: Data for power law fit for flow rate vs pressure loss of the most constricted geometry T15-Long.

Row B of table 6.4 shows the total pressure loss of T15 within the common geometry section (between plane SGI and outlet) shared with T15-S. As described previously, the truncated geometry shows slightly larger pressure loss than the full geometry measured over a common section, due to the different inflow conditions. Assuming a power law relationship between resistance and flowrate, table 6.4 indicates an exponent of 1.96 for the full geometry (T15), and 1.91 for T15-S. Both are closely comparable with the power law exponent of 2 suggested by Brouns et al [19] for an approximately equivalent constriction of 85% in an idealized model. Using the suggested K factor of 1.2 [19] as an effective orifice loss parameter, their proposed model (see D.5) predicts a loss of approximately 276 Pa and 90 Pa for the T15 and T4 geometries respectively at 23.5 l.min^{-1}. This is in good agreement with the overall tracheal loss for T15, (276.8 Pa), and T4, (109 Pa), at the same flowrate. However the present geometries show proportionately much higher losses in the supraglottic airway; discounting these, the comparison is not as good, with the computed subglottic loss for T15 (206.8 Pa) considerably lower (column 3 of table 6.4).

Figure 6.15 compares the computed pressure loss distributions for different flow rates up to 50 l.min^{-1}, and those derived by simply scaling the curve calculated for the lowest flow rate (23.5 l.min^{-1}) according to the square of the flow rate. The close agreement between calculated and scaled losses throughout the varying geometries of both the supraglottic and subglottic portions appears remarkable.

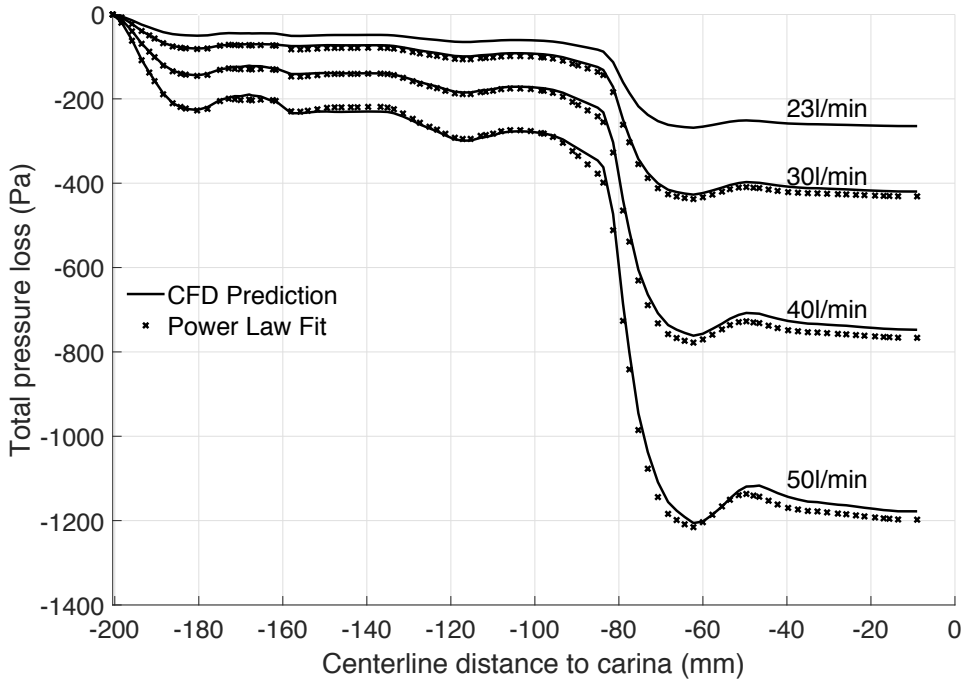


Figure 6.15: Power law predictions of T15 geometry with four different flow rates.

Chapter 7

Discussion, conclusions and suggestions for further work

In this work, computational modelling was applied to study the airflow in the airways from the nose to the carina, divided into separate investigations: (1) nasal air flow and conditioning performance; (2) flow in the larynx; (3) flow in the pathologically compressed trachea.

The study of airflow in the nasal airways set out to investigate the influence of geometry on the behaviour of the flow and how this affected its performance in terms of heat and water exchange. In total 10 healthy subjects were selected and the geometries were segmented by an ENT surgeon Dr. Cetto using Mimics, as described further in his thesis [123]. The scan data for each subject comprised two separate acquisitions, the first in the normal state (refer to as congested) and the second approximately 10 mins after application of a topical alpha adrenergic agent xylometazoline hydrochloride 0.1% drop, administered by a clinical assistant. All the subjects placed their heads in a coil and remained immobilized between scans [123].

The investigation of flow in the larynx compared the inspiratory flow behaviour and associated pressure losses for flow in a whole normal subject specific airway with the vocal folds fully abducted (maximal glottis aperture) with corresponding results for the case where the vocal

folds are partly abducted (small glottis aperture). The effect of different apertures of glottis was studied with multiple flowrates that ranging from 20 to 80 L.min^{-1} with 10 L.min^{-1} interval.

The retrospective pathological tracheal flow studies include four geometries that were obtained from three pre- and one post-surgical scans. The flowrate used for this study corresponds to the peak flow rate for a half sinusoidal inhalation of duration 2 s at a tidal volume of 500 ml (23.5 L.min^{-1}).

7.1 Nasal airway flow: discussion and conclusions

In the first section of nasal cavity analysis, pure flow mechanics is analyzed which provides the foundation for latter heat and mass transfer analysis as the air-conditioning of nasal cavity is highly correlated with the flow patterns.

From the geometric analysis of subject D, it shows the CSA distribution along the cavity centerline from nostril and nasopharynx plane increases initially and then encounters the first decrease at nasal valve constriction. After the anterior septum, the extruded turbinates lead to the variations of the CSA. Further posteriorly, after the posterior septum, two sides of the cavity join as one and shows a sudden increase of the CSA. This CSA distribution pattern is particularly evident for congested cavity due to the consistency narrower cavity until the posterior septum. Comparing the congested and decongested cavities CSA, we can see that the decongestion can dramatically increase the CSA after nasal valve. However, it is evident to notice that the congested cavity CSA distribution along the pre-defined CSA planes does not indicate the nasal valve as the minimum area, but for decongested cavities it dose. There are potentially two possible reasons, one of them can attribute to the narrow cavity at congested state, while the other reason might due to the definition of cross-sectional planes, e.g. the magenta line in figure 3.2 which is quoted from Zhao et al. paper and the way they define those cross-sectional plane are different from that of this study. Thus the plot does not show an indication of nasal valve at all.

Applying the definition of cross-sectional planes, as illustrated for a given subject, to all the cohort subjects provided a means to calculate the averaged CSA variation as shown in plot 3.17. Firstly, we can see the mean CSA distribution across the cavity volume are comparable to the results from Zhao et al. [2] which is also a mean intranasal distribution from 22 healthy subjects. Secondly, the change in CSA distribution with decongestion for the single subject D was found to be similar to that for the cohort mean CSA distribution for the decongested cavity.

In order to quantify the geometry change caused by decongestion, metrics including cavity surface area, cavity volume, SAVR are defined and calculated. We can conclude that decongestion can enlarge the cavity CSA roughly one and half times comparing to that of congested state. For the cohort results, it also shows that the surface area before and after decongestion does not change much (even with the same median value), and it also does not show statistical significance within the level of 5% from Wilcoxon signed-rank test. On the contrary, the rest of the geometric measures show statistically significant changes. Although the cavity surface and cavity volume change by different amounts, the cavity SAVR shows a statistically significant decrease after decongestion. By evaluating the geometry in more detail, we compared the SAVR changes after decongestion of top, middle and lower cavities separately. Not surprisingly, the results show that only the change of SAVR of top cavities is not statistically significant after application of a topical decongestant. Interestingly, the anterior min CSA was not found to be significantly altered by decongestion. However, this does not imply the absence of change, given the greater relative uncertainty in lumen segmentation at an area minimum. Moreover, reprocessing the data in terms of a plane (likewise defined by maximum anterior mean flow speed, but free to move up to the anterior septum) may produce a different result.

The distribution of Reynolds number of the cavity indicates that both the anterior and posterior part of the cavity have relatively higher values. In the anterior part of the cavity, the maxima Reynolds number is located around the nasal valve, while for the posterior cavity it

is located around the nasopharynx where the geometry cross-sectional area get narrowed down caused by the presence of the base of the tongue. Although the redistribution of mass flow split between left and right cavities can alter the dominance of cavity's Reynolds number as shown in figure 3.3, the bilateral Reynolds number of the decongested cavity might keep nearly the same as that of the congested cavity. This is can be seen through the mean Reynolds number of the cohort simulations. On the other hand, the change of flowrate can effectively increase the corresponding Reynolds number, i.e., double the flowrate can nearly double the Reynolds number intranasally, as shown in figure 3.18. In general, the Reynolds number in the turbinate region (after plane 1V and before PS) has an order of 1000 at the higher flowrate of 30 L.min^{-1}. This is consistent with the results reported by other researchers.

Although each side of the cavity has different flowrates due to the different anatomical shapes, it shows the same flow characteristic that nasal valve in the anterior cavity experience the peak velocity of the cavity and the velocity reduces gradually with the increase of CSA. After the flow passes the nasal valve, it can lead to some recirculation region that caused by the high flow speed at the nasal valve. In addition, recirculation also can be found after the posterior septum where the cavities joined as one and the immediate sharp turn of the pharynx (figure 3.4 and 3.5). This flow pattern gets amplified by the decongestion effect. Apart from that, it also can be seen that the flow velocity of the lower and middle cavity are generally higher than that of the top section of the cavity due to higher mass flow portion accordingly. The walls shear stress distribution on the cavity surface shows that the vestibule, as well as the head of the turbinates, have the local highest WSS for both congested and decongested cavities. However, for the head of superior turbinate, it might not always have a high WSS value because of the flow redistribution that caused by decongestion, e.g., as shown in figure 3.6.

When the flow goes through the cavity from nostril to nasopharynx, the total pressure decreases, or equivalently, the resistance, increases from anterior to posterior of the cavity. Averaged over the whole cohort, statistical testing shows that decongestion significantly reduces pressure loss or resistance. In fact, decongestion is found to reduce the total pressure loss (and likewise

reduce resistance) by nearly half, for either higher or lower flowrates.

Furthermore, as reported in previous study that the anterior cavity is the most resistive region of the cavity [118] due to nasal valve and the flow impact on turbinates head, thus the significance test also performed both in the anterior and posterior part of the cavity separately. The insignificant testing results indicate that the anterior part of the cavity is the most resistive region either before or after the decongestion. However, the posterior cavity resistance does show a statistically significant decrease after the decongestion, a two-thirds reduction of the median value.

A scaling and modelling approach has been applied while analyzing the hydrodynamic characteristics of the cavity flow. It has been well studied for both circular and non-circular ducts but with constant CSA, i.e., Shah [168] and Yilmaz [169]. The asymptotic analysis reported by Muzychka et al. [141] shows the flow Poiseuille number has a constant value and it is in the range between 12 and 24 for developed laminar flow in a duct with constant CSA. Consequently, the calculated mean Poiseuille number of the bilateral nasal cavity for all the subjects shown in figure 3.28 and the same distribution for unilateral cavities is also being plotted in figure 3.39. The overall Poiseuille number of each subject's cavity all seems below about 50, which is slightly high compared with the value get from laminar developed duct flow. This is expected due to non-constant as well as the arbitrary shape of the nasal cavity CSA. However, after splitting the nasal cavity into two sections by plane 1V, namely anterior and posterior nasal cavity, we can see that the Poiseuille number in the anterior part of the cavity is relatively higher than the mean values of 50 because the flow is still developing after it passes the nasal valve. As proposed by Muzychka et al. [141] the developing flow in the short duct would have a Poiseuille number roughly 2.6 times larger. The CSA distribution of cavity before plane 1V looks like a converging-diverging nozzle, might not quite for congested cavities but it is evident for decongested cavities. Considering the Poiseuille number in the posterior half cavities (between 1V and PS), the distribution is quite even along the cavity and with the value around 30. The slightly higher Poiseuille number of the nasal cavity is acceptable

because the flow through the cavity is way more complex than that of an ideal pipe. Although the nasal cavity CSA is also not constant and has an arbitrary shape, however, it is surprising that the even distribution of Poiseuille number in the turbinate only region that shows the hydrodynamics of the flow filed behaves like laminar flow under both higher and lower flowrates.

The heat and water exchange of the nasal cavity is first introduced by the surface dry heat flux and water flux. The results show that both sides of the vestibule surface are suffering the highest heat and moisture loading, although similar order of loading also being found on the turbinates head. This distribution pattern is associated with the wall shear stress distributions as well and consistent with the previous researches.

The air-conditioning performance of the nasal cavities is also quantified by multiple measurements, e.g., intranasal temperature and moisture content level distribution, film coefficients as well as non-dimensional film coefficients. The increase of total inhaled air can accordingly reduce the state of conditioned air, which is indicated by the dropping of air temperature and moisture content level at posterior septum. By contrast, the increase of heat and film coefficients with the increase of flowrate indicates that the higher heat and moisture transfer efficiency, although this is not enough to compensate for the effect of increasing volumetric flow. The investigation also varies the ambient conditions at the same flowrate and reveals that the nose can achieve higher conditioned air temperature and humidity with the reduction in the demand posed by the external environment. It is surprising to notice that the mass film coefficient of the nasal cavity will not change under different ambient conditions, while the heat film coefficient shows large variations.

The cohort simulation results show that doubling the flowrate can roughly reduce the air temperature at the posterior septum about 5% and the moisture content level 10% under both congested and decongested states, although the efficiency of cavity heat and water transfer are increased (reflected by the higher heat and mass film coefficient). Similarly, the geometry

change caused by decongestion also shows a negative effect on air-conditioning, which is in a similar order as the effect of doubling the flowrate. It can roughly reduce the conditioned air temperature at the posterior septum about 1°C and 10% for moisture content level. Furthermore, the statistical analysis (Wilcoxon signed-rank test) shows both the change of the geometry (by decongestion) and the change of flowrate (doubled) have a significant reduction in the conditioned air temperature and humidity level at the significant level of 5%. Thus the decongestion not only reduces the air-conditioning performance but also it shows this reduction is statistically significant. By contrast, the heat and moisture transfer efficiency are increased significantly by doubling the flowrate. Statistical testing showed there to be no bias in the dominance of one side of the nasal cavity over the other; furthermore similar relations between metrics and parameters were found to hold for both the unilateral and bilateral cavities. This suggests that we can treat each half cavity as an individual geometry.

Within the limited sample size of this study, the ratio between cavity mean frictional coefficient and film coefficient, as well as Stanton number, indicates that the heat and mass transfer of the cavity behaves similar to the fully developed pipe flow, as shown in table 4.6. This is consistent with the preceding findings about the flow hydrodynamic characteristics as reflected by the Poiseuille number.

In summary, the decongestion, as well as the change of flowrate, has a statistically significant effect on reducing the nasal cavity overall resistance and the final state of conditioned air. Furthermore, the hydrodynamics of the flow in nasal airway behaves more or less like a fully developed duct flow, especially in the posterior part of the cavity. The approach to a fully developed thermal and mass transport boundary layer in the posterior nasal cavity also applies to the heat and mass transfer.

7.2 Laryngeal airway flow: discussion and conclusions

During inspiration, for the purpose of delivering flow efficiently onwards to the lungs, the larynx ideally should minimize flow disturbances and pressure losses. In this limited study, we wish to determine how pressure losses are affected by flowrate and by geometry. The effect of reduced glottis aperture was shown to dramatically increase the strength of the laryngeal jet, as shown in figure C.2b, and the associated pressure loss, shown by figure C.2b. Damage to the larynx can significantly reduce glottal aperture and during strenuous exercise, the increased flow velocity can lower the static pressure and cause conditions such as EILO (exercise-nduced laryngeal obstruction).

As the laryngeal jet increases in strength, the associated flow Reynolds number increases e.g., from 1547 to 6189 as flow increases from 20 to 80 L.min^{-1} for fully open glottis (53 degrees) and from 1668 to 6675 for a partly open glottis (10 degrees model), with corresponding reductions in static pressure. Fully resolved computations of the flow become excessively demanding at higher Reynolds number so that some form of turbulence modelling is required. Comparison with experiment for a demanding flow (50 L.min^{-1}), showed excellent agreement (within the experimental accuracy) for highly resolved (qDNS) calculations (approximately 15 million mesh elements, and 1e-5 second time step), figure C.2b. Excellent agreement was obtained for LES modelling at slightly reduced mesh density and coarser time step (11 million mesh elements, 1e-4 second time step), gave 0.2% relative error refer to qDNS simulation. Unsteady laminar computations at one-fifth of the mesh density showed an error of approximately 8%, whilst steady RANS modelling showed slightly higher error (10%) compared to qDNS with the same mesh density as laminar model.

For both fully abducted and partly abducted glottis, pressure loss is found to scale nearly quadratically at higher flowrates (exponents respectively 1.8 and 1.9 for fully abducted vs partly abducted). This scaling is similar to that found in previous investigations (e.g. Brouns et al. [19]).

7.3 Tracheal airway flow: discussion and conclusions

During inspiration, flow in the normal trachea is dominated by the dissipation of the laryngeal jet, as described in the preceding section. However in the pathological trachea, the presence of tracheal stenosis or external compression may alter tracheal geometry to such extent that the trachea becomes a significant or even dominant in airway resistance to flow.

This study describes the first use of energy flux analysis to investigate the mechanics of flow losses associated with reduction in tracheal lumen in a progressive retrosternal goitre, both pre- and post-operatively. The effects of inflow domain truncation are systematically incorporated. Analysis reveals differences in the location of jet breakdown with truncation and the effectiveness of simple quadratic scaling of loss despite geometric complexity.

Typically, to diagnose respiratory pathology, a spirometry test is undertaken. The traditional flow volume loop (FVL), provides good insight into a wide variety of respiratory disorders [170]. However, although FVLs are extremely useful they have various limitations, mainly the inspiratory limb is effort dependent and they cannot give localized quantities as CFD does. The approach proposed in the present study complements spirometry by providing mechanistic insight into the effects of an extrinsic compression on breathing mechanics. Firstly, the airway morphology can be quantified by volumetric reconstruction. Secondly, using computational fluid dynamics, the distribution of resistance and energy loss throughout the length of the trachea can be derived, providing an objective measure of the effect of a progressive extrinsic compression.

A common issue in applying CFD to patient image data is that of inflow domain truncation. Capturing the supra-glottic airway allows its contribution to airway resistance to be included, but it may not be imaged due to other clinical priorities. The necessity of including the complete or partial airway above the larynx to fully model tracheal flow has been addressed previously,

including [16, 110, 171, 172]. In this work, inflow truncation was shown both to remove flow disturbances due to shear layer breakdown in the supra-glottic airway and to delay the breakdown of the jet issuing from the tracheal contraction. The effect of inflow disturbances is of broad interest [167]. Although the present results point to differences in flow behaviour that may prove significant for applications such as aerosol delivery, inflow truncation was found to have relatively minor (less than 10%) effect on predicted flow loss due to tracheal compression. Computation of the expiratory flow was found to produce similar values of airway resistance to that during inspiration.

The major contribution to energy dissipation and airway resistance was found to be associated with the region of minimum area. Since predictions of subglottic losses differ significantly from idealised model, factors other than supra-glottic losses, such as the degree of lumen and axis distortion, may be significant. Nevertheless, it was found that losses scaled with constriction area and with flow rate nearly as a simple quadratic power law, similar to the scaling observed in the idealized model of Brouns et al [19].

Finally, an important simplification of the present model is the assumption of a rigid airway. The effect of the different pressure loadings on the tracheal wall during inspiration versus expiration may produce very different cross-sectional shapes and thus values for tracheal resistance, analogous to those seen in upper airway collapse [173]. The CT studies were acquired in quiet respiration, to minimize the effect of dynamic airway collapse. Dynamic airway CT imaging is available but requires specialized equipment, is technically challenging, particularly in breathless patients, and increases the radiation dose to the patient. It also would require procedures to merge typically low frame rate CT or MRI images with the high-temporal-resolution discretisation required by CFD (as described in Bates et al. [135]).

Apart from considering the dynamic imaging, it is also necessary to investigate the particle deposition through the trachea geometry with stenosis; the effectiveness of inhaled aerosolized medications have been studied extensively in recent decades [174], but not for such geometries.

7.4 Further work

There are several aspects that can be improved for further studies.

Firstly, as mentioned above, it would be worthwhile to incorporate dynamical imaging while performing subject specific analysis if possible. Some work in this direction has been introduced by Bates et al. study [135]. Future work on laryngotracheal flow limitation could make use of data from dynamic airway imaging when these data sets become more readily available in order to incorporate the effect of airway geometry changes on pressure and energy losses.

Next, from the modelling perspective, currently the mucosal membrane is assumed to be sharing the same property as water and it also assumes an unlimited water and heat supply. Ideally, a separate model study coupled with experimental validation could address the present shortcomings and lead to a more physiological membrane model. However it would be technically challenging to perform the measurements needed to assess the water resupply rate and other parameters required for a more realistic model.

Thirdly, the lack of expiratory or breathing cycle is another limitation of this study that can be improved by performing extra studies. In addition, this study only includes the healthy subject's nose, thus in the future work including the pathological cohort study could bring more direct clinical benefits.

Last but not least, from the statistical perspective, due to the limitation of subject specific study, a larger cohort study should be investigated. The non-dimensional analysis is also encouraged in all future work.

Bibliography

[1] Tilman Keck and Jörg Lindemann. Numerical simulation and nasal air-conditioning. *GMS current topics in otorhinolaryngology, head and neck surgery*, 9, 2010.

[2] Kai Zhao and Jianbo Jiang. What is normal nasal airflow? a computational study of 22 healthy adults. In *International forum of allergy & rhinology*, volume 4, pages 435–446. Wiley Online Library, 2014.

[3] Michael Wolf, Sara Naftali, Robert C Schroter, and David Elad. Air-conditioning characteristics of the human nose. *The Journal of Laryngology & Otology*, 118(2):87–92, 2004.

[4] Niels Mygind. *Nasal allergy*. Blackwell Scientific Publications, 1978.

[5] Donald F Proctor and Ib Harald Peder Andersen. *The nose, upper airway physiology and the atmospheric environment*. Elsevier Biomedical Press, 1982.

[6] DONALD F Proctor. Airborne disease and the upper respiratory tract. *Bacteriological reviews*, 30(3):498, 1966.

[7] FP Primiano, GM Saidel, FW Montague, KL Kruse, CG Green, and JG Horowitz. Water vapour and temperature dynamics in the upper airways of normal and cf subjects. *European Respiratory Journal*, 1(5):407–414, 1988.

[8] Pedro Alberto Escada, Carlos Lima, and José Madeira da Silva. The human olfactory mucosa. *European Archives of Oto-Rhino-Laryngology*, 266(11):1675–1680, 2009.

[9] Pedro Escada. Localization and distribution of human olfactory mucosa in the nasal cavities. *Acta medica portuguesa*, 26(3):200–207, 2013.

[10] Bruce W Jafek, B Murrow, R Michaels, D Restrepo, and M Linschoten. Biopsies of human olfactory epithelium. *Chemical senses*, 27(7):623–628, 2002.

[11] Donald A Leopold, Thomas Hummel, James E Schwob, Seok Chen Hong, Michael Knecht, and Gerd Kobal. Anterior distribution of human olfactory epithelium. *The Laryngoscope*, 110(3):417–421, 2000.

[12] Edward E Morrison and Richard M Costanzo. Morphology of the human olfactory epithelium. *Journal of Comparative Neurology*, 297(1):1–13, 1990.

[13] Tadashi Nakashima, Charles P Kimmelman, and James B Snow. Structure of human fetal and adult olfactory neuroepithelium. *Archives of otolaryngology*, 110(10):641–646, 1984.

[14] Charles B Croft. Clinical anatomy of the nose, nasal cavity and paranasal sinuses, johannes lang, translated by pm stel1. *Clinical Otolaryngology & Allied Sciences*, 16(4): 430–430, 1991.

[15] S Naftali, RC Schroter, RJ Shiner, and D Elad. Transport phenomena in the human nasal cavity: a computational model. *Annals of biomedical engineering*, 26(5):831–839, 1998.

[16] Ching-Long Lin, Merryn H Tawhai, Geoffrey McLennan, and Eric A Hoffman. Characteristics of the turbulent laryngeal jet and its effect on airflow in the human intra-thoracic airways. *Respiratory physiology & neurobiology*, 157(2):295–309, 2007.

[17] AJ Bates, A Comerford, R Cetto, RC Schroter, NS Tolley, and DJ Doorly. Power loss mechanisms in pathological tracheas. *Journal of biomechanics*, 49(11):2187–2192, 2016.

[18] Stephen H Loring, Mauricio Garcia-Jacques, and Atul Malhotra. Pulmonary characteristics in copd and mechanisms of increased work of breathing. *Journal of applied physiology*, 107(1):309–314, 2009.

[19] Mark Brouns, Santhosh T Jayaraju, Chris Lacor, Johan De Mey, Marc Noppen, Walter

Vincken, and Sylvia Verbanck. Tracheal stenosis: a flow dynamics study. *Journal of Applied Physiology*, 102(3):1178–1184, 2007.

[20] Juan R Cebral and Ronald M Summers. Tracheal and central bronchial aerodynamics using virtual bronchoscopy and computational fluid dynamics. *IEEE transactions on medical imaging*, 23(8):1021–1033, 2004.

[21] Andrew Hall, Mike Thomas, Guri Sandhu, and James H Hull. Exercise-induced laryngeal obstruction: a common and overlooked cause of exertional breathlessness. *Br J Gen Pract*, 66(650):e683–e685, 2016.

[22] Steffan Arthur Griffin, Emil S Walsted, and James H Hull. Breathless athlete: exercise-induced laryngeal obstruction. *Br J Sports Med*, pages bjsports–2018, 2018.

[23] Savinda Liyanagedara, Robert McLeod, and Hassan A Elhassan. Exercise induced laryngeal obstruction: a review of diagnosis and management. *European Archives of Oto-Rhino-Laryngology*, 274(4):1781–1789, 2017.

[24] Ronald Eccles. Nasal airflow in health and disease. *Acta oto-laryngologica*, 120(5):580–595, 2000.

[25] Maurice Mcgregor, William Adam, and Paul Sekelj. Influence of posture on cardiac output and minute ventilation during exercise. *Circulation Research*, 9(5):1089–1092, 1961.

[26] Kevin Price, Philippe Schartz, and Alan HD Watson. The effect of standing and sitting postures on breathing in brass players. *SpringerPlus*, 3(1):210, 2014.

[27] JR Wheatley, TC Amis, and LA Engel. Nasal and oral airway pressure-flow relationships. *Journal of Applied Physiology*, 71(6):2317–2324, 1991.

[28] S Morris, MS Jawad, and R Eccles. Relationships between vital capacity, height and nasal airway resistance in asymptomatic volunteers. *Rhinology*, 30(4):259–264, 1992.

[29] NC Syabbalo, A Bundgaard, P Entholm, A Schmidt, and JG Widdicombe. Measurement and regulation of nasal airflow resistance in man. *Rhinology*, 24(2):87–101, 1986.

[30] T Havas, M Gutierrez, J Morton, and L Rhodes. Nasal airway resistance in patients with cystic fibrosis. *Aust J Otolaryngol*, 1:434, 1994.

[31] Peter S Vig and David J Zajac. Age and gender effects on nasal respiratory function in normal subjects. *The Cleft palate-craniofacial journal*, 30(3):279–284, 1993.

[32] R Eccles, M Reilly, and KSJ Eccles. Changes in the amplitude of the nasal cycle associated with symptoms of acute upper respiratory tract infection. *Acta oto-laryngologica*, 116(1): 77–81, 1996.

[33] Philip Flanagan and Ronald Eccles. Spontaneous changes of unilateral nasal airflow in man. a re-examination of the nasal cycle. *Acta oto-laryngologica*, 117(4):590–595, 1997.

[34] R Kayser. Die exacte messung der luftdurchgangigkeit der nase. *Arch Laryngol*, 94: 149–156, 1895.

[35] Dewey R Heetderks. Observations on the reaction of normal nasal mucous membkane. *The American Journal of the Medical Sciences*, 174(2):231–243, 1927.

[36] NS Dallimore and R Eccles. Changes in human nasal resistance associated with exercise, hyperventilation and rebreathing. *Acta oto-laryngologica*, 84(1-6):416–421, 1977.

[37] RD Forsyth, P Cole, and RJ Shephard. Exercise and nasal patency. *Journal of Applied Physiology*, 55(3):860–865, 1983.

[38] Makoto Hasegawa, Yasuhiro Kabasawa, Motofumi Ohki, and Isamu Watanabe. Exercise-induced change of nasal resistance in asthmatic children. *OtolaryngologyHead and Neck Surgery*, 93(6):772–776, 1985.

[39] NC Syabbalo, A Bundgaard, and JG Widdicombe. Effects of exercise on nasal airflow resistance in healthy subjects and in patients with asthma and rhinitis. *Bulletin europeen de physiopathologie respiratoire*, 21(6):507–513, 1985.

[40] Hal B Richerson and Paul M Seebohm. Nasal airway response to exercise. *Journal of Allergy*, 41(5):269–284, 1968.

[41] Catherine E Rennie, Kevin A Gouder, Donal J Taylor, Neil S Tolley, Robert C Schroter, and Denis J Doorly. Nasal inspiratory flow: at rest and sniffing. In *International forum of allergy & rhinology*, volume 1, pages 128–135. Wiley Online Library, 2011.

[42] Alister J Bates, Denis J Doorly, Raul Cetto, Hadrien Calmet, AM Gambaruto, NS Tolley, Guillaume Houzeaux, and RC Schroter. Dynamics of airflow in a short inhalation. *Journal of the Royal Society Interface*, 12(102):20140880, 2015.

[43] J Lindemann, Richard Leiacker, Gerhard Rettinger, and Tilman Keck. Nasal mucosal temperature during respiration. *Clinical Otolaryngology & Allied Sciences*, 27(3):135–139, 2002.

[44] Sho Hanida, Futoshi Mori, Kiyoshi Kumahata, Masahiro Watanabe, Shigeru Ishikawa, and Teruo MATSUZAWA. Influence of latent heat in the nasal cavity. *Journal of biomechanical science and engineering*, 8(3):209–224, 2013.

[45] P Nithiarasu, O Hassan, K Morgan, NP Weatherill, C Fielder, H Whittet, P Ebden, and KR Lewis. Steady flow through a realistic human upper airway geometry. *International Journal for Numerical Methods in Fluids*, 57(5):631–651, 2008.

[46] C Paz, M Concheiro, J Porteiro, et al. Cfd transient simulation of a breathing cycle in an oral-nasal extrathoracic model. *Journal of Applied Fluid Mechanics*, 10(3), 2017.

[47] L Yu Bosykh, VL Ganimedov, MI Muchnaya, and AS Sadovskii. Influence of the respiratory cycle structure on the flow field in human nasal cavity at a fixed level of breath depth. In *AIP Conference Proceedings*, volume 1770, page 030085. AIP Publishing, 2016.

[48] Intaek Hahn, PETER W Scherer, and Maxwell M Mozell. Velocity profiles measured for airflow through a large-scale model of the human nasal cavity. *Journal of Applied Physiology*, 75(5):2273–2287, 1993.

[49] KPWMM Keyhani, PW Scherer, and MM Mozell. Numerical simulation of airflow in the human nasal cavity. *Journal of biomechanical engineering*, 117(4):429–441, 1995.

[50] Ravi P Subramaniam, Regina B Richardson, Kevin T Morgan, Julia S Kimbell, and Raymond A Guilmette. Computational fluid dynamics simulations of inspiratory airflow in the human nose and nasopharynx. *Inhalation Toxicology*, 10(2):91–120, 1998.

[51] Kai Zhao, Peter W Scherer, Shoreh A Hajiloo, and Pamela Dalton. Effect of anatomy on human nasal air flow and odorant transport patterns: implications for olfaction. *Chemical senses*, 29(5):365–379, 2004.

[52] JT Kelly, AK Prasad, and AS Wexler. Detailed flow patterns in the nasal cavity. *Journal of Applied Physiology*, 89(1):323–337, 2000.

[53] DONALD F Proctor, I Andersen, and G Lundqvist. Nasal mucociliary function in humans. *Respiratory Defense Mechanisms: Lung Biology in Health and Disease (Brain JD, Proctor DF, Reid LM, eds). New York: Marcel Dekker*, pages 427–452, 1977.

[54] Marc Girardin, Ertugrul Bilgen, and Pierre Arbour. Experimental study of velocity fields in a human nasal fossa by laser anemometry. *Annals of Otology, Rhinology & Laryngology*, 92(3):231–236, 1983.

[55] Ingolf Hörschler and Wolfgang Schröder. On the geometry dependence of the nose flow. *Ercoftac Bulletin*, 68, 2006.

[56] Kiao Inthavong, Jiawei Ma, Yidan Shang, Jingliang Dong, Annicka SR Chetty, Jiyuan Tu, and Dennis Frank-Ito. Geometry and airflow dynamics analysis in the nasal cavity during inhalation. *Clinical Biomechanics*, 2017.

[57] Kiao Inthavong, ZF Tian, HF Li, JY Tu, William Yang, CL Xue, and Chun Guang Li. A numerical study of spray particle deposition in a human nasal cavity. *Aerosol Science and Technology*, 40(11):1034–1045, 2006.

[58] Heow Pueh Lee, Hee Joo Poh, Fook Hin Chong, and De Yun Wang. Changes of airflow pattern in inferior turbinate hypertrophy: a computational fluid dynamics model. *American journal of rhinology & allergy*, 23(2):153–158, 2009.

[59] Heow Peuh Lee De Yun Wang and Bruce R Gordon. Impacts of fluid dynamics simulation in study of nasal airflow physiology and pathophysiology in realistic human three-dimensional nose models. *Clinical and experimental otorhinolaryngology*, 5(4):181, 2012.

[60] A Singh, N Patel, G Kenyon, and G Donaldson. Is there objective evidence that septal surgery improves nasal airflow? *The Journal of Laryngology & Otology*, 120(11):916–920, 2006.

[61] P Illum. Septoplasty and compensatory inferior turbinate hypertrophy: long-term results after randomized turbinoplasty. *European Archives of Oto-rhino-laryngology*, 254(1):S89–S92, 1997.

[62] JS Kimbell, DO Frank, Purushottam Laud, GJM Garcia, and JS Rhee. Changes in nasal airflow and heat transfer correlate with symptom improvement after surgery for nasal obstruction. *Journal of biomechanics*, 46(15):2634–2643, 2013.

[63] Paulo Borges Dinis and Haula Haider. Septoplasty: long-term evaluation of results. *American journal of otolaryngology*, 23(2):85–90, 2002.

[64] Achim G Beule. Physiology and pathophysiology of respiratory mucosa of the nose and the paranasal sinuses. *GMS current topics in otorhinolaryngology, head and neck surgery*, 9, 2010.

[65] DJ Willatt. Continuous infrared thermometry of the nasal mucosa. *Rhinology*, 31(2): 63–67, 1993.

[66] NOAH D FABRICANT. The topical temperature of clinically normal nasal and pharyngeal mucous membranes. *AMA archives of otolaryngology*, 66(3):275–277, 1957.

[67] Neil Molony, C Caroline Blackwell, and Anthony Busuttil. The effect of prone posture on nasal temperature in children in relation to induction of staphylococcal toxins implicated in sudden infant death syndrome. *FEMS Immunology & Medical Microbiology*, 25(1-2): 109–113, 1999.

[68] J Yang and Q Zhang. Twenty-three cases of atrophic rhinitis treated by deep puncture at three points in the nasal region. *Journal of traditional Chinese medicine= Chung i tsa chih ying wen pan*, 19(2):115–117, 1999.

[69] Tilman Keck, Richard Leiacker, Herbert Riechelmann, and Gerhard Rettinger. Temperature profile in the nasal cavity. *The Laryngoscope*, 110(4):651–654, 2000.

[70] Tilman Keck, Richard Leiacker, Andreas Heinrich, Stephan Kühnemann, and Gerhard Rettinger. Humidity and temperature profile in the nasal cavity. *Rhinology*, 38(4):167–171, 2000.

[71] Paul Webb. Air temperatures in respiratory tracts of resting subjects in cold. *Journal of applied physiology*, 4(5):378–382, 1951.

[72] Jörg Lindemann, Richard Leiacker, Gerhard Rettinger, and Tilman Keck. The effect of topical xylometazoline on the mucosal temperature of the nasal septum. *American journal of rhinology*, 16(4):229–234, 2002.

[73] J Lindemann, R Leiacker, K Wiesmiller, G Rettinger, and T Keck. Immediate effect of benzalkonium chloride in decongestant nasal spray on the human nasal mucosal temperature. *Clinical Otolaryngology & Allied Sciences*, 29(4):357–361, 2004.

[74] Joerg Lindemann, Diana Sannwald, and Kerstin Wiesmiller. Age-related changes in intranasal air conditioning in the elderly. *The Laryngoscope*, 118(8):1472–1475, 2008.

[75] Philip Cole. Further observations on the conditioning of respiratory air. *The Journal of Laryngology & Otology*, 67(11):669–681, 1953.

[76] James EC Walker and Roe E Wells. Heat and water exchange in the respiratory tract. *The American journal of medicine*, 30(2):259–267, 1961.

[77] Philip Rouadi, Fuad M Baroody, David Abbott, Edward Naureckas, Julian Solway, and Robert M Naclerio. A technique to measure the ability of the human nose to warm and humidify air. *Journal of applied physiology*, 87(1):400–406, 1999.

[78] Dov Ophir, Yigal Elad, Elza Fishler, Aaron Fink, and Gabriel Marshak. Effects of elevated intranasal temperature on subjective and objective findings in perennial rhinitis. *Annals of Otology, Rhinology & Laryngology*, 97(3):259–263, 1988.

[79] Joerg Lindemann, Tilman Keck, Kerstin Wiesmiller, Bjoern Sander, Hans-Juergen Brambs, Gerhard Rettinger, and Daniela Pless. A numerical simulation of intranasal air temperature during inspiration. *The Laryngoscope*, 114(6):1037–1041, 2004.

[80] D Pless, T Keck, K Wiesmiller, G Rettinger, AJ Aschoff, TR Fleiter, and J Lindemann. Numerical simulation of air temperature and airflow patterns in the human nose during expiration. *Clinical Otolaryngology & Allied Sciences*, 29(6):642–647, 2004.

[81] Joerg Lindemann, Tilman Keck, Kerstin Wiesmiller, Bjoern Sander, Hans-Juergen Brambs, Gerhard Rettinger, and Daniela Pless. Nasal air temperature and airflow during respiration in numerical simulation based on multislice computed tomography scan. *American journal of rhinology*, 20(2):219–223, 2006.

[82] Prihambodo H Saksono, Perumal Nithiarasu, and Igor Sazonov. Numerical prediction of heat transfer patterns in a subject-specific human upper airway. *Journal of Heat Transfer*, 134(3):031022, 2012.

[83] LM Hanna and PW Scherer. Measurement of local mass transfer coefficients in a cast model of the human upper respiratory tract. *Journal of biomechanical engineering*, 108 (1):12–18, 1986.

[84] Gavin Hamilton. *Investigations of the thermal properties of human and animal tissues*. PhD thesis, University of Glasgow, 1998.

[85] Sara Naftali, Moshe Rosenfeld, Michael Wolf, and David Elad. The air-conditioning capacity of the human nose. *Annals of biomedical engineering*, 33(4):545–553, 2005.

[86] Guilherme JM Garcia, Neil Bailie, Dário A Martins, and Julia S Kimbell. Atrophic rhinitis: a cfd study of air conditioning in the nasal cavity. *Journal of applied physiology*, 103(3):1082–1092, 2007.

[87] K Inthavong, ZF Tian, and JY Tu. Cfd simulations on the heating capability in a human nasal cavity. In *16th Australasian Fluid Mechanics Conference (AFMC)*, pages 842–847. School of Engineering, The University of Queensland, 2007.

[88] Kiyoshi Kumahata, Futoshi Mori, Shigeru Ishikawa, and Teruo Matsuzawa. Nasal flow simulation using heat and humidity models. *Journal of Biomechanical Science and Engineering*, 5(5):565–577, 2010.

[89] Dan Wu, Merryn H Tawhai, Eric A Hoffman, and Ching-Long Lin. A numerical study of heat and water vapor transfer in mdct-based human airway models. *Annals of biomedical engineering*, 42(10):2117–2131, 2014.

[90] Jiawei Ma, Jingliang Dong, Yidan Shang, Kiao Inthavong, Jiyuan Tu, and Dennis O Frank-Ito. Air conditioning analysis among human nasal passages with anterior anatomical variations. *Medical engineering & physics*, 57:19–28, 2018.

[91] Maria E Tsu, Albert L Babb, David D Ralph, and Michael P Hlastala. Dynamics of heat, water, and soluble gas exchange in the human airways: 1. a model study. *Annals of biomedical engineering*, 16(6):547–571, 1988.

[92] Jong-Hoon Lee, Yang Na, Sung-Kyun Kim, and Seung-Kyu Chung. Unsteady flow characteristics through a human nasal airway. *Respiratory physiology & neurobiology*, 172(3): 136–146, 2010.

[93] Kai Zhao, Kara Blacker, Yuehao Luo, Bruce Bryant, and Jianbo Jiang. Perceiving nasal patency through mucosal cooling rather than air temperature or nasal resistance. *PLoS One*, 6(10):e24618, 2011.

[94] Reidar Moe. *The effect on the respiratory functions of the nose of the lumen dilating nasal operations*. Nationaltr., 1941.

[95] Joerg Lindemann, Tilman Keck, Richard Leiacker, Rene Dzida, and Kerstin Wiesmiller. Early influence of bilateral turbinoplasty combined with septoplasty on intranasal air conditioning. *American journal of rhinology*, 22(5):542–545, 2008.

[96] Kerstin Wiesmiller, Tilman Keck, Gerhard Rettinger, Richard Leiacker, Rene Dzida, and Joerg Lindemann. Nasal air conditioning in patients before and after septoplasty with bilateral turbinoplasty. *The Laryngoscope*, 116(6):890–894, 2006.

[97] PS Arunachalam, E Kitcher, J Gray, and JA Wilson. Nasal septal surgery: evaluation of symptomatic and general health outcomes. *Clinical Otolaryngology & Allied Sciences*, 26 (5):367–370, 2001.

[98] Michael G Stewart, Timothy L Smith, Edward M Weaver, David L Witsell, Bevan Yueh, Maureen T Hannley, and Jonas T Johnson. Outcomes after nasal septoplasty: results from the nasal obstruction septoplasty effectiveness (nose) study. *Otolaryngology–Head and Neck Surgery*, 130(3):283–290, 2004.

[99] Ajnacska Rozsasi, Richard Leiacker, Stephan Kühnemann, Jörg Lindemann, Thomas Kappe, Gerhard Rettinger, and Tilman Keck. The impact of septorhinoplasty and anterior turbinoplasty on nasal conditioning. *American journal of rhinology*, 21(3):302–306, 2007.

[100] J Lindemann, R Leiacker, V Stehmer, G Rettinger, and T Keck. Intranasal temperature and humidity profile in patients with nasal septal perforation before and after surgical closure. *Clinical Otolaryngology & Allied Sciences*, 26(5):433–437, 2001.

[101] B Drettner, B Falck, and H Simon. Measurements of the air conditioning capacity of the nose during normal and pathological conditions and pharmacological influence. *Acta oto-laryngologica*, 84(1-6):266–277, 1977.

[102] Jörg Lindemann, Richard Leiacker, Thomas Sikora, Gerhard Rettinger, and Tilman Keck. Impact of unilateral sinus surgery with resection of the turbinates by means of midfacial degloving on nasal air conditioning. *The Laryngoscope*, 112(11):2062–2066, 2002.

[103] Xiao Bing Chen, Heow Pueh Lee, Vincent Fook Hin Chong, and De Yun Wang. Numerical simulation of the effects of inferior turbinate surgery on nasal airway heating capacity. *American journal of rhinology & allergy*, 24(5):e118–e122, 2010.

[104] Guanxia Xiong, Jiemin Zhan, Kejun Zuo, Jianfeng Li, Liangwan Rong, and Geng Xu. Numerical flow simulation in the post-endoscopic sinus surgery nasal cavity. *Medical & biological engineering & computing*, 46(11):1161–1167, 2008.

[105] Merryn H Tawhai and Ching-Long Lin. Airway gas flow. *Compr. Physiol.*, 1:1135–1157, 2011.

[106] Laurie A Loevner. Anatomic and functional lesions resulting in partial or complete upper airway obstruction. In *Seminars in roentgenology*, volume 36, pages 12–20. Elsevier, 2001.

[107] Scott M Graham, Geoffrey McLennan, Gerry F Funk, Henry T Hoffman, Timothy M McCulloch, Janice Cook-Granroth, and Eric A Hoffman. Preoperative assessment of obstruction with computed tomography image analysis. *American journal of otolaryngology*, 21(4):263–270, 2000.

[108] Donald B Hawkins. Glottic and subglottic stenosis from endotracheal intubation. *The Laryngoscope*, 87(3):339–346, 1977.

[109] Sukgi S Choi and George H Zalzal. Pitfalls in laryngotracheal reconstruction. *Archives of Otolaryngology–Head & Neck Surgery*, 125(6):650–653, 1999.

[110] Jiwoong Choi, Merryn H Tawhai, Eric A Hoffman, and Ching-Long Lin. On intra-and intersubject variabilities of airflow in the human lungs. *Physics of Fluids*, 21(10):101901, 2009.

[111] Soo-Jin Jeong, Woo-Seung Kim, and Sang-Jin Sung. Numerical investigation on the flow characteristics and aerodynamic force of the upper airway of patient with obstructive sleep apnea using computational fluid dynamics. *Medical engineering & physics*, 29(6): 637–651, 2007.

[112] Mihai Mihaescu, Shanmugam Murugappan, Ephraim Gutmark, Lane F Donnelly, Siddarth Khosla, and Maninder Kalra. Computational fluid dynamics analysis of upper airway reconstructed from magnetic resonance imaging data. *Annals of Otology, Rhinology & Laryngology*, 117(4):303–309, 2008.

[113] Mihai Mihaescu, Goutham Mylavarapu, Ephraim J Gutmark, and Nelson B Powell. Large eddy simulation of the pharyngeal airflow associated with obstructive sleep apnea syndrome at pre and post-surgical treatment. *Journal of biomechanics*, 44(12):2221–2228, 2011.

[114] Fong-Lin Chen, Tzyy-Leng Horng, and Tzu-Ching Shih. Simulation analysis of airflow alteration in the trachea following the vascular ring surgery based on ct images using the computational fluid dynamics method. *Journal of X-ray science and technology*, 22(2): 213–225, 2014.

[115] Xingli Liu, Weiwei Yan, Yang Liu, Yat Sze Choy, and Yikun Wei. Numerical investigation of flow characteristics in the obstructed realistic human upper airway. *Computational and mathematical methods in medicine*, 2016, 2016.

[116] AF Heenan, E Matida, A Pollard, and WH Finlay. Experimental measurements and computational modeling of the flow field in an idealized human oropharynx. *Experiments in Fluids*, 35(1):70–84, 2003.

[117] David Elad. Biotransport in the human respiratory system. *Technology and Health Care*, 7(4):271–284, 1999.

[118] James SJ Haight and Philip Cole. The site and function of the nasal valve. *The Laryngoscope*, 93(1):49–55, 1983.

[119] Santhosh T Jayaraju, Mark Brouns, Chris Lacor, Johan De Mey, and Sylvia Verbanck. Effects of tracheal stenosis on flow dynamics in upper human airways. In *ECCOMAS CFD 2006: Proceedings of the European Conference on Computational Fluid Dynamics, Egmond aan Zee, The Netherlands, September 5-8, 2006*. Citeseer, 2006.

[120] Jean-Claude Chevrolet. Helium oxygen mixtures in the intensive care unit. *Critical Care*, 5(4):179, 2001.

[121] Emily L Lin, Jonathan M Bock, Carlton J Zdanski, Julia S Kimbell, and Guilherme JM Garcia. Relationship between degree of obstruction and airflow limitation in subglottic stenosis. *The Laryngoscope*, 128(7):1551–1557, 2018.

[122] Tracy Cheng, David Carpenter, Seth Cohen, David Witsell, and Dennis O Frank-Ito. Investigating the effects of laryngotracheal stenosis on upper airway aerodynamics. *The Laryngoscope*, 128(4):E141–E149, 2018.

[123] Raul Cetto. The form and functional assessment of the human upper airway (thesis). Technical report, Imperial College London, 2019.

[124] Technical report.

[125] SiemensPLMSoftware. Star-ccm+ manual. `https://documentation.thesteveportal.plm.automation.siemens.com/starccmplus_latest_en/index.html?param=r84ky&authLoc=https://thesteveportal.plm.automation.siemens.com/AuthoriseRedirect`. Accessed: 2015-09.

[126] DJ Taylor, DJ Doorly, and RC Schroter. Inflow boundary profile prescription for numerical simulation of nasal airflow. *Journal of the Royal Society Interface*, 7(44):515–527, 2010.

[127] DJ Doorly, DJ Taylor, AM Gambaruto, RC Schroter, and N Tolley. Nasal architecture: form and flow. *Philosophical Transactions of the Royal Society of London A: Mathematical, Physical and Engineering Sciences*, 366(1879):3225–3246, 2008.

[128] Alister Bates. Mechanics of airflow in human inhalation. 2014.

[129] Man Kong Yau and RR Rogers. *A short course in cloud physics*. Elsevier, 1996.

[130] Nathan Geurkink. Nasal anatomy, physiology, and function. *Journal of allergy and clinical immunology*, 72(2):123–128, 1983.

[131] Richard W Johnson. *Handbook of fluid dynamics*. Crc Press, 2016.

[132] DJ Doorly, DJ Taylor, and RC Schroter. Mechanics of airflow in the human nasal airways. *Respiratory physiology & neurobiology*, 163(1-3):100–110, 2008.

[133] Xiao Bing Chen, Heow Pueh Lee, Vincent Fook Hin Chong, and De Yun Wang. Assessment of septal deviation effects on nasal air flow: a computational fluid dynamics model. *The Laryngoscope*, 119(9):1730–1736, 2009.

[134] Milovan Peric. Flow simulation using control volumes of arbitrary polyhedral shape. *ERCOFTAC bulletin*, 62:25–29, 2004.

[135] Alister J Bates, Andreas Schuh, Gabriel Amine-Eddine, Keith McConnell, Wolfgang Loew, Robert J Fleck, Jason C Woods, Charles L Dumoulin, and Raouf S Amin. Assessing the relationship between movement and airflow in the upper airway using computational fluid dynamics with motion determined from magnetic resonance imaging. *Clinical Biomechanics*, 2017.

[136] Sylvain Laizet and Eric Lamballais. High-order compact schemes for incompressible flows: A simple and efficient method with quasi-spectral accuracy. *Journal of Computational Physics*, 228(16):5989–6015, 2009.

[137] A Shams, F Roelofs, EMJ Komen, and E Baglietto. Optimization of a pebble bed configuration for quasi-direct numerical simulation. *Nuclear Engineering and Design*, 242:331–340, 2012.

[138] A Shams, F Roelofs, EMJ Komen, and E Baglietto. Quasi-direct numerical simulation of a pebble bed configuration. part i: Flow (velocity) field analysis. *Nuclear Engineering and Design*, 263:473–489, 2013.

[139] R Benzi, S Ciliberto, R Tripiccione, C Baudet, F Massaioli, and S Succi. Extended self-similarity in turbulent flows. *Physical review E*, 48(1):R29, 1993.

[140] Angélique Delafosse, Marie-Laure Collignon, Michel Crine, and Dominique Toye. Estimation of the turbulent kinetic energy dissipation rate from 2d-piv measurements in a vessel stirred by an axial mixel ttp impeller. *Chemical Engineering Science*, 66(8):1728–1737, 2011.

[141] YS Muzychka and MM Yovanovich. Pressure drop in laminar developing flow in noncircular ducts: A scaling and modeling approach. *Journal of Fluids Engineering*, 131(11): 111105, 2009.

[142] HC Claiborne. Heat transfer in noncircular ducts part i. Technical report, Oak Ridge National Lab., 1951.

[143] RF Woolson. Wilcoxon signed-rank test. *Wiley encyclopedia of clinical trials*, pages 1–3, 2007.

[144] Carlos Eduardo Nazareth Nigro, Josiane Faria de Aguiar Nigro, Olavo Mion, and João Ferreira Mello Jr. Nasal valve: anatomy and physiology. *Brazilian journal of otorhinolaryngology*, 75(2):305–310, 2009.

[145] Sophie Svensson, Anna Carin Olin, and Johan Hellgren. Increased net water loss by oral compared to nasal expiration in healthy subjects. *Rhinology*, 44(1):74, 2006.

[146] Wojciech Kukwa, Christian Guilleminault, Magdalena Tomaszewska, Andrzej Kukwa, Antoni Krzeski, and Ewa Migacz. Prevalence of upper respiratory tract infections in habitually snoring and mouth breathing children. *International journal of pediatric otorhinolaryngology*, 107:37–41, 2018.

[147] Sven Ingelstedt and Nils Gunnar Toremalm. Air flow patterns and heat transfer within the respiratory tract: a new method for experimental studies on models. *Acta physiologica Scandinavica*, 51(2-3):204–217, 1961.

[148] Frank M White. Fluid mechanics. Technical report, McGraw-hill, 1986.

[149] Kyung J Park, Colleen J Bergin, and Jack L Clausen. Quantitation of emphysema with three-dimensional ct densitometry: comparison with two-dimensional analysis, visual emphysema scores, and pulmonary function test results. *Radiology*, 211(2):541–547, 1999.

[150] AJ Bates, R Cetto, DJ Doorly, RC Schroter, NS Tolley, and A Comerford. The effects of curvature and constriction on airflow and energy loss in pathological tracheas. *Respiratory physiology & neurobiology*, 234:69–78, 2016.

[151] XG Cui and E Gutheil. Large eddy simulation of the unsteady flow-field in an idealized human mouth–throat configuration. *Journal of biomechanics*, 44(16):2768–2774, 2011.

[152] Shouliang Qi, Zhenghua Li, Yong Yue, Han JW van Triest, and Yan Kang. Computational fluid dynamics simulation of airflow in the trachea and main bronchi for the subjects with left pulmonary artery sling. *Biomedical engineering online*, 13(1):85, 2014.

[153] A Comerford, V Gravemeier, and WA Wall. An algebraic variational multiscale–multigrid method for large-eddy simulation of turbulent pulsatile flows in complex geometries with detailed insight into pulmonary airway flow. *International Journal for Numerical Methods in Fluids*, 71(10):1207–1225, 2013.

[154] M Malvè, A Pérez del Palomar, S Chandra, JL López-Villalobos, A Mena, EA Finol, A Ginel, and M Doblaré. Fsi analysis of a healthy and a stenotic human trachea under impedance-based boundary conditions. *Journal of biomechanical engineering*, 133(2): 021001, 2011.

[155] Goutham Mylavarapu, Mihai Mihaescu, Laszlo Fuchs, Georgios Papatziamos, and Ephraim Gutmark. Planning human upper airway surgery using computational fluid dynamics. *Journal of biomechanics*, 46(12):1979–1986, 2013.

[156] Kai Zhao, Prashant Malhotra, David Rosen, Pamela Dalton, and Edmund A Pribitkin. Computational fluid dynamics as surgical planning tool: a pilot study on middle turbinate resection. *The Anatomical Record*, 297(11):2187–2195, 2014.

[157] Dennis O Frank-Ito, Julia S Kimbell, Purushottam Laud, Guilherme JM Garcia, and John S Rhee. Predicting postsurgery nasal physiology with computational modeling: current challenges and limitations. *Otolaryngology–Head and Neck Surgery*, 151(5):751–759, 2014.

[158] John S Rhee, Daniel E Cannon, Dennis O Frank, and Julia S Kimbell. Role of virtual surgery in preoperative planning: assessing the individual components of functional nasal airway surgery. *Archives of facial plastic surgery*, 14(5):354–359, 2012.

[159] Erik K Alexander, Elizabeth N Pearce, Gregory A Brent, Rosalind S Brown, Herbert Chen, Chrysoula Dosiou, William A Grobman, Peter Laurberg, John H Lazarus, Susan J Mandel, et al. 2017 guidelines of the american thyroid association for the diagnosis and management of thyroid disease during pregnancy and the postpartum. *Thyroid*, 27(3): 315–389, 2017.

[160] Marina Piccinelli, Alessandro Veneziani, David A Steinman, Andrea Remuzzi, and Luca Antiga. A framework for geometric analysis of vascular structures: application to cerebral aneurysms. *IEEE transactions on medical imaging*, 28(8):1141–1155, 2009.

[161] Hadrien Calmet, Alberto M Gambaruto, Alister J Bates, Mariano Vázquez, Guillaume Houzeaux, and Denis J Doorly. Large-scale cfd simulations of the transitional and turbulent regime for the large human airways during rapid inhalation. *Computers in biology and medicine*, 69:166–180, 2016.

[162] Mihai Mihăescu, Ephraim J Gutmark, Ravindhra Elluru, and J Paul Willging. Large eddy simulation of the flow in a pediatric airway with subglottic stenosis, 2009.

[163] CG Ball, M Uddin, and A Pollard. High resolution turbulence modelling of airflow in an idealised human extra-thoracic airway. *Computers & Fluids*, 37(8):943–964, 2008.

[164] Goutham Mylavarapu, Shanmugam Murugappan, Mihai Mihaescu, Maninder Kalra, Sid Khosla, and Ephraim Gutmark. Validation of computational fluid dynamics methodology used for human upper airway flow simulations. *Journal of biomechanics*, 42(10):1553–1559, 2009.

[165] Michael T Stang, Michaele J Armstrong, Jennifer B Ogilvie, Linwah Yip, Kelly L McCoy, Christopher N Faber, and Sally E Carty. Positional dyspnea and tracheal compression as indications for goiter resection. *Archives of Surgery*, 147(7):621–626, 2012.

[166] J Vétel, A Garon, D Pelletier, and M-I Farinas. Asymmetry and transition to turbulence in a smooth axisymmetric constriction. *Journal of Fluid Mechanics*, 607:351–386, 2008.

[167] Vladeta Zmijanovic, Simon Mendez, Vincent Moureau, and Franck Nicoud. About the numerical robustness of biomedical benchmark cases: Interlaboratory fda's idealized medical device. *International journal for numerical methods in biomedical engineering*, 33(1), 2017.

[168] RK Shah. A correlation for laminar hydrodynamic entry length solutions for circular and noncircular ducts. *Journal of Fluids Engineering*, 100(2):177–179, 1978.

[169] T Yilmaz. General equations for pressure drop for laminar flow in ducts of arbitrary cross sections. *Journal of Energy Resources Technology*, 112(4):220–223, 1990.

[170] SA Nouraei, S Mahmoud Nouraei, Anil Patel, Kevin Murphy, Dino A Giussani, Elias F Koury, James M Brown, P Jeremy George, Andrew C Cummins, and Guri S Sandhu. Diagnosis of laryngotracheal stenosis from routine pulmonary physiology using the expiratory disproportion index. *The Laryngoscope*, 123(12):3099–3104, 2013.

[171] Jinxiang Xi, P Worth Longest, and Ted B Martonen. Effects of the laryngeal jet on nano-and microparticle transport and deposition in an approximate model of the upper tracheobronchial airways. *Journal of Applied Physiology*, 104(6):1761–1777, 2008.

[172] A Pollard, M Uddin, A-M Shinneeb, and CG Ball. Recent advances and key challenges in investigations of the flow inside human oro-pharyngeal-laryngeal airway. *International Journal of Computational Fluid Dynamics*, 26(6-8):363–381, 2012.

[173] David M Wootton, Sanghun Sin, Haiyan Luo, Alireza Yazdani, Joseph M McDonough, Mark E Wagshul, Carmen R Isasi, and Raanan Arens. Computational fluid dynamics upper airway effective compliance, critical closing pressure, and obstructive sleep apnea severity in obese adolescent girls. *Journal of Applied Physiology*, 121(4):925–931, 2016.

[174] Shahab Taherian, HR Rahai, Jeremy Bonifacio, BZ Gomez, and Thomas Waddington. Particulate deposition in a patient with tracheal stenosis. *Journal of Engineering and Science in Medical Diagnostics and Therapy*, 1(1):011005, 2018.

[175] Fabrizio Donati, C Alberto Figueroa, Nicolas P Smith, Pablo Lamata, and David A Nordsletten. Non-invasive pressure difference estimation from pc-mri using the work-energy equation. *Medical image analysis*, 26(1):159–172, 2015.

[176] IHS ESDU. ESDU Datasheet. `https://www.esdu.com/cgi-bin/ps.pl?sess=unlicensed_1180412115642hsc&t=gen&p=home`, 2018. [Online; accessed 19-March-2018].

Appendix A

For chapter 2

A.1 Mesh quality check guidelines

- Face validity: face validity > 0.9 is recommended while a couple of cells with $0.8 <$ face validity < 0.9 are acceptable, but should avoid as much as possible having face validity < 0.8.

- Volume change: volume change $>$ 1e-3 is recommended while a couple of cells with 1e-4 $<$ volume change $<$ 1e-3 are acceptable, but should avoid as much as possible having volume change $<$ 1e-4.

A.2 Temporal mean range

The total pressure values that used for convergence check and also the analysis within this study is calculated between 0.1s and 0.3 s. The decision is based on the calculation of cumulative average of total pressure loss between inlet and outlet of subject D. Figure below shows the cumulative averaged total pressure loss along with the simulation physical time. The x-axis is

start from 0.01 s in order to get ride of the initial transient effect. The plot shows that after 0.1 s, the variation of total pressure loss is less than 1%.

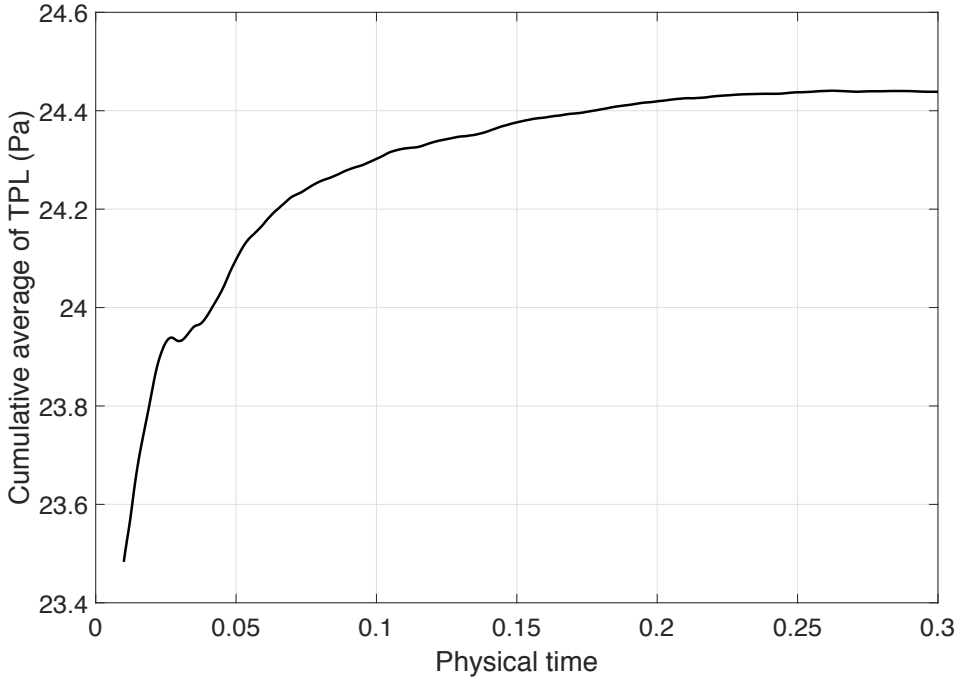


Figure A.1: Cumulative averaging of total pressure loss with simulation physical time.

A.3 Nasal cavity mesh statistics

The mesh setting statistics of Subject-D (congested case) are listed in the following table A.1:

Mesh elements (million)	2.5	3.5	4.0	5	6.3
Face validity<0.95	0%	0%	0%	0%	0%
Volume change<1e-3	0%	0%	0%	0%	0%
Mesh base size (mm)	5	4.5	4	3.5	3
Surface growth rate	1.1	1.1	1.1	1.1	1.1
Number of prism layer	7	7	7	7	7
Prism layer thickness (mm)	0.3	0.3	0.3	0.3	0.3
First prism layer thickness (mm)	0.01	0.01	0.01	0.01	0.01

Table A.1: Nasal cavity mesh statistics with multiple mesh settings.

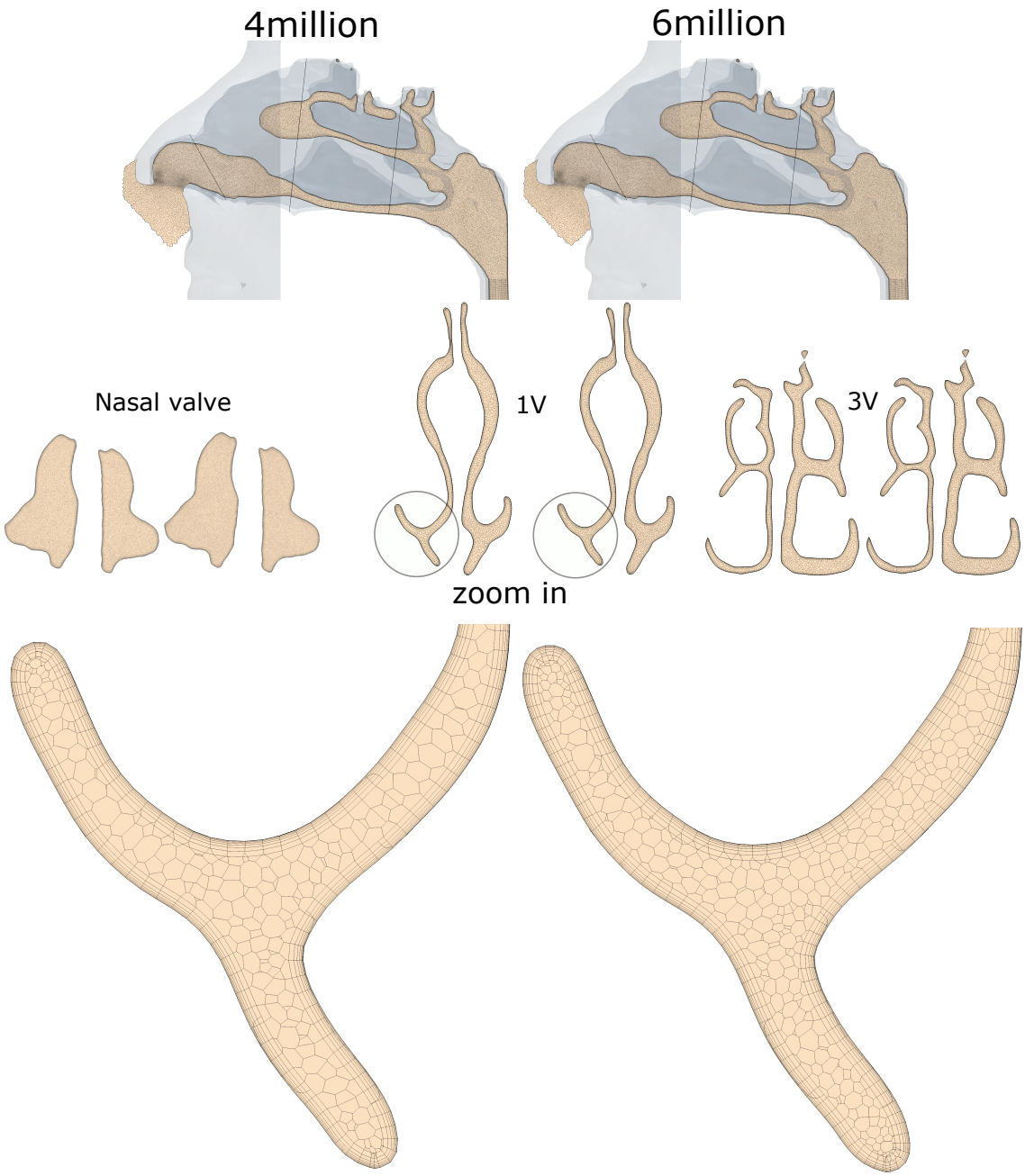


Figure A.2: The mesh structure difference between 4 million cells and 6 million cells simulations. There are one sagittal and 3 cross-sectional planes (nasal valve, plane 1V and plane 3V) are used for distribution and with one zoomed in view of plane 1V. For three cross-sectional views, the left pair corresponds to the 4 million cells mesh while the right side is the 6 million cells mesh.

A.4 Subject D cavity mesh independent check

Table A.2 shows the convergence of mean total pressure lost between the simulation domain inlet and outlet. There is clear trend that the relative error reduces while increasing the amount of mesh elements.

Subject(mesh identifier)	D(a)	D(b)	D(c)	D(d)	D(e)	D(f)
Mesh elements (million)	2.5	3.4	4.0	4.9	6.3	6.3
Time step (ms)	1	1	1	1	1	0.1
Mean total pressure loss between inlet and outlet (Pa)	24.1	24.2	24.2	24.3	24.5	24.5
Relative error (%)	1.6	1.2	1.2	0.8	0	0
Total water transfer across the cavity (e-5) (kg/s)	1.12	1.12	1.12	1.12	1.12	1.12

Table A.2: Subject D congested mesh independent check. The finest case D(f) have the same amount mesh element of D(e) but with one tenth of its times step.

Rather that shows the single overall values above, figure A.3 also shows the mean total pressure loss along the centerline of subject D left cavity. It can be see that the mismatch of each line happens after the nasal valve where the jet is formed.

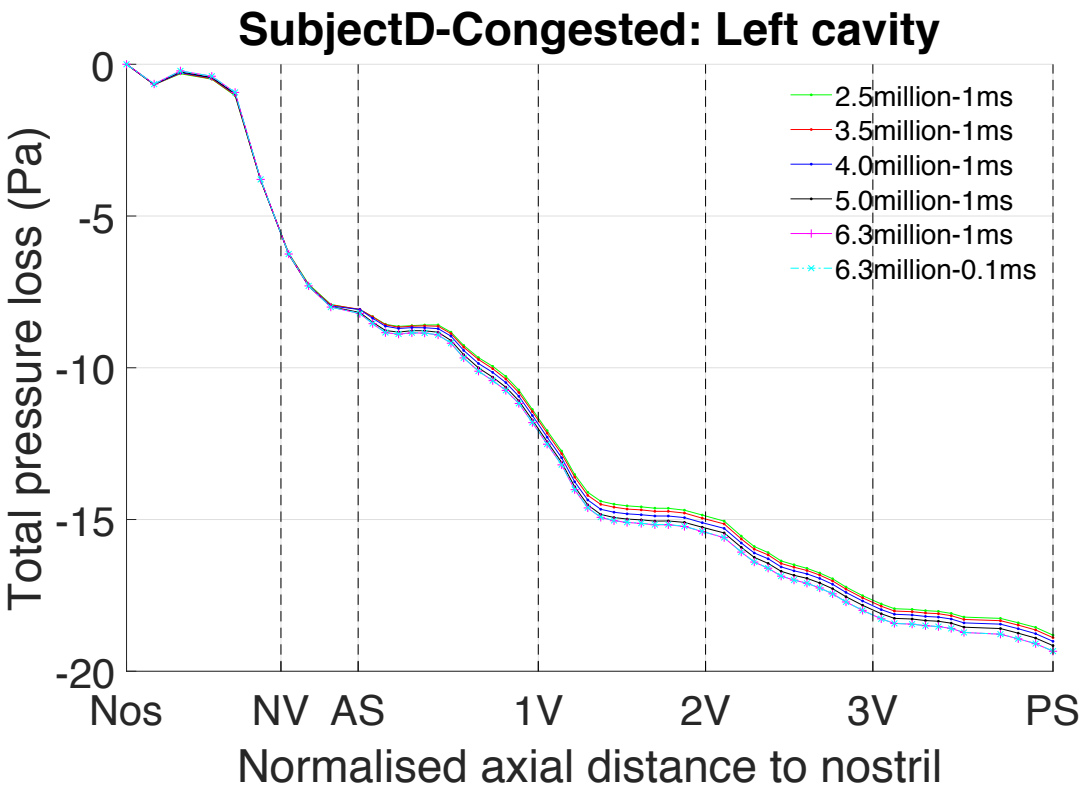


Figure A.3: Total pressure loss within left cavity of Subject-D congested case. The x-axis origin from the nostril plane until the posterior septum plane.

Table A.3 also summarise the mesh independent check of subject D decongested cavity. It also shows that with the increase of mesh elements the relative error keep reducing and simulation with 4 million mesh elements only has a relatively error of 1.5 %.

Total mesh elements (million)	2.5	3.4	4.0	4.9	6.3
Time step (ms)	1	1	1	1	1
Mean total pressure loss between inlet and outlet (Pa)	13.43	13.41	13.49	13.55	13.60
Relative error (%)	4.6	1.6	1.5	0.8	0

Table A.3: Subject D decongested mesh independent check.

A.5 Two-film theory

As shown by diagram 2.2, the water flux originate from membrane into the cavity volume should be the same in theory which gives the relation below:

$$\dot{w}_{memb} = \dot{w}_s \tag{A.1}$$

where $\dot{w}_{memb}$ represents the water flux through the membrane and $\dot{w}_s$ is the water flux into the cavity volume. The water model of this study is calculating the $\dot{w}_s$ using the mass fraction of fully saturated wet air at the surface temperature, while BC5 is suing another relation:

$$D_{memb} \cdot \frac{F_s - F_o}{\delta_{memb}} = D_{bl} \cdot \frac{F_{bl} - F_s}{\delta_{wall}} \tag{A.2}$$

where D_{memb} and D_s are the mass diffusion coefficient of the membrane and the boundary layer. F_s, F_o, F_{bl} are the mass fraction of water vapor on the cavity surface, organ and boundary layer mass fraction of water vapor separately, By rearrange the equation we can get the mass fraction of water vapor on the surface is:

$$F_s = \frac{(\frac{D_{memb}}{\delta_{memb}})F_o + (\frac{D_{bl}}{\delta_{bl}})F_{bl}}{(\frac{D_{memb}}{\delta_{memb}}) + (\frac{D_{bl}}{\delta_{bl}})} \tag{A.3}$$

A.6 Complete airway mesh statistics

The complete airway mesh statistics are summarised in table A.4, but only the laminar simulation and qDNS simulation are shown here. From the table we can see that for both mesh setting it all have a good mesh quality, although the total amount of mesh elements have an order of 5 difference.

Turbulence model	Laminar	qDNS
Mesh elements (million)	2.9	14.6
Face validity < 0.9	0%	0%
Volume change $<$ 1e-3	0%	0%
Mesh base size (mm)	3.5	1.8
Surface growth rate	1.3	1.3
Prism layer thickness (mm)	0.2	0.27
Number of prism layer	7	7
Prism layer stretching	1.3	1.3

Table A.4: Simulation of complete airway mesh statistics.

Ideally, for conducting DNS simulation, the mesh scale should be comparable to Kolmogorov scale which theoretically is the smallest scale in the turbulence. Table A.5 distributes the details of the simulation scales compared with the Kolmogorov scales both in spacial and temporal domain. In the table, η is the Kolmogorov length scale and τ_η the is corresponding time scale. The simulation length scale is represented by the mesh element length: $\sqrt[3]{V}$ (V is the cell volume) and time scale is represented directly by the simulation time step: Δt. For ideal DNS requirements, the value of $\frac{\sqrt[3]{V}}{\eta}$ should less or equal than unit as well as the value of $\frac{\Delta t}{\tau_\eta}$. Thus the simulation we conducted here is quasi DNS which has decent enough mesh density to capture most of the turbulence scales in the flow field.

Complete airway qDNS	Simulation refinement statistics
Mean $y+$	0.23
Maximum $y+$	0.91
Mean $\frac{U \cdot \Delta t}{\eta}$	0.36
Mean $\frac{\sqrt[3]{V}}{\eta}$	3.44
Mean $\frac{\Delta t}{\tau_\eta}$	0.024

Table A.5: qDNS mesh refinement details of complete airway

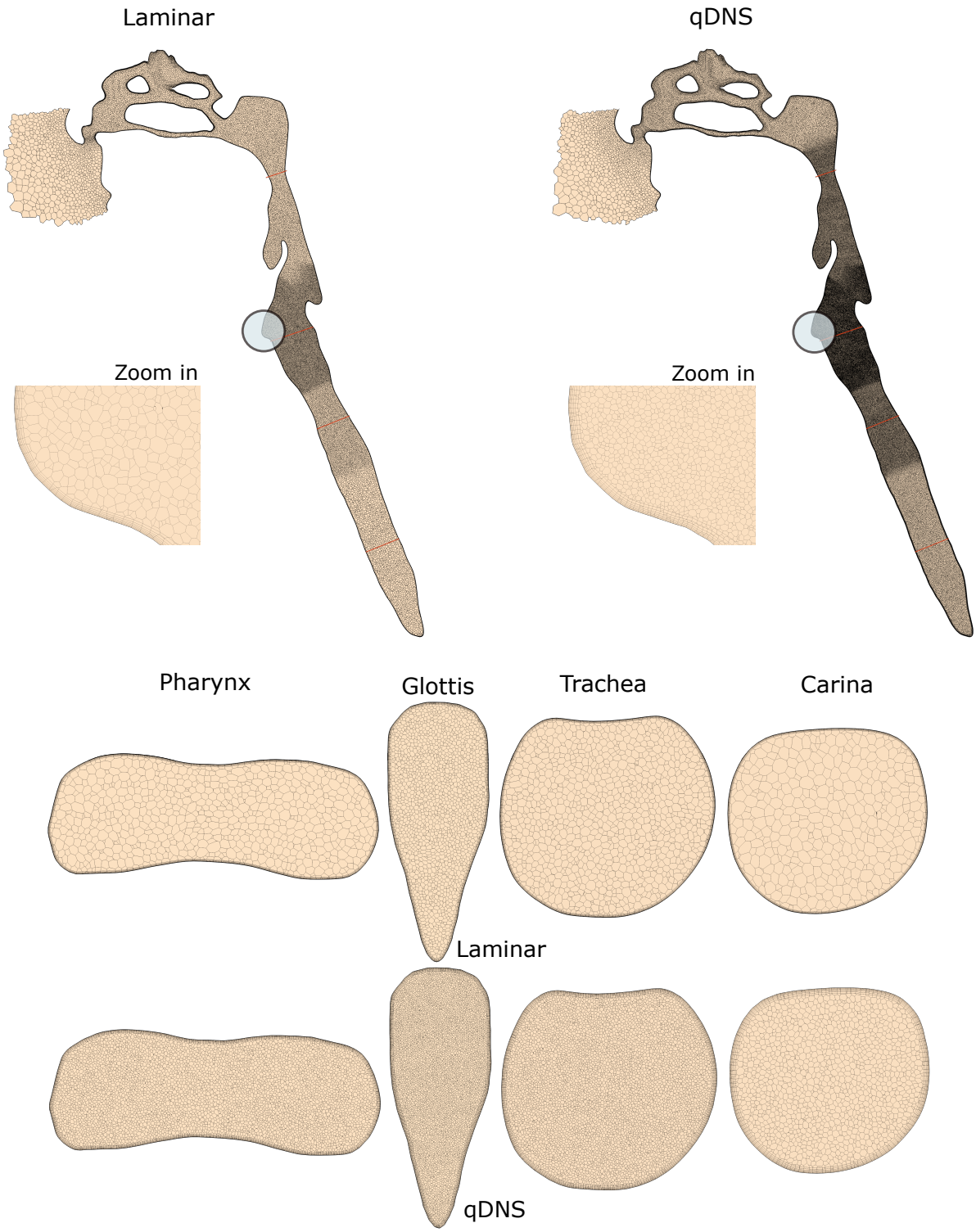


Figure A.4: Mesh details comparison between laminar model and qDNS model for complete airway simulation.

A.7 T15 mesh statistics

As one of the important for LES simulation mesh requirement is the $y+$ value which need to less that unit to ensure the viscous sublayer can be accurately captured. Table A.6 shows that the mean value $y+$ within the domain of the simulation is around 1.12.

Turbulence model	LES	qDNS
Mesh elements (million)	2.2	10.2
Face validity < 0.9	0%	0%
Volume change $<$ 1e-3	0%	0%
Mesh base size (mm)	0.25	0.15
Surface growth rate	1.3	1.3
Prism layer thickness (mm)	0.45	0.39
Number of prism layer	5	10
Prism layer stretching	1.2	non
Thickness of near wall prism layer (mm)	non	0.01
Average $y+$	1.12	0.19

Table A.6: Simulation of T15 mesh statistics.

Table A.7 shows the similar results as table A.5 which also indicates a valid mesh to conduct qDNS simulation.

T15 qDNS	Simulation refinement statistics
Mean $y+$	0.19
Maximum $y+$	0.91
Mean $\frac{U \cdot \Delta t}{\eta}$	0.83
Mean $\frac{\sqrt[3]{V}}{\eta}$	2.46
Mean $\frac{\Delta t}{\tau_\eta}$	0.057

Table A.7: qDNS mesh refinement details of T15

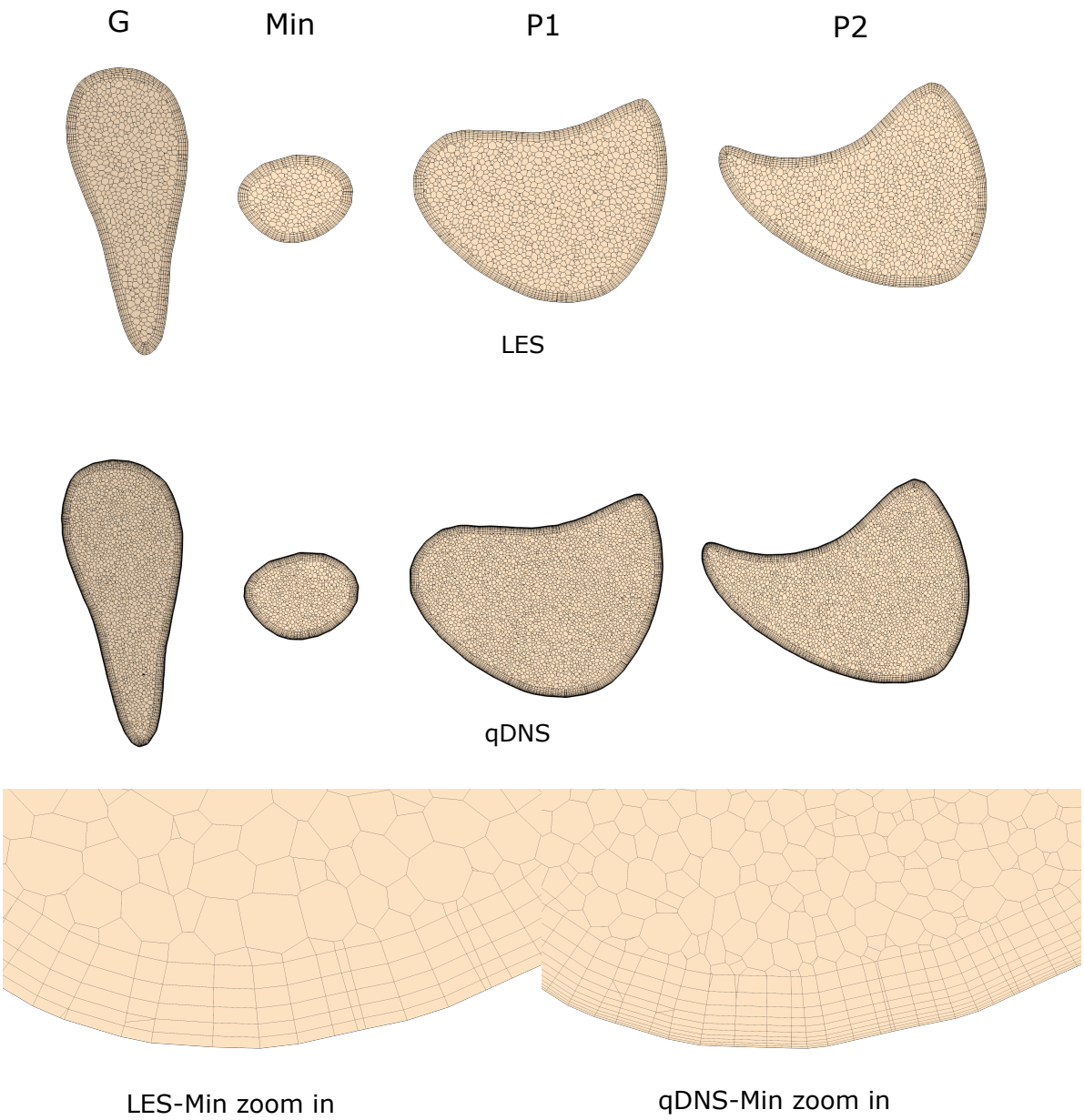


Figure A.5: Mesh details comparison between LES model and qDNS model for pathological tracheal simulations.

Appendix B

For chapter 3

B.1 Bilateral geometric data

Nose	A	B	C	D	E	F	G	H	I	1
Congest Area(cm^2)	198.17	159.07	195.76	238.52	199.51	208.23	240.32	183.75	213.36	199.76
Decongest Area(cm^2)	201.66	159.89	173.46	218.20	179.70	219.04	230.50	175.47	213.12	197.96
Congest Volume(cm^3)	17.16	11.01	19.32	21.52	14.66	25.32	21.81	19.86	23.43	18.56
Decongest Volume(cm^3)	27.27	17.99	19.06	31.77	20.86	28.28	29.36	20.79	28.59	18.91
Congest A/V Ratio	11.54	14.45	10.13	11.08	13.61	8.23	11.02	9.25	9.10	10.76
Decongest A/V Ratio	7.39	8.89	9.10	6.87	8.61	7.75	7.85	8.44	7.46	10.47

Table B.1: Nasal cavity surface area and volume data.

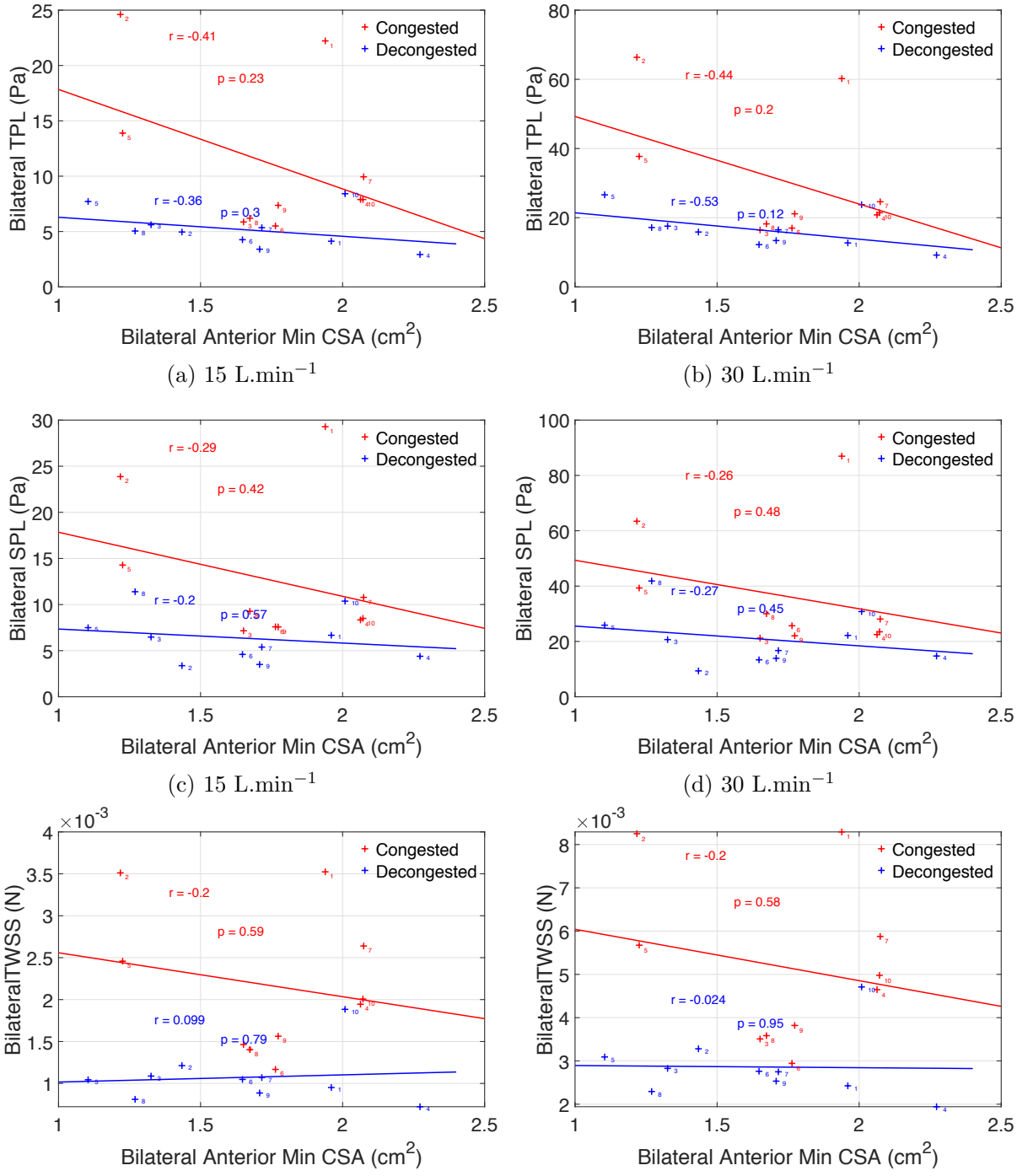
Congested A/V Ratio($1/cm$)	A	B	C	D	E	F	G	H	I	1
Top	14.45	18.40	9.86	12.64	13.15	10.54	12.97	11.23	10.46	13.89
Mid	12.11	13.83	8.32	10.56	11.21	6.56	10.47	8.28	7.64	9.85
Bot	11.61	14.83	9.77	10.19	13.41	7.29	11.53	7.95	9.78	9.25

Table B.2: Congested area volume ratio.

Decongested A/V Ratio($1/cm$)	A	B	C	D	E	F	G	H	I	1
Top	11.05	14.94	10.97	9.59	10.66	11.24	13.93	12.82	9.66	18.42
Mid	6.19	7.49	6.49	5.15	5.45	6.63	7.37	6.42	5.22	8.99
Bot	6.18	7.43	7.07	5.33	5.81	6.16	5.98	6.36	7.58	7.90

Table B.3: Decongested area volume ratio.

B.2 Bilateral Correlations



(a) 15 L.min^{-1} (b) 30 L.min^{-1}

(c) 15 L.min^{-1} (d) 30 L.min^{-1}

(e) 15 L.min^{-1} (f) 30 L.min^{-1}

Figure B.1: Bilateral NVArea, TPL and TWSS.

B.3 Unilateral geometric data

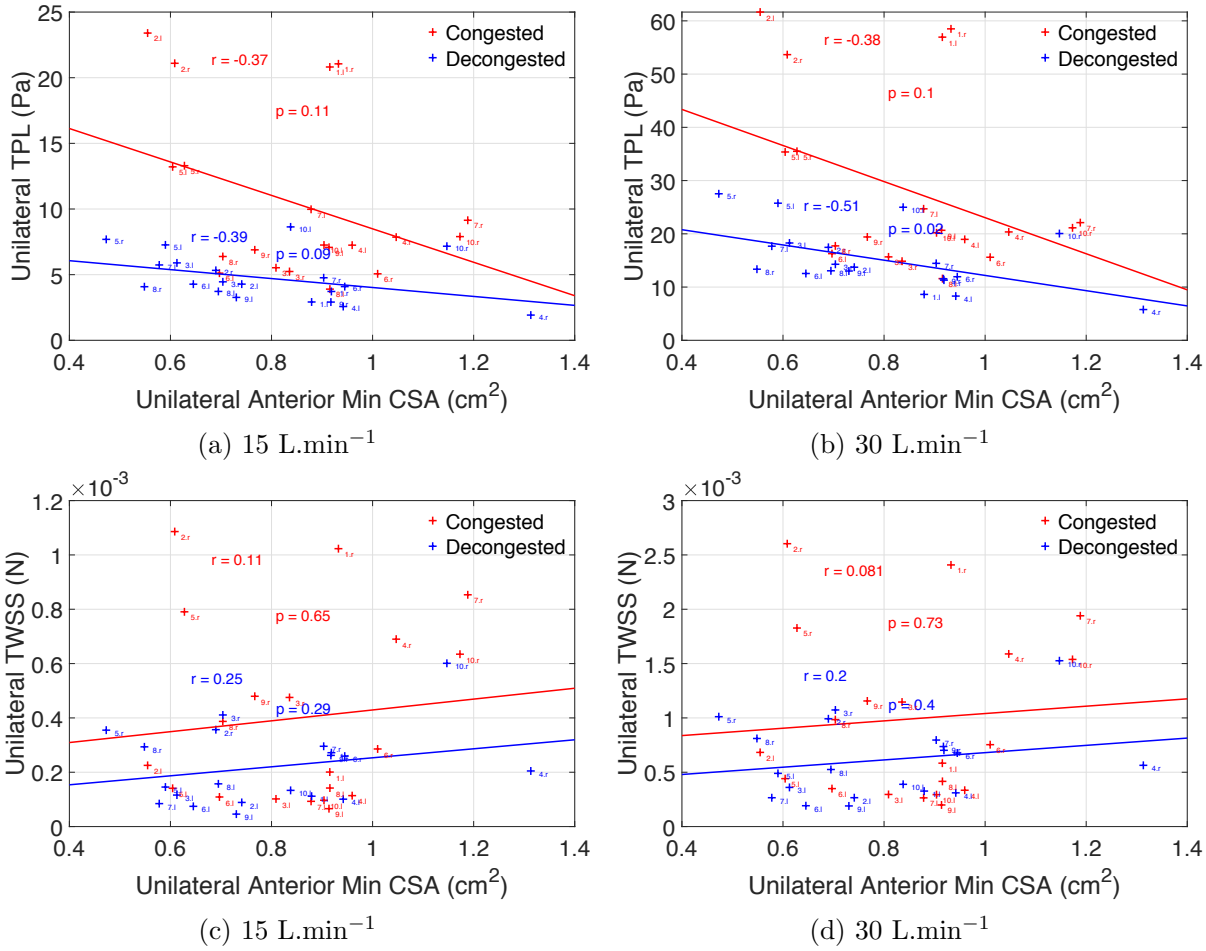
Subject	A	B	C	D	E	F	G	H	I	1
Congested Left area(cm^2)	93.12	66.89	81.75	102.57	79.72	92.10	108.13	83.56	103.06	84.67
Decongested Left area(cm^2)	97.21	69.48	73.03	96.01	71.97	97.90	100.73	80.24	104.93	84.32
Congested Right area(cm^2)	91.22	73.86	84.16	101.34	80.83	93.58	112.99	78.06	96.52	88.69
Decongested Right area(cm^2)	90.55	74.61	73.43	95.17	73.31	98.90	112.96	75.37	97.41	88.27
Congested Left volume(cm^3)	8.96	5.18	9.56	12.20	7.19	12.31	9.84	12.73	12.78	9.73
Decongested Left volume(cm^3)	15.28	8.82	8.12	15.48	10.60	14.78	12.91	10.56	15.50	9.09
Congested Right volume(cm^3)	8.17	5.77	9.66	9.19	7.34	12.92	11.90	7.07	10.61	8.73
Decongested Right volume(cm^3)	11.95	9.12	10.86	16.18	10.13	13.40	16.39	10.17	13.05	9.73

Table B.4: Unilateral nasal cavity surface area and cavity volume.

Subject	A	B	C	D	E	F	G	H	I	1
Congested Left AV(1/cm)	10.39	12.90	8.55	8.41	11.08	7.48	10.99	6.56	8.06	8.70
Decongested Left AV(1/cm)	6.36	7.88	9.00	6.20	6.79	6.62	7.80	7.60	6.77	9.27
Congested Right AV(1/cm)	11.17	12.80	8.71	11.02	11.01	7.24	9.50	11.04	9.10	10.16
Decongested Right AV(1/cm)	7.58	8.18	6.76	5.88	7.24	7.38	6.89	7.41	7.47	9.07

Table B.5: Unilateral nasal cavity area volume ratio.

B.4 Unilateral correlations



(a) 15 L.min^{-1} (b) 30 L.min^{-1}

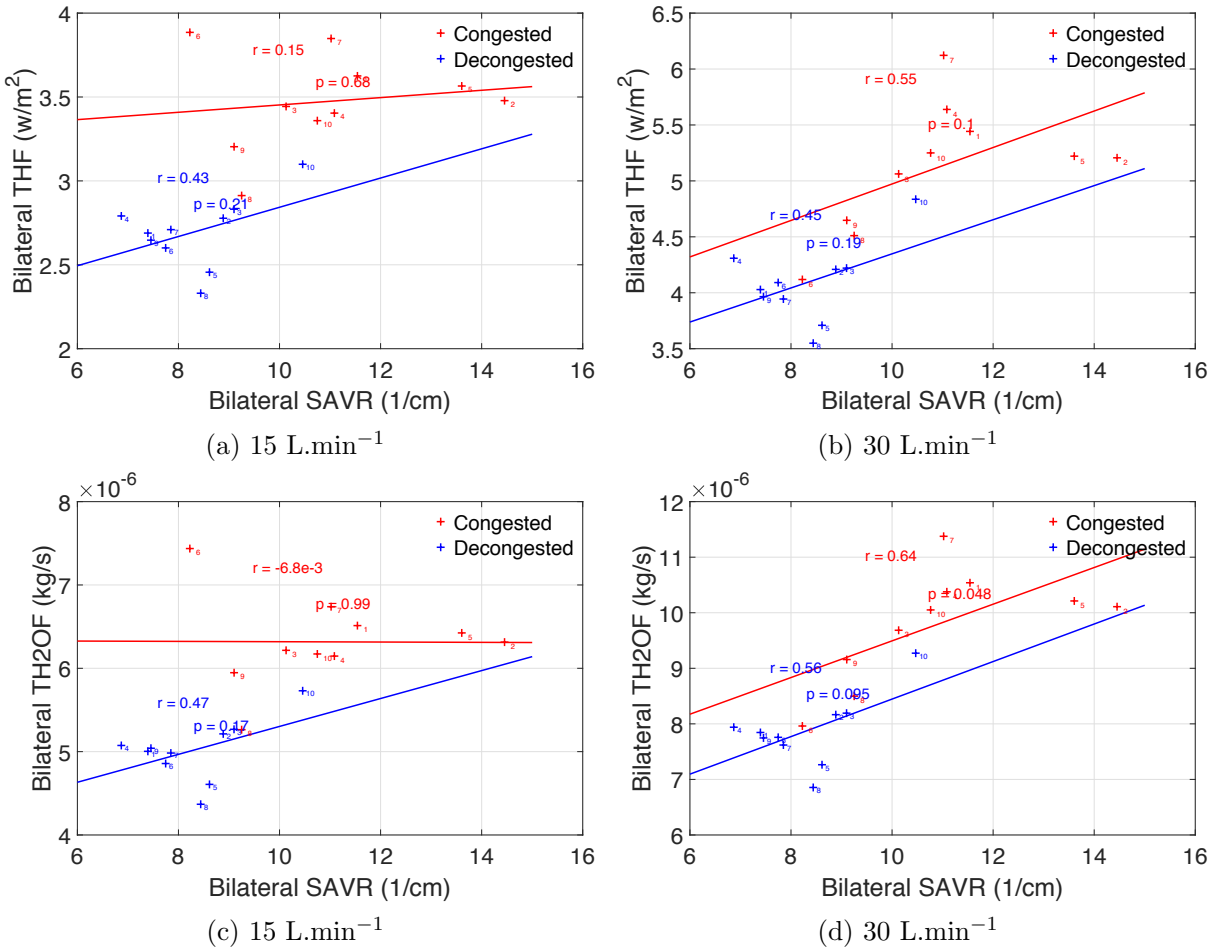
(c) 15 L.min^{-1} (d) 30 L.min^{-1}

Figure B.2: Correlations between NV area and other physical measures.

Appendix C

For chapter 4

C.1 Bilateral SAVR and THF, TH2OF

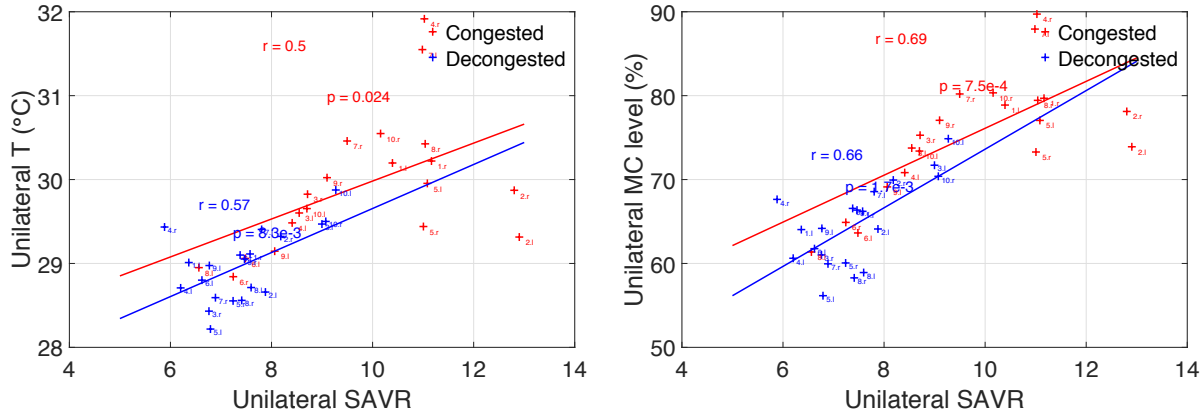


(a) 15 L.min^{-1} (b) 30 L.min^{-1}

(c) 15 L.min^{-1} (d) 30 L.min^{-1}

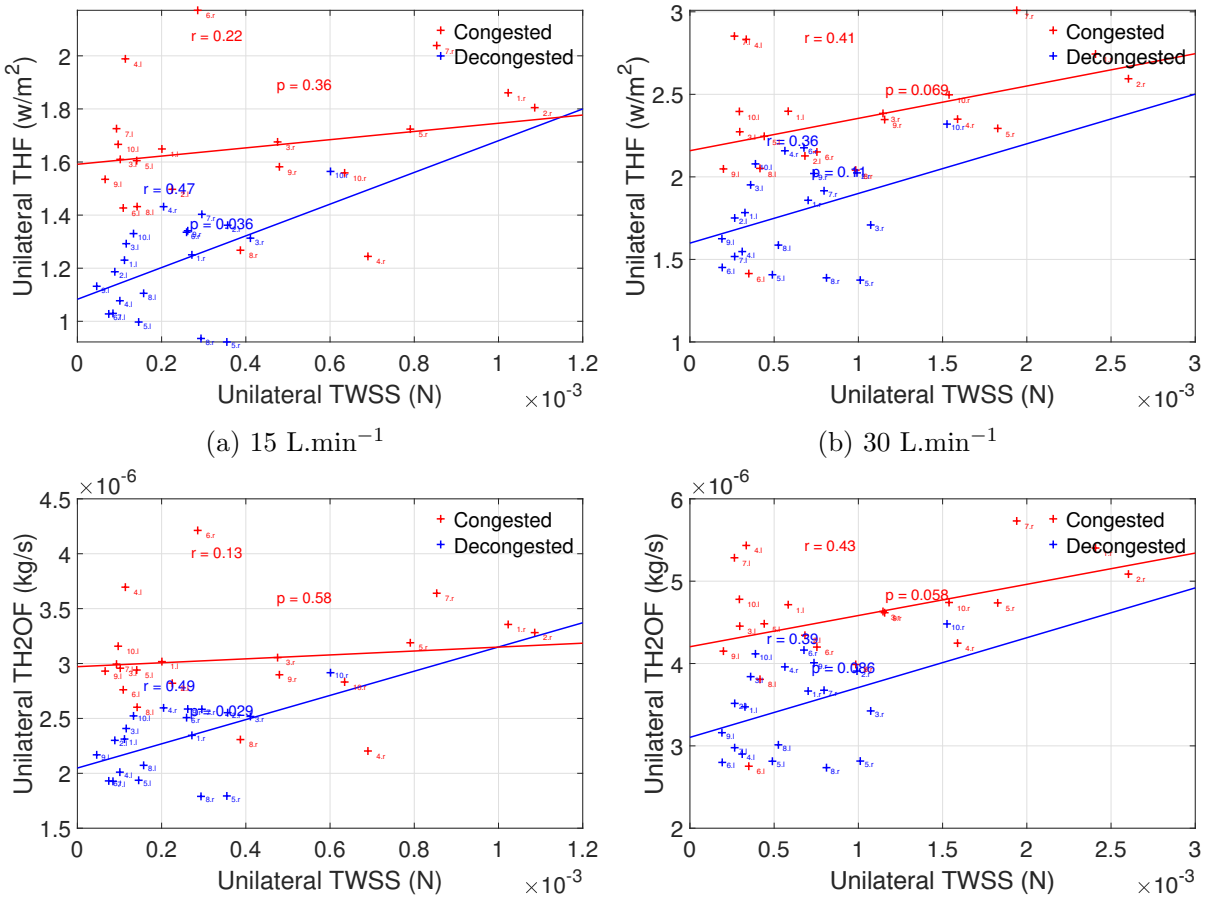
Figure C.1: Bilateral cavity correlations between SAVR and THF and TH2OF.

C.2 Unilateral SAVR correlations



(a) 30 L.min^{-1} (b) 30 L.min^{-1}

Figure C.2: Unilateral cavity correlations between SAVR and posterior septum temperature and moisture content level.



(a) 15 L.min^{-1} (b) 30 L.min^{-1}

(c) 15 L.min^{-1} (d) 30 L.min^{-1}

Figure C.3: Unilateral cavity correlations between total cavity WSS with THF and TH2OF.

Appendix D

For chapter 6

D.1 Convergence Analysis

	2.2million	3.8million	5.8million	10million
Flow Model	LES	LES	LES	qDNS
Time Step (ms)	0.1	0.05	0.05	0.01
First Wall Layer Thickness (mm)	0.03	0.023	0.014	0.005
Number of Prism Layers	5	5	8	10
Prism Layer Thickness (mm)	0.45	0.36	0.45	0.38
Overall Pressure Loss (Pa)	284.8	275.3	274.5	268.7
Relative Error	5.9%	2.4%	2.1%	0%

Table D.1: Mesh convergence check.

Results for a mesh independence check are shown in table D.1. A quasi-DNS simulation employing a 10 million element mesh and 10^{-5} s time step served as a benchmark. Table D.1 shows that when the mesh resolution increases from 3.8 million to 5.8 million, the reduction of the relative error is modest and both are within 2.5% of the qDNS result, deemed acceptable for loss estimation given other uncertainties associated with geometry definition. The cost of

LES simulation is high: 3.8 million elements requiring 2272 core-hours on a HP workstation with two Intel(R) Xeon(R) CPU E5-2630 v3@2.4GHz processors. .

D.2 Work-Energy Balance

The relation between the flow work-energy balance and pressure is described at some length by Donati et al [175]. For the case of a rigid duct, and neglecting the contribution of boundary shear work, the equation simplifies to

$$\frac{\partial}{\partial t}\int_V \frac{1}{2}\rho|\mathbf{u}|^2 dV + \int_{S_1 \cup S_2} (\mathbf{u}\cdot\mathbf{n})[P_s + \frac{1}{2}\rho|\mathbf{u}|^2]dS = \int_V \Phi dV \tag{D.1}$$

where V is the volume of the duct between inflow and outflow planes S_1 and S_2 respectively, Φ represents the dissipation function, $\Phi = \tau : \nabla\mathbf{u}$ with τ the viscous stress tensor. For steady inflow conditions, time averaging removes the fluctuating (turbulent) kinetic energy represented in the first term, and from the above, the difference in total energy flux at some station "i"

$$E_{F,i}\int_S (\mathbf{u}\cdot\mathbf{n})[P_s + \frac{1}{2}\rho|\mathbf{u}|^2]dS \tag{D.2}$$

and that at inflow reveals the accumulated energy loss in the volume from inflow to the specified station.

D.3 Turbulence Intensity and Wall Shear Stress

Conventionally, the formula of calculating turbulence intensity is defined by:

$$TI = \frac{u^{'}}{U} \tag{D.3}$$

where $u^{'}$ is the root mean square of the velocity fluctuations and U is the mean velocity. Within this study, the mean velocity is defined by the mean velocity at the first trachea ring and used

for all the other cases as a reference value (4.2 m/s).

Figure D.1 compares the wall shear stress on the back of the trachea of all the T15 geometries. As shown, As shown, regions of elevated shear stress correspond both to the constriction and to the impingement of the downstream jet on the trachea wall. There is a marked variation across the various T15 geometries for the shear stress at impingement, with T15 and T15-SG1 corresponding most closely, reflecting the similar breakup of the jet flow in both cases. There is however a pronounced difference in impingement wall shear stress for the simple, truncated geometry (T15-S), compared to all cases incorporating a real or modelled glottis.

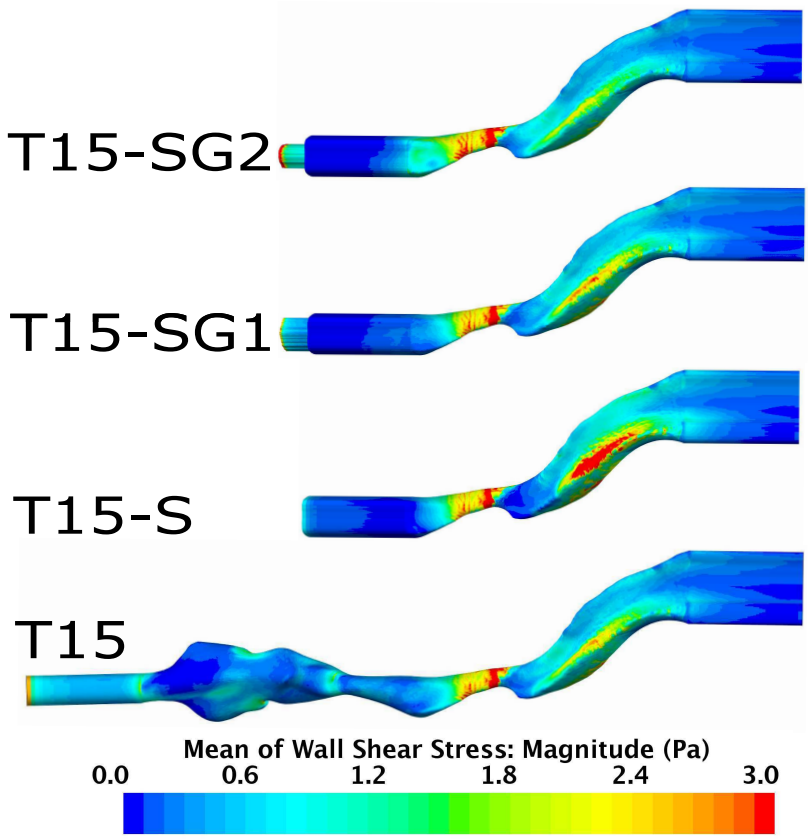


Figure D.1: Wall shear stress is shown on the back of trachea surface.

Figure D.2 shows the static pressure recovery within various inflow conditions of T15 case, showing that prolonging the jet breakdown leads to significantly greater differences in the immediate static pressure recovery than was found for total pressure.

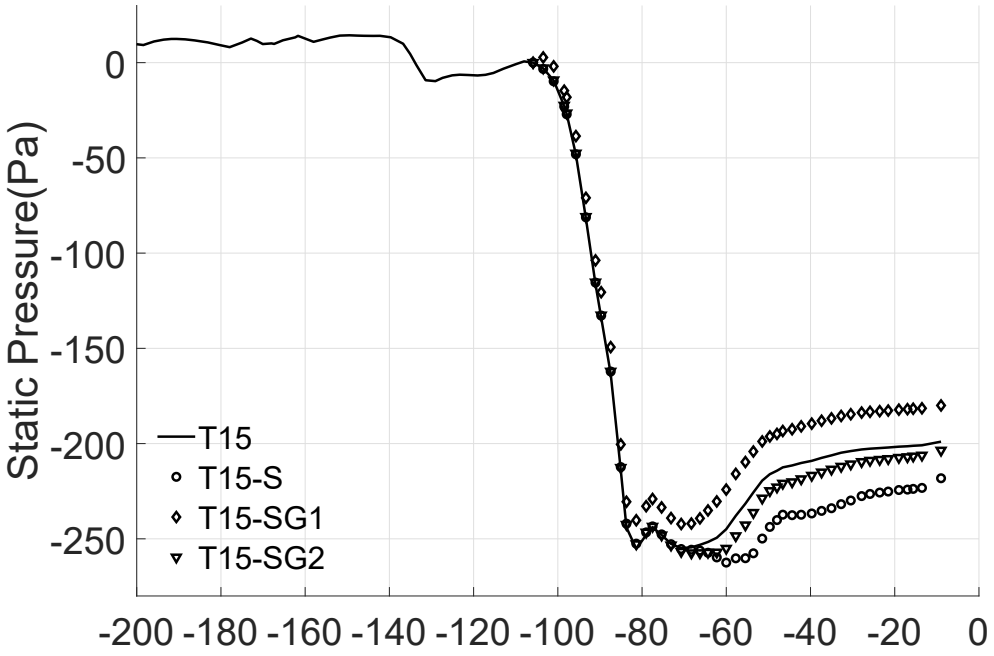


Figure D.2: Static pressure distribution of T15 related geometries.

D.4 Pressure Loss of T4-L

Flow rate (l/min)	23.5
T4-L. Overall pressure loss (Pa)	109
T4-L. Bronchi pressure loss (Pa)	4

Table D.2: Pressure loss over bronchi of T4-L.

D.5 Flow loss factors

Traditionally, losses due to restrictions or orifices are estimated using pressure loss factors of the form

$$\Delta P = \frac{1}{2}\rho K \frac{Q^2}{{A_C}^2} = \frac{1}{2}\rho K V_C^2, \tag{D.4}$$

where Q is the flow rate, A_C is the contraction area and V_C is the jet velocity at the constriction. For the overall resistance of a manufactured duct, various correlations exist, e.g. ESDU data sheet [176] for localised loss factors, to which are added estimated losses due to pipe friction. Anatomical geometries, being irregular are devoid of neatly defined geometries and are more difficult to characterise. In their study of losses associated with tracheal stenosis Brouns et al [19], found that applying an average value for K of 1.2 gave a good fit to predict losses over the range of constrictions (50% to 90% reduction in tracheal lumen area) studied in their idealised stenotic tracheal geometry. Similarly, for contraction ratios between 75% and 85%, ref [176] suggests K values in the range 1 to 1.2 as appropriate for the longer constriction lengths observed here (length/diameter of narrowest region $\sim$ 3 - 4, fig 6.4, (derived by choosing ESDU parameters λ_b=0.9, and $K_{0.8}$ in the range 1.35 - 1.15).